



UDR-TR-2008-00064

Report

IMPROVED NAVY MAINTENANCE THROUGH CORROSION-FATIGUE ASSESSMENT PROGRAM

.....

March 2008

Wally Hoppe



Report Documentation Page			Form Approved OMB No. 0704-0188		
Public reporting burden for the collection of information is estimated to average 1 hour per response, including the time for reviewing instructions, searching existing data sources, gathering and maintaining the data needed, and completing and reviewing the collection of information. Send comments regarding this burden estimate or any other aspect of this collection of information, including suggestions for reducing this burden, to Washington Headquarters Services, Directorate for Information Operations and Reports, 1215 Jefferson Davis Highway, Suite 1204, Arlington VA 22202-4302. Respondents should be aware that notwithstanding any other provision of law, no person shall be subject to a penalty for failing to comply with a collection of information if it does not display a currently valid OMB control number.					
1. REPORT DATE MAR 2008		2. REPORT TYPE Technical Report		3. DATES COVERED 16-09-2005 to 25-09-2007	
4. TITLE AND SUBTITLE Improved Navy Maintenance Through Corrosion-Fatigue Assessment Program			5a. CONTRACT NUMBER		
			5b. GRANT NUMBER		
			5c. PROGRAM ELEMENT NUMBER		
6. AUTHOR(S) Wally Hoppe			5d. PROJECT NUMBER		
			5e. TASK NUMBER		
			5f. WORK UNIT NUMBER		
7. PERFORMING ORGANIZATION NAME(S) AND ADDRESS(ES) University of Dayton Research Institute, Structural Integrity Division, 300 College Park, Dayton, OH, 45469-0120			8. PERFORMING ORGANIZATION REPORT NUMBER UDR-TR-2008-00064		
9. SPONSORING/MONITORING AGENCY NAME(S) AND ADDRESS(ES) Naval Air Systems Command, 47123 Buse Road, Patuxent River, MD, 20670-1547			10. SPONSOR/MONITOR'S ACRONYM(S)		
			11. SPONSOR/MONITOR'S REPORT NUMBER(S)		
12. DISTRIBUTION/AVAILABILITY STATEMENT Approved for public release; distribution unlimited					
13. SUPPLEMENTARY NOTES					
14. ABSTRACT The High-Strength Steel Corrosion-Fatigue Assessment program was designed to ensure reliability and supportability of current and emerging Naval aircraft by providing requisite engineering support to evaluate issues relevant to corrosion-fatigue of aircraft components. In this multi-year, multi-contract program, tools have been developed to assist in the establishment of maintenance options for corroded components. Experimental and analytical tools have been developed to classify corrosion in a manner tied to a reduction in fatigue life, to assess corrosion classifications by corrosion metrics, to measure these metrics with nondestructive methods, and to model the effect of corrosion on fatigue life. This report describes the work accomplished during the second two years and second contract of the program.					
15. SUBJECT TERMS High-Strength Steel; AF1410; Corrosion; Fatigue; Inspection; Crack Initiation; Metrics; Corrosion Methods					
16. SECURITY CLASSIFICATION OF:			17. LIMITATION OF ABSTRACT Same as Report (SAR)	18. NUMBER OF PAGES 236	19a. NAME OF RESPONSIBLE PERSON
a. REPORT unclassified	b. ABSTRACT unclassified	c. THIS PAGE unclassified			

**IMPROVED NAVY MAINTENANCE THROUGH CORROSION-FATIGUE
ASSESSMENT PROGRAM**

Contract No.: F4260-00-D-0028, 0040

March 11, 2008

FINAL REPORT

Prepared for:

Dr. Paul Hoffman
Government Technical Program Manager
Naval Air Warfare Center – Aircraft Division
Code 4.3.3.1
48110 Shaw Rd., Unit 5
Patuxent River, MD 20670-1906

Prepared by:

Wally Hoppe, Principal Investigator
UNIVERSITY OF DAYTON RESEARCH INSTITUTE
Structural Integrity Division
300 College Park
Dayton, OH 45469-0120

Table of Contents

	Page
SECTION 1 Executive Summary	1
SECTION 2 Introduction	3
2.0 Background.....	3
2.1 Purpose and Goals	3
2.2 Relationship to other Contracts/Programs	4
2.3 Summary of Accomplishments.....	5
SECTION 3 Effects of Corrosion Damage on Fatigue Life	12
3.0 Introduction.....	12
3.1 Corrosion-Fatigue Tests on AF1410 Set A	12
3.2 Tests on AF1410 Set B	14
3.3 Supporting Tests on AF1410 Set B	14
3.4 Tests on 300M.....	14
SECTION 4 Metric Development.....	17
4.0 Introduction.....	17
4.1 Roughness Metrics.....	17
4.2 K_t Metrics.....	22
4.3 Resolution Study	24
SECTION 5 Modeling	28
5.0 Introduction.....	28
5.1 Review of FEA, Pit Metric and Elasticity Approaches	28
5.2 Review of ESRD Modeling Studies	34
5.3 Region of Interest (ROI) Analysis	35
5.4 Reliability Modeling	37
5.4.1 Pixel/Area Approach	38
5.4.2 Equivalent Stress Riser Approach.....	43
SECTION 6 Nondestructive Evaluation	45
6.0 Introduction.....	45
6.1 Ultrasonic Inspection of Corrosion-Fatigue Specimens	45
6.2 Eddy Current Inspection of Corrosion-Fatigue Specimens	48
6.3 Global Statistics	49
SECTION 7 Implementation Scheme	51
SECTION 8 Conclusion.....	53
SECTION 9 References	54
 APPENDIX A ESRD Final Report.....	 A-1
APPENDIX B ESRD StressCheck [®] Implementation Report.....	B-1
APPENDIX C Boeing Final Report	C-1
APPENDIX D Computational Mechanics Inc. Final Report.....	D-1
APPENDIX E Computational Mechanics Software Instructions & Examples.....	E-1
APPENDIX F Abbreviations and Symbols	F-1

List of Figures

	Page
Figure 3.1-1	AF1410 Set A Fatigue Test Results13
Figure 3.4-1	SEM images of Crack 1 on Specimen 622-215
Figure 3.4-2	Electron Induced X-ray Analysis performed on the specimen showing the composition of the inclusion16
Figure 4.1-1	Average Surface Profile Roughness vs. Crack Initiation Life for AF141018
Figure 4.1-2	RMS Surface Profile Roughness vs. Crack Initiation Life for AF141019
Figure 4.1-3	Normalized Volume Loss vs. Crack Initiation Life for AF141019
Figure 4.1-4	Average Surface Profile Roughness vs. Crack Initiation Life for AF141021
Figure 4.1-5	RMS Surface Profile Roughness vs. Crack Initiation Life for AF1410 plotted as a function of maximum applied load21
Figure 4.1-6	Normalized Volume Loss vs. Crack Initiation Life for AF141022
Figure 4.2-1	Stress Weighted Average Surface Profile Roughness vs. Crack Initiation Life...23
Figure 4.2-2	Stress Weighted RMS Surface Profile Roughness vs. Crack Initiation Life23
Figure 4.2-3	Stress Weighted Normalized Volume Loss vs. Crack Initiation Life24
Figure 4.3-1	Normalized RMS vs. Gaussian Blur Full Width at Half Maximum 1 hr. exposure26
Figure 4.3-2	Normalized RMS vs. Gaussian Blur Full Width at Half Maximum 3 hr. exposure26
Figure 4.3-3	Normalized RMS vs. Gaussian Blur Full Width at Half Maximum 6-hr. exposure27
Figure 5.1-1	Candidate pit metric for stress concentration factor estimation30
Figure 5.1-2	Elasticity approach for corroded surface modeling31
Figure 5.1-3	Elasticity solution for each surface profile frequency component32
Figure 5.1-4	Combined stress concentration factor implications33
Figure 5.4.1-1	Predicted life distribution for corrosion-fatigue Set A specimen 1642
Figure 5.4.1-2	Life predictions using the pixel/area model & experimental lives to crack initiation43
Figure 6.1-1	Example Ultrasonic Time-of-Flight and White Light Interference Microscope Profiles for 3-hr. exposure48
Figure 6.2-1	Example Eddy Current Liftoff and White Light Interference Microscope Profiles for 3-hr. exposure49
Figure 6.3-1	R_a from White Light Interference Microscope Profiles vs. R_a from Ultrasonic Time-of-Flight Profiles50
Figure 6.3-2	R_q from White Light Interference Microscope Profiles vs. R_a from Ultrasonic Time-of-flight Profiles50
Figure 7.1	Implementation Strategy52

List of Tables

	Page
Table 3.1-1	Corrosion Critical Notch Sizes for AF141013
Table 4.1-1	Summary of Surface Metrics18
Table 6.1-1	Typical Ultrasonic Setup Parameters46
Table 6.1-2	Ultrasonic Scan Preparation Procedures47

Foreword

This report describes the technical work accomplished during the period from 16 September 2005 through 25 September 2007, for the Naval Air Warfare Center – Aircraft Division under Contract Number F4260-00-D-0028-0040 under subcontract to Aerospace Engineering Spectrum, Ltd. (AES), which was the prime contractor for the effort. Engineering Software Research and Development, Inc. (ESRD), The Boeing Company and Computational Mechanics, Inc. were the major subcontractors on the program. Dr. Paul Hoffman was the Contract Monitor.

Mr. Wally Hoppe of the UDRI Structural Integrity Division was the Principal Investigator for the contractual effort. Mr. Robert Andrews (until 30 June 2007) and Mr. Michael Bouchard (after 1 July 2007), Division Heads of the Structural Integrity Division, served as overall Program Managers. Ms. Ollie L. Scott and Ms. Gloria Hardy provided program management services and Ms. Andrea Snell manuscript editing. The following UDRI employees contributed to the major accomplishments on this contract: Dr. Bill Braisted, Mr. Garry Abfalter, Ms. Jennifer Pierce, Mr. Eric Burke, Mr. Brian Frock, Mr. Bob Olding, and Dr. Ray Ko. Additional contributors included: Mr. Dave Rusk of NAVAIR; Dr. Barna Szabo, Dr. Ricardo Actis and Mr. Brent Lancaster of ESRD; and, Dr. Krishnan K. Sankaran, Dr. Herb Smith, Jr., and Mr. Bert Neal of Boeing.

Section 1

Executive Summary

In June 2003, UDRI was placed on contract, as prime, to lead in an effort to study the effect that corrosion has on the fatigue life of high-strength steels on Navy applications. In September 2005, UDRI was placed under contract to AES to continue the effort begun by the earlier program. The Navy High-Strength Steel Corrosion-Fatigue Assessment Program and then the Improved Navy Maintenance Through Corrosion-Fatigue Assessment Program were designed to ensure reliability and supportability of current and emerging Naval aircraft by providing requisite engineering support to evaluate issues relevant to corrosion-fatigue of airframe components. Their purpose was to develop tools that can be used to specify the maintenance options for corroded components and to provide a sound engineering basis for selecting the best fleet maintenance options. Essentially, the program was to provide quantifiably justified maintenance criteria for environmentally induced damage (i.e., corrosion) in high-strength steels.

The overall objectives of these programs included the following outcomes:

- A corrosion severity classification scheme (i.e. cosmetic, mild and severe) tied to component reliability or reduction in fatigue life,
- Corrosion metrics associated with these corrosion classifications,
- Nondestructive inspection (NDI) methods, requirements and procedures for measuring corrosion severity via these corrosion metrics, and,
- Component disposition tools and procedures to make engineering disposition decisions based on detailed corrosion profiles and validated life prediction assessment models.

The plan to meet these overall objectives consisted of the following activities: determining the effect of corrosion on fatigue life of high-strength steels through corrosion-fatigue experiments supported by other baseline tests; developing corrosion metrics-based on surface profiles, correlating metrics to life reduction and using these results to develop corrosion classification criteria; investigating and developing NDI methods and procedures that can determine corrosion severity via correlations of NDI to corrosion metrics; and, developing notch-based analysis methods to determine effective stress concentration factors for corrosion – correlating the analysis predictions to corrosion-fatigue tests and validating on component tests.

These research tasks are part of a multi-year, multi-contract program. The first contract was initially funded in June 2003 for one year, followed by a second year of funding and extensions to August 2006. The second contract was awarded in September 2005 for one year and was extended to September 2007. The third and final contract was awarded in September 2006 and will run to 31 March 2008. When completed, the entire effort will have lasted four years and ten months. The University of Dayton Research Institute was prime on the first contract, with Engineering Software Research and Development (ESRD), Inc. and The Boeing Company as subcontractors. UDRI was a subcontractor to AES on the second contract, with ESRD, Boeing, and Computational Mechanics, Inc. as second-tier subcontractors under UDRI. UDRI is again the prime on the third contract to ONR.

This document reports activities under the second of these three contracts supporting the overall objectives of the program. The second program contract has significantly overlapped the timeframe of the first. The second contract has focused on completion of the data acquisition and analysis of the first set of AF1410 corrosion-fatigue specimens, development of reliability models for life prediction, development of corrosion metrics and a corrosion classification scheme, manufacture and test of the second set of AF1410 corrosion-fatigue specimens (without grit blasting) and associated analysis of the test results, preparation of 300M test specimens, and preparation of Aermet 100 test specimens. The final contract on this program will complete all testing and analysis, complete model development and validation, complete corrosion classification descriptions via accepted corrosion metrics, and complete the definition of NDI requirements for transition and implementation of the overall program objectives.

Section 2

Introduction

2.0 Background

Navy carrier-based aircraft employ high-strength steel in many components including landing gear and arrestment shanks. The service life of these components are generally defined by fatigue caused by load cycles. However, aircraft must operate in coastal environments that result in corrosion-assisted fatigue of airframe components. The effect of corrosion on component fatigue life has not been quantified. This problem is most acute for high-strength steel, such that it is important to determine how to quantify remaining life considering both cycle-dependent and time-dependent damage mechanisms. A quantifiable metric must be established to estimate remaining life due to the presence of corrosion.

2.1 Purpose and Goals

The Navy High-Strength Steel Corrosion-Fatigue Assessment and the following programs were designed to ensure reliability and supportability of current and emerging Naval aircraft by providing requisite engineering support to evaluate issues relevant to corrosion-fatigue of airframe components. The purpose was to develop tools that can be used to specify the maintenance options for corroded components and to provide a sound engineering basis for selecting the best fleet maintenance options. Essentially, the program was to provide quantifiably justified maintenance criteria for environmentally induced damage (i.e., corrosion) in high-strength steels.

The overall objectives of this program included the following outcomes:

- A corrosion severity classification scheme (i.e., cosmetic, mild, and severe) tied to component reliability or reduction in fatigue life,
- Corrosion metrics associated with these corrosion classifications,
- Nondestructive inspection (NDI) methods, requirements, and procedures for measuring corrosion severity via these corrosion metrics, and
- Component disposition tools and procedures to make engineering disposition decisions based on detailed corrosion profiles and validated life prediction assessment models.

The plan to meet these overall objectives consisted of the following activities:

- Determine the effect of corrosion on fatigue life of high-strength steels through corrosion-fatigue experiments supported by other baseline tests;
- Develop corrosion metrics based on surface profiles, correlating metrics to life reduction and using these results to develop corrosion classification criteria;
- Investigate and develop NDI methods and procedures that can determine corrosion severity via correlations of NDI to corrosion metrics; and,
- Develop notch-based analysis methods to determine effective stress concentration factors for corrosion, correlating the analysis predictions to corrosion-fatigue tests and validating on component tests.

2.2 Relationship to Other Contracts/Programs

These research tasks are part of a multi-year, multi-contract program. The first contract was initially funded in June 2003 for one year, followed by a second year of funding and extensions to August 2006. The second contract was awarded in September 2005 for one year and was extended to September 2007. The third and final contract was awarded in September 2006 for one year and was extended to March 2008. When completed, the entire effort will have lasted four years and ten months. The University of Dayton Research Institute was prime on the first contract, with Engineering Software Research and Development (ESRD), Inc. and The Boeing Company as subcontractors. UDRI was a subcontractor to AES on the second contract, with ESRD, Boeing, and Computational Mechanics, Inc. as second-tier subcontractors under UDRI. UDRI is again prime on the third contract to ONR. The ESRD Final Report for the second contract is included in this report in Appendix A. The ESRD Implementation Report for variable materials properties is given in Appendix B. The Boeing Final Report for the second contract is found in Appendix C. The Computational Mechanics, Inc. final report is included in Appendix D. While these subcontractors have played important roles in this program, specific references to their final reports are not necessarily made in this report. Details of their activities are found in the respective final reports.

2.3 Summary of Accomplishments

This document reports activities under the second of these three contracts supporting the overall objectives of the program. Specific activities during this timeframe have made use of the tools and methods developed during the first contract and reported on in the final report of that program [1]. Activities of the second contract focused primarily on test and characterization of corrosion-fatigue experiments, as well as developing methods to model the effect that corrosion topography has on fatigue, including the development of reliability methods for predicting life of corroded components. A transition plan was also developed during this period.

During the first contract, NAVAIR, UDRI, and its team members designed, manufactured, and subsequently tested in fatigue 54 AF 1410 corrosion-fatigue test specimens. Each specimen had been prepared according to a test matrix that included growing corrosion according to a UDRI-developed protocol for various exposure times: zero, 3, 6, and 12 hours, respectively, using the electrochemical method developed for this purpose. Subsequent to growing corrosion in circular patches, the specimens were cleaned in a Turco solution to remove the corrosion products without further altering the specimen surface. After this, the specimens were ultrasonically inspected. Later, specimens were also eddy current inspected. The final step prior to fatigue testing provided high-resolution surface profiles of the corroded surface via a white light interference microscopic system. The test matrix also stipulated load conditions covering a range of loads of interest. During test, marker bands were introduced on any fracture surface by varying the R value of the load in a predetermined manner. In addition, some specimens were monitored by penetrent inspections to identify crack initiation sites. As of the end of the first contract, all AF1410 specimens in the first set had been fatigued until failure. Several specimens had been subject to additional investigation to attempt preliminary validation of models being developed as described below. Results of these tests in terms of peak stress versus cycles to crack initiation were reported in the final report.

Also, during the first contract, a significant effort was put forth to develop corrosion-fatigue models. Initial efforts were directed at implementation of finite element analysis (FEA) methods to calculate stress concentration due to the corrosion based on detailed profiles of the corrosion surface. This approach was discovered to be intractable, in that the FEA mesh required to capture the fine details of the corrosion surface made computation so excessively long, as to

be impossible. Further efforts to simplify the surface profile produced unreliable FEA results, given that the simplifications that were designed to reduce computation time required more manageable meshes, which were then not representative of the actual surface profile. Similarly, efforts to simplify the corrosion details by assuming simpler geometric profiles, such as rounded cones, produced stress concentrations that were overly dependent on small changes in the assumed shape of the corrosion feature.

In parallel with these efforts, a study was being conducted to develop so-called global/local models, which attempted to provide the requisite detail at a local level, while using less detail at the global level. Unfortunately, these approaches were also unsuccessful.

In a related study, a pit metric was developed that could estimate the stress concentration of a semi-ellipsoidal pit with a simple formula, based on the dimensions of the principal axes of the pit and also accounting for load direction. This simple formula was used in further developments later in the program.

When faced with the intractable nature of the FEA methods to the problem of calculating the stress concentration of a corroded surface, UDRI took an innovative tact to the problem by decomposing the surface into two-dimensional spatial frequency components. The stress concentration for each component was then estimated and the net effect of all components was determined by an inverse Fourier Transform. The theoretical basis for this admittedly approximate method to determine stress concentration is documented in the final report of the first contract on this program. Also included in that report are results of case studies performed to compare this so-called elasticity approach to FEA results for special cases. These studies defined practical limits for the applicability of the elasticity solution, which happen to be realistic for the levels of corrosion of interest on this program. That is, the levels of corrosion seen in the specimens tested on this program fall well within the region that should produce small errors in the estimation of stress concentration. There is, to be sure, a residual concern over this approach, or any approach, that is limited by the resolution of the surface profile. However, there is hope, as will be seen later, that the extremely small features that would produce large stress concentrations might be mitigated by a notch size effect.

Near the end of the first contract, the elasticity approach to estimation of stress concentration was tested by comparing the location of crack initiation sites on corroded specimens with the high-stress regions found from the elasticity solution. The results on these preliminary checks were exceptionally promising and indicated that, while not all high-stress points cracked, all cracks did initiate in high-stress regions and very near the peak stress in that local area. Additional validation of this model would have to wait until the second contract.

An issue arose during the development and execution of the first set of AF1410 corrosion-fatigue tests (Set A specimens). The associated specimens had been grit blasted and were suspected to have a resultant residual stress. After X-ray diffraction measurements confirmed this suspicion, a decision was made to manufacture a second set of AF1410 specimens which was started during the first contract.

It was also of interest to extend the methods being developed to other high-strength steels, such as 300M. However, previously conducted tests on a USAF program suggested that 300M would be extremely sensitive to corrosion attack, possibly due to the introduction of intergranular corrosion. A decision was made to test only nine 300M corrosion-fatigue specimens to confirm the results of the USAF study. Creation of these specimens was started on the first contract on the Navy Corrosion-Fatigue program.

Aermet 100 was also selected for study. Specimen manufacture and tests on this material were primarily the focus of the third contract.

A nondestructive evaluation (NDE) investigation was also conducted on the first contract. After studying several methods to address the problem, it was concluded that the most promising NDE method is ultrasound. Subsequently, a series of ultrasonic measurements were made of various corroded surfaces. Included in these experiments were angle beam, and normal incidence pulse-echo techniques using amplitude, time-of-flight, and frequency domain techniques. Normal incidence time-of-flight and Fourier phase slope methods seemed the most promising of the techniques.

As it has turned out, the second program contract significantly overlapped the timeframe of the first. Activities on the second contract have focused on completion of AF1410 Set A tests, completion of AF1410 Set B tests, extending the modeling effort to reliability models for life prediction, development of corrosion metrics, preparation of 300M and Aermet 100 specimens (including preliminary tests on these materials), and the development of an implementation scheme.

To finish the analysis of the AF1410 Set A corrosion-fatigue tests, each fracture surface on the specimens was compared to the corrosion profile on the adjacent surface to identify the corrosion feature that initiated the crack. Dimensional measurements were taken of each corrosion feature and used to estimate stress concentration factors. Simple life predictions based on these estimates were compared to actual life measured in the fatigue tests.

Baseline and corrosion-fatigue tests were conducted in a second batch of AF1410 (Set B) specimens. The corrosion-fatigue specimens were designed to exclude the grit blasting. They also had smoother surfaces than Set A. As a result of both of these facts, the test matrix included lighter corrosion exposure levels: zero, 1.5, 3, and 6 hours, respectively. As was true of the first set, this set was prepared in the same way, including ultrasonic and eddy current, as well as white light interference measurements of the surface profile. After fatigue testing, each specimen was examined to microscopically ascertain the number of cycles to crack initiation and to measure the dimensions of the critical feature, which initiated the crack.

A small number of 300M corrosion-fatigue specimens were manufactured for the purpose of verifying the results of the earlier USAF study showing that 300M could tolerate very little corrosion without losing the majority of its fatigue life. Other associated tests were conducted in anticipation of these fatigue tests. Unfortunately, once fatigue testing was initiated and as fracture surfaces were examined, it became apparent that the batch of 300M that was used for these specimens, including earlier NAVAIR strain-life specimens, was contaminated with titanium inclusions. This contamination renders all test specimens and previous test results of little value. At this point, these activities on 300M were terminated.

In the interest of extending the methods developed on this program to other materials, quantities of Aermet 100 were purchased and the manufacture of test specimens was initiated.

A major objective of this program was to develop modeling techniques to predict the effect that corrosion-induced surface roughness has on fatigue life. As mentioned above, an elasticity approach had been developed on the first contract to estimate the stress concentration due to corrosion. On the second contract, the results of this method were compared to the stress concentration calculated on pits using FEA and the UDRI pit metric. It was found that, while the elasticity approach could identify spots of high stress, it did not always find stress concentrations in precise agreement with FEA.

In addition to this finding, attempts to make life predictions directly from the stress concentration map from the elasticity model were unsuccessful. In particular, UDRI attempted to make life predictions based on the stress concentration maps by treating each pixel in the map as having a certain probability of failure that was based on extensions of Weibull's formalism, accounting for area effects in the same way Weibull accounted for specimen length. The probability of failure of each pixel was calculated using the stress concentration, the stress-strain curve, a fit to the Coffin-Manson relationship for strain-life data, Morrow's factor, and an extension of the Weibull formalism to account for pixel size. A statistical manipulation then produced the probability of failure (to crack initiation in this case) for all pixels in the corrosion patch. Preliminary trials were encouraging, but additional test cases revealed that the method was not always conservative in its predictions.

Subsequent to the above discoveries, NAVAIR developed the Equivalent Stress Riser (ESR) model, which models the life – not of pixels, but of individual pit-like features in the corrosion identified by the elasticity model. The stress concentration for each feature is estimated using the UDRI pit metric, as improved by ESRD's extension to account for both differences between FEA results and the pit metric and pit orientation with respect to load direction. In the ESR model, the probability of failure is calculated from strain-life data and a Peterson notch sensitivity factor, which moderates the effect of the stress riser by a factor dependent on the size of the notch. In particular, notches with smaller root radii are hypothesized to have smaller effects on life than notches with the same stress concentration, but larger root radii. The cumulative effect of all features is handled probabilistically. A set of algorithms was developed on the program to search through the stress concentration map to find regions of interest (ROIs) with high stress concentration. An ellipsoid is fit to each ROI and the root radii are estimated. Tests of the ESR model on the corrosion-fatigue specimens have shown a consistent conservativeness in the life predictions. The question of how to deal with this conservativeness was a topic for the third contract and is reported in the corresponding final report.

In parallel with efforts to develop life prediction models, a study of various statistical metrics for corrosion severity was conducted. In particular, standard and novel roughness statistics were calculated and compared to corrosion-fatigue test results to investigate the effectiveness of each candidate metric as a measure of both corrosion severity and effect on fatigue life. Standard roughness metrics included R_a , the mean of the absolute difference between the surface height and the mean surface height, and R_q , the standard deviation of the surface height (or more accurately, the root-mean-square of the surface height). Variations on these metrics included scaling the metric by the applied load and constructs involving the stress concentration values. While some of these novel metrics showed improved correlations to reduction in fatigue life, the improvements were marginal. R_q and R_a seem to provide the most robust metrics for surface roughness; however, there remains a need to account for the local applied load. In addition, studies were carried out to understand the effect of spatial resolution on the metric values and on correlation to reduction in fatigue life. This work anticipates the ultimate implementation of low-resolution NDE methods to screen components and categorize corrosion severity. Down-sampled and filtered white light surface height profiles were used to calculate surface roughness metrics, which were then compared to the same metrics determined from full-resolution surface height profiles.

Finally, during the second contract on the Navy Corrosion-Fatigue Assessment Program, an implementation strategy was developed. This scheme is described by a flow chart starting with a visual inspection of the component on-board an aircraft carrier. If corrosion is observed, it is cleaned and an inspection performed. The relatively low resolution of this inspection prohibits a detailed application of the equivalent stress riser model; however, the inspection can be used to calculate corrosion metrics, such as R_a or R_q , and then to classify the corrosion as cosmetic, mild, or severe. If the corrosion is cosmetic, it will have no significant impact on component life and the component can be cleaned and coated (to prevent corrosion) and returned to service. If the corrosion is deemed to be severe, then the component is removed from service; the reduction in fatigue life is too great to allow the component to remain in service. If the corrosion is mild, then a replica is made of the corrosion, which is then sent to the depot for a high-resolution surface height mapping and subsequent analysis. At this point, the Equivalent Stress Riser model is applied in order to make a disposition decision concerning the component.

Just as there was much overlap in schedule between the first and second contracts on this program, there was much overlap between the second and third. During the third contract, the program focused on AF1410 arrestment shank life predictions and fatigue tests, continued preparation of Aermet 100 tests (some of which were started), investigations into methods to calibrate the ESR model, NDI resolution studies, development of a grid method of corrosion classification, and verification and validation of the various models developed on the program. Verification and validation included both a series of tests on micro-machined fatigue test specimens and manufacture and tests of cadmium-plated AF1410 corrosion-fatigue test specimens.

This report and the other reports referenced herein, give detail to the above accomplishment on this second program contract.

Section 3

Effects of Corrosion Damage on Fatigue Life

3.0 Introduction

A key component of this program has been the creation of a statistically significant database of test results that could be used to support the creation and validation of models to predict cycles to crack initiation in high-strength steels. As part of the first contract on the program, a set of AF1410 corrosion-fatigue test specimens were manufactured and tested. Supporting material property tests were conducted, including fatigue crack growth rate tests and various others. These results were reported in the final report of the first contract [1]. Subsequent to the end of the first contract, additional measurements were made of the crack initiation sites on the AF1410 Set A corrosion-fatigue specimens. These results are reported in Section 3.1. Additional analysis on these specimens is included as part of the discussion of model development elsewhere in this report.

One challenge encountered in the first tests on AF1410 was that large residual stresses were left in the surface of the corrosion-fatigue test specimens due to the grit-blasting process that was applied to them. Consequently, a second set of AF1410 corrosion-fatigue specimens, without the grit-blasting step, was manufactured as part of the second contract. Additional supporting tests were also accomplished on this second batch of AF1410 specimens. Sections 3.2 and 3.3 deal with these tests.

With the intent of extending the program to other high-strength steels, a set of 300M steel corrosion-fatigue specimens were prepared. As previously documented [1], an Air Force study indicated that 300M is highly sensitive to corrosion, in that a large majority of the fatigue life is lost with a minimal corrosion attack. This is likely due to intergranular corrosion. Consequently, only a small number of corrosion-fatigue tests and test specimens were planned in order to simply confirm the results of the Air Force study. Section 3.4 summarizes what was found in these 300M tests.

3.1 Corrosion-Fatigue Tests on AF1410 Set A

Figure 3.1-1 shows a plot of the AF1410 Set A (or Batch A) fatigue test results.

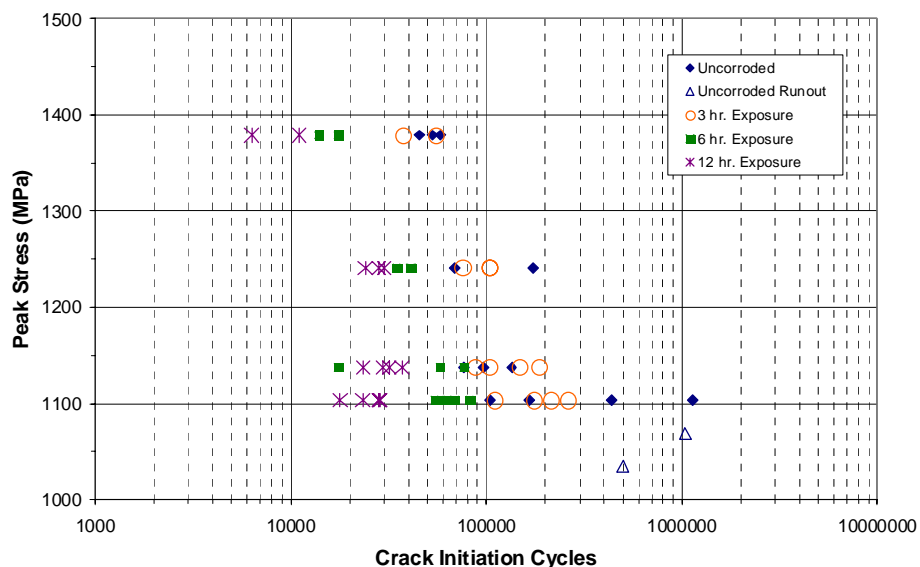


Figure 3.1-1. AF1410 Set A fatigue test results.

Each corroded AF1410 Set A corrosion-fatigue specimen was examined microscopically to identify the corrosion feature at which the crack initiated. Each critical feature (or notch) was measured to determine its length, width, and depth. Table 3.1-1 lists the critical notch sizes for this set and these values were used in the development of the corrosion-fatigue model described in Section 5.

Table 3.1-1. Corrosion Critical Notch Sizes for AF1410 Set A Corrosion-Fatigue Tests

Specimen	Combined Notch Dimensions		
	Width (μm)	Height (μm)	Depth (μm)
3-Hr. Exposure			
15	138	48	21
29	134	61	43
62	217	56	28
36	69	38	23
21	119	36	29
6-Hr. Exposure			
41	109	75	41
37	166	78	35
59	128	70	28
14	75	64	21
6	151	61	29
12	179	86	29
58	165	63	40
5	70	66	28
20	74	75	41
42	124	83	61
12-Hr. Exposure			
35	332	85	88
46	342	115	90
38	635	119	96

3.2 Corrosion-Fatigue Tests on AF1410 Set B

A total of 62 corrosion-fatigue test specimens were tested from a second set of AF1410. Four different corrosion exposure levels were applied to the specimens: zero, 1.5, 3, and 6 hours of exposure with the electrochemical method described more fully in the final report of the first contract on this program [1]. Corrosion products were chemically removed and the surface profiles mapped with the white light interference microscope as well as ultrasound and, in many cases, eddy current inspections. Specimens were tested in fatigue to selected maximum loads with marker bands introduced periodically. After testing, each fracture surface was examined to quantify the number of cycles to crack initiation. Further measurements identified the corrosion feature at which the crack initiated. Surface profiles were also analyzed to estimate stress concentration and regions-of-interest (ROIs) on the surface of the corrosion patch. These steps provided input for the modeling efforts described in more detail in Section 5 and the metric development study described in Section 4. Details of these AF1410 Set B corrosion-fatigue tests are found in the report given in Reference 3.

3.3 Supporting Tests on AF1410 Set B

A series of supporting tests were conducted on the second batch of AF1410 high-strength steel. These tests are also summarized in Reference 3.

3.4 Tests on 300M

In anticipation of conducting corrosion-fatigue tests on 300M high-strength steel, NAVAIR purchased a quantity of material and manufactured a large number of strain-life specimens. A portion of this material was made available to UDRI to manufacture corrosion-fatigue and associated materials property test specimens. NAVAIR subsequently had an entire suite of strain-life tests performed. UDRI manufactured appropriate test specimens and conducted several tests. Additionally, material and microscopic examinations were performed on the actual Air Force corroded fatigue specimens. A study was conducted of various corrosion growth methods and another to investigate whether or not the corrosion growth method would adversely affect the material composition of the alloy. Time-of-exposure tests were conducted on 300M wafers and a plan was prepared defining how to grow corrosion of appropriate severity on the corrosion-fatigue specimens. Tests were conducted to ascertain a proper method of removing the corrosion products without further damaging the base material. After the preliminary work was completed, work started to

prepare and test the corrosion and baseline fatigue specimens. This included removing corrosion products and taking white light profiles of the corrosion surfaces.

Fatigue tests were initiated and the first baseline (uncorroded) specimen failed prematurely. Microscopic examination and materials characterization tests revealed the presence of microscopic titanium inclusions. Figure 3.4-1 is (a) an SEM image from fatigue specimen 622-2 showing the fracture surface and the initiation site for one of two cracks on this specimen, and (b) an SEM at higher magnification showing a cubic-shaped inclusion just below the surface at which the crack initiated. The other crack on this specimen also initiated at a near-surface subsurface inclusion. This specimen was tested at room temperature with $R = 0.1$ and maximum stress of 170 ksi – the crack initiated at 17,500 cycles. Inclusions were documented at other places on the fracture surface, as well as on random cross-sections cut from the specimen, indicating that there were many inclusions in the material.

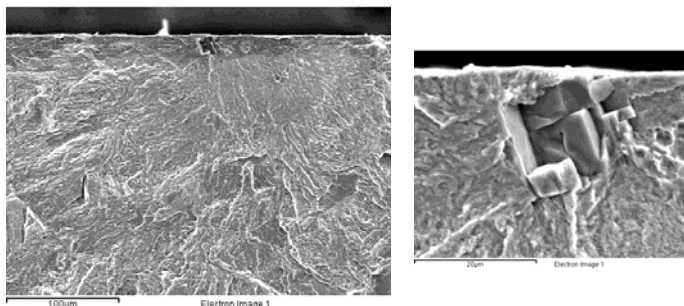


Figure 3.4-1. SEM images of Crack 1 on Specimen 622-2 showing that the fatigue crack was initiated by a cubic-looking, subsurface inclusion, at two different magnifications (a) and (b).

Electron Induced X-ray Analysis has shown that the inclusions in this specimen are mostly composed of titanium. Zirconium and carbon were also found in the inclusions. Figure 4.3-2 shows the results of the electron induced X-ray analysis on the inclusion from the first crack indicating the presence of titanium.

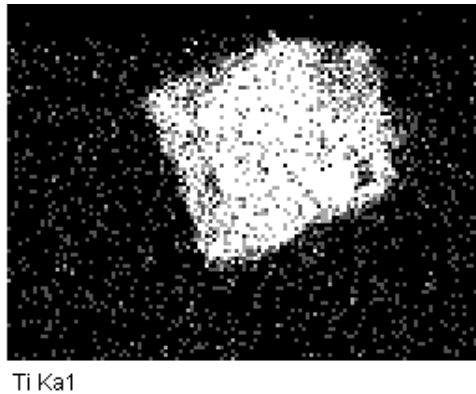


Figure 3.4-2. *Electron Induced X-ray Analysis performed on the specimen shows the composition of the inclusion – in this case, titanium. Zirconium and carbon were also found in the inclusion.*

Examination of the NAVAIR strain-life specimens confirmed that four of six had evidence of titanium-rich inclusions at the crack initiation sites showing that these test specimens were also contaminated. Interestingly, it appears that the inclusions did not significantly reduce the fatigue life of the strain-life specimens. Specimen geometry might have been a factor in this result. After discussions with material suppliers and material scientists, it was learned that titanium particles could be produced in the manufacturing process of 300M, but proper protocols for high-quality material call for the removal of these inclusions by appropriately segregating the material during processing.

After carefully considering the impact of these results, it was concluded that this batch of material was unsuitable for the purposes of this program. All testing of this material was stopped. Further results of these tests are not reported herein.

Section 4

Metric Development

4.0 Introduction

A primary objective of the Corrosion-Fatigue Assessment Program is the development of a corrosion classification scheme whereby a patch of corrosion is identified as cosmetic, mild, or severe. Cosmetic corrosion will have no measurable impact on life; severe corrosion will produce unacceptable reductions in fatigue life; and mild corrosion is expected to have a measurable, but not a severe, reduction in fatigue life. Mild corrosion requires additional study to make a disposition decision.

In order to create a corrosion-severity classification scheme, corrosion metrics must be found that can quantify the severity of the corrosion in terms of measurable parameters. These metrics must also be correlated to certain levels of fatigue life reduction. Ideally, these metrics will be measurable by fleet-level inspection methods. There are a number of standard roughness metrics that have been introduced in the report “Navy High-Strength Steel Corrosion-Fatigue Modeling Program” [1] and will be discussed below. More sophisticated metrics were studied that were based on parameters derived from stress concentration maps. Finally, a study was performed to investigate the effect of spatial resolution on the calculation of the metric values for a corroded surface.

4.1 Roughness Metrics

Forty surface height roughness metrics, both standard and novel, were evaluated on the program to look for correlations to fatigue life (i.e., cycles to crack initiation) for AF1410 Set A and B results. Several of the standard metrics are listed and defined in Table 4.1-1. The first two in the table, as well as the normalized volume loss (NVL), have been found to be the most relevant to this program.

Table 4.1-1. Summary of Surface Metrics

Ra	Average Surface Roughness
Rq	Root Mean Square surface roughness.
Rp	Maximum Surface Height Peak.
Rv	Maximum Surface Height Valley
Rt	Maximum difference from the highest peak to the lowest valley.
R _{sk} , Skewness	A measure of the symmetry of the profile about the mean line.
R _{ku} , Kurtosis	A measure of the sharpness of the profile about the mean line.
Rz	Average maximum height of the profile.
S index (Surface Area Index)	The ratio of the surface area of the profile to the surface area of an ideal plane.
NVL (Normalized Volume Loss)	The ratio of the volume missing to the lateral area.
Rpk (Reduced Peak Height)	The top portion of the surface that will be worn away during the run-in period.
Rvk (Reduced Valley Depth)	The lowest portion of the surface that will retain lubricant.
Htp	Defined by setting the tp1 (peak threshold bearing ratio value) and tp2 (the valley threshold bearing ratio value) to be separated by 40%.

Figures 4.1-1 through 4.1-3 show plots of R_a , R_q , and NVL, respectively, versus fatigue life for AF1410 Set A (red) and Set B (green) tests, with a power law fit and the R^2 value showing goodness of fit in each case. One observation that can be made from these plots is that Set B is shifted down compared to Set A – most likely due to the fact that Set A had large residual stresses present in the specimen surfaces from the grit-blasting process. A surface with a compressive residual stress will be more tolerant to surface roughness than one without this stress. Stated another way, it will take a larger surface roughness in Set A to produce the same reduction in fatigue life as produced in Set B at a smaller surface roughness.

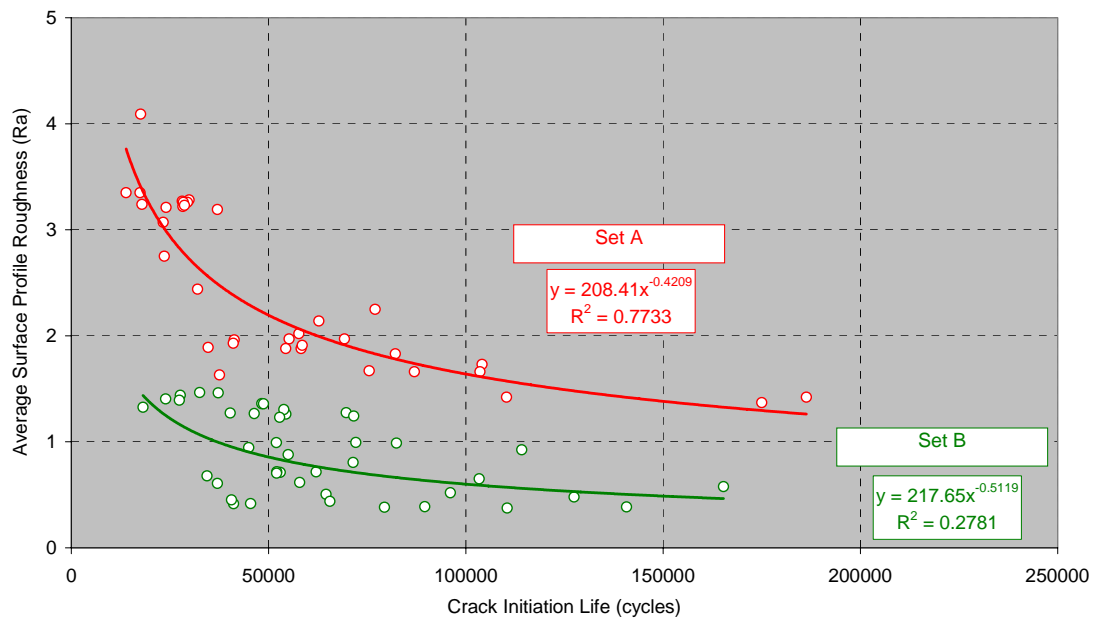


Figure 4.1-1. Average Surface Profile Roughness (R_a) versus Crack Initiation Life (cycles) for AF1410 Set A (red) and Set B (green).

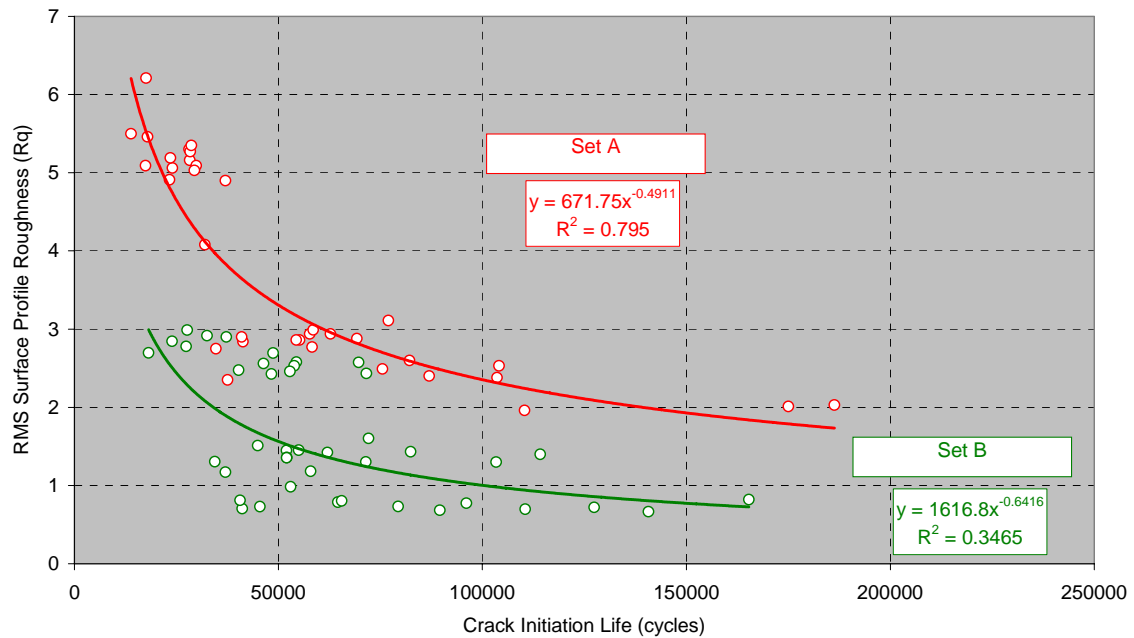


Figure 4.1-2. RMS Surface Profile Roughness (R_q) versus Crack Initiation Life (cycles) for AF1410 Set A (red) and Set B (green).

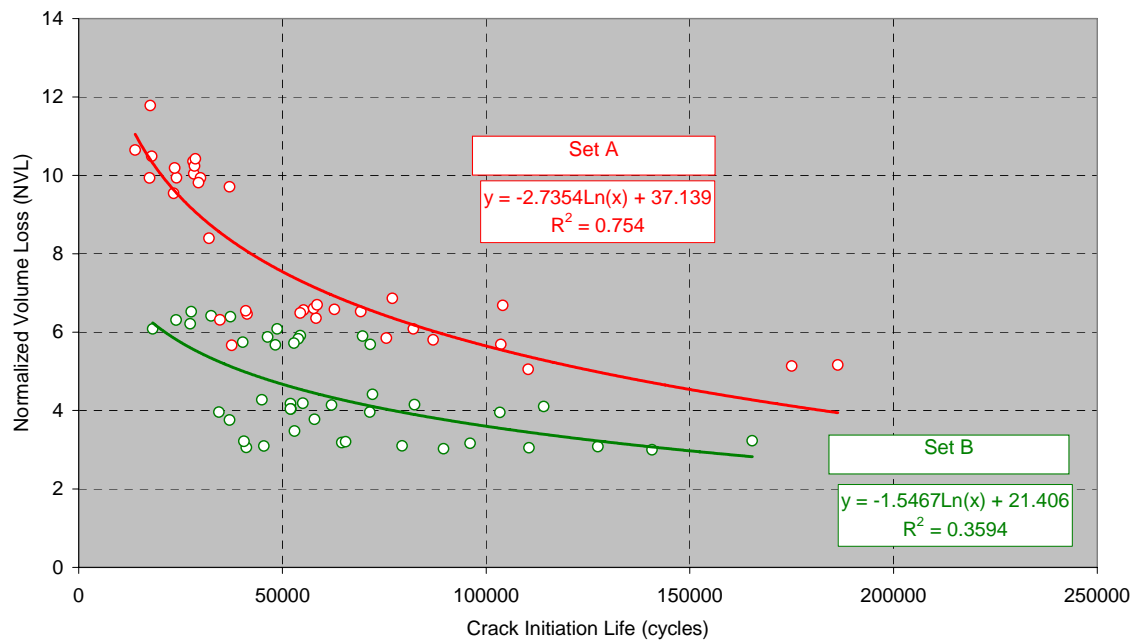


Figure 4.1-3. Normalized Volume Loss versus Crack Initiation Life (cycles) for AF1410 Set A (red) and Set B (green).

It is the goal of this study to identify metrics that can be correlated to reduction in fatigue life. As can be seen from these figures, R_a , R_q and NVL correlate well with fatigue life measured by cycles to crack initiation for Set A; however, the fits are not so good for Set B. It is hypothesized that this is due, in part, to the fact that Set B specimens were not as severely corroded as Set A, resulting in a much smaller range of roughness metric values for Set B. In addition, these plots and fits do not account for the expected dependence of the initiation life on applied maximum load. For Set B, the variation in the maximum applied load produces a scatter in the lives that is comparable to the range of roughness metric values. In this case, the dependency on roughness is confounded with the dependency on applied maximum load, producing a situation in which no clear trend is present with poor goodness-of-fit values. On the other hand, for Set A, the range of roughness metric values is larger than the scatter in lives due to the applied maximum load. This fact allows the dependency on roughness to become apparent in Set A and allows for a better fit to the data.

Figure 4.1-4 through 4.1-6 illustrates this reasoning. In these figures, the data for each set is plotted as a function of applied maximum load for each roughness metric. The dependency on maximum applied load is clearly evident in the plots showing that lives are, in general, shorter for specimens tested at higher applied maximum loads. There are some exceptions to this trend seen in fits that cross over. These cases are probably a result of small data sets produced by segregating the data in this manner, combined with the relatively large scatter in lives present in the data. Still, the trend is evident: larger applied maximum loads are associated with smaller lives. This suggests that simple roughness metrics, by themselves, are not sufficient to account for reduction in fatigue life; there must be an accounting for applied load.

It should be commented that these plots exclude the baseline specimens that have not been corroded. In addition, the metric values shown in these plots were calculated over the entire scanned area with no attempt to define the metric only within the corrosion patch.

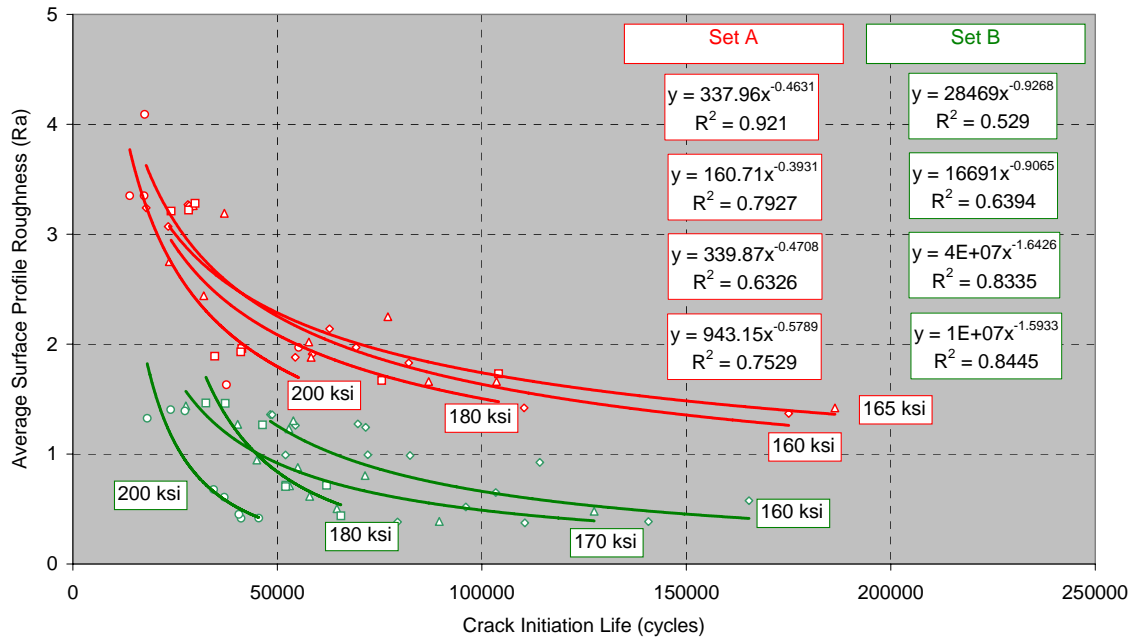


Figure 4.1-4. Average Surface Profile Roughness (R_a) versus Crack Initiation Life (cycles) for AF1410 Set A (red) and Set B (green) plotted as a function of maximum applied load; fit equations listed in ascending order of applied load.

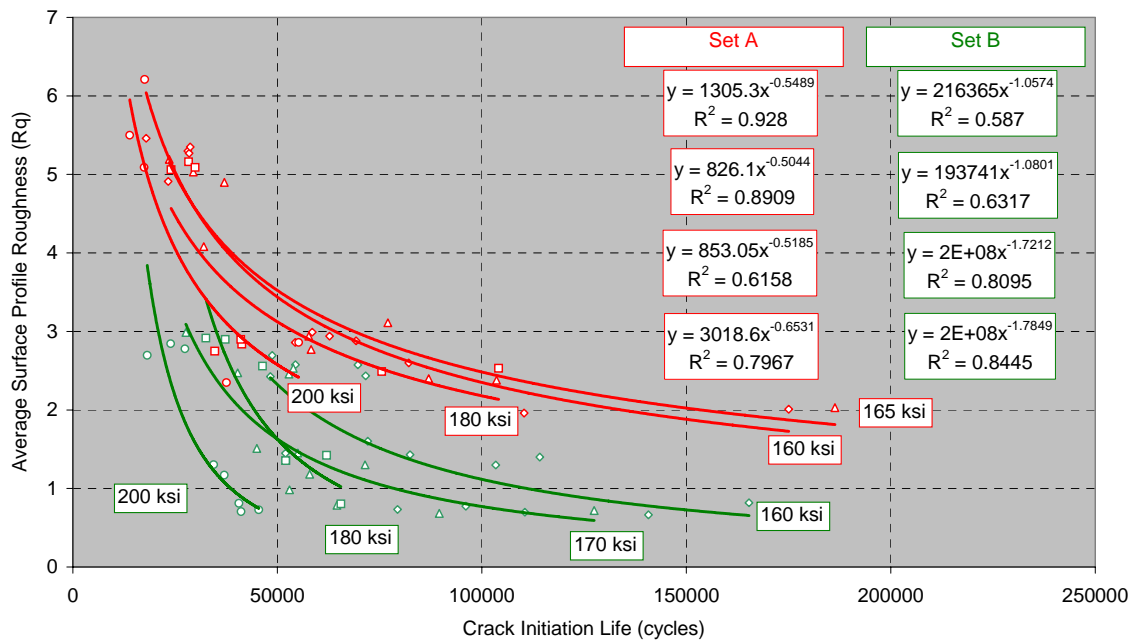


Figure 4.1-5. RMS Surface Profile Roughness (R_q) versus Crack Initiation Life (cycles) for AF1410 Set A (red) and Set B (green) plotted as a function of maximum applied load; fit equations listed in ascending order of applied load.

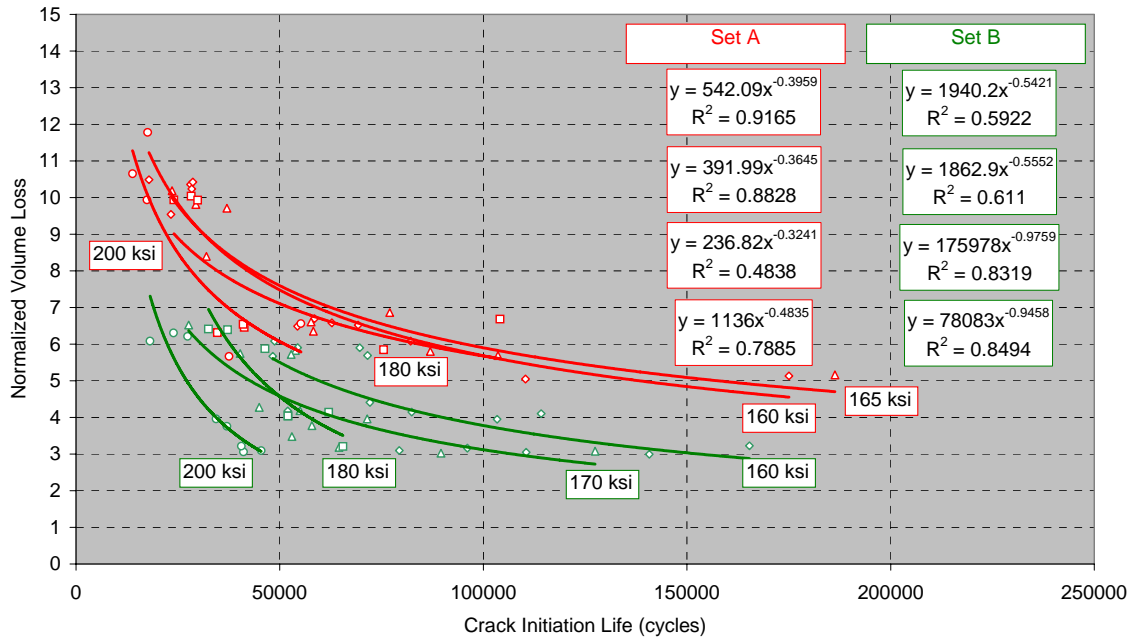


Figure 4.1-6. Normalized Volume Loss versus Crack Initiation Life (cycles) for AF1410 Set A (red) and Set B (green) plotted as a function of maximum applied load; fit equations listed in ascending order of applied load.

4.2 K_t Metrics

Given the conclusion of the last section, it was deemed important to consider metrics that would, in some way, account for the applied maximum load. Several were studied. One approach simply scales the roughness metric by the ratio of the applied maximum load to the yield strength of the uncorroded material. For the purposes of this study, the yield strength of AF1410 was assumed to be 235 ksi. Figures 4.2-1 through 4.2-3 show plots of this so-called stress weighted metrics (R_a , R_q and NVL, respectively) versus the crack initiation life for Sets A (red) and B (green). Since these innovative metrics are designed to account for applied maximum load, they are not plotted as a function of applied load. The Set B fits are somewhat better here than in Figures 4.1-1 through 4.1-3, but not dramatically so. Other novel metrics that were studied did not perform significantly better than these metrics.

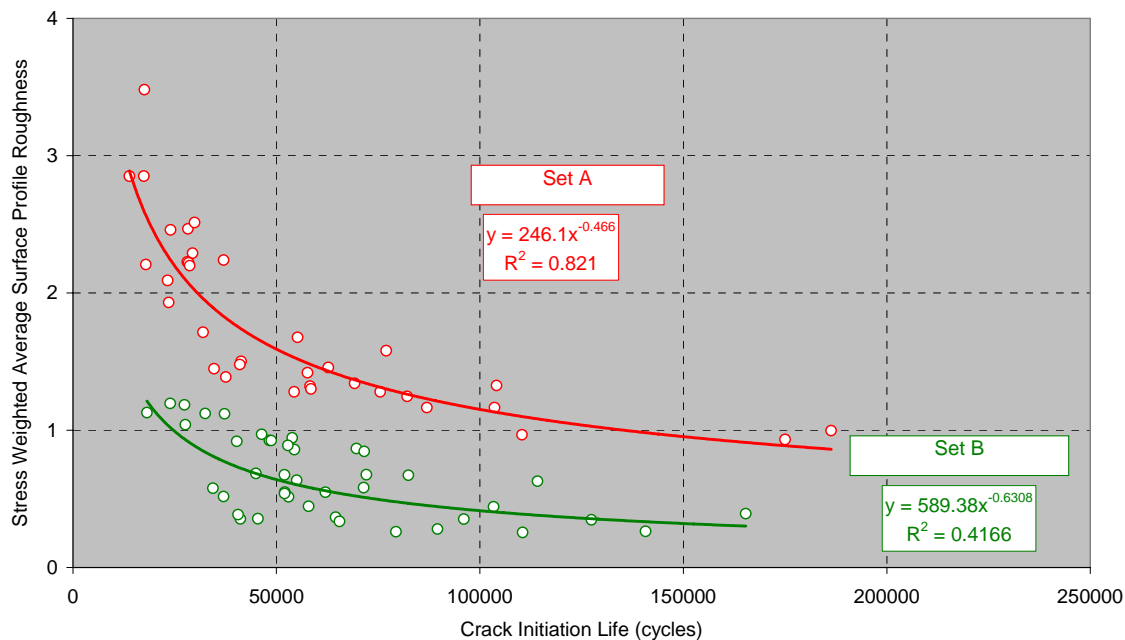


Figure 4.2-1. Stress Weighted Average Surface Profile Roughness versus Crack Initiation Life (cycles) for Af1410 Set A (red) and Set B (green).

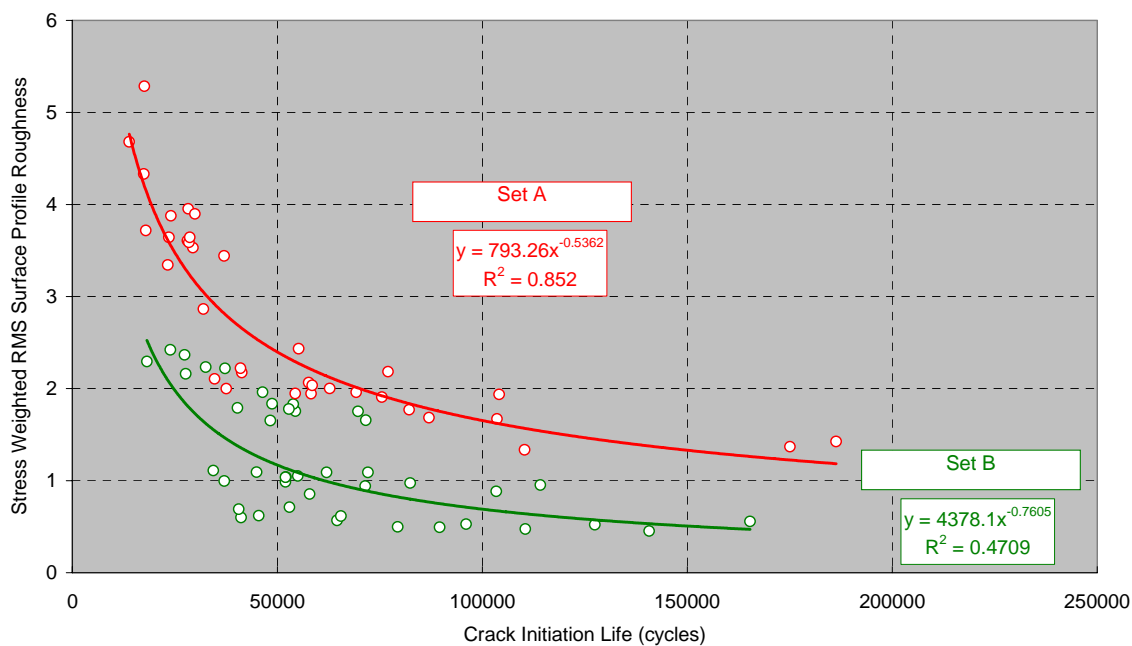


Figure 4.2-2. Stress Weighted RMS Surface Profile Roughness versus Crack Initiation Life (cycles) for Af1410 Set A (red) and Set B (green).

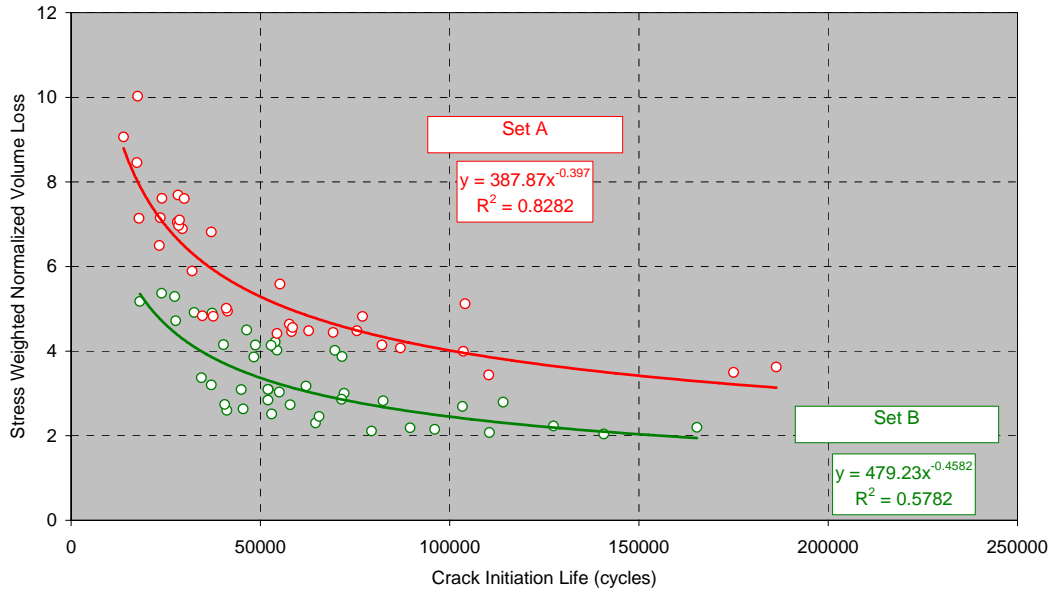


Figure 4.2-3. *Stress Weighted Normalized Volume Loss versus Crack Initiation Life (cycles) for Af1410 Set A (red) and Set B (green).*

In summary, standard surface roughness metrics do provide some indication of severity of corrosion in terms of reduction in fatigue life, and certainly, there is ample evidence that supports the hypothesis that fatigue life is reduced by surface roughness; however, there is a need to account for applied loads. The novel metrics studied and presented here, while showing an improved correlation over standard surface roughness metrics, probably do not provide a reliable measure, by themselves, of reduction in fatigue life. There is a need for more advanced metrics and methods to classify corrosion severity. One particular method being considered as part of the third contract on this program is a surface roughness grid mapping approach that would allow the calculation of local roughness values and account for the local stress within each grid in an adaptation of the equivalent stress riser model (described in Section 5.4.2). This approach is described in more detail in the corresponding final report and associated modeling report [4].

4.3 Resolution Study

A study was performed to understand the effect of spatial resolution on the calculation of the metrics. This study was intended to provide insight into the limitations of determining metrics from traditional nondestructive inspection techniques, like ultrasound, that have a poorer spatial resolution than the white light interference microscope used to create surface profiles on this program. Starting with the white light profiles for a number of AF1410 Set B specimens, the Root-Mean-Square (RMS) roughness was calculated in a circular region positioned inside the corrosion

patch. The diameter of the circle was slightly smaller than the diameter of the circular patch of corrosion. Each image was filtered with Gaussian blur filters of various widths to simulate different spatial resolutions. RMS values were determined for each processed image in the circular region of interest. RMS values were normalized by the RMS value of the original white light profile and were plotted as a function of the Gaussian blur full width at half maximum in mils. Figure 4.3-1 shows a plot of normalized RMS versus Gaussian blur full width at half maximum for 1.5-hour exposure data on some of the AF1410 Set B specimens. Figure 4.3-2 is a plot of several 3-hour exposure specimens. Also shown in each plot is a best-fit line with the corresponding equation. It is interesting to note that the slope of the fit is similar for all data. Apparently, the effect of the low-pass filter is to reduce the effective roughness, but in a manner such that the effective roughness is proportional to the actual roughness determined from the full-resolution white light profile. This suggests that the surface profile characteristics are present across a range of spatial frequencies. When the low-pass filter removes the higher frequencies, there are still lower-frequency roughness components present to give an indication of the overall roughness.

Figure 4.3-3 is a plot of the normalized RMS versus the Gaussian blur full width at half maximum for a specimen from AF1410 Set A that had been exposed for 6 hours. This figure shows RMS both inside and outside the corrosion patch. As can be seen in this plot, there is a deviation of the RMS in the corrosion patch from a straight line. It is believed that this is due to the fact that the AF1410 Set A specimens were grit blasted prior to growing corrosion, leaving the surface with a dimpled texture, even outside of the corrosion patch. The effect of filtering on this grit-blasted surface roughness is seen in the curve representing the region outside the corrosion patch. Apparently, the grit-blasted surface contains a significant amount of high-frequency roughness. As the low-pass filter removes these higher-frequency components, the effective roughness decreases dramatically. This knowledge helps explain the shape of the curve for the RMS values in the corrosion patch. There appears to be a significant influence on the RMS value of the original white light profile due to the surface roughness from the grit blasting. As the low pass filter is applied to remove more of the high-frequency roughness components, relatively more of the roughness due to the corrosion is left, which shows a similar behavior to that shown on the AF1410 Set B specimens. Since the Set B specimens were not grit blasted and had a much smoother surface prior to growing corrosion, there is only the corrosion roughness characteristic present in these specimens.

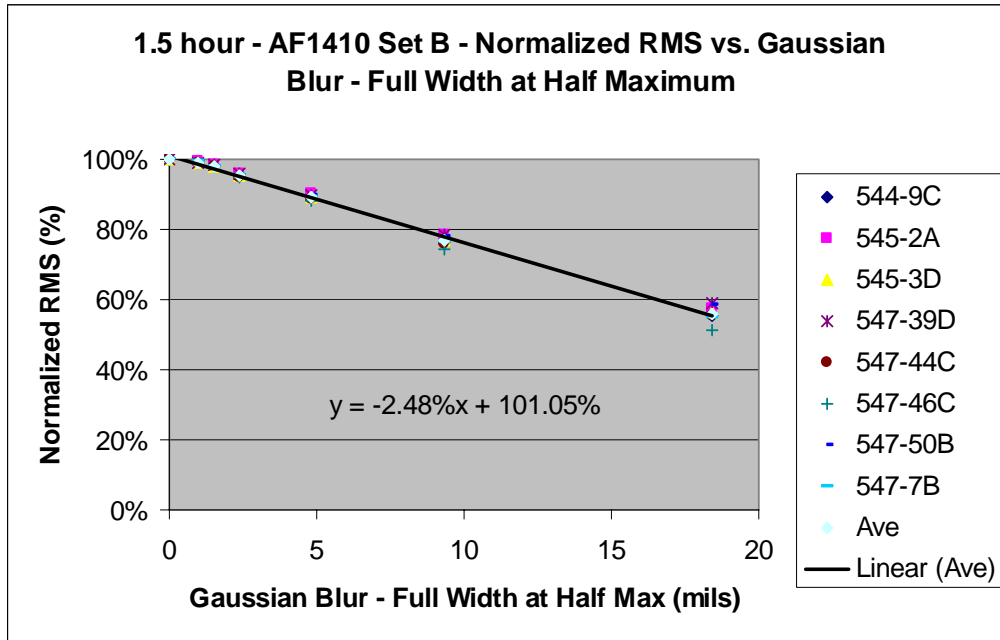


Figure 4.3-1. Normalized RMS versus Gaussian Blur Full Width at Half Maximum for several AF1410 Set B 1.5-hour exposure specimens.

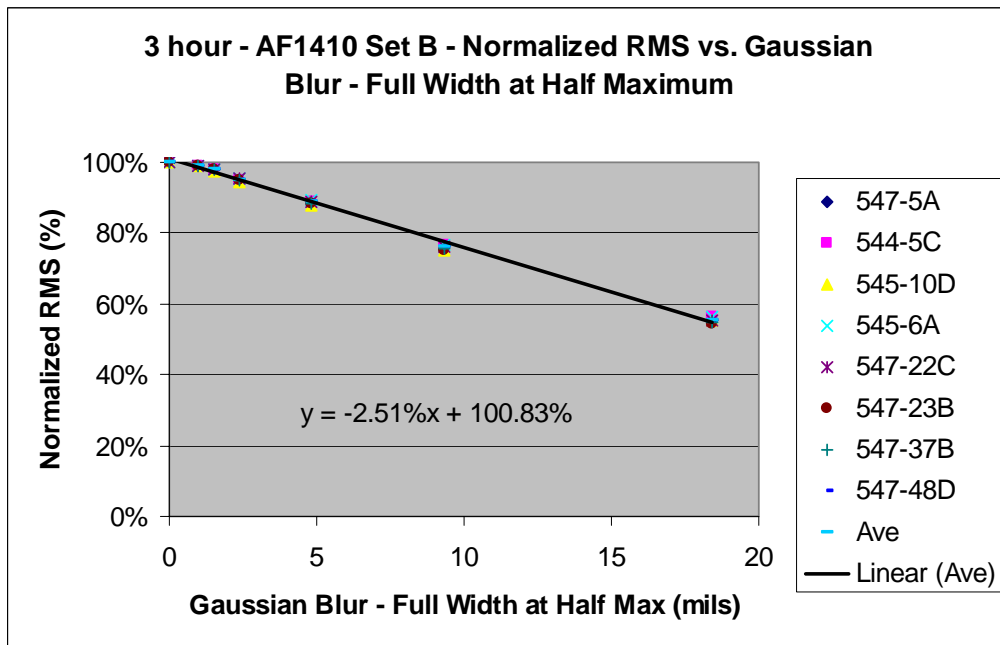


Figure 4.3-2. Normalized RMS versus Gaussian Blur Full Width at Half Maximum for several AF1410 Set B 3-hour exposure specimens.

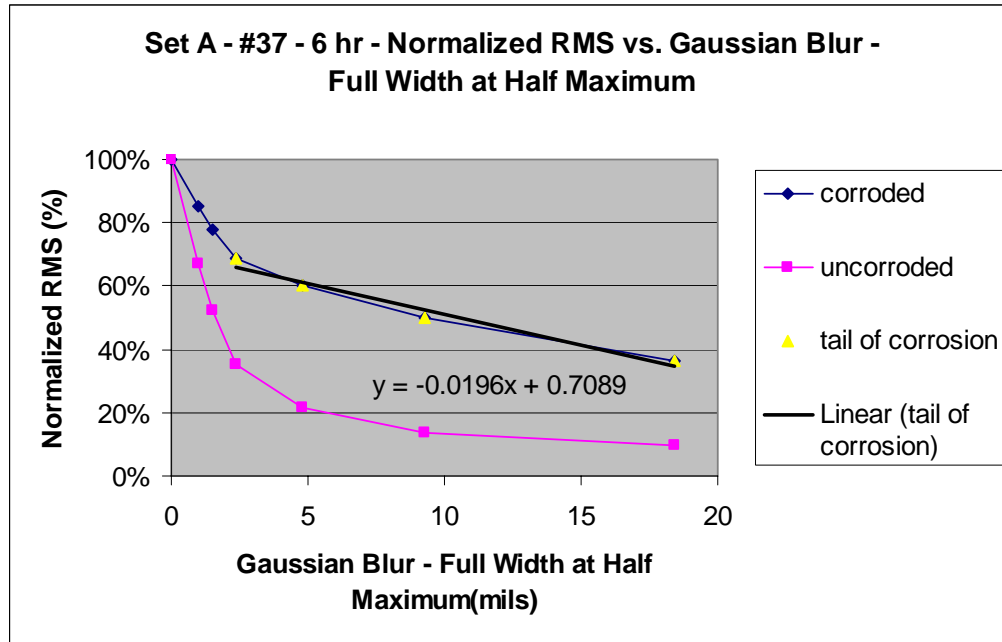


Figure 4.3-3. Normalized RMS versus Gaussian Blur Full Width at Half Maximum for AF1410 Set A 6-hour exposure specimen number 37.

For reference, the RMS roughness values of the specimen shown in Figure 4.3-3 for the original white light profile inside and outside the corrosion patch were 5.3 and 4.1 microns, respectively. Average RMS roughness values for the AF1410 Set B specimens shown in Figures 4.3-1 and 4.3-2 are 1.2 and 2.2 microns, respectively. RMS roughness sampled outside the corrosion patch for three different AF1410 Set B specimens ranged from 0.1 to 0.4 microns. Apparently, the roughness of the surface prior to growing corrosion has a significantly smaller effect on the roughness of the corrosion patch after corrosion for Set B compared to Set A. One possible hypothesis that could be made from these observations is that a poorer-resolution inspection might actually give a better measure of roughness due to corrosion. The poor-resolution inspection is less sensitive than the better-resolution white light instrument to the higher-frequency components present in the grit-blasted surface. More research is required to confirm this hypothesis.

Section 5

Modeling

5.0 Introduction

The objective of the modeling portion of this program was to develop a methodology to model the effect of corrosion on high-strength steel components and to estimate the remaining life of these components based on a suitable metric. The UDRI corrosion modeling efforts consisted of evaluating finite element, boundary element, and elasticity techniques for the prediction of stress concentration factors of corroded surfaces as a means to quantify corrosion severity. Reliability modeling approaches were developed. The remainder of this section of the report summarizes ESRD, UDRI, and NAVAIR modeling efforts. Boundary Element modeling efforts are summarized in the Computational Mechanics Final Report in Appendix D.

5.1 Review of FEA, Pit Metric and Elasticity Approaches

This section summarizes the major modeling activities on the first contract on this program.

ESRD conducted a study of profilometry data and meshing in the context of StressCheck, their finite element software analysis tool. Early in the program, white light interference microscopy profiles were not available, so ESRD used laser profile data from a prior Boeing program. Two-dimensional slices through the corroded surface were processed by spline fitting. It was understood that two-dimensional analysis is unlikely to provide an adequate approximation to real corrosion. An investigation was performed of a two-dimensional model of corrosion to investigate the effects of surface representation on the computed K_{teff} . One significant conclusion drawn from this study was that the complexities of the computational problem increases drastically with increased spatial resolution of the corrosion maps. The problem will only get worse when three-dimensional analysis is attempted, unless it can be demonstrated that the smaller-scale features are unimportant.

Subsequently, ESRD developed an approach to geometrically idealize a corroded surface in StressCheck[®] by using features actually observed in corroded specimens, such as rings, pits, and waviness. The goal was to simplify a corroded surface into basic Parasolid geometries without adversely affecting, to any substantial degree, the maximum K_{teff} for each geometry. ESRD

also included a study of the effects of residual stress on the results. ESRD found that K_{teff} is very sensitive to the details of idealization. Residual stress was modeled as a temperature distribution. They found that residual stress will delay the initiation of fatigue failure, but will tend to accelerate the growth of defects once the defect has penetrated the surface layer where the residual stresses are compressive.

In addition to the analyses described above, efforts were made to develop an analysis technique to compute stress concentration factors for actual corroded surfaces. Given the volume of data generated from a detailed mapping of a corroded surface from laser profilometry and/or white light interferometry, it was not practical to model the entire corroded surface of an actual component or test coupon. Reduced sampling techniques to make the analytical problem tractable, unfortunately, had a significant effect on the stress concentration factor. Thus, in order to obtain accurate stress concentration factors, one must utilize an approach that retained the detailed local surface information as much as possible.

Accordingly, a global-local modeling technique was developed. The global model was used to capture the overall stress field in the part. The local model estimated the influence of the local corroded surface on the stress concentration factor. Displacement boundary conditions from the global model were applied to the local model to account for the remaining structure.

The global-local modeling technique was demonstrated to provide reasonable stress concentration factor estimates of corroded surfaces including residual stress effects. The local model consisted of just a small region around the geometric features of interest. In the global analysis, the axial loading and residual stress (via the temperature profile discussed in the previous section) were applied to an uncorroded geometry. The results from this analysis were used to drive a local model with corroded surface features. Unfortunately, to analyze numerous sites or an entire corroded surface with the global-local technique, required a large series of local models that were not practical to evaluate. Alternate means of corrosion surface modeling were required.

Because of the geometric complexity, direct analysis of the corroded surface profile did not appear to be practical, so an alternative approach was developed to estimate the local stress concentration factor via a pit metric based on the local surface geometry. A candidate pit metric was developed, as indicated in Figure 5.1-1.

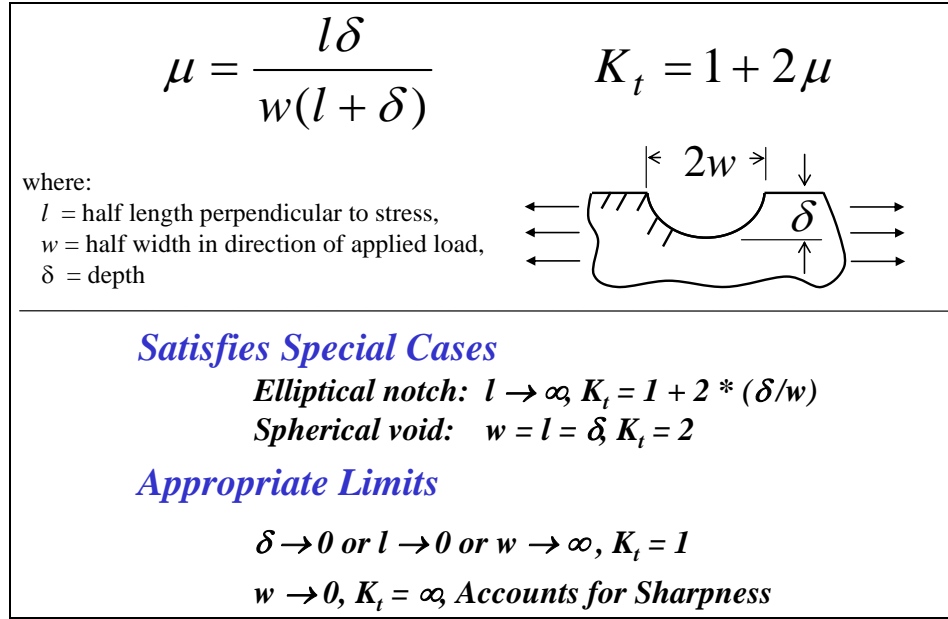


Figure 5.1-1. Candidate pit metric for stress concentration factor estimation.

This easily computed metric provided very accurate stress concentration factors for special cases, such as a semi-elliptical notch or a hemispherical void. Additionally, the pit metric had the correct limiting trends so that, for a smooth and shallow pit, the stress concentration factor went to unity, but as the pit became very sharp and deep, the stress concentration factor went to infinity, indicating a crack tip.

A series of analyses was performed to determine pit metric performance on a wide variety of hemispherical and semi-elliptical notch defects. Results from these analyses showed that the pit metric was accurate when the geometric parameters were precisely known. Unfortunately, efforts to directly apply the pit metric to actually corroded surfaces were not successful because of the difficulty in computing the pit metric parameters from the chaotic local surface geometry.

The challenges of applying the pit metric led to the development of an elasticity solution that would not suffer from the difficulties of defining geometric parameters directly from the corroded surface geometry. The elasticity solution approach, shown in Figure 5.1-2, involved performing a two-dimensional Fast Fourier Transform (FFT) of the corroded surface data to represent the actual surface profile as a linear combination of sinusoidal components in the frequency domain. Because each of the frequency components was a smooth, continuous function, one could estimate the stress variation over the surface of each frequency component with an approximate

elasticity solution. The stress values corresponding to each frequency component were then re-combined, via an inverse FFT, to provide an estimate of the stress field and stress concentration factor over the entire corroded surface.

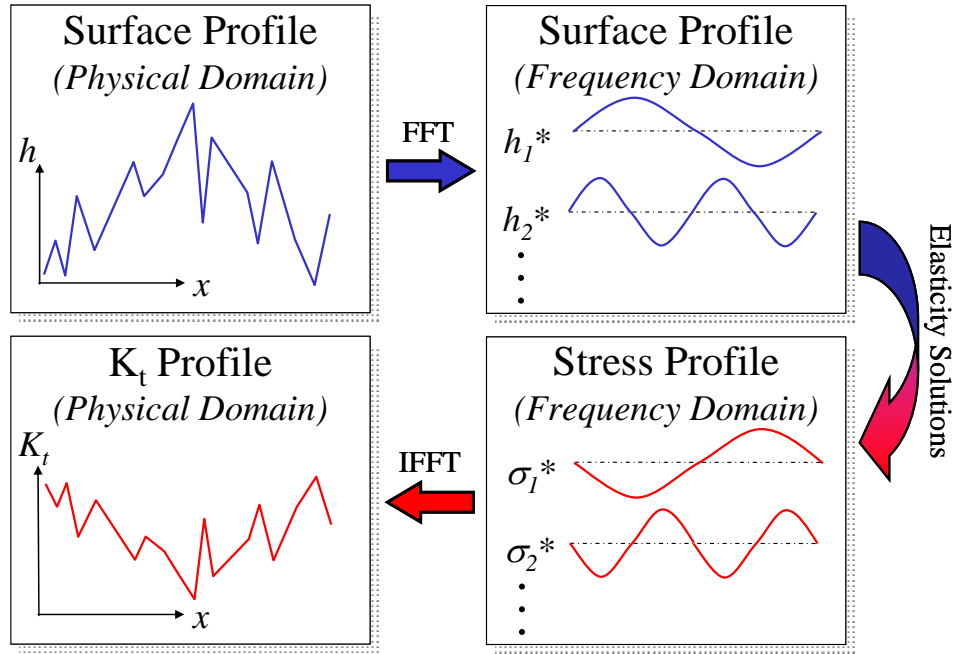


Figure 5.1-2. Elasticity approach for corroded surface modeling.

The elasticity stress function solution, depicted in Figure 5.1-3, was developed based on observations from analyses of axial load components with sinusoidally varying surface geometries. These observations indicated that, for shallow surface height variations, the surface stress varies 180 degrees out of phase from the local surface height. When the surface was low, corresponding to a local pit, the stress was raised; and when the surface was raised, corresponding to a local peak, the stress was reduced. From the elasticity solution, a simple expression was developed that defined the stress variation over a sinusoidal surface in terms of the surface profile parameters (height and wavelength in each surface direction) and the applied axial loading.

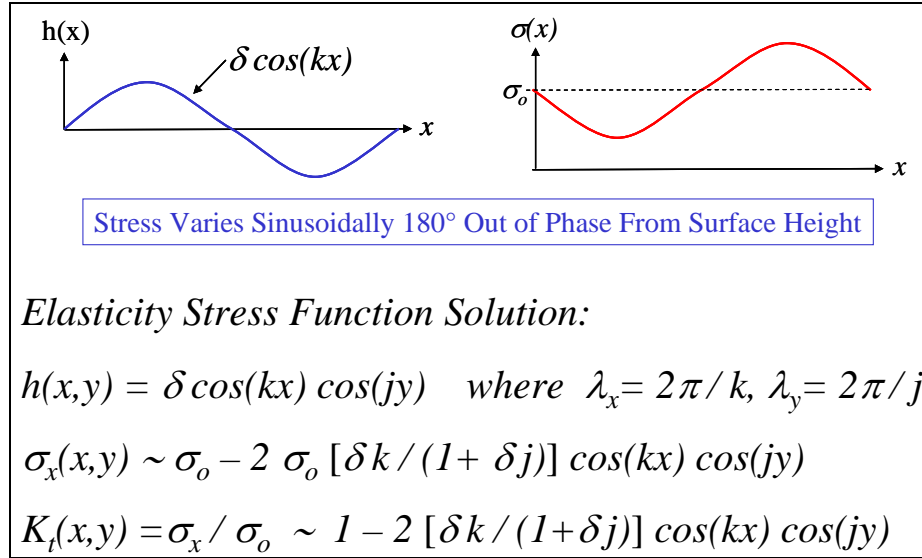


Figure 5.1-3. Elasticity solution for each surface profile frequency component.

A series of finite element analyses was performed to estimate the stress concentration factors for a variety of idealized corroded surfaces having increasing complexity. The elasticity solution approach was applied to each of these idealized surfaces and correlated well with the finite element results. These results indicated that the elasticity solution accurately predicted both the amplitude and spatial variation of the stress profile corresponding to a single frequency component from the FFT of the corroded surface profile.

ESRD and UDRI performed a series of detailed finite element analyses to determine the accuracy of the individual frequency component elasticity solutions over a wide variety of conditions. These results indicated that the elasticity solution was accurate over most conditions, except when the surface height of one of the frequency components was large compared to the corresponding wavelength. Review of measured surface profile data from actual AF 1410 corroded specimens found that the surface heights were significantly smaller than the corresponding wavelengths. This implied that the elasticity solution approach would be used in the most accurate regime and remained viable for estimating the severity of actual corroded surfaces.

Having demonstrated that the individual frequency components were reasonably accurate, a series of finite element analyses was performed to determine if the individual frequency components could be superimposed via an inverse FFT to represent the overall surface stress profile.

The justification for superposition was based on the observation that the effects of multiple stress concentrations factors, such as a pit within a pit, were known to combine as the product of the individual stress concentration factors, as indicated in Figure 5.1-4. When the individual elasticity solutions were inserted in the product expression and higher order terms were neglected, the total stress concentration factor was estimated by a summation of terms related to the stress state of the individual frequency components. It was this summation that was computed as the result of the inverse FFT step in the elasticity solution in Figure 5.1-4.

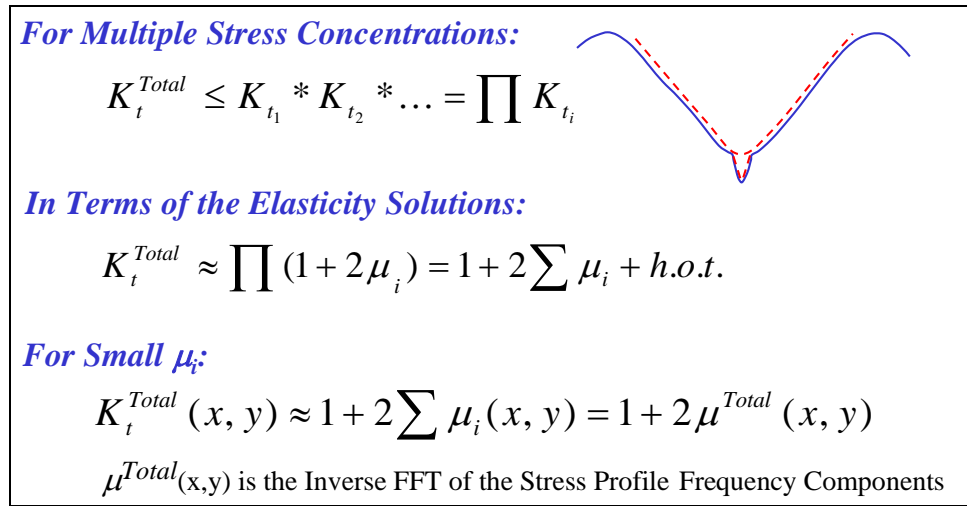


Figure 5.1-4. Combined stress concentration factor implications.

To demonstrate the validity of the superposition approach, analysis results were compared for the elasticity (FFT), finite element (FEA), and boundary element (BEA) solutions corresponding to an axial load applied to a component having a surface geometry composed of three different sinusoidal terms. These results indicated that the superposition of the individual elasticity solutions accomplished via the inverse FFT accurately predicted both the amplitude and spatial variation of the stress variation over a complex surface profile.

Finally, the elasticity approach was applied directly to an actual AF1410 corroded surface geometry from one of the test specimens. The post-fracture corrosion surface and the corresponding surface height profile from white light interferometry were compared. A number of crack locations from the fatigue testing were identified and labeled accordingly. The elasticity solution accurately identified the high-stress locations and remained the only practical approach to estimating full-field stress concentration factors of arbitrarily corroded surfaces.

Finally, a comparison was made of maximum k_t values found for each crack on a specimen and the maximum k_t values found in the region of each crack. In all cases, the crack contains the region's largest k_t value, or nearly the largest value. From these observations, it is clear that the elasticity model is identifying true stress risers and candidate crack initiation sites. It was concluded that the elasticity model provides a foundation for further life prediction and disposition decisions.

5.2 Review of ESRD Modeling Studies

During the second contract on the Corrosion-Fatigue Assessment program, ESRD conducted a series of studies that are described in detail in their final report included in this report as Appendix A. Section 6.1 of their report reviews an investigation by ESRD to determine what, if any, useful information can be extracted from corroded surface profiles via corrosion metrics. They studied surface profile filtering and spatial resolution of the profile images being used on the program to map the surface height. They also looked for correlations between the root-mean-square (RMS) metric and exposure times, comparison of RMS for a pristine and corroded surface, and looked for correlations between locally calculated RMS values and crack initiation sites. In Section 6.2, an equivalent crack size approach to life prediction is outlined. Section 6.3 of their report describes ESRD efforts to design a discovery experiment involving micro-machined features. A pattern of six different features with nominally the same stress concentration was to be machined into ten fatigue specimens. These specimens were manufactured and were being prepared for test at the end of the contract. Section 6.4 describes a study by ESRD to investigate the stress concentration from real pit-like features found in the corrosion-fatigue specimens. This study provided insight into the crack initiation details, including the effect of intersecting or interfering pits. In addition, this study led to improvements in the UDRI pit metric described in Section 5.1 above, including a modification to the coefficient of the metric term in the calculation of stress concentration, the inclusion of a small second order term in this expression, and a method for accounting for orientation of the feature with respect to the load direction. Finally, they describe in this section of their report the effect of biaxial loads on the calculation of stress concentration when using the pit metric. Section 7 of their final report describes plans for deployment of the software improvements added to their product, StressCheck[®]. Section 8 is a summary for their report, and Section 9 includes recommendations for future work, which lays the foundation for verification and validation – a topic of the third contract on this program.

5.3 Region of Interest (ROI) Analysis

White light interference microscopy surface height profiles generated on each corrosion-fatigue specimen formed the basis and input of further stress concentration and life prediction modeling steps on this program. As mentioned in Section 5.1, a stress concentration map can be generated from the white light surface profiles through the use of the elasticity solution. This estimate of stress concentration has been shown to correlate well with regions likely to initiate a crack. Consequently, methods were developed to better define these regions of interest (ROIs). Standard software plug-ins and algorithms that are a part of the ImageJ product released by the National Institute of Health were used in this development effort. Additional custom software plug-ins were also developed for the purposes of this research. The following paragraphs define the processing steps performed on the white light and stress concentration images for the region-of-interest analysis.

First, the white light data, which was collected in small 11 mm by 11 mm sections, is stitched together to form a larger 41 mm by 41 mm image using a 1 mm overlap between sections. Then, a “data restore” step is performed to correct bad pixels, which occur occasionally; these are pixels that have no value assigned during the data acquisition step and must be fixed prior to further processing in ImageJ. These pixels are assigned an interpolated value from nearby good pixels. Next, any tilt in the image is removed, which is designed to account for tilt of the specimen while collecting surface height data. These three steps are accomplished with built-in software routines within the Veeco software that comes with the white light interference microscope system. The next several steps, performed with ImageJ software plug-ins and built-in routines, starts with a rotation to align the image with the specimen load direction (the long direction of the specimen). The white light profile is then preprocessed first by applying an 8-mm waviness filter to remove waviness produced during the surface topography measurement process (an artifact of the stitching process), and then by removing the mean surface height, which accounts for vertical offsets present in data acquisition. At this point, this pre-processed white light image is used either for calculation of the stress concentration map or further processing for the ROI analysis.

As a preliminary step to calculation of the stress concentration map, the pre-processed white light image is further processed with a Gaussian blur filter of radius 3 pixels and a median filter of radius 4 pixels – each step done with ImageJ software routines. Each pixel is 6.34 by

6.34 microns and 7.66 by 7.66 microns for data collected with the WYKO NT2000 (used for approximately 30 percent of the Set A specimens) and WYKO NT8000 (used for the rest of Set A specimens and all of set B specimens), respectively. The Gaussian blur processing is a low-pass filter, removing high-spatial-frequency components from the image that will tend to produce extremely high-stress concentration factors. The median filter removes outlier pixels replacing them with the median value of the immediately surrounding pixels. These outliers are deemed by engineering judgment to be bad pixels, but are not removed by the “data restore” function, since a height value was assigned to them (e.g., a full-scale value). Outlier pixels also produce extremely large and anomalous stress concentration factors. The resulting image is used as input to the stress concentration calculation routine described in Section 5.1 above.

The pre-processed white light image defined at the end of the second paragraph of this section, is further processed and used in the definition of ROIs and their statistics. After the mean is removed (see above), a median filter is applied of radius 4 pixels. The mean is removed again to account for changes in the mean height produced by the median filter. This image is then used, together with the stress concentration map, to identify ROIs and to calculate statistics and parameters for the ROIs.

The first step in ROI analysis is to identify Regions of Interest. The processed white light image is first further processed by converting all pixels with values above 0.001 (a small number with no other significance) to 255, and all other pixels being set to zero. Since the white light images are of the specimens themselves, all pixels associated with material removal will have negative heights that will then be converted to a zero value by this operation. The image is then converted to a binary image (all values of 255 set to one and the rest remaining set to zero) and then the image is inverted (all values of one being set to zero and the rest set to one). The final inversion step will make those pixels that are associated with material removal into ones. Similarly, the stress concentration map is passed through a threshold, with all values above 1.3 for Set A, and 1.1 for Set B, being set to 255 and the rest being set to zero. The image is then converted to a binary image. In this case, the ImageJ software automatically performs an inversion of the image because the image is primarily black¹. The image must be inverted again to make all high kt values one, setting all values of one to zero and values of zero to one. These two binary images

¹ ImageJ documentation explains that this inversion takes place in certain cases without giving much in the way of motivation.

are then combined in a logical “AND” process, which will find all pixels that have negative heights (i.e. material removed) and high k_t values. The new image must then be inverted again for the next step. Finally, the resulting image is processed with the ImageJ plug-in called Particle Analyzer, which groups into ROIs contiguous pixels with values of zero and with areas of size equal to 36 square pixels for Set A and 4 square pixels for Set B. All regions of smaller area are ignored. Each ROI is placed in a table with the coordinates of the ROI.

The next step in the ROI analysis is to determine the depth of each ROI. This is accomplished by shifting each surface height pixel within each ROI by the height of a plane that is fit to height data from triangular regions in the four corners of the full-scanned image (outside the corrosion patch). The largest shifted depth with a given ROI is then included in the table for that ROI. Other statistics are also determined for each ROI using the surface height data such as area, mean, standard deviation, mode, maximum, minimum, integrated density, median, skewness, kurtosis, as well as the major and minor axes dimensions and orientation of an ellipse fit to the ROI. The UDRI pit metric, described in Section 5.1 above, was then used in a generalized stress concentration formula developed by ESRD that accounts for pit orientation and includes a small term that is second order in the pit metric to estimate the stress concentration factor, k_t , of each ROI. An additional step was performed for each ROI in order to approximate the root radius of the ROI. This involved a second order fit to the bottom and sides of the ROI in the load direction. This value is important for modeling fatigue life in the context of a Peterson notch sensitivity factor. Details of the use of these parameters in the model are found in Reference 4.

5.4 Reliability Modeling

The goal of the Navy Corrosion-Fatigue Assessment program is to produce quantifiable and justifiable maintenance intervals. This implies that life can be predicted based on applied stress and estimates of the effect that corrosion has on life. Corrosion effects on life are hoped to be estimated from corrosion profiles, metrics, estimates of k_t , or other factors. To compare measured life to predicted life in a meaningful way requires the ability to predict a distribution of lives for each test case. In the following discussion, life is defined by the number of cycles to crack initiation (i.e., the existence of a 0.010 inch crack).

5.4.1 Pixel/Area Approach

To predict life in uncorroded pieces requires the use of stress and strain amplitudes derived from stress-strain plots; life is not derived directly from maximum or applied stresses. For example, a 200 ksi applied stress at a $k_t=1$ and $R = 0.1$ gives a stress amplitude of only 90 ksi, which is then compared to strain-life data to estimate life. Plastic deformation modifies the effect of any stress risers and is captured by Neuber's rule for calculating maximum stress, stress amplitude, mean stress, and strain amplitude:

$$\varepsilon\sigma = ((k_t S)^2)/E,$$

where ε is strain, σ is stress, S is the applied stress, k_t is the stress concentration factor, and E is Young's modulus. The Coffin-Manson relationship models strain-life data:

$$\varepsilon_a = \frac{\sigma'_f}{E} (2N_f)^b + \varepsilon'_f (2N_f)^c,$$

where N_f is the life, ε_a is the strain amplitude, and σ_f , ε_f , b and c are fit parameters of the model. For cases that are not fully reversed, such as in the Navy program corrosion-fatigue tests ($R = 0.1$ and $R = 0.7$), there is a mean stress that effects life and can be accounted for using Morrow's approach:

$$N^* = X(\sigma_{\text{mean}})N_f,$$

where the life in the Coffin-Manson relation is subsequently interpreted as N^* and X is the Morrow factor, which is, in turn, a function of the mean stress. Non-constant amplitudes (e.g., marker bands cycles) also require cycle counting to make life predictions. Essentially, the procedure for constructing the models and doing the calculations outlined above are described in textbooks such as "Mechanical Behavior of Materials" by Dowling.

Unfortunately, the above method describes the mean behavior of the test cases and does not provide a statistical scatter in the life of a test specimen. Weibull has addressed this issue by an approach that empirically models the scatter in lives by a formalism that accounts for stress, life, and probability [2]. In this method, strain-life data are categorized by probability percentiles. The S-N data for each probability percentile are modeled with a convenient function and endurance limits are found for each percentile. A Weibull distribution is fit to these endurance limits, which is used to find smoothed endurance limits that are then used to fit the original data, again, to the model for S-N. This results in a family of curves for each probability percentile (P). The S-N model parameters can also be modeled as a function of P to interpolate to other P values. Weibull's approach can be used to predict a distribution of lives for a given stress by solving for N for each P at the given S .

The above method applies directly to the simple case of uniform load and macroscopic stress risers. The question remains as to how to apply this approach to a corroded surface with a k_t map. Incorporation of this map requires accounting for the contribution to the cumulative probability distribution of life of each pixel in the k_t map. The proposed pixel/area model makes use of an extension of Weibull's sizing effect approach to surface area elements (dA). In Weibull's paper, he explains how his methodology can be scaled by the gage length of the test specimen. He suggests that it can also be generalized to volume, but warns of potential problems in doing so, including the possibility that there might be surface effects that would make the model invalid. In the approach proposed herein, it is these surface effects that are to be modeled. As motivation for this proposed approach, it is noted here that all cracks in Navy corrosion-fatigue and strain-life specimens have initiated on the surface of the specimens, suggesting that a surface area scaling is warranted. Admittedly, this assumption has not been independently proved valid, and is, therefore, posited as a working hypothesis to be tested by experiment.

Weibull accounts for specimen length by the weakest link formalism. The probability of a specimen failing, defined in the Navy context as crack initiation (i.e., the presence of a 0.010-inch crack), is one minus the probability of no failure. When a specimen is twice the length of the original strain-life specimens in the gage section, then the probability of no failure in N cycles or less is just the square of the probability of no failure of the original-length specimen. Similarly, the probability of no failure of a specimen of arbitrary gage length, L , is just the probability of no failure for the original length specimen, L_0 , raised to the L/L_0 power. The form of Weibull's distribution is such that the probability of no failure in the original length specimen is simply:

$$1-F_1(N,S) = \exp\{-\exp(b)(S - U)^a\},$$

where a , b , and U are model parameters and F is the probability of failure in N cycles or less at applied stress S . Therefore, the probability of no failure of a specimen of length L is:

$$\begin{aligned} 1-F_L(N,S) &= (1-F_1(N,S))^{L/L_0} \\ &= \exp\{-(L/L_0)\exp(b)(S - U)^a\}. \end{aligned}$$

And the probability of failure of this specimen is:

$$F_L(N,S) = 1 - \exp\{-(L/L_0)\exp(b)(S - U)^a\}.$$

To generalize this to a surface area element, the expression is converted from length to area by defining an area element by dA , the size of a pixel in the k_t maps (and white light profilometry maps). Instead of L_0 , A_0 is used, which is the surface area of the gage section of the original strain-life specimens. The resulting probability of no failure at surface area element dA is given by:

$$F_{dA}(N,S) = 1 - \exp\{-(dA/A_0)\exp(b)(S - U)^a\}.$$

where S is the stress at the surface area element. This formalism can be adjusted to define S as the applied stress by replacing S with $k_t S$. The probability of no failure of a collection of such area elements is the product of the probabilities of no failure for each individual element:

$$1 - F_{\text{total}}(N,S) = \prod_i \{1 - F_{dA}(N,k_{ti}S)\}$$

where “i” is an index for area elements. This can be re-stated in terms of the k_t histogram, $h(k_t)$:

$$1 - F_{\text{total}}(N,S) = \prod_j \{1 - F_{dA}(N,k_{tj}S)\}^{h(k_{tj})}$$

where “j” is an index for k_t in the histogram of k_t . Finally, the probability of failure can be fully expressed in terms of the entire k_t histogram:

$$\begin{aligned} F_{\text{total}}(N,S) &= 1 - \prod_j \{1 - F(N,k_{tj}S)\}^{h(k_{tj})} \\ &= 1 - \exp\{\sum_j [-(dA/A_0)h(k_{tj})\exp(b)(k_{tj}S - U)^a]\} \end{aligned}$$

where the product is now expressed as a sum in the exponent and the power of $h(k_{tj})$ is now a factor in the exponent.

There are a few more details that allow this methodology to be applied in practice. The formalism can be generalized to account for plastic deformation by replacing $k_t S$ with σ_a , the stress amplitude at a given location. This requires calculating the stress amplitude for each k_t value and each applied stress. The parameters a , b , and U need to be modeled as functions of N . Mean stress effects need to be incorporated in the analysis through the use of Morrow’s approach, which causes a , b , and U to be evaluated for N^* , which is now a function of k_t . Including these details, the form of the model is:

$$\begin{aligned} F_{\text{total}}(N_f,S) &= 1 - \\ &\exp\{\sum_j [-(dA/A_0)h(k_{tj})\exp(b(N^*))(\sigma_a - U(N^*))^{a(N^*)}]\} \end{aligned}$$

Finally, the entire Weibull approach can be developed based on strain instead of stress; in that case, σ_a is replaced with ϵ_a in the above expression and all models are in strain instead of stress.

The following steps are used to apply this proposed approach in practice:

- For each N_f :
 - For each k_t :
 - Determine maximum stress and stress amplitude from the applied peak stress;
 - Determine mean stress (difference between maximum stress and amplitude);
 - Calculate X (the Morrow factor);
 - Calculate N^* ;
 - Determine strain amplitude;
 - Determine fit parameters for Weibull at that N^* and that strain amplitude;
 - Calculate contribution to the exponent for this k_t , weighting by the histogram value for this k_t and scaling by dA/A_0 ;
 - Sum over all k_t values;
 - Probability = $1 - \exp(\text{sum over contributions from all } k_t \text{ values})$.
 - Repeat for a spread of N_f values for a probability distribution across N_f .

To this point of the discussion, cases with non-constant amplitude, such as the Navy corrosion-fatigue tests ($R = 0.1$ and $R = 0.7$), have not yet been covered. This situation is normally handled with methods of cycle counting. Fortunately, in the Navy corrosion-fatigue tests, cycle counting simplifies considerably. This conclusion arises from the fact that, for even the highest applied stress (i.e., 200 ksi) and a k_t as high as 3.5, for the $R = 0.7$ cycles, the stress amplitude (115 ksi) is well below the endurance limit; the $R = 0.7$ cycles have infinite life. Mean stress considerations (i.e., Morrow's factor) will not change this fact, since mean stress would simply modify the life by a finite factor. But, modifying an infinite life by a finite factor still results in an infinite life. Thus, the $R = 0.7$ portions of the corrosion-fatigue tests add cycles to the life of the test specimen without using any of the life. Therefore, when comparing test results to life prediction, the $R = 0.7$ cycles should be either added to the life predicted from the $R = 0.1$ cycles or subtracted from the tested life. As a consequence, predicted life is based on $R = 0.1$ calculations only.

As a test case and example of this process, specimen 16 test results from the Navy AF1410 corrosion-fatigue specimen Set A were considered. This specimen was found to have a fatigue life to crack initiation of 17,580 cycles. The number of cycles included at $R = 0.7$ were 12,000, leaving only 5,580 cycles at $R = 0.1$. The above-proposed life prediction method was applied to the strain-life data collected on AF1410 to develop the underlying models. In addition, white light interference profilometry data from specimen 16 was processed with the UDRI elasticity approach to develop k_t maps of the corrosion surface. The k_t histogram and models were then used to predict a probability distribution for lives at the applied peak stress of 200 ksi. This prediction is shown in Figure 5.4.1-1.

It is to be noted that some reasonable filtering was done to the k_t map (i.e., eliminating isolated high k_t pixels) and to the analysis (i.e., clipping stress and strain by ultimate limits). It should also be noted that Set A specimens have high surface residual stress that has not been included in the model or in the life prediction. As a result of this residual stress, life predictions are expected to underestimate the measured life of the specimen. It is also understood by the industry that life predictions based on k_t values will, in general, underestimate the life. This effect is known as the notch effect. The smaller the notch, the greater the conservativeness expected in the life prediction. The data in Figure 5.4.1-1 do not account for this notch effect in any way. Efforts to incorporate the notch effect by using Peterson's or Neuber's formula for a correction factor to k_t are discussed in the next section. Given these considerations, there appeared to be a promising correlation to the measured life in this one example. Obviously, additional data and support are needed in order to develop confidence in the proposed approach.

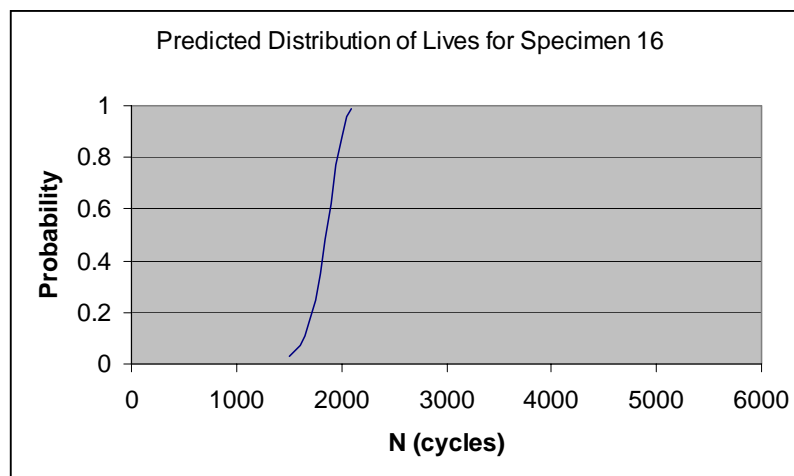


Figure 5.4.1-1. Predicted life distribution for corrosion-fatigue Set A specimen 16.

After this approach and preliminary data were presented to the Corrosion-Fatigue Assessment team, NAVAIR performed additional calculations on other AF1410 set specimens. Figure 5.4.1-2 gives the results of these calculations for specimens 42 and 36. In each case, the predictions are non-conservative.

In summary, a proposed approach to life prediction has been presented that accounts for the stress-strain curve, Neuber's rule, stress and strain amplitudes, mean stresses, strain-life data, the k_t histogram, size effects, non-constant amplitude stress profile (cycle counting), and the need for a life distribution. Preliminary results were favorable, but additional trials were not. Other reliability models are needed.

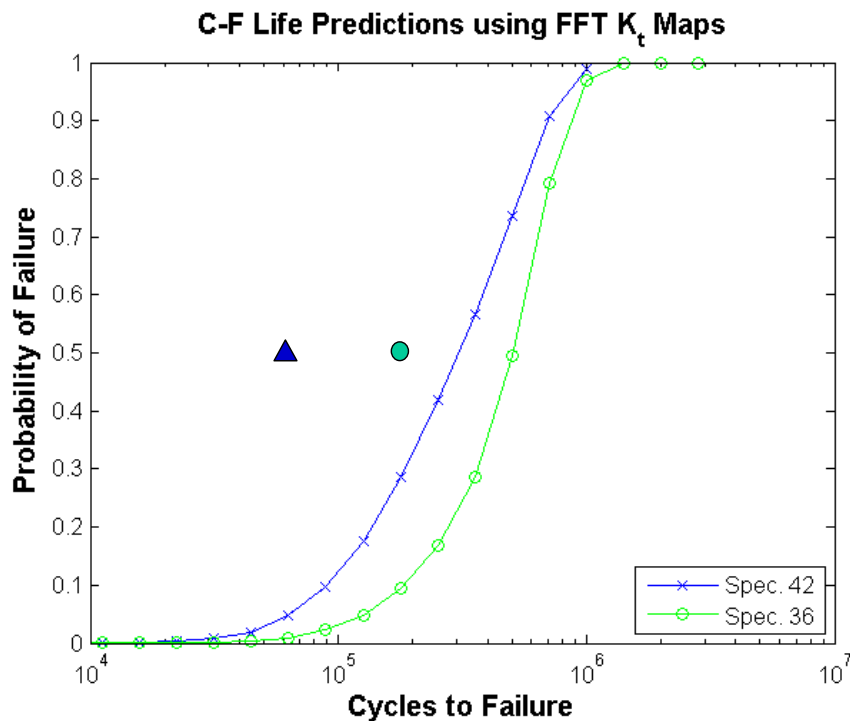


Figure 5.4.1-2. Life predictions using the pixel/area model for AF1410 Set A specimens 42 (blue) and 36 (green) curves. Also shown are experimental lives to crack initiation (triangle and circle).

5.4.2 Equivalent Stress Riser Model

Subsequent to the above study, NAVAIR developed the Equivalent Stress Riser (ESR) model, which models the life, not of pixels, but of individual pit-like features in the corrosion identified by the elasticity model. The stress concentration for each feature is estimated using the UDRI pit metric, as improved by ESRD's extension, to account for differences between FEA

results and the pit metric, as well as to account for orientation of the pit with respect to the load direction. In the ESR model, the probability of failure is calculated from strain-life data and a Peterson notch sensitivity factor, which moderates the effect of the stress riser by a factor dependent on the size of the notch. In particular, notches with smaller root radii are hypothesized to have smaller effects on life than notches with the same stress concentration, but larger root radii. The cumulative effect of all features is handled probabilistically. A set of algorithms was developed on the program to search through the stress concentration map to find regions of interest (ROIs) with high stress concentration (see Section 5.3 above). An ellipsoid is fit to each ROI and the root radii are estimated. Tests of the ESR model on the corrosion-fatigue specimens have shown a consistent conservativeness in the life predictions. The question of how to deal with this conservativeness was a topic for the third contract and is reported in the corresponding final report. Additional detail on the ESR model is found in an ancillary report [4].

Section 6

Nondestructive Evaluation

6.0 Introduction

The purpose of the nondestructive evaluation study was to develop methods to classify corrosion found in components on board an aircraft carrier or in the depot using traditional inspection techniques or modifications to those techniques. Classification requires correlating metrics determined from inspections with reduction in fatigue life. This correlation allows a classification scheme with severities of cosmetic, mild, and severe. Cosmetic corrosion has no impact on fatigue life. Severe corrosion has such a drastic effect on fatigue life, that the component must be removed from service. Mild or moderate corrosion produces some effect on fatigue life, but it is not clear without additional analysis whether the component should be replaced or returned to service. It is important to be able to make this classification on board the aircraft carrier or in the depot based on nondestructive inspection results.

During the first contract on this program, several inspection methods were investigated to ascertain the potential for use in this application. As a result of that study, ultrasonic and eddy current methods were selected for further study. As part of this contract, ultrasonic and eddy current data were collected from the AF1410 Set A and Set B specimens. From this data, a study was performed to compare roughness statistics calculated from the detailed white light interference microscopic surface height profiles to that determined from the NDE data.

6.1 Ultrasonic Inspection of Corrosion-Fatigue Specimens

Earlier in the program, several ultrasonic inspection techniques were considered as candidate NDE methods for corrosion-fatigue metric assessment. Of the several techniques investigated, normal incidence time-of-flight approaches performed as well as, or better than, any other technique. There are at least two methods for determining time-of-flight to the surface in order to map surface height profiles. The most direct method is to determine the time-of-flight to the peak indication within a gate. The other method is to use the slope of the phase in the frequency domain of the ultrasonic waveforms. Other potential metrics can be based on amplitude of the peak received from the backscatter from the surface of the component. The peak amplitude is one such metric. Finally, a local RMS can be determined from the slope of the Fourier magnitudes. Each of these metrics is described in more detail in Reference 1. While these metrics have been de-

terminated for the AF1410 Set B specimens from ultrasonic data, the focus of subsequent study has been the time-of-flight measurements based on the phase slope calculation derived from the ultrasonic waveforms. This method is more computationally intensive than a simple time-of-flight to the peak amplitude in the waveform, but it tends to be less sensitive to noise.

Typical setup parameters for the ultrasonic inspections are given in Table 6.1-1. AF1410 Set B specimens were inspected and complete waveforms were captured and stored for post-processing. In order to account for variations in the mechanical scanning standoff that produce surface height anomalies, a plastic plate was positioned between the transducer and the specimen. Data were collected from this plastic plate and used to remove these anomalies in the surface height profiles. In order to avoid producing additional corrosion in the steel specimens, ultrasonic inspections were performed with the specimens immerse in Ethyl alcohol. Procedures for preparing for an inspection are included in Table 6.1-2. Maps of the various metrics described above were prepared using custom MathCad routines.

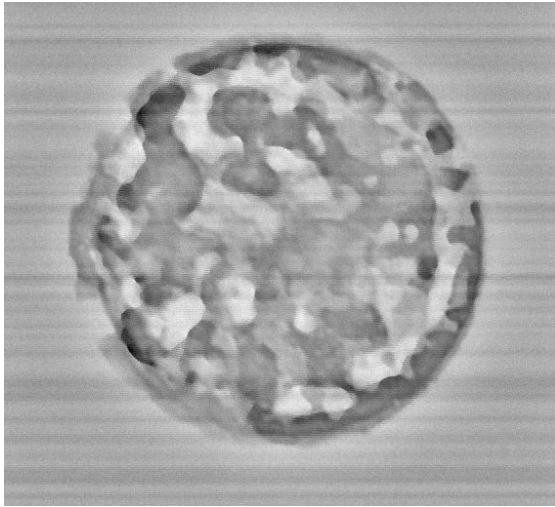
Table 6.1-1. Typical Ultrasonic Setup Parameters

Acquisition System	UTEX
Purpose	Corrosion Surface Characterization for 547-50B Front
Specimen Information	
ID	547-50B
Material	AF-1410 Steel
Geometry	Fatigue Specimen
Surface Condition	Polished to 400 grit
Pulser/Receiver Information	
Manufacturer	JSR
Model	PR35
Rep Rate & Filters	RR=min, HPF=5.0, LPF=out
Energy	1
Gain	67
Damping	~7.4
Trigger	Internal
Transducer Information	
Manufacturer	Krautkramer S/N 013W12
Bandwidth Type	Alpha
Center Frequency	~25 MHz
Diameter	6.35mm
Focal Type	Spherical
Focal Length	51 mm
Scan Plan Information	
Type	Normal incidence 3D RF B-scan
Focal Plane	Front surface
Data Gate Location	Over entire surface echoes (see below)
Data Digitizing Rate	1 GHz
Scan Length	1.7 in
Scan Increment	0.0025 in
Index Length	1.5 in
Index Increment	0.0025 in
Scan Velocity	0.2 in/sec

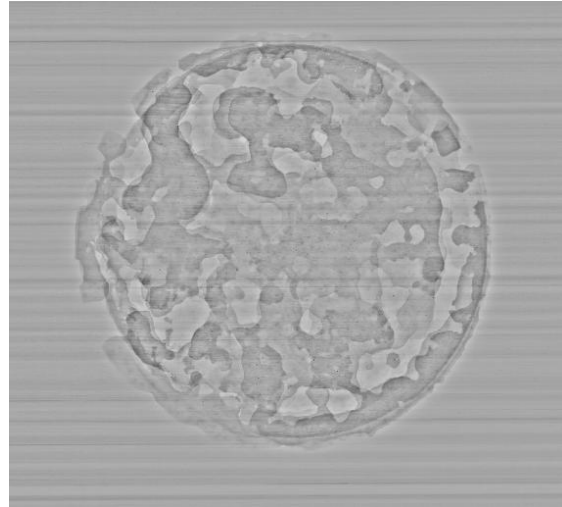
Table 6.1-2. Ultrasonic Scan Preparation Procedures

<p>Part I – Collection of Data from the Corroded Steel Specimen</p> <ul style="list-style-type: none">a. Level the steel specimen without the plastic reflector plate in placeb. Place the plastic reflector plate over the steel specimen<ul style="list-style-type: none">i. Center the plastic reflector plate over the corrosion patchii. Level the plastic reflector plate – multiple reflections from the entry and back surfaces of the plastic reflector plate must not overlap the entry-surface echo from the steel specimenc. Focus the ultrasonic beam on the entry surface of the steel specimend. Set five (5) gates<ul style="list-style-type: none">i. Gate 1 – time-of-flight over the first echo from the entry surface of the plastic reflector plateii. Gate 2 – time-of-flight over the first echo from the back surface of the plastic reflector plateiii. Gate 3 – time-of-flight over the first echo from the entry surface of the steel specimeniv. Gate 4 – maximum amplitude over the first echo from the entry surface of the steel specimenv. Gate 5 – waveform over the first echo from the entry surface of the steel specimen
<p>Part II – Collection of Data from the Glass Calibration Standard</p> <ul style="list-style-type: none">a. Level the glass calibration standard without the plastic reflector plate in placeb. Place the plastic reflector plate over the glass calibration standard<ul style="list-style-type: none">i. Center the plastic reflector plate over the glass calibration standardii. Level the plastic reflector plate – multiple reflections from the entry and back surfaces of the plastic reflector plate must not overlap the entry-surface echo from the glass calibration standardc. Focus the ultrasonic beam on the entry surface of the glass calibration standardd. Set five (5) gates<ul style="list-style-type: none">i. Gate 1 – time-of-flight over the first echo from the entry surface of the plastic reflector plateii. Gate 2 – time-of-flight over the first echo from the back surface of the plastic reflector plateiii. Gate 3 – time-of-flight over the first echo from the entry surface of the glass calibration standardiv. Gate 4 – maximum amplitude over the first echo from the entry surface of the glass calibration standardv. Gate 5 – waveform over the first echo from the entry surface of the glass calibration standard

Figure 6.1-1 is an example of ultrasonic time-of-flight and white light interference microscope surface height profiles for an AF1410 Set B specimen number 545-6A, a 3-hour exposure specimen. The ultrasonic time-of-flight image captures much of the detail seen in the white light image, but with poorer resolution, as is expected for this technique.



Ultrasonic Image of 545-6A



White Light Image of 545-6A

Figure 6.1-1. Example Ultrasonic Time-of-Flight (left) and White Light Interference Microscope (right) Profiles for 3-hour exposure AF1410 Set B specimen number 545-6A.

6.2 Eddy Current Inspection of Corrosion-Fatigue Specimens

Eddy current inspections were performed on the AF1410 Set B specimens and a study was conducted to determine the ability of eddy currents to map surface profiles and measure surface roughness. A 0.080-inch diameter absolute eddy current coil with a ferrite core was used for these inspections. A second coil was prepared that had the ferrite core slightly extended from the windings with the core sharpened to a point. This probe was used to investigate the possibility of improving lateral resolution for this application. Standoff was adjusted to 0.003 inches above the specimen with the liftoff signal, which is being used to monitor changes in surface height, rotated to the vertical channel of the eddy current instrument. The probe drive frequency was 4 MHz and 8 MHz. The high-pass filter of the instrument was bypassed for these absolute measurements and the specimen was leveled for each inspection. Data were collected at several different liftoffs to allow the calibration of a scaling factor to convert from eddy current response to actual liftoff.

Figure 6.2-1 shows a typical eddy current inspection (left) and the corresponding white light interference microscope profile image (right). This is the same specimen displayed in Figure 6.1-1. As can be seen from these images, the eddy current inspection captures the general pattern of the corrosion, but has a poorer resolution than both the ultrasonic inspection and the white light interference microscope measurements. Tests have shown that these 0.080-inch diameter coils have a spatial resolution of approximately 0.71 mm at 4 MHz. The sharpened coil has a

spatial resolution of 0.67 mm at 4 MHz and 0.63 mm at 8 MHz. Details and results of this study were presented at the Review of Progress in Nondestructive Evaluation and will be published in the Conference Proceedings [5].

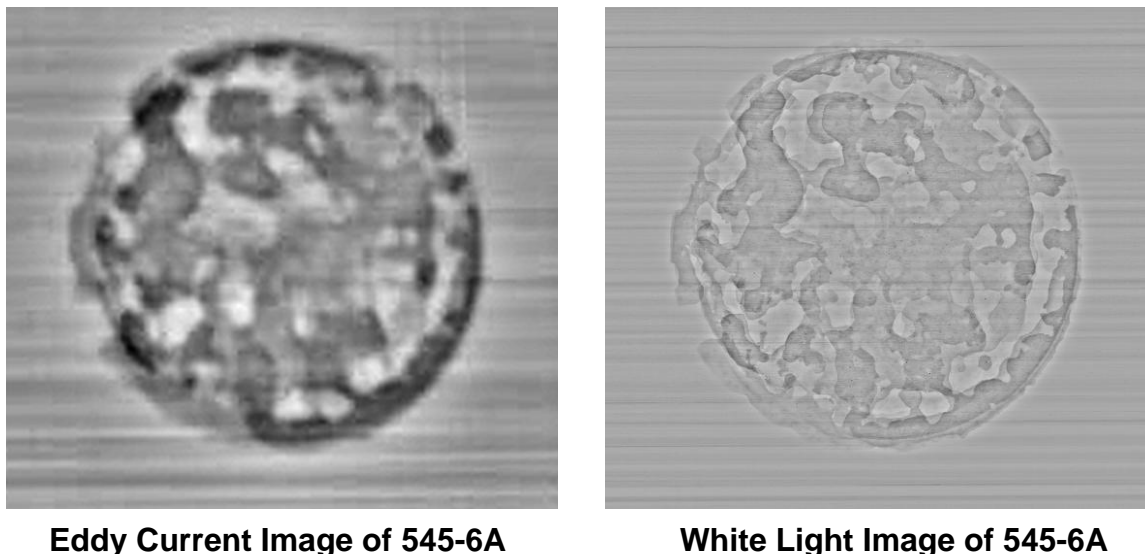


Figure 6.2-1. Example Eddy Current Liftoff (left) and White Light Interference Microscope (right) Profiles for 3-hour exposure AF1410 Set B specimen number 545-6A.

6.3 Global Statistics

In order to assess the effectiveness of the ultrasonic inspection technique to categorize corrosion severity via the calculation of different metrics, a study was performed to compare the metrics determined from the ultrasonic data to that obtained from the white light interference microscopy data. The first step in this process was to register the ultrasonic images to the white light images. This was accomplished by identification of landmarks in both images and using TurboReg plug-ins. Images are despeckled (twice in the case of the ultrasonic image), and edge images are created from the white light and ultrasonic images. The images are visually compared with magnifying software to judge the degree of registration. When finished, the images are considered registered and ready for further comparisons and calculations. A large circular region of interest is selected within the corrosion patch for roughness metric calculations. The same region of interest is defined for both registered images. Roughness statistics are then calculated for this region of interest in both images for comparisons. The statistics include mean, modal, median, skewness, kurtosis, R_a , R_q , maximum, minimum, and range. Figure 6.3-1 shows a plot of R_a from the white light profiles versus R_a from the ultrasonic profiles for a subset of AF1410 Set B specimens.

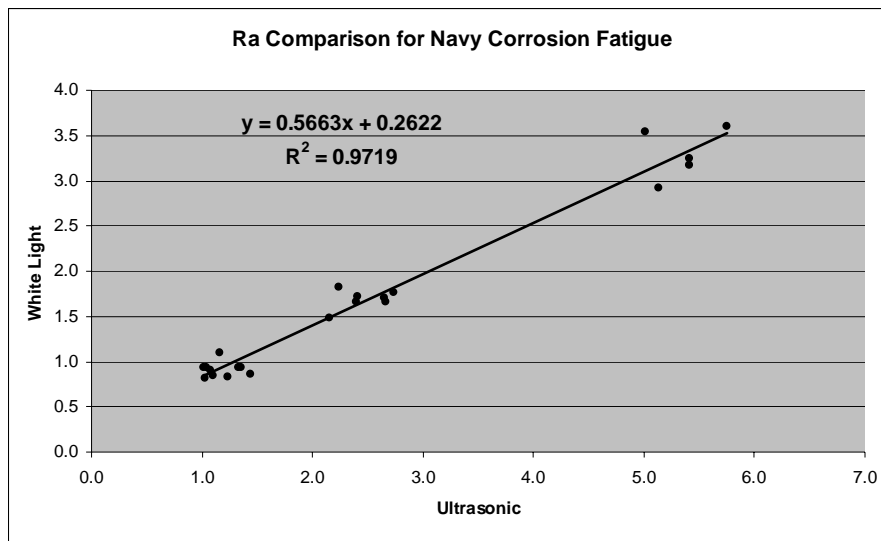


Figure 6.3-1. R_a from White Light Interference Microscope Profiles versus R_a from Ultrasonic Time-of-Flight Profiles for a subset of AF1410 Set B specimens.

Figure 6.3-2 shows a plot of R_q from white light interference microscope profiles versus R_q from ultrasonic time-of-flight profiles for a subset of AF1410 Set B specimens. Each plot and the associated fit show very good correlations between these metrics determined from the ultrasonic and white light interference microscope profiles. These results suggest that the use of ultrasonic time-of-flight is a very promising NDE method for determining the severity of corrosion.

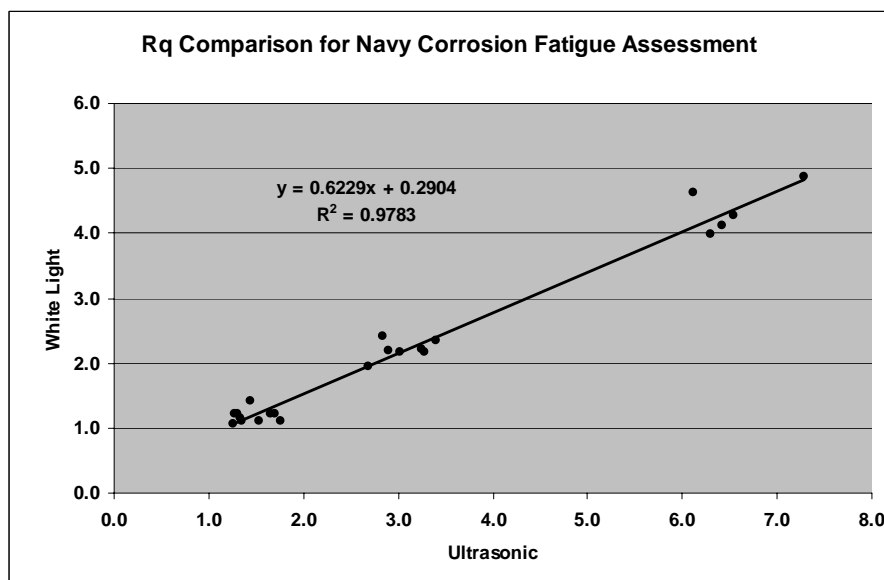


Figure 6.3-2. R_q from White Light Interference Microscope Profiles versus R_q from Ultrasonic Time-of-Flight Profiles for a subset of AF1410 Set B specimens.

Section 7

Implementation Scheme

The ultimate goal of this program was to develop tools that can be used to specify the maintenance options for corroded components and to provide a sound engineering basis for selecting the best fleet maintenance options. Essentially, the program was to provide quantifiably justified maintenance criteria for environmentally induced damage (i.e., corrosion) in high-strength steels.

During the second contract on the Navy Corrosion-Fatigue Assessment Program, an implementation strategy was developed. This scheme is described by a flowchart, shown in Figure 7.1, starting with a visual inspection of the component onboard an aircraft carrier. If corrosion is observed, it is cleaned and an inspection is performed. The relatively low resolution of this inspection prohibits a detailed application of the equivalent stress riser model; however, the inspection can be used to calculate corrosion metrics, such as R_a or R_q , and then to classify the corrosion as cosmetic, mild, or severe. If the corrosion is cosmetic, it will have no significant impact on component life, the component can be cleaned and coated (to prevent corrosion), and returned to service. If the corrosion is deemed to be severe, then the component is removed from service; the reduction in fatigue life is too great to allow the component to remain in service. If the corrosion is mild, then a replica is made of the corrosion, which is then sent to the depot for a high-resolution surface height mapping and subsequent analysis. At this point, the Equivalent Stress Riser model is applied in order to make a disposition decision concerning the component.

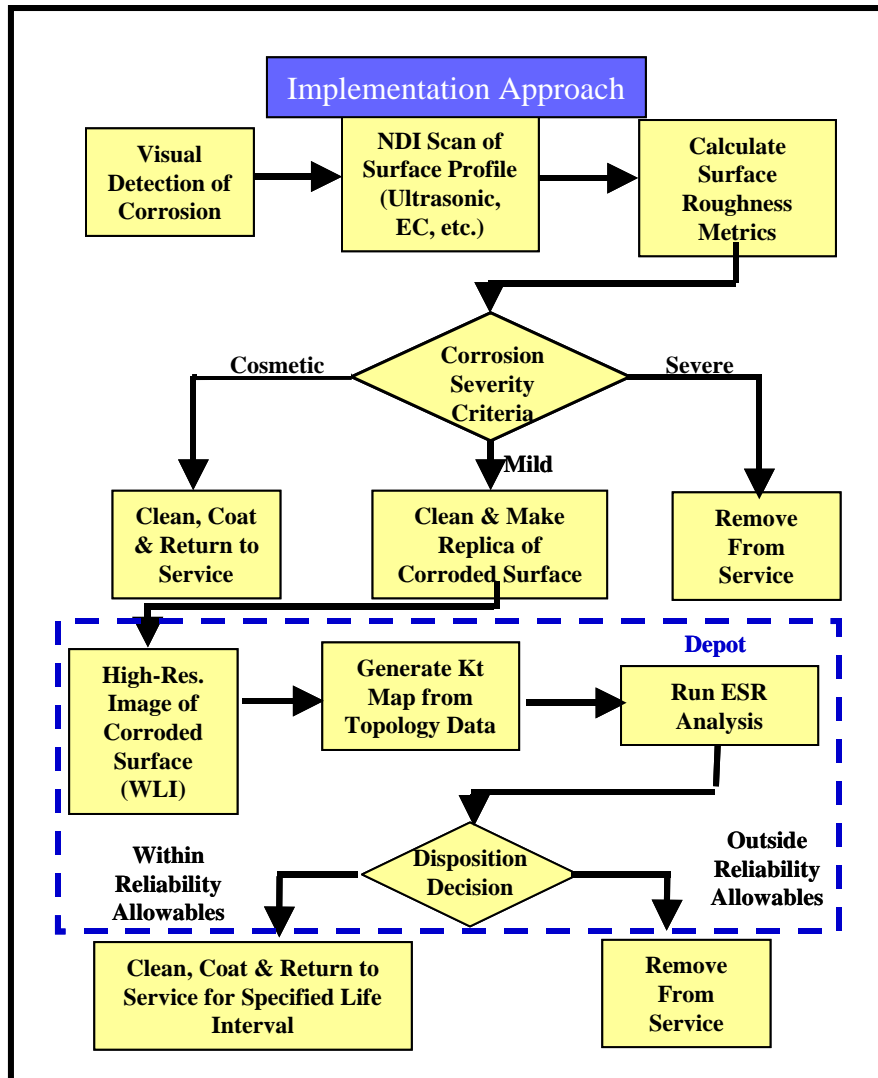


Figure 7.1. Implementation Strategy.

Section 8

Conclusion

Significant progress has been made towards the development of a maintenance program for high-strength steels that includes the effects of corrosion. Once corrosion has been identified visually, the plan will be to assess the severity of the corrosion with an NDI method based on a corrosion metric. If the corrosion is judged to be cosmetic, the component will be return to service after cleanup and recoating of the corroded area to eliminate subsequent corrosion damage growth. If the corrosion is judged to be severe, the component will be removed from service until it can be reworked at the depot. If the corrosion is judged to be mild, a replica of the corroded surface will be made and sent to a laboratory for detailed white light interference microscopic measurements of the profile and subsequent disposition analysis.

This program contract has met it goals in the overall plan to develop tools that can be used to specify the maintenance options for corroded components and provides a foundation on which to build the next program contract that will further advance these tools in the development of maintenance practices for high-strength steels.

Section 9

References

1. W. Hoppe, et. al., “Navy High-Strength Steel Corrosion-Fatigue Modeling Program”, final report, UDR-TR-2007-00039.
2. W. Weibull, “A Statistical Representation of Fatigue Failure in Solids”, Transactions of the Royal Institute of Technology, Stockholm, Sweden, 1949.
3. D. Rusk, et. al., “Results of Fatigue Tests of Bare Af1410 Steel Unnotched Flat Plates with Surface Corrosion Damage”, Navy report: NAWCADPAX/EDR-2008/10.
4. D. Rusk, W. Hoppe, W. Braisted, and N. Powar, “Modeling and Prediction of Corrosion-Fatigue Failures in AF1410 Steel Test Specimens”, NAVAIR Technical Report: NAWCADPAX/TR-2008/60.
5. R. Ko, N. Schehl, “Eddy Current Monitoring of Surface Roughness”, Presented at Review of Progress in Quantitative Nondestructive Evaluation, Golden, Colorado, July 22-27, 2007. To be published in Conference Proceedings.

Appendix A

ESRD Final Report

US Navy High Strength Steel Corrosion-Fatigue Modeling Program

Final Technical Report FY2006

January 19, 2007²

Brent Lancaster, Ricardo Actis and Barna Szabó³
Engineering Software Research and Development (ESRD), Inc.
111 West Port Plaza, Suite 825
St. Louis, MO 63146
314-744-5021 ext. 11
Contact: barna.szabo@esrd.com

This report was prepared for the University of Dayton Research Institute, Dayton, OH under subcontract RSC05037, as part of US prime contract No. F42620-00-D-0028/0040. Period of performance: October 1, 2005 – August 31, 2006

² Revision Date June 26, 2007

³ Principal Investigator

TABLE OF CONTENTS

1. Scope	7
1.1 Original terms of reference	7
1.2 Deliverables	8
1.3 Accomplishments	9
2. Importance	9
3. Goals	10
4. Numerical Simulation	10
5. Planning	12
6. Approaches/Methodologies	13
6.1 Study of White Light Interferometry (WLI) Topology Data for Potential Metrics	15
6.1.1 Introduction	15
6.1.2 Study Approach and Results	15
6.1.2a MATLAB/Visual Basic Application for Statistical Analysis of Corroded Specimens	15
6.1.2b Visual Comparison of 1/16th and Full Dataset of UDRI Corroded Test Specimens.....	19
6.1.2c Corroded Specimen WLI Measurements: Filtering Approaches and Issues	24
6.1.2d RMS Studies of Corroded Surface Profiles	26
6.1.2e RMS Field vs. Crack Initiation Locations for AF1410 Set A Specimen 16.....	28
6.1.3 Summary	30
6.2 An Alternative Method for Life Prediction: Equivalent Crack Size (ECS)	30
6.2.1 Introduction	30
6.2.2 Study Approach and Results	30
6.2.2a Preliminary Studies Using AFGROW to Predict EIFS for AF1410 Batch A	30
6.2.2b Using AFGROW to Determine ECS for AF1410 Batch A Specimens	35
6.2.2c AF1410 Set A Specimen ECS vs. WLI Depth Measurements.....	39
6.2.2d ECS vs. Crack Initiation Site Maximum Pit Depths for AF1410 Set A 6 Hour Corrosion ..	42
6.2.2e StressCheck Analysis of the Effect of Pit Dimension on the Stress Intensity Factor	43
6.2.3 Summary	43
6.3 Discovery Experiment: Micro-Machined Features of Similar Kt	44
6.3.1 Introduction	44
6.3.2 Study Approach and Results	44
6.3.2a Proposed Features for Micro-machined Geometry.....	44
6.3.2b Conical Feature Dimensions	45
6.3.2c Ellipsoidal Feature Dimensions	45
6.3.2d Pill-Shape Feature Dimensions.....	46
6.3.2d StressCheck Kt Verification for Micro-machined Geometry	46
6.3.3 Summary	47
6.4 Parametric Pit Studies Based on Idealized Corroded Surface Topologies	47
6.4.1 Introduction	47
6.4.2 Study Approach and Results	47
6.4.2a Case 1: Single Pit Configuration (Specimen #20).....	47
6.4.2b Case 2: Elongated Pit (Specimen #15).....	50
6.4.2c Case 3: Two Interfering Pits (Specimen #36).....	52
6.4.2d Case 4: Four Interfering Pits (Specimen #46)	54
6.4.2e Parametric Studies of Pit Metric Kt vs. StressCheck Kt for Ellipsoidal Features	60
6.4.2f Effect of Orientation on Ellipsoidal Feature Kt	63
6.4.2g Effect of Biaxial States of Stress on Kt for Single Pit Configurations	66
6.4.3 Summary	68

7. Plan for Deployment	68
8. Summary.....	69
9. Recommendations for Future Work	69
10. Appendix.....	70
10.1 Additional ECS Post-Diction Results for AF1410 Set A Specimens	71
10.2 Case of Misleading Local RMS Prediction for Crack Initiation Location	74
10.3 Selected References on Verification and Validation.....	75

FIGURES

Figure 1. Contour Plot of Dogbone 16: 1/16 th Dataset (All Values in Millimeters)	16
Figure 2. Visual Basic Application for Corroded Surface Patch Extraction.....	17
Figure 3. Loading of Full Dataset and Subsequent Extraction Message	18
Figure 4. Dogbone 16 Full Dataset Partition: 33X33 Pixel Patch (All Values in Millimeters).....	18
Figure 5. Sample Statistical Extraction from Dogbone 16 Partition.....	19
Figure 6. ImageJ Rendering of Dogbone 2 Full Dataset.....	20
Figure 7. Surface Plot 3D Rendering of Selected Region in Figure 6	21
Figure 8. Surface Plot 3D Rendering of Selected Region in Figure 6: 50% Smoothing	21
Figure 9. 1/16th Resolution Plot of Tilt-Corrected Dogbone 2 Corroded Surface	22
Figure 10. Contour Plot of 1/16 th Resolution Patch Taken From Figure 9	23
Figure 11. Contour Plot of Full Resolution Patch Taken From Figure 9.....	23
Figure 12. Dogbone 2 Original White Light Measurements (with Smoothing)	24
Figure 13. Dogbone 2 8mm Gaussian Filtering with Tilt-Correction.....	25
Figure 14. Dogbone 2 White Light Surface Profile w/ Potential Noise Characteristic	25
Figure 15. Dogbone Surface Profiles for Varying Corrosion Severity	26
Figure 16. Dogbone 2 Plot Comparison of Pristine and Corroded Regions	27
Figure 17. Schematic of RMS Field Generation for a Sample Specimen Surface.....	28
Figure 18. Specimen 16 RMS Field (50K Pts, 30X30 Sample Area).....	29
Figure 19. Specimen 16 with Failure Location Identified	29
Figure 20. A vs. N Crack Length Prediction for Specimen 55	32
Figure 21. A vs. N Crack Length Prediction for Specimen 44	33
Figure 22. A vs. N Crack Length Prediction for Specimen 19	33
Figure 23. A vs. N Crack Length Prediction for Specimen 50 (Baseline).....	34
Figure 24. Summary of EIFS Values for AF1410 Set A Pristine Specimens	34
Figure 25. Process Map of ECS Method.....	36
Figure 26. Computation of ECS.....	36
Figure 27. Summary of ECS/EIFS Values for AF1410 Set A Specimens.....	37
Figure 28. AF1410 Set A Specimen 16 Crack Size versus Cycles: ECS Post-Diction	38
Figure 29. Specimen 16 Failure Region Feature.....	39
Figure 30. Maximum Extracted Depth vs. ECS (5000 points)	40
Figure 31. Mean of the Twenty (20) Maximum Extracted Depths vs. ECS (5000 points).....	41
Figure 32. Mean of the Twenty (20) Maximum Extracted Depths vs. ECS (16000 points).....	41
Figure 33. Comparison of ECS and Actual Measured Pit Depth.....	42
Figure 34. Sensitivity Study of the Effect of Pit Size on the SIF.....	43
Figure 35. Proposed Arrangement of Features for Micro-machining Experiment	44
Figure 36. Conical Feature Dimensions.....	45
Figure 37. Ellipsoidal Feature Dimensions.....	45
Figure 38. Pill-Shape Feature Dimensions	46
Figure 39. Kt Verification for Micro-machined Geometry.....	46
Figure 40. Case 1 Pit Configuration.....	47
Figure 41. Case 1: Maximum Kt is 2.126 (0.00% Error).....	48
Figure 42. Strain-Life Methodology (Shown with the Neuber's Rule Equation)	49
Figure 43. Cyclic and Monotonic Stress-Strain Curves for AF1410	49
Figure 44. Specimen 20 Crack Initiation Pit and Finite Element Mesh Idealization.....	49
Figure 45. Specimen 16 Load Step Analysis: ϵ_1 -S Profile	50
Figure 46. Case 2 Pit Configuration (Subcase 1 is shown).....	51
Figure 47. Case 2, Subcase 1: Maximum Kt is 2.543 (0.19% Error).....	51
Figure 48. Case 2, Subcase 2: Maximum Kt is 2.512 (0.38% Error).....	52
Figure 49. Case 3 Pit Configuration (Subcase 1 is shown).....	52

Figure 50a. Case 3, Subcase 1 (No Blending): Maximum Kt is 3.561 (0.03% Error).....	53
Figure 50b. Case 3, Subcase 1 (With Blending): Maximum Kt is 3.391 (0.28% Error)	53
Figure 51. Case 3, Subcase 2: Maximum Kt is 2.251 (0.20% Error).....	54
Figure 52. Case 4 Pit Configuration (Subcase 1 Shown).....	55
Figure 53a. Case 4, Subcase 1 (No Blending): Maximum Kt is 12.72 (0.00% Error).....	55
Figure 53b. Case 4, Subcase 1 (With Blending): Maximum Kt is 8.654 (0.43% Error)	56
Figure 54. Case 4, Subcase 2: Maximum Kt is 3.860 (0.05% Error).....	56
Figure 55. Schematic of Pit Interference Level	57
Figure 56. Interfering Pit Geometry.....	57
Figure 57. Interference Level of 0.001 mm (Kt=23.26)	58
Figure 58. Interference Level of 0.005 mm (Kt=11.41)	58
Figure 59. Interference Level of 0.01 mm (Kt=8.11)	59
Figure 60. Interference Level of 0.025 mm (Kt=4.74)	59
Figure 61. Comparison of Interference Level with Kt.....	60
Figure 62. Original Pit Metric Kt.....	60
Figure 63. Pit Metric Kt (Pink) versus StressCheck FEA Kt (Navy)	61
Figure 64. Proposed Modification to Pit Metric Kt	62
Figure 65. Modified pit metric Kt* (Pink) versus StressCheck FEA Kt (Navy)	62
Figure 66. Results from Modified Pit Kt* Validation Study	63
Figure 67. Pit Metric Kt(θ)	63
Figure 68. Pit Metric Kt(θ) (blue) versus StressCheck Kt(θ) (pink).....	64
Figure 69. Revised Pit Metric Kt(θ).....	64
Figure 70. Revised Pit Metric Kt(θ) (blue) versus StressCheck Kt(θ) (pink).....	65
Figure 71. Revised Pit Metric Kt*(θ).....	65
Figure 72. Final Summary of StressCheck FEA Kt(θ) and Proposed Pit Metric Kt(θ)'s	66
Figure 73. Biaxial Stress/Displacement for Pit Configuration.....	67
Figure 74. Kt Results Summary of Biaxial Applied Traction Load Case.....	67
Figure 75. Kt Results Summary for Biaxial Imposed Displacement Load Case for $\mu=1.0$	68
Figure 76. The main elements of numerical simulation and the associated errors.	70
Figure 77. ECS Method Post-Diction for Specimen 16.....	72
Figure 78. ECS Method Post-Diction for Specimen 59.....	72
Figure 79. ECS Method Post-Diction for Specimen 22.....	72
Figure 80. ECS Method Post-Diction for Specimen 56.....	73
Figure 81. Normalization of Computed (Post-Diction) Lives with Experimental Lives	73
Figure 82. AF1410 Set A Specimen #5 Crack Initiation Location	74
Figure 83. AF1410 Set A Specimen #5 Local RMS Extraction	75

TABLES

Table 1. NASGRO Equation Material Parameters	31
Table 2. Typical Residual Stress Distribution from Surface.....	32
Table 3. Representative Pit Dimensions	61
Table 4. Equivalent Crack Size (ECS) Computed from # of Cycles to Crack Nucleation	71
Table 5. Crack Initiation and Total Life Cycles, Measured and Predicted	71

1. Scope

This report covers year three of a multi-year effort, the principal objective of which is to achieve significant cost savings and enhanced readiness through the development of definitive corrosion maintenance criteria, the supporting diagnostics and enhanced repair capability to effectively manage structural maintenance of Naval aviation assets. This is a collaborative project among NAVAIR, the University of Dayton Research Institute (UDRI), Boeing Phantom Works in St. Louis and Engineering Software Research and Development, Inc. (ESRD).

1.1 Original terms of reference

ESRD, Inc. was to provide engineering services in support of this collaborative project. Specifically, ESRD was to perform the following tasks:

1. Provide numerical stress analysis services in support of the investigation of the predictability of onset of failure events caused by surface damage resulting from corrosion. The results of preliminary investigation summarized in reference [1] indicate that highly simplified representation of surface damage allows the estimation of stress concentration factors (K_t values) very efficiently. At the present time it is not known however whether the simplifications are permissible from the point of view of successful correlation of computed K_t values based on idealizations of corroded surfaces with onset of failure events. ESRD understands that validation experiments will be performed with the objective to collect statistical information and establish the range of predictability of onset of failure events in an experimental setting. ESRD will undertake to perform interpretation of validation experiments utilizing its software product StressCheck® and apply appropriate quality control procedures with the objective to verify the reliability of computed information.
2. In collaboration with NAVAIR, Boeing and UDRI, ESRD will develop criteria for validation of the predictive capabilities of the mathematical model. The validation protocol is to involve “blind” prediction of experimental results.
3. Based on the results of validation experiments, ESRD will modify the mathematical model as necessary for obtaining improved predictions of failure initiation events.

4. Develop a plan for the distribution the corrosion assessment technology developed under this project to the Navy and its subcontractors, utilizing the COM and Java interfaces of StressCheck®. The development of simple-to-use Windows desktop and web-based (or cross-platform) applications is envisioned. The interfaces are to provide a convenient communication protocol to integrate the necessary functions of other applications (e.g. MatLab probability and statistical functions) needed to quantifiably assess the useful remaining life of a corroded part. ESRD will expand the COM interface to include any new capabilities developed under this contract.
5. Coordinate project activities with the University of Dayton Research Institute, NAVAIR and Boeing Phantom Works in St. Louis.

Note that during the reporting period the state of development of the mathematical model for prediction was such that items 2 and 3 in the original terms of reference could not be completed. These items will be addressed under the activities of the next final report.

1.2 Deliverables

1. ESRD will provide monthly engineering status reports. These reports will include technical program status, accomplishments, issues and concerns and planned activities for the following quarter.
2. ESRD will provide a draft of the final engineering report thirty (30) days prior to the end of the contract period. The final engineering report will detail all studies, analyses and accomplishments completed in the course of this project.
3. ESRD will provide documentation of the examples that demonstrate the enhanced capabilities of StressCheck® and provide guidelines for proper application of StressCheck®. As a part of this deliverable, ESRD was to provide a means to include the effects of quasi-random material property variations into StressCheck®. This has been accomplished through a COM interaction with MATLAB, and tested in the Planar Elasticity reference using a plate with a center hole. A document outlining this procedure, entitled ESRDFY06Deliverable3.doc, is attached with this report. Further development is currently on hold as this technology is under review by NAVAIR.

1.3 Accomplishments

The accomplishments are detailed in the body of this report. Certain objectives, originally envisioned at the beginning of the project were modified by mutual agreement at project meetings.

2. Importance

As the naval aviation fleet ages, corrosion and environmental degradation have become major contributors to spiraling naval aviation maintenance costs, burgeoning repair backlog, and increased aircraft failure rates. The corrosion problem is most observable in high strength steels (HSS) which comprise critical aircraft components; AF 1410 is one such HSS. In fact, many recent aircraft losses due to corrosion/environmental degradation failures can be traced to a failure of HSS components. Aircraft including F/A-18, F-14, EA-6B and E-2C have been plagued by these corrosion-load cycle failures, forcing the USN the costly measure of grounding these aircraft for extended periods of time.

Much of the increasing cost and risk are attributable to the lack of definitive, clear-cut corrosion maintenance criteria, necessitating the repair and/or replacement of all corroded parts. Therefore, the U.S. Navy (USN) needs workable corrosion maintenance criteria that can be followed in today's operational environments providing safety and readiness within the limited operations and maintenance resources. With respect to corrosion, maintenance teams must be able to differentiate between corrosion with potential safety impacts and corrosion that does not have substantial impact on life. In other words, maintenance personnel must quickly determine what must be removed immediately and what can be tolerated for some time period. The distinction must be justified quantitatively. The USN needs corrosion maintenance criteria that are accessible for routine assessment of corroded components. In short, a reliable and robust geometrically and mechanically defined metric or directive for quantitatively predicting remaining corroded part lives is necessary for a reliable assessment. This approach must be timely and efficient in order to meet USN maintenance scheduling requirements.

Furthermore, it is imperative that workable metrics or models are properly filtered from those that are not feasible. For example, a proposed model that takes a very long time to compute a valid numerical result may be too costly because time is a crucial variable in terms of quantitative approaches; therefore it cannot be used as part of a maintenance program and has to be rejected. On the other hand, a complex (more detailed) model may be too costly to be used within a maintenance program but it can be used to generate benchmarks in order to avoid selecting an oversimplified model. An ideal model may be defined as one that does not imply extended grounding of aircraft during evaluation, yet produces reliable results.

3. Goals

This project was aimed at establishing intervals of inspection based on sound scientific principles and the latest analytical technology to reduce the number of occurrences of in-service failures. It was also hoped that unnecessary inspection procedures could be reduced or eliminated, leading to increased safety and reduced cost. Thus, the focus was on quantitative USN high strength steel corrosion-cycle fatigue modeling and the formulation of reliable predictions for remaining fatigue life. Specifically, developments of prediction models focus on current states of corrosion, as long-term corrosion is highly unpredictable in terms of both extent of damage and location.

In order to achieve these goals, methodical testing involving validation of proposed metrics and models must be performed both through laboratory testing and through numerical methods, such as the finite element method (FEM). Verification is a process by which the quality of the numerical solution is ascertained, and validation is the process for which a mathematical model is deemed to be an appropriate representation of the physical reality it is intended to represent. Validation of a model is performed through comparison with independently obtained experimental and numerical data.

FEM is a numerical method useful for obtaining approximate solutions to the equations of continuum mechanics. The accuracy of the approximate solution can be estimated. The technological prerequisites for verification of stresses in pristine (uncorroded) components, specifically in locations where corrosion occurs or is expected to occur, are currently available through the capabilities of StressCheck®.

StressCheck® is the finite element software product of ESRD Inc., of St. Louis, MO. It was chosen as the primary investigative analytical tool for the function of extracting potential mechanical relationships between corrosion and fatigue life. ESRD was to provide detailed mathematical corrosion model verification and validation for the USN and its project team, as well as to provide recommendations for improving the USN mathematical corrosion model.

4. Numerical Simulation

Working models are mathematical problems formulated so as to capture the essential characteristics of some physical system with the expectation that the data computed from the solution of a working model will be a reliable predictor of the data of interest. Proper selection of a working model is the most important decision when undertaking finite element analysis. Formulation of a working model involves a theoretical formulation, specification of input data and a statement of objectives.

1. Theoretical formulation. The applicable physical laws, together with certain simplifications, are stated as a mathematical problem in the form of ordinary or partial differential equations, or extremum principles.
2. Specification of input data. The input data are comprised of the following:
 - Data that characterize the solution domain.
 - Physical properties elastic moduli, yield stress, coefficients of thermal expansion, thermal conductivities, etc.
 - Boundary conditions (loads, constraints, prescribed temperatures, etc.) Information or assumptions concerning the reference state (initial conditions).
 - Uncertainties. It is useful to distinguish between two types of uncertainties: When some information needed in the formulation of a working model is unknown then the uncertainty is said to be cognitive (also called epistemic). For example, the magnitude and distribution of residual stresses is usually unknown, some physical properties may be unknown, In addition, there are statistical uncertainties (also called aleatory uncertainties): Even when the average values of needed physical properties, loading and other data are known, there may be very substantial statistical variations. Consideration of uncertainties is necessary in the interpretation of computed data.
3. Statement of objectives. Definition of the data of interest and the corresponding permissible error tolerances.

Associated with each working model is a modeling error. The process by which a working model is evaluated and modified to ensure that it meets necessary conditions for acceptance is called validation. The goal of validation is to ensure that the model is a sufficiently accurate mathematical description of the physical system or process it is supposed to represent⁴. Validation involves calibration and prediction. The determination of physical properties and other model parameters through correlation with experiments is called calibration. The use of a model to foretell the data of interest corresponding to some set of input data is called prediction.

Working models are solved by numerical means, most commonly by the finite element method. In this process the exact solution is approximated. Determination of the accuracy of data computed from the approximate solution of a particular mathematical model is called verification. In verification accuracy is understood to be with respect to the exact solution of the working model, not with respect to physical

⁴ American Institute of Aeronautics and Astronautics, Guide for Verification and Validation of Computational Fluid Dynamics Simulations AIAA G-077-1998 (1998).

reality. Verification is concerned with estimation and control of the discretization error; errors associated with iterative solution procedures and determination that the program is functioning properly.

5. Planning

As stated, the main objective of this study is the development of metric(s) that characterize HSS corrosion with respect to structural integrity providing viable maintenance guidelines with respect to fatigue life. In the US Navy, the effective stress concentration factor ($K_{t_{eff}}$) is used as a basis for estimating the FLE⁵. The basic assumption adopted by the corrosion project group was that the onset of crack initiation, defined by the first appearance of a 0.01 inch long crack, can be correlated with $K_{t_{eff}}$. This assumption implies that (a) heterogeneities occurring in the material do not contribute to crack initiation, only the averaged properties of the heterogeneities are important; (b) corrosion progresses along a sharp front and (c) the surface features that determine the critical values of $K_{t_{eff}}$ can be reliably measured. In this context averaging is understood to be over length scales that are not larger than the corrosion features. Progression along a sharp front means that once the corrosion products were removed by cleaning, the remaining material has the same mechanical properties as the uncorroded material. Given this assumption, estimation of the maximum effective stress concentration factor of a corroded part is required. StressCheck[®] is well suited for both computation and verification of $K_{t_{eff}}$ for idealizations of corrosion features. The definition of $K_{t_{eff}}$ in reference to this study is the ratio of the first principal stress in a corroded part to the local first principal stress in a pristine, or uncorroded, part. The stress concentration in a pristine part will be referred to as K_t .

The effects of corrosion damage on fatigue life expended (FLE) depend on the location of the damage. Therefore inspection must be focused not only on regions of high corrosion, but also where K_t is high in the pristine part. Cases in point are the bench-tested F-18 tailhook shanks, in which the regions where corrosion damage was observed were not the regions with the highest K_t .

Since it would be impractical to perform detailed analysis on the effects of corrosion on each part, it is necessary to develop methods that involve two processes: a) the determination of K_t in an uncorroded (pristine) part, and b) based on corrosion metrics obtainable by field observations, or experience based on exposure to various operating environments, estimation of $K_{t_{eff}}$. These methods would provide a basis for evaluating the effects of corrosion on the maximum $K_{t_{eff}}$. Estimation of the rate of corrosion is not within the scope of this project. Process a) can be readily solved using StressCheck[®]; process b) poses a challenging problem in that computation of $K_{t_{eff}}$ in a corroded part is possible only if the surface details are known with sufficient accuracy and multi-scale methods are properly applied. The available

⁵ $K_{t_{eff}}$ is a characteristic input for the determination of the fatigue notch factor (K_f), which is applied to FLE probabilistic strain life calculations.

information on the details of the corroded surface is limited by the resolution of the system used for mapping the surface features. Additionally, the usability of the available information is limited by our ability to represent highly irregular surface features in a form suitable for computation. This is a problem of multi-scale modeling. In an attempt to avoid these difficulties, ESRD undertook a parallel investigation based on crack growth theory (Section 6.2). The basic assumption of that theory is that, given the surface irregularities caused by corrosion, crack-like defects, comparable in size to the depth of corrosion, will develop following a few cycles of loading. Therefore it is reasonable to assume that many initial cracks of small size are present after just a very few cycles of loading. Using crack growth methodology, one could estimate the number of cycles to the first appearance of a 0.01 inches long crack. The problem with this approach is that, owing to the very small initial crack lengths, the range of stress intensity factors is generally smaller than the threshold value of the published crack growth curves and hence estimation of growth rates below the threshold value is required. Regardless, this approach is considered by the Navy to be inconsistent with the existing USN probabilistic strain life (PSL) framework. Therefore, this approach was not pursued any further.

6. Approaches/Methodologies

The approach to HSS corrosion classification centers on formulating the impact corrosion has on a structural component in terms of probabilistic strain life (PSL) analysis. As stated, the original objective was to characterize corrosion with a metric corresponding to $K_{t_{eff}}$ values.

As identified above, the sensitivity of these $K_{t_{eff}}$'s when a corroded surface is replaced by an idealized surface is of interest, because simplification of local surface roughness due to corrosion is essential for making the problem accessible to numerical analysis. However, it is known that oversimplification of topological detail may lead to a potentially lower computed maximum $K_{t_{eff}}$ than the actual maximum $K_{t_{eff}}$ and therefore lead to a potentially non-conservative estimation of predicted life.

Because the corrosion topology and predicted life are so strongly coupled in the current USN mathematical corrosion model, high resolution topological measurements must be performed in carefully controlled environments in order to approach the closest approximation to the real surface; these measurements currently exist in the form of White Light Interferometry (WLI) data. These measurements are currently the foundation for all ensuing $K_{t_{eff}}$ computations and strain life predictions. It is not known at this time how accurately the topological details can be captured under shipboard conditions. Various techniques are being investigated.

A series of studies were performed in the last year to gain perspective of the observed topological details and how these details may be used as input to life prediction computations. The studies were organized in the following manner: 1) observed topological detail for a number of AF1410

corroded specimens, 2) explored an alternate method for life computation based on the available topological detail, 3) organized a discovery experiment aimed at controlling errors in topological detail by using simple topologies, and 4) improved a method for determining an approximate $K_{t_{eff}}$ based on simplified AF1410 Set A topologies.

In Section 6.1 an investigation performed to determine the useful information that could be extracted from artificially corroded surface WLI profiles of AF1410 Set A specimens is described. Topological characteristics of the surface profile (depth, RMS, etc.) were analyzed and an attempt to correlate this information with corrosion exposure and observed lives was procured. If $K_{t_{eff}}$ cannot be determined from a surface measurement profile with sufficient accuracy then the goal is to identify a surface measurement metric that will permit estimation of the reduction in service life.

In Section 6.2 the results of a preliminary investigation of life prediction based on crack growth methodology are described. This alternative method involves the use of linear elastic fracture mechanics in conjunction with the depth extremum of WLI or NDI instrument data to determine the number of cycles; the details of this method are in the section content. It was also reasoned that if the $K_{t_{eff}}$ cannot be accurately and consistently determined from the Fourier mapping of the WLI data, and therefore the lower resolution NDI data, then life prediction is unlikely. At this point, the $K_{t_{eff}}$ appeared to be highly influenced by the point density used in the Fourier transform, as well as the number of terms in the expansion of K_t ; it must first be proven that the $K_{t_{eff}}$ of the surface is independent of the resolution and number of terms in K_t in order to make a reasonable prediction of cycles to crack initiation (CI) and the approximate CI location.

In Section 6.3 a discovery experiment was initiated because of the uncertainty in determining the feature attributes and locations of potential (or even existing) crack initiation sites in AF1410 Set A specimens, and thus the $K_{t_{eff}}$. It was hoped that this experiment can be used to help identify and control these errors of interpretation. Geometries of pre-defined size and spatial location would be developed, each having roughly the same geometric stress concentration (K_t) and therefore roughly the same probability of failure. The goal is to see whether any features are favored in fatigue testing, or failure is a random event. Since the FFT $K_{t_{eff}}$ results indicate that regions of high stress may be “washed out” by lack of resolution (Ultrasound techniques) or excess filtering, it is important to understand the effect of these discrete features of known K_t .

In Section 6.4, a study was performed for the purpose of analyzing AF1410 Set A failed specimens following fractographic analysis that identified the probable failure initiation sites. In this study, several crack initiation sites in which distinct features could be adequately discerned were isolated and idealized via simple geometries; in effect, an approximate $K_{t_{eff}}$ could be determined for each feature. These geometries were roughly ellipsoidal in shape, and were organized in combinations (intersecting or

isolated) such that complex stress interactions could potentially occur. In addition, the orientation of these features was of interest, as it determined the influence of the $K_{t_{eff}}$. The goal was to use StressCheck to incorporate these geometries into finite element models and determine the $K_{t_{eff}}$ to high certainty.

6.1 Study of White Light Interferometry (WLI) Topology Data for Potential Metrics

6.1.1 Introduction

A study was performed to determine the useful information that could be extracted from artificially corroded surface WLI profiles of AF1410 Set A specimens. Topological characteristics of the surface profile (depth, RMS, etc.) were analyzed and an attempt to correlate this information with corrosion exposure and observed lives was procured.

6.1.2 Study Approach and Results

6.1.2a MATLAB/Visual Basic Application for Statistical Analysis of Corroded Specimens

The objective of this investigation was to examine statistical measures of surface irregularity and the effects of alternative data filtering techniques from the point of view of regularization for the purposes of numerical stress analysis.

The topological measurements (White Light X,Y,Z data) of corroded test specimens received by ESRD in 2004 (Specimens 16, 24, 27, 30, 65, and 66) were reevaluated in a three-dimensional setting using MATLAB 6.5.

The original (full) dataset supplied by UDRI exceeded the memory limitations of MATLAB; only the $1/16^{\text{th}}$ X-direction & $1/16^{\text{th}}$ Y-direction pixel size dataset could be read and processed within memory limits. Once the X,Y,Z arrays corresponding to the corroded surface were extracted in MATLAB, a contour plot could be produced. See Figure 1 for an example contour plot of the corroded surface.

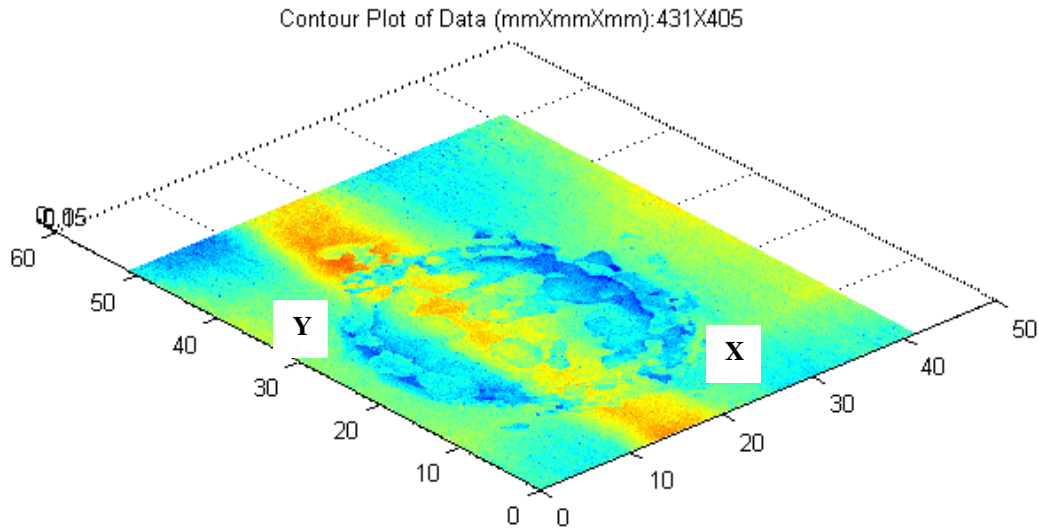


Figure 1. Contour Plot of Dogbone 16: 1/16th Dataset (All Values in Millimeters)

It is desired to study an arbitrarily selected patch (small area) of the corroded surface at full resolution of the white light data. Thus, a Visual Basic 6.0 application was developed to read the full data set and parse it into a patch according to supplied X & Y grid locations. This Visual Basic application (CorrosionDataExtractor.exe) reads in the 1/16th size data set, and allows the user to select two X and two Y coordinates (the patch dimensions and starting location). This can be seen below in Figure 2.

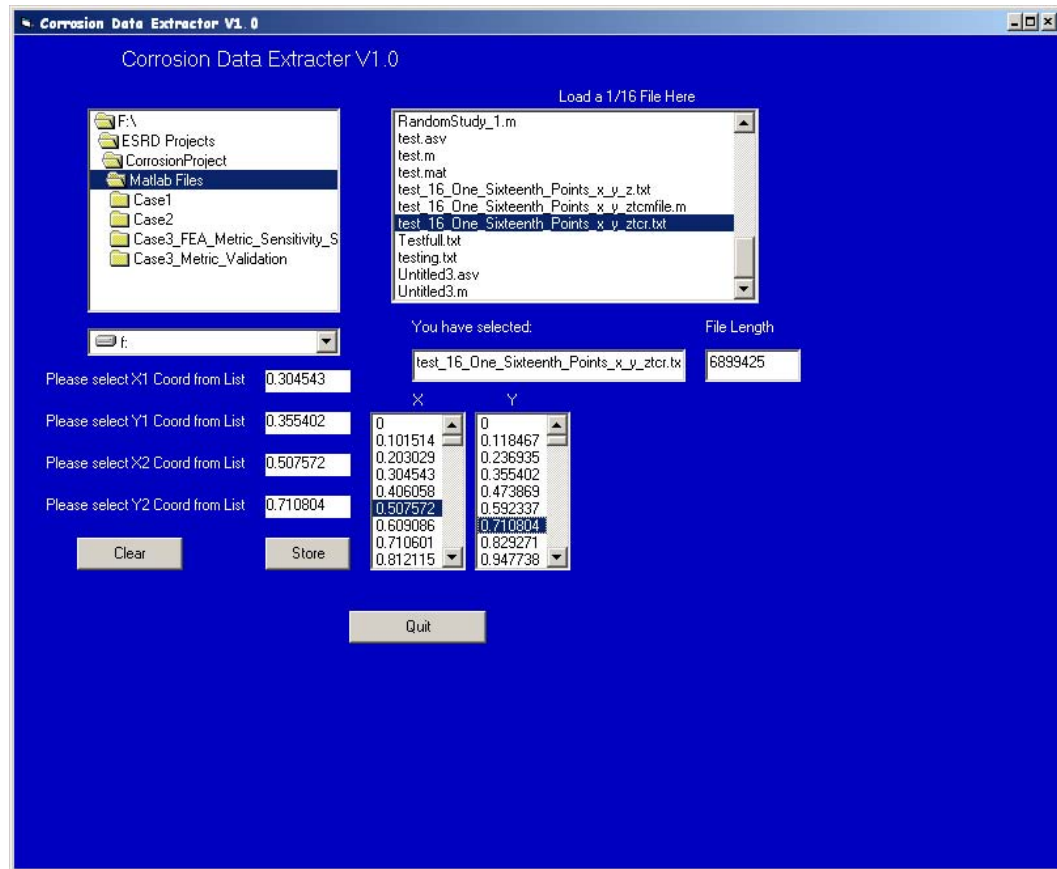


Figure 2. Visual Basic Application for Corroded Surface Patch Extraction

Once the user specifies the X1, Y1 and X2, Y2 locations for the patch, the “Store” button is utilized to store these X & Y inputs. The program then walks the user through the following steps (see Figure 3):

- 1) Program asks the user for the corresponding full dataset (i.e. Dogbone 16 full set)
- 2) Program automatically opens the file for extraction
 - a. A search for the selected X & Y coordinates within full set is performed
 - b. Once these coordinates are found, a grid corresponding to the patch is written out to a new text file. This text file (X,Y,Z format) can then be read into MATLAB for processing

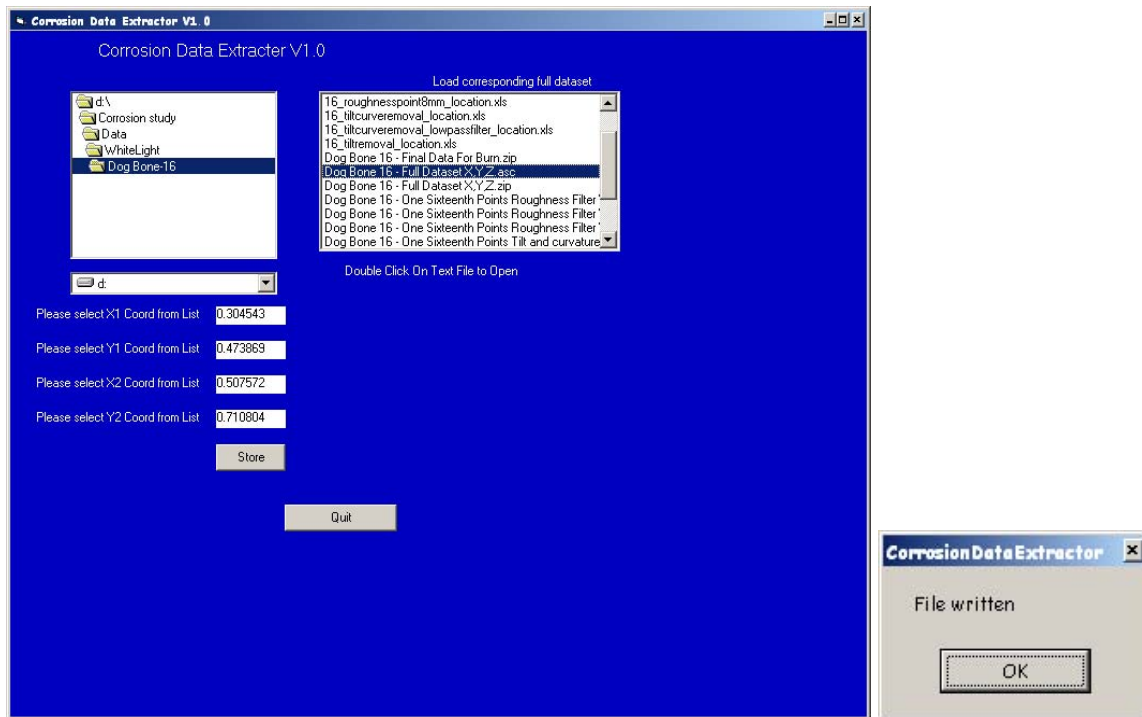


Figure 3. Loading of Full Dataset and Subsequent Extraction Message

After the patch-sized text file is loaded into MATLAB, the user should be able to see (and analyze) with finer detail the regions of interest. See Figure 4 for an example of a partitioned region.

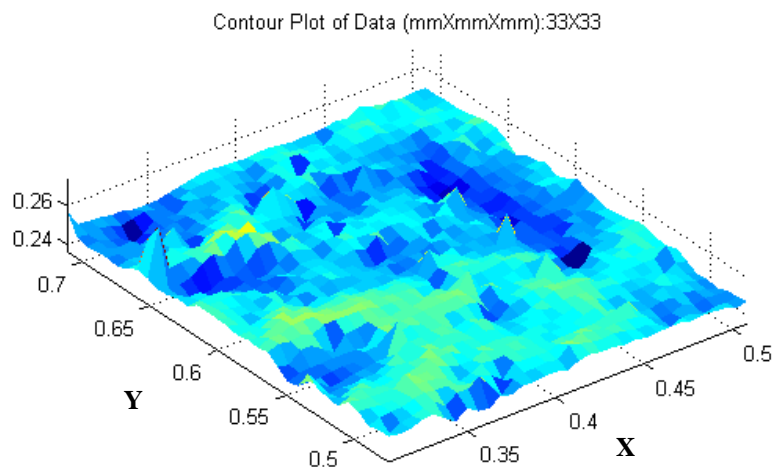


Figure 4. Dogbone 16 Full Dataset Partition: 33X33 Pixel Patch (All Values in Millimeters)

The user will now have the option to perform simple statistical analysis on the region of interest. The statistical parameters currently available are mean, standard deviation, and covariance of the data. See Figure 5 for an example statistical analysis.

```
# of pixel rows in file (Y-dir) is 33.00
# of pixel columns in file (X-dir) is 33.00
Mean of Depth is 0.2487
Median of Depth is 0.2489
Standard Deviation of Depth is 0.0034
Covariance of Depth is 0.0114
```

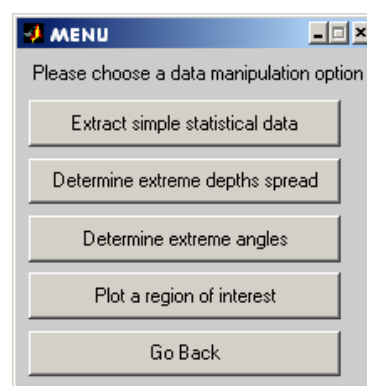


Figure 5. Sample Statistical Extraction from Dogbone 16 Partition

The above statistical analyses were performed on the dataset patch without any prior filtering or altering of the data. That is to say that there was no tip, tilt, or Gaussian filter corrections performed on the partition as it is difficult to accurately extract the global reference surface without utilizing the full spectrum of data. This limitation was lessened as ESRD received the new corroded surface profile data from UDRI in November 2005, as the full dataset was in a format such that it could be read and manipulated via MATLAB.

6.1.2b Visual Comparison of 1/16th and Full Dataset of UDRI Corroded Test Specimens

In early November 2005, ESRD received a set of 12 DVD's containing the most recent surface measurements of corroded specimens. UDRI also supplied ESRD with the preferred tool (ImageJ) to view and manipulate these data sets. An example ImageJ plot of a corroded surface (Dogbone 2 Full Stitch Text Image Resize) is shown in Figure 6.

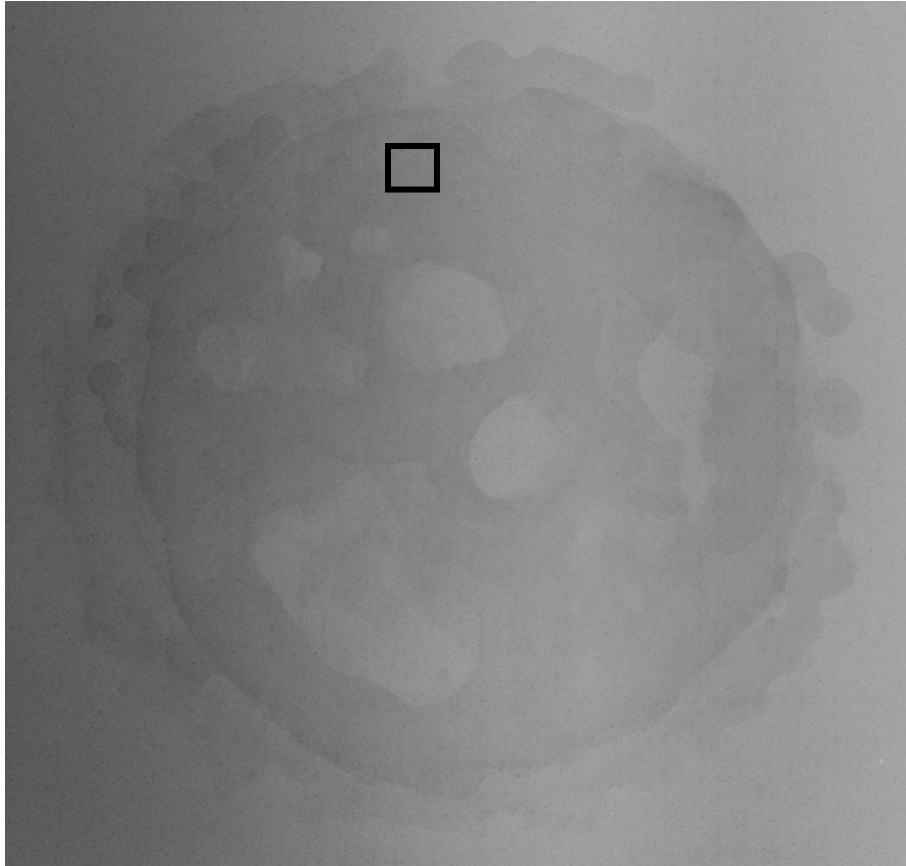


Figure 6. ImageJ Rendering of Dogbone 2 Full Dataset

A certain plug-in within ImageJ, called Surface Plot 3D, allows the user to perform a zoom-in on a region of interest. Figure 7 shows the zoomed region corresponding to the black box shown in Figure 6. This data does not contain any sort of tip, tilt, or other correctional filtering. Notice that at this level of detail and at this scale, the surface profile appears to be jagged in nature (high resolution allows for “jumps” in surface profile). Figure 8 shows the result of 50% smoothing of the region shown in Figure 7, allowing the user to gain a better appreciation for the “true” surface. It is apparent, however, that applying this magnitude of smoothing may remove key features of the corroded surface, especially low-wavelength cracks. Although it is not clear in the user’s manual how this smoothing function operates, it is assumed to be a type of Gaussian blurring.

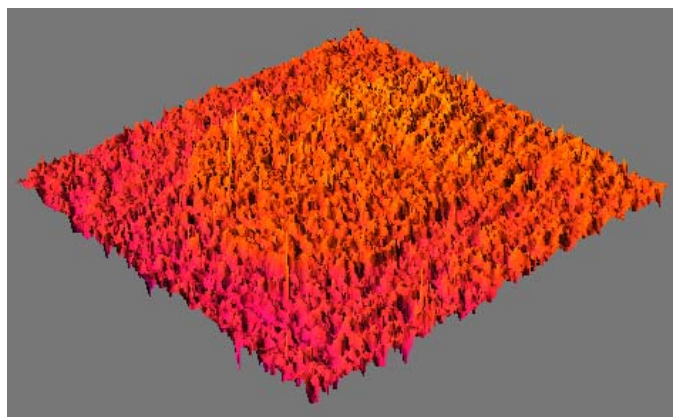


Figure 7. Surface Plot 3D Rendering of Selected Region in Figure 6

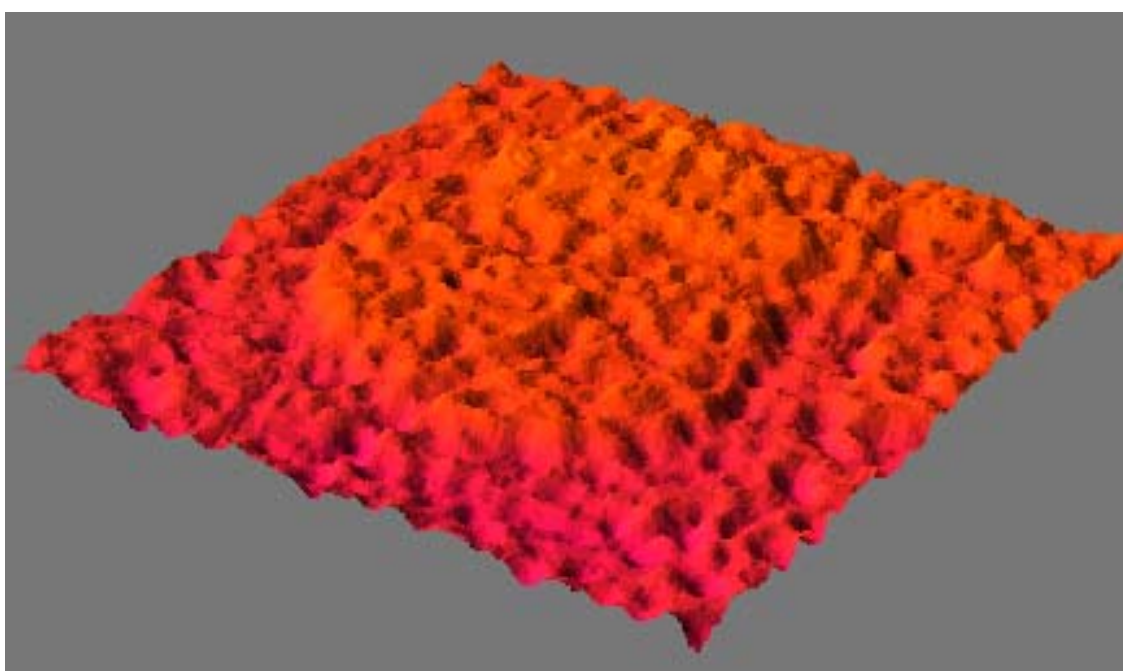


Figure 8. Surface Plot 3D Rendering of Selected Region in Figure 6: 50% Smoothing

A plug-in is available for ImageJ called SurfCharJ, which allows for surface roughness characteristic calculations as well as automatic tilt correction by regression plane. ESRD successfully converted a sample data set (Dogbone 2 Full Stitch Text Image Resize) into tilt-corrected surface profile data, such that the reference plane is the mean horizontal. Gaussian or median filtering was not performed at this time, only tilt-correction.

The surface profile data is in TIFF image format, but can be converted into a MATLAB readable text format through the provided Text Image generator. Once the Text Image is generated, the output file is in pixel and micrometer format. For these corroded specimens, pixels can be converted into X and Y coordinates through the provided measurement resolution (in this case, 6.345×10^{-3} millimeters/pixel). A

MATLAB program was written to read in these Text Image files, properly convert them into spatial coordinates (millimeters), and allow the user to interactively select a patch for visual review (statistical analysis is in progress).

The program allows the user to specify the sizing of the grid for plotting (i.e. 1/factor of full dataset) as the full dataset cannot be properly plotted due to the high resolution of the data. A 1/16th X & Y resolution plot of the tilt-corrected corroded surface profile obtained through SurfCharJ is shown in Figure 9.

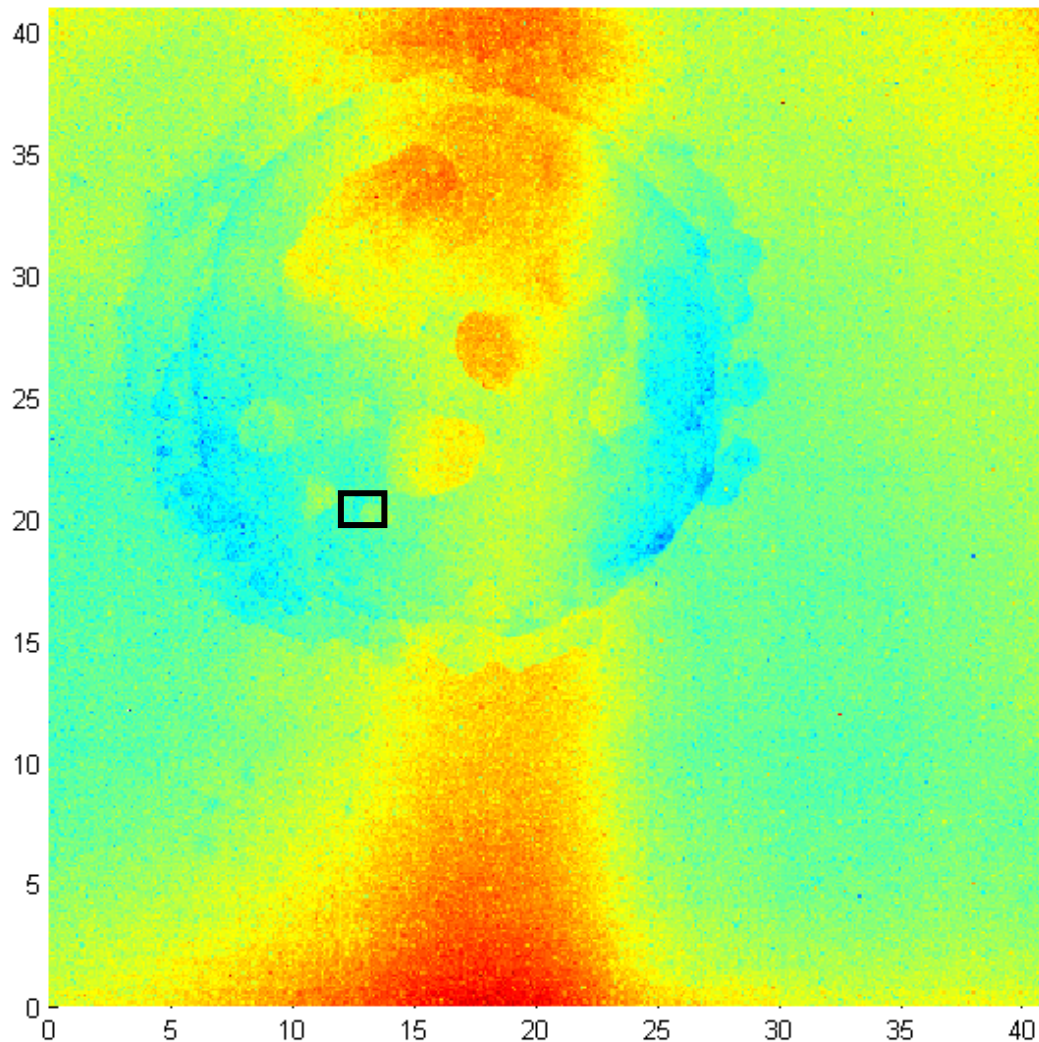


Figure 9. 1/16th Resolution Plot of Tilt-Corrected Dogbone 2 Corroded Surface

The user now has the ability to interactively select from the above plot a box from which to partition a patch for detailed viewing. A sample box is shown in Figure 9. This box is created by clicking on the plot in an initial X & Y location, clicking “OK” for the initial X-coordinate and “OK” for

the initial Y-coordinate, then performing the same steps again for the final X & Y coordinates. The partitioned grid is then created and placed into arrays for further processing by the user. The program then automatically creates two plots from this array data, one detail plot of the full dataset and one detail plot of the 1/factor data set. These plots can be seen in Figures 10 and 11, with the factor in this case being 16 (chosen by UDRI).

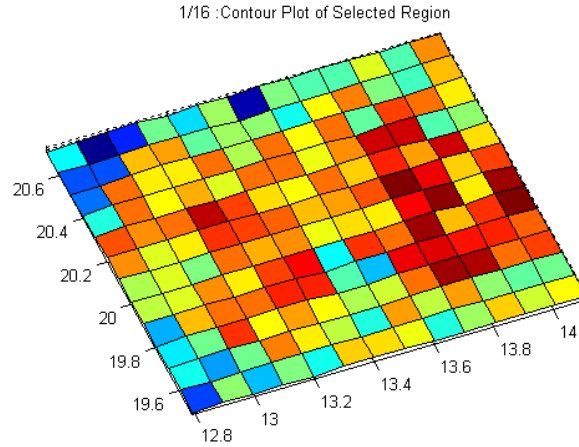


Figure 10. Contour Plot of 1/16th Resolution Patch Taken From Figure 9

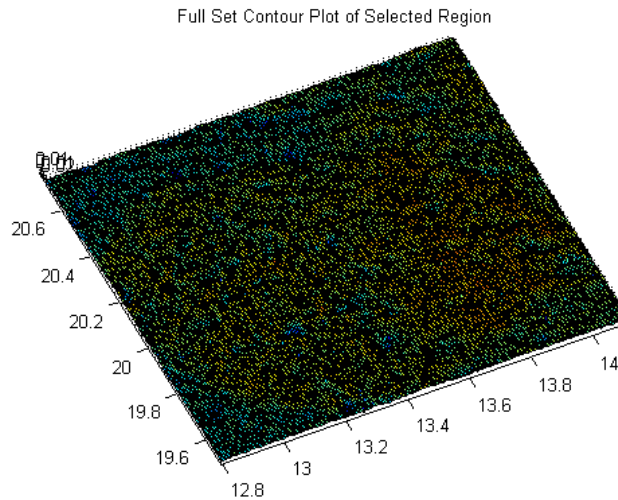


Figure 11. Contour Plot of Full Resolution Patch Taken From Figure 9

It is seen that while the 1/16th contour plot (first plot) gives useful general information of the surface variation, it may not capture the most extreme features and details that will ultimately drive crack initiation in fatigue. With the generation of AF1410 Set A fractographic images and the knowledge of the locations of the cracks responsible for corrosion-fatigue failure, it appears that some of these crack initiation location features will not be apparent when using lower resolution techniques.

6.1.2c Corroded Specimen WLI Measurements: Filtering Approaches and Issues

The issue of surface profile filtering, in addition to resolution filtering, was also studied in some detail. It is known that UDRI is currently using a filtering scheme of 8 mm wavelength Gaussian Filtering in addition to regression plane tilt correction in an attempt to normalize the original White Light output. The original measurements have an inherent waviness characteristic (due to the machining process) as well as a tilted orientation (due to mounting of the specimen in the measurement device). An example of the original measurements is shown in Figure 12 (Dogbone 2). The top image shows the raw surface profile of Dogbone 2, while the bottom image shows the top image with tilt-correction applied. Both images have been smoothed.

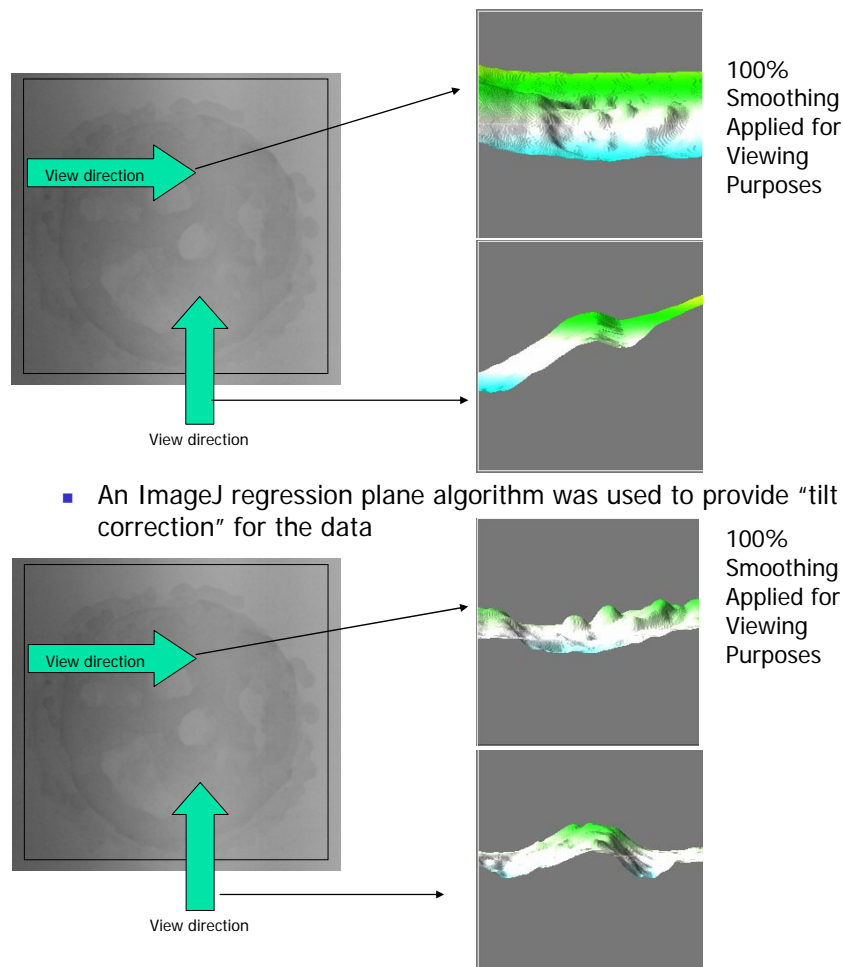


Figure 12. Dogbone 2 Original White Light Measurements (with Smoothing)

In contrast, the 8 mm Gaussian filtered and normalized surface profiles do not have the same waviness characteristic as is seen in Figure 12. The White Light surface profile of Dogbone 2 with 8 mm Gaussian filtering and tilt-removal is shown in Figure 13.

■ 8mm Gaussian Filtering+Tilt-Correction Applied

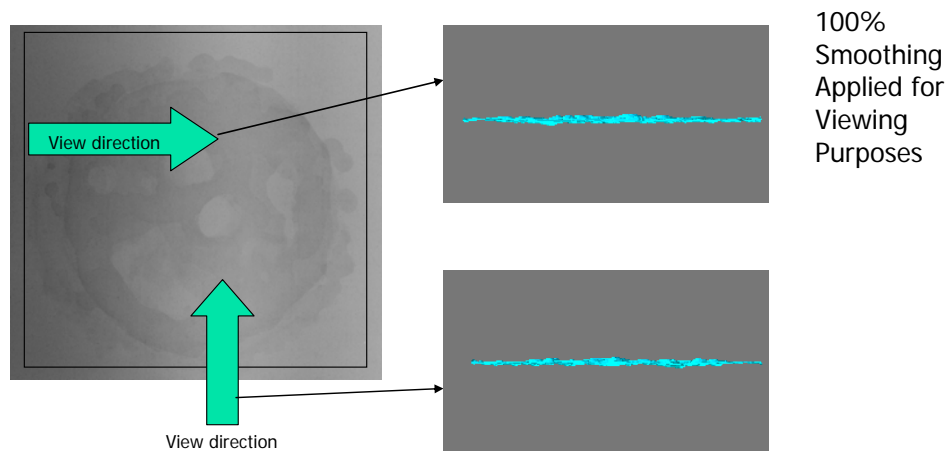


Figure 13. Dogbone 2 8mm Gaussian Filtering with Tilt-Correction

An additional consideration is the definition and filtering of White Light “noise.” In this setting, noise can be defined as random “jumps” or variations in the data which do not appear to directly convey the actual surface profile at that point. It will be important to understand the nature of noise in the measurements, if noise does indeed exist, when numerical simulations are performed using the White Light interferometer data to generate topology. If noise does exist, a filtering scheme must be carefully defined. An example of a potential noise characteristic is shown in Figure 14, extracted from a randomly selected region of the corroded surface profile. The scales, respectively, are 0.08 millimeters in the x and y directions, and -0.02 to 0.02 millimeters (0.04 millimeters total) in the z direction. A sudden spike is observed in the surface data. This spike is now regarded to be characteristic of noise, dust, or another anomaly.

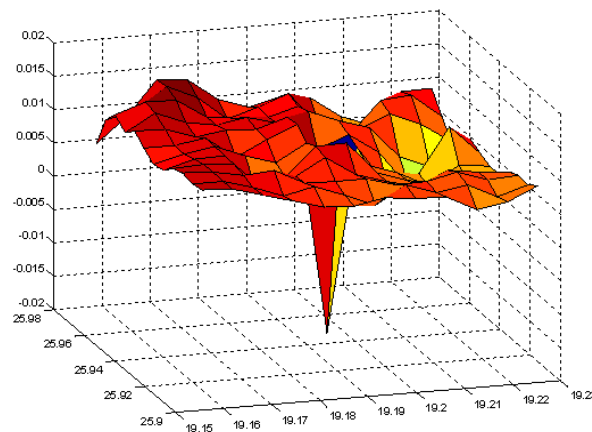


Figure 14. Dogbone 2 White Light Surface Profile w/ Potential Noise Characteristic

6.1.2d RMS Studies of Corroded Surface Profiles

The RMS (root-mean-square) surface roughness measure represents a degree of variation over a region. By definition:

$$R.M.S = \sqrt{\left(\frac{1}{m * n} \sum_{i=1}^n \sum_{j=1}^m (Z(j,i) - Z_0)^2 \right)}$$

where m is the number of rows in the grid, n is the number of columns in the grid, $Z(j,i)$ is the surface height at row j and column i , and Z_0 is the average surface height value for the grid of m by n surface height values.

The first RMS study involves an investigation of correlation between exposure times and regional surface roughness. A 1 mm by 1 mm region was selected at the center of the corrosion patch for every test specimen, and sets of RMS values were generated for the region by observing both the row and column variations. An example of the study is shown in Figure 15. Here, Dogbone 4 (12 hour-severe), Dogbone 66 (6 hour-moderate), and Dogbone 5 (3 hour-mild) row and column surface profiles are shown. Each of these profiles have been filtered using 8 mm Gaussian filtering and have been tilt-corrected. RMS values for these data range between 0.0029 and 0.0058 millimeters RMS, but this is a very small population of the surface profiles.

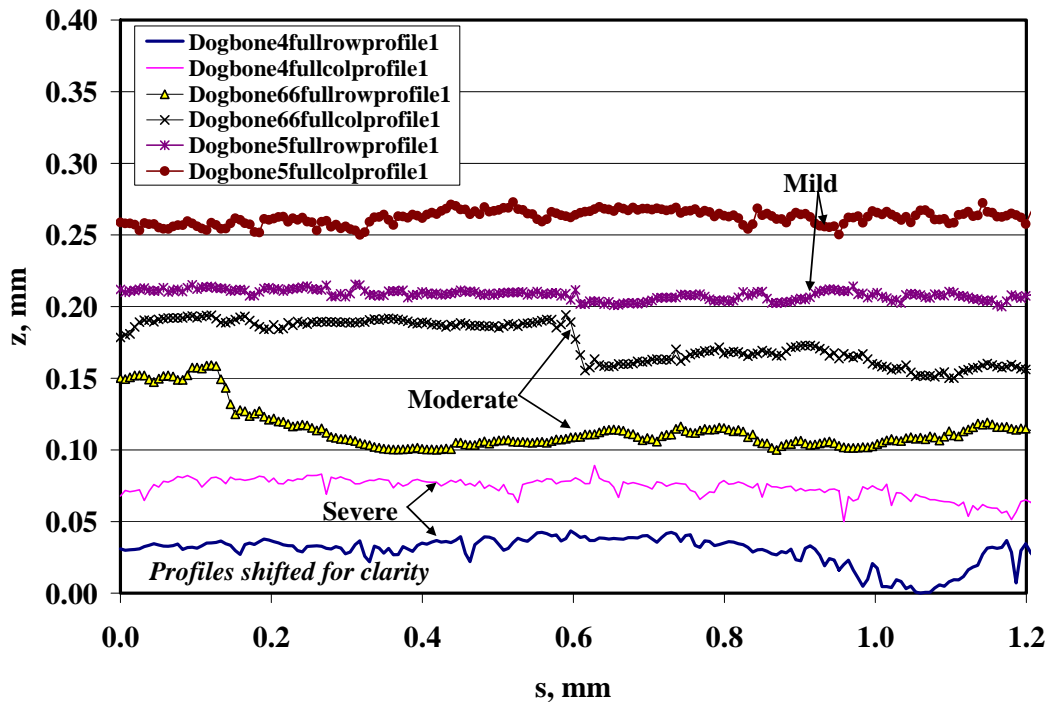


Figure 15. Dogbone Surface Profiles for Varying Corrosion Severity

The second RMS study involves the comparison of the pristine surface (the part of the test specimen that has not been subjected to corrosion) RMS against the RMS values generated from the first study. A visual inspection of Figure 16 indicates that the RMS values between the corroded region and pristine region are quite similar. This is attributed to the fact that the surface was grit blasted prior to corroding the specimen, increasing the overall surface roughness of the specimen. The top image shows the Dogbone 2, 8 mm Gaussian filtered and tilt-corrected sample (mild or 3 hour corrosion), with a box selection drawn to represent the region of interest (bottom image). This comparison between pristine and mildly corroded regions clearly shows that it is difficult to discern the two in terms of surface roughness. For example, the RMS of the pristine region is 0.0033725 mm, and the RMS of the corroded region is 0.0037435. This may explain why cracks occurred outside of the corroded region in many 3 hour corrosion specimens.

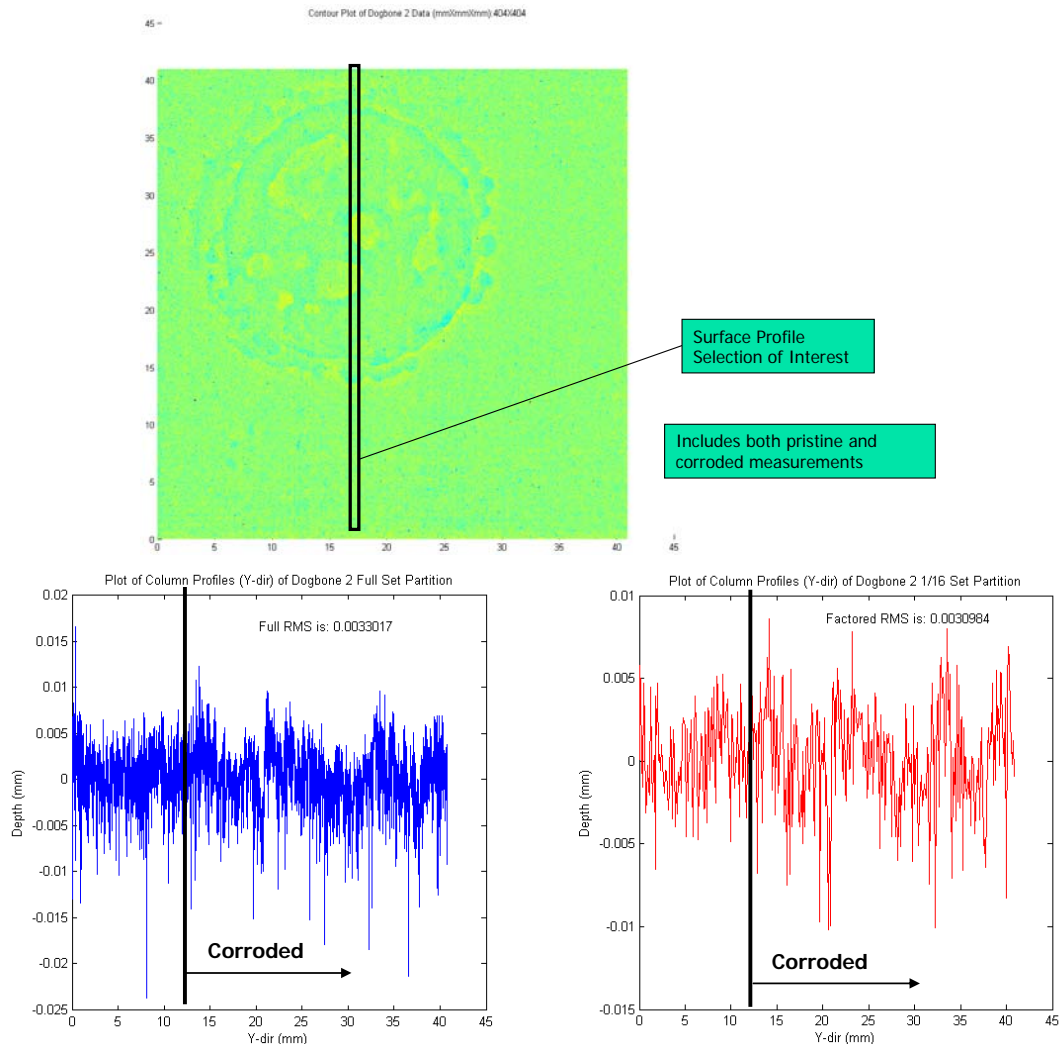


Figure 16. Dogbone 2 Plot Comparison of Pristine and Corroded Regions

6.1.2e RMS Field vs. Crack Initiation Locations for AF1410 Set A Specimen 16

A MATLAB script was written for the purpose of determining if certain surface regions of Specimen 16 were more influential in crack initiation than others based on the identified crack initiation locations. The criterion in this case study was the localized RMS value for a given location, which led to the “RMS field”. The reasoning behind this is that when computing the global RMS for a specimen surface one cannot always obtain a clear picture of what is occurring on a local scale. It is possible that the localized RMS, and the subsequent RMS field, may provide some direction into this issue by isolating regions of severity.

The White Light data for Specimen 16, supplied by UDRI with 8 mm Gaussian filtering and tilt-removal applied, was read as a text file into MATLAB and an “RMS field” for the surface data was generated. The RMS field is simply a collection of RMS values, each corresponding to a point with a given sample X and Y dimension. Below in Figure 17 is a schematic of the generation of the RMS field.

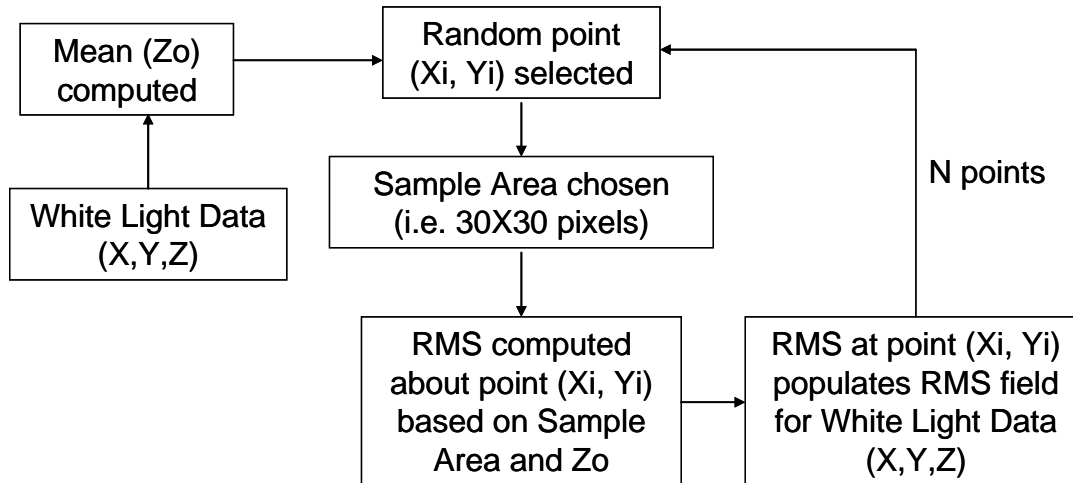


Figure 17. Schematic of RMS Field Generation for a Sample Specimen Surface

The above process was used with Specimen 16, and using a field size of 50,000 points and a sample area of 30X30 pixels, the following RMS field was generated (Figure 18). Figure 19 shows the failure crack location for Specimen 16 (marked with a small yellow line). Based on the preliminary findings, it appears that the peak localized RMS and the failure crack location are indeed coincident. However, additional experiments with other corroded specimen profiles showed that the method did not always predict the crack initiation location. The results were misleading in many cases, with the predicted failure location occurring far from the actual crack initiation site(s). An example of a misleading case is shown in the Appendix.

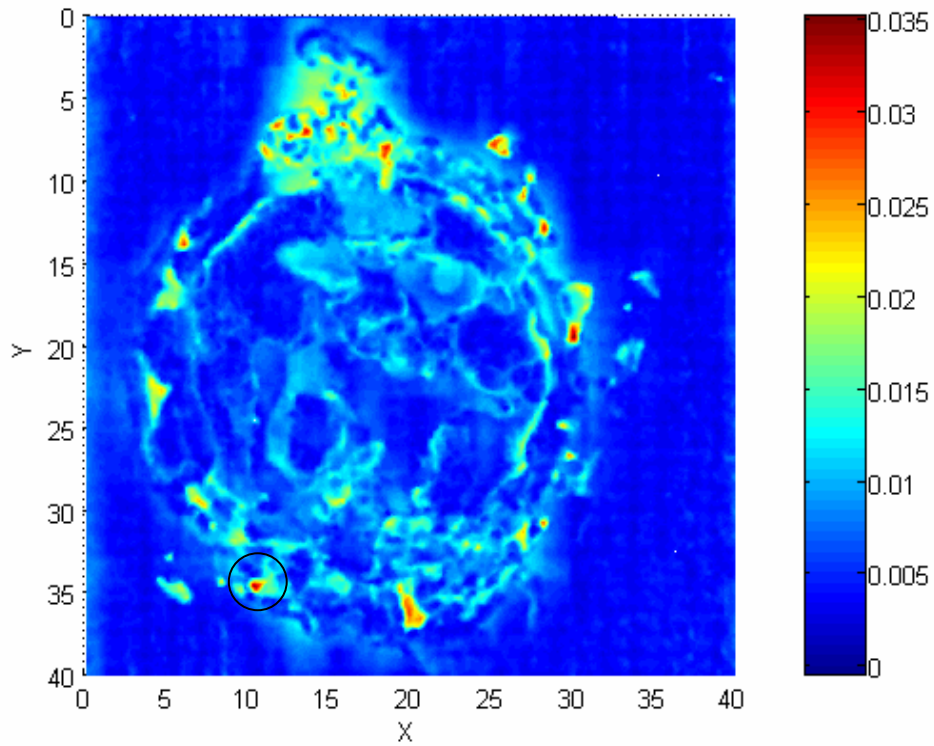


Figure 18. Specimen 16 RMS Field (50K Pts, 30X30 Sample Area)

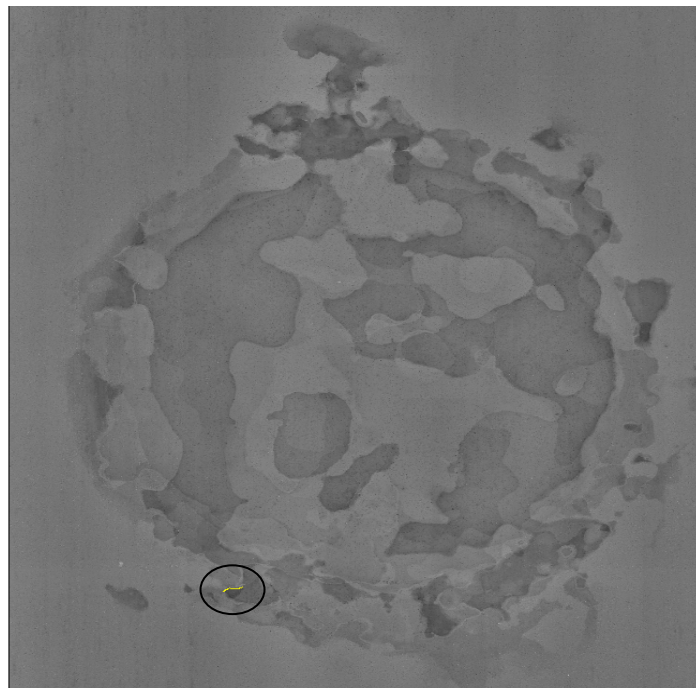


Figure 19. Specimen 16 with Failure Location Identified

6.1.3 Summary

Based on the available information, it appears that reducing the sampling resolution may cause some potentially crack initiation inducing features to be removed. It is known that the available NDI techniques will only detect roughly 1 of every 1120 WLI points. Therefore, computed crack initiation lives based on NDI obtained data may not match those predicted using WLI obtained data. Calibration experiments are necessary to link the two predictions.

A characteristic, also identified in Study 6.1, was the similarity of surface profile measurements between the as-manufactured (grit-blasted) pristine specimens and the corroded specimens. In some cases (mild or 3 hr corroded specimens), it was difficult to discern a corroded surface from a pristine surface due to the roughness induced by grit-blasting. This may indicate that if a specimen or part is not adequately polished, or if grit-blasting techniques are used to treat the surface, then failure may occur outside of the corroded region; in fact, 8 of the 13 three (3) hour corroded specimens, failed outside of the corroded region.

6.2 An Alternative Method for Life Prediction: Equivalent Crack Size (ECS)

6.2.1 Introduction

An alternative method for life prediction was studied due to concerns regarding the ability of surface roughness characteristics (depth, RMS, etc.) to consistently correlate to existing crack initiation lives and therefore to predict crack initiation life for a given scenario of geometry, corrosion, and loading. This alternative method involves the methods of linear elastic fracture mechanics in conjunction with depth extrema determined by WLI or other NDI techniques, and crack growth curves at small values of the stress intensity factor range (ΔK_I).

6.2.2 Study Approach and Results

6.2.2a Preliminary Studies Using AFGROW to Predict EIFS for AF1410 Batch A

Preliminary studies were performed to try to reproduce the crack growth behavior observed by the fractographic examinations of AF1410 Batch A uncorroded specimens. These studies utilized the AFGROW crack propagation software. It was assumed that some inherent, pre-fatigue discontinuities at the specimen surface must have existed to cause the uncorroded (pristine) specimen to fail. This inherent discontinuity is modeled as an EIFS, or Equivalent Initial Flaw Size (EIFS), within the AFGROW framework. The problem is to identify the best candidate NASGRO equation⁶ material curve for

⁶ Initially developed by Forman, Newman, de Koning and Henriksen

AF1410, as the crack growth is obviously quite sensitive to changes in material curve parameters. Also, once a material curve is selected the parameters defining that curve must remain constant for the duration of the AF1410 Batch A study. The material curve parameters for the AF1410 NASGRO equation are shown in Table 1, along with the corresponding crack growth curve.

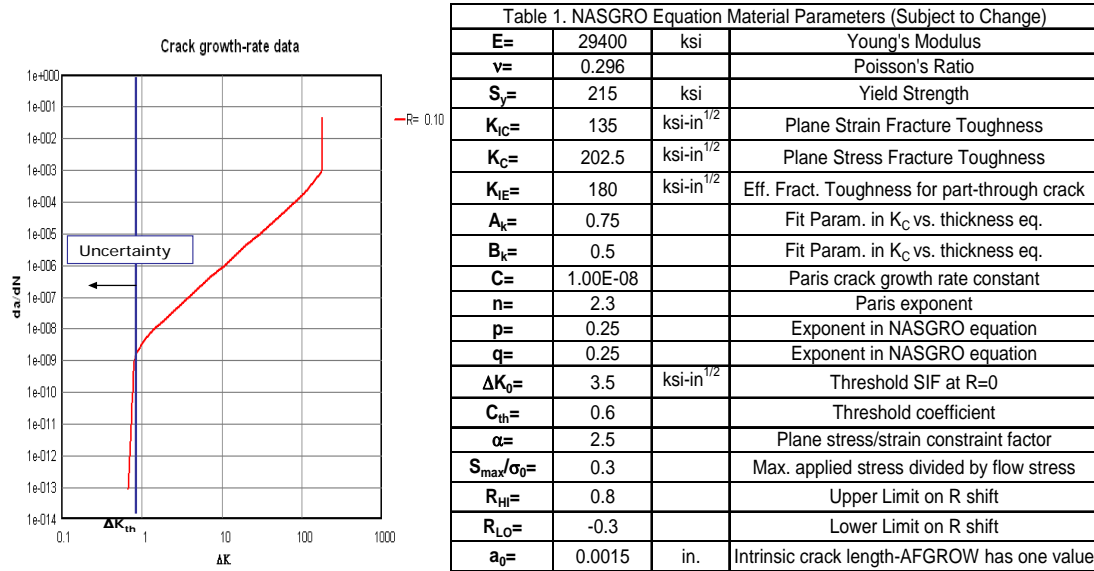


Table 1. NASGRO Equation Material Parameters

As this was a preliminary investigation, these parameters are tentative. The only modified parameter settings are Young's Modulus, Poisson's Ratio, Yield Strength, and the Paris exponent (originally 30000 ksi, 0.33, 220 ksi, and 2.2 respectively). These were modified based on available experimental results as well as best-fit criteria.

The preliminary investigation focused on specimens 55 and 44 (200 ksi max load), as well as 19 and 50 (165 ksi max load). All of these specimens were subjected to the same load spectrum, and were assumed to have the same cross-sectional dimensions (4 inches width by 1/8th inches thick). The crack geometry for each specimen was assumed to be elliptical (thumbnail) in shape and located in the plate center. In addition, a compressive residual stress profile was modeled through the thickness using the data presented in Table 2; an AFGROW interpolation procedure was incorporated in order to ensure continuity.

Table 2. Residual Stress Distribution from Surface	
Depth (in)	Stress (ksi)
0	-97.08
0.001	-100.42
0.0021	-22.52
0.0031	-5.13

Table 2. Typical Residual Stress Distribution from Surface

Finally, an iterative process was performed to determine the EIFS per specimen. This involved selecting the initial crack depth and width (A and C respectively) necessary to reproduce, within a confidence interval, the A versus N curve generated by fractographic measurements. Preliminary results were promising (see the following Figures 20-23) when compared with available optical measurements, though selection of the appropriate material curve was somewhat arbitrary. A summary of EIFS values is provided in Figure 24.

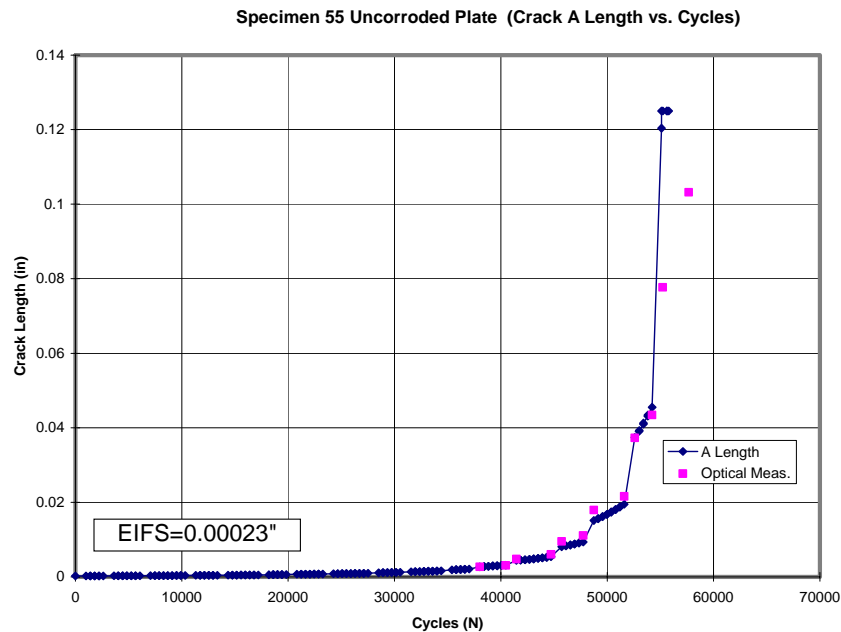
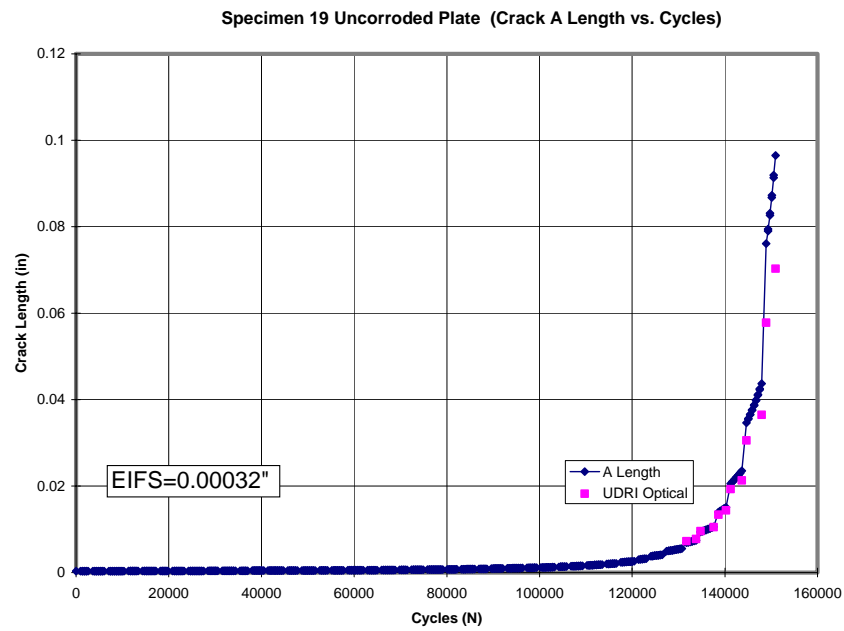
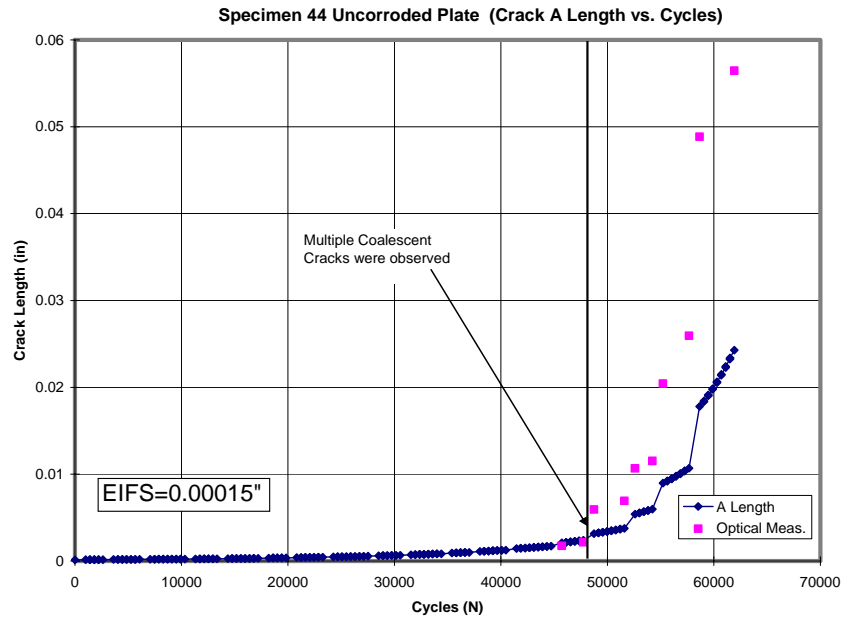


Figure 20. A vs. N Crack Length Prediction for Specimen 55



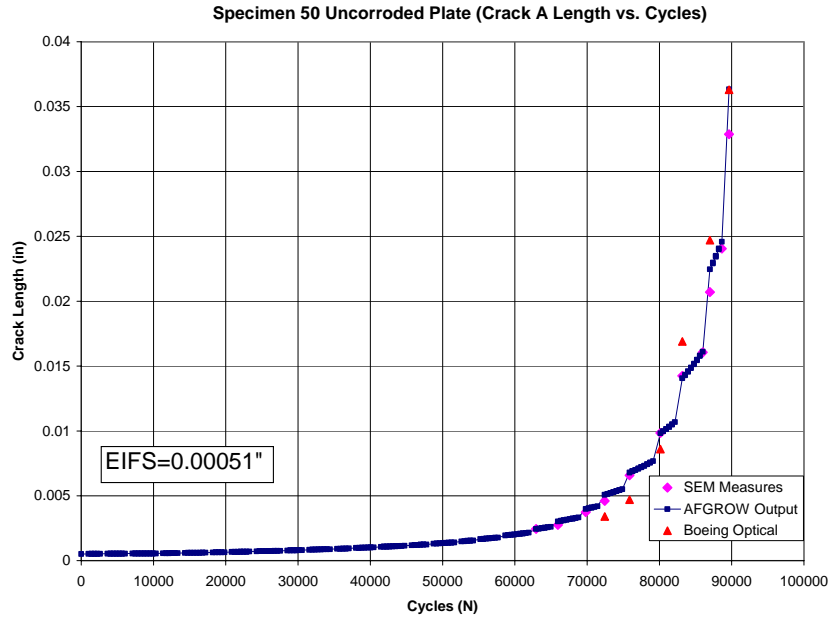


Figure 23. A vs. N Crack Length Prediction for Specimen 50 (Baseline)

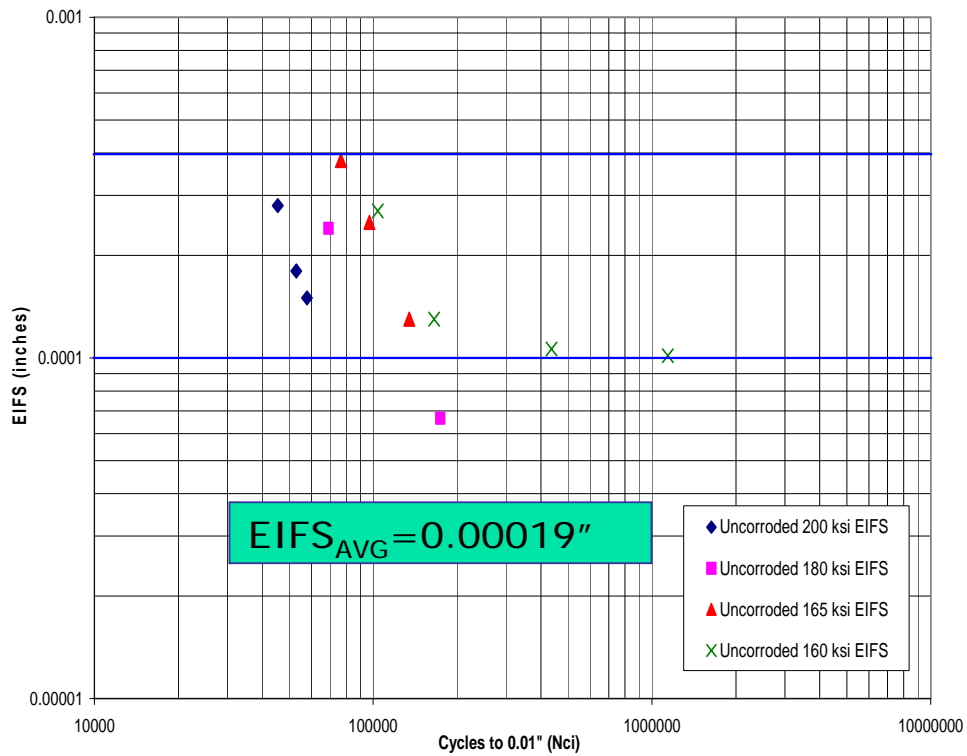


Figure 24. Summary of EIFS Values for AF1410 Set A Pristine Specimens

As was previously mentioned, future studies with the objective to determine the validity of the current crack growth model for these uncorroded specimens are recommended. Preliminary results (with the exception of Specimen 44, due to multiple crack coalescence) are quite promising at predicting the low to mid-range of crack lengths when compared with available fractographic measurements made by

Boeing, NAVAIR, and UDRI. The next step, if the uncorroded specimen crack growth model can be validated, would be to determine how corroded surface metrics (RMS, Depth) can be related to an equivalent crack size that will produce the same crack initiation times. This topic is addressed in Section 6.2.2c.

6.2.2b Using AFGROW to Determine ECS for AF1410 Batch A Specimens

AF1410 specimens, subjected to a few cycles of loading, can be expected to develop small crack-like defects at the surface. This assumption could be tested through TEM examination. These small crack-like defects may be attributed to surface flaws due to machining processes or precipitates/voids from the material generation process. The study described in Section 6.2.2a was intended for determining the sizes of the crack-like defects necessary to cause the failure distributions observed in the AF1410 Set A pristine specimens. These quantities were termed EIFS (Equivalent Initial Flaw Size) values, and served as a baseline estimation of the pre-fatigue surface flaws. Because of the inherent uncertainties in the adequate representation of corroded surfaces, and therefore the maximum $K_{t_{eff}}$ for the mapped surface, an alternative life prediction approach was adopted and implemented. This alternative life prediction is termed the ECS (Equivalent Crack Size) method and is partially attributed to the 2002 DSTO-RR-0237 paper written by Thomas Mills in collaboration with APES, Inc. The approach behind the ECS method centers on the ability to superimpose characteristic EIFS values with characteristic surface parameters, such as feature depth and RMS values. This superimposition is then used as input to an AFGROW simulation as a conservative estimate of the pre-fatigue crack-like defect. The crack (superimposition) is then subjected to the appropriate load history and is grown to the desired size, such as 0.01” in crack depth. The goal is to relate a surface parameter to ECS so as to define a potential metric. The outcome may then be related to an equivalent knock down factor, such as a K_f (‘fatigue knockdown factor’). The process is outlined in Figure 25.

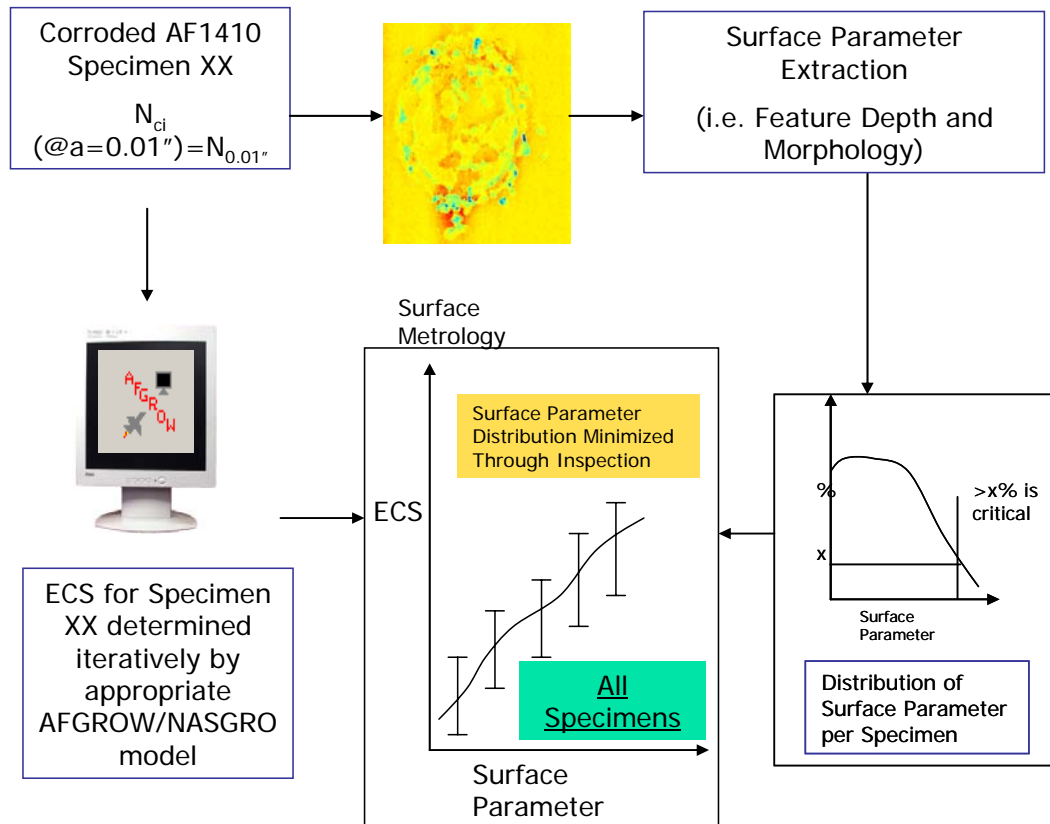


Figure 25. Process Map of ECS Method

Assume that the maximum observable depth (δ_{MAX}) is the parameter responsible for failure initiation and can be used for the computation of an ECS value for that specimen. These depths are sampled from the available WLI data for that specimen via a search algorithm. The ECS may be computed as shown in Figure 26.

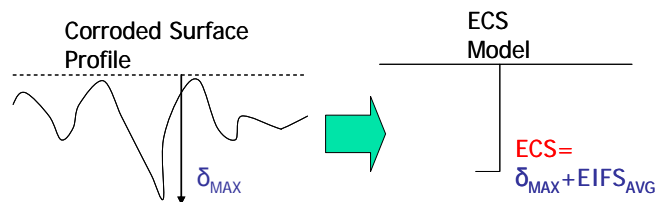


Figure 26. Computation of ECS

Since the shape of the feature accounting for δ_{MAX} is treated as the extreme case of a crack, this is considered a conservative “first iteration” for the estimated life. As mentioned, the goal is to relate an ECS value for the specimen to an observable and measurable surface parameter such as maximum depth. What can be done with the available AF1410 Set A corroded specimens, then, is to “back calculate”, similar to the EIFS approach, the “post-diction” ECS necessary to cause specimen failure at the observed

cycle count. Once the ECS has been determined for a given specimen, the characteristic depth value may be determined by subtracting the ECS value from the characteristic EIFS value. A summary of the ECS and EIFS values for the available AF1410 Set A specimens is shown in Figure 27.

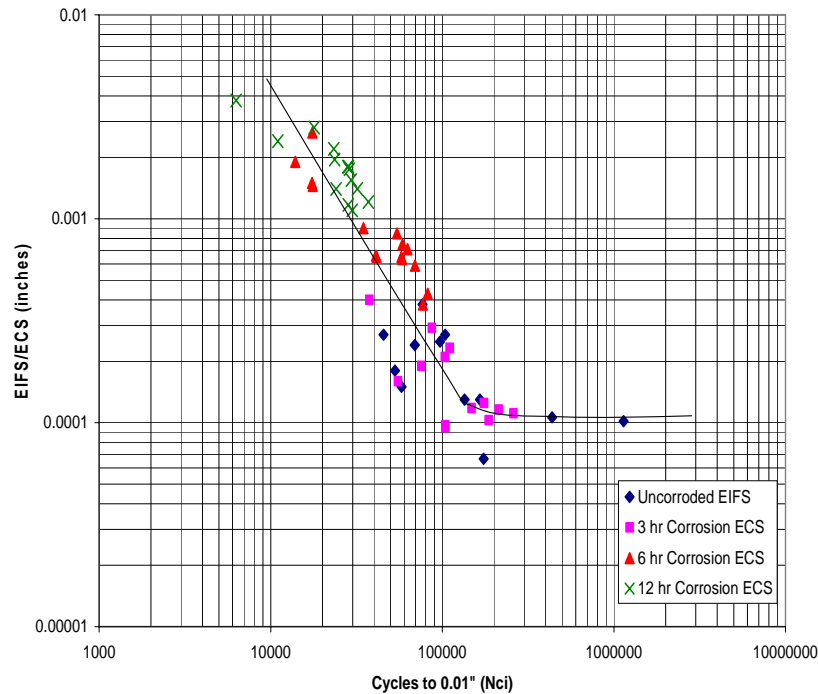
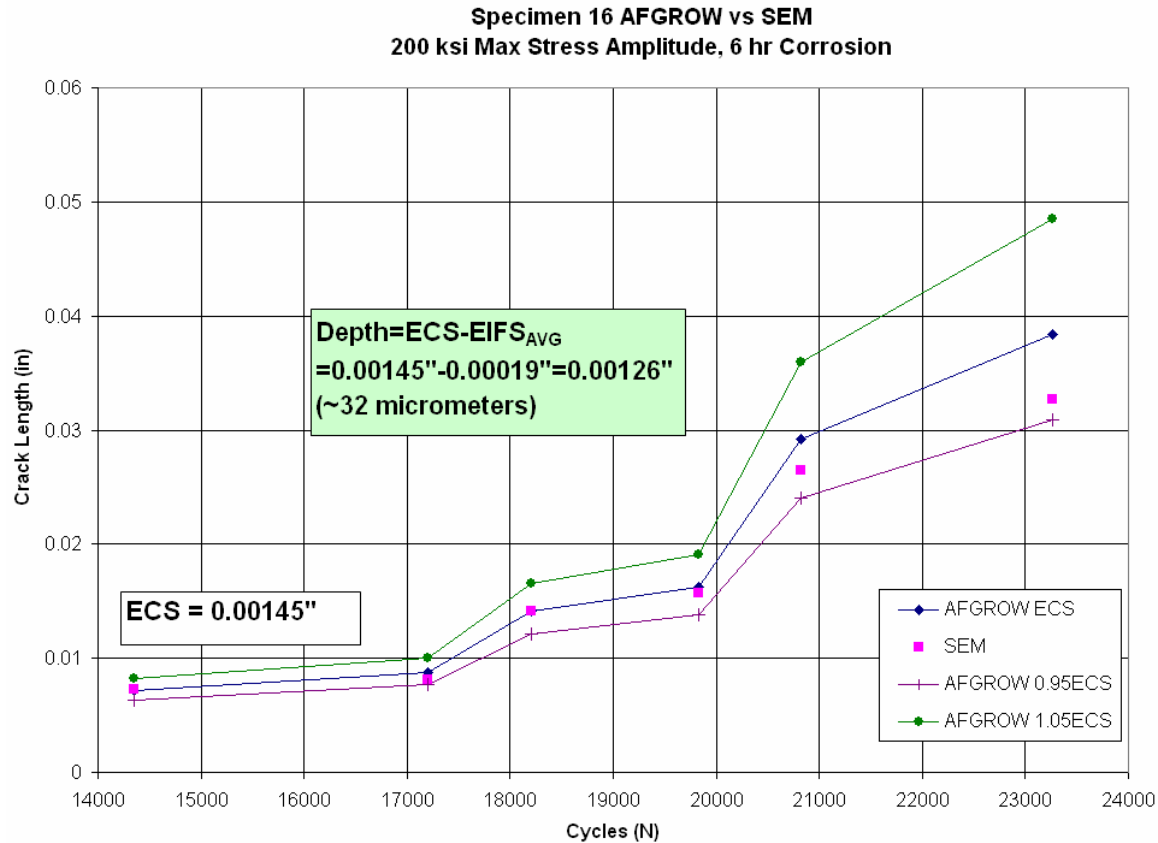


Figure 27. Summary of ECS/EIFS Values for AF1410 Set A Specimens

A validation experiment was performed using AF1410 Set A Specimen #16. The specimen was corroded for 6 hours and subjected to a maximum tensile stress of 200 ksi. It is known that crack initiation (0.01" flaw) occurred after 17580 cycles in fatigue testing. Using the appropriate estimated growth curve (Table 1 in this report) and the given load spectrum, the ECS was iteratively determined, through comparison with available SEM measurements, to be about 0.00145" for Specimen 16. See Figure 28 for the crack size vs. cycles outcome for the AFGROW post-diction for Specimen 16, as well as the computed ECS.



Turning to the WLI information regarding Specimen 16, the crack initiation location was found and the maximum depth of the feature corresponding to the likely site of crack initiation was scrutinized for the maximum recorded depth. The maximum depth of the feature, shown in Figure 29, was found to be roughly 30-35 micrometers. When the characteristic EIFS was subtracted from the ECS determined from Specimen 16, it was found that the predicted maximum depth was 32 micrometers. Additional ECS post-dictions may be found in the Appendix.

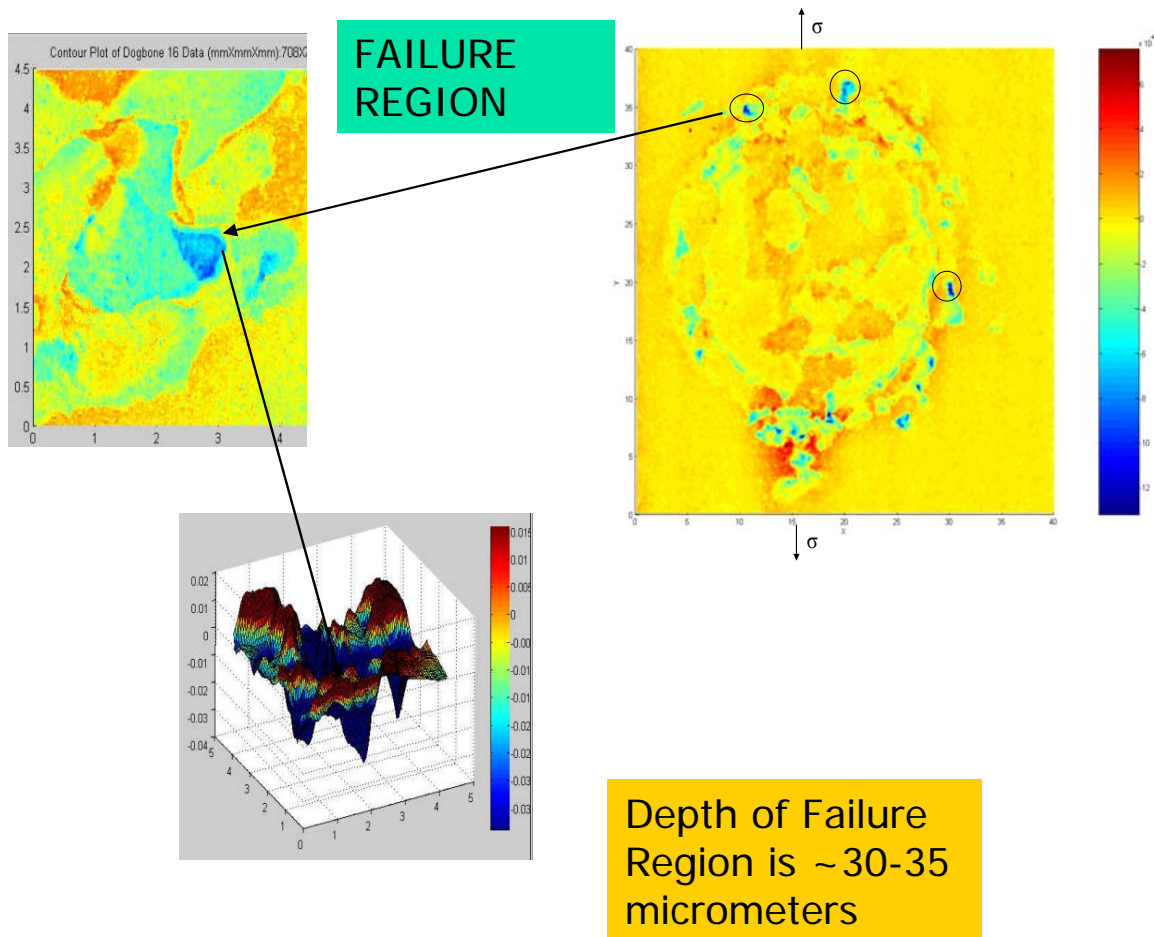


Figure 29. Specimen 16 Failure Region Feature

6.2.2c AF1410 Set A Specimen ECS vs. WLI Depth Measurements

A study was performed to determine whether a discernable trend, or metric, can be extracted from comparisons between specimen WLI (**White Light Interferometer**) data and corresponding ECS (**Equivalent Crack Size**) values deduced from AFGROW a posteriori life prediction studies. The specimens studied were those subjected to a corrosion exposure time of 6 hours, and the WLI data of interest were the maximum twenty extracted depths per specimen. The goal was to determine if there is any relationship between the ECS value necessary to fail the specimen after N cycles of loading, and the maximum twenty depths observed to occur at the surface of the corroded specimen. It is expected that this study will provide information on whether or not the specimen surface features corresponding to the most extreme depths, most likely initiated by corrosion assisted degradation, can be modeled under the equivalent crack size (ECS) assumption.

As the study progressed it became clear that there are too many independent variables available that significantly influence the relationship between the ECS and the maximum observable depths per

specimen, the most influential being the number of sample points chosen for the extraction (5000 or 16000) as well as the number of maximum depths (20) acquired per specimen. It must be noted that the maximum depth per specimen alone was found to have a very poor correlation with the corresponding ECS value, and was disregarded as a potential metric (see Figure 30). Instead, the average value of the maximum twenty (20) depths per specimen was used to establish a consistent basis for this study, as it appeared to increase correlation.

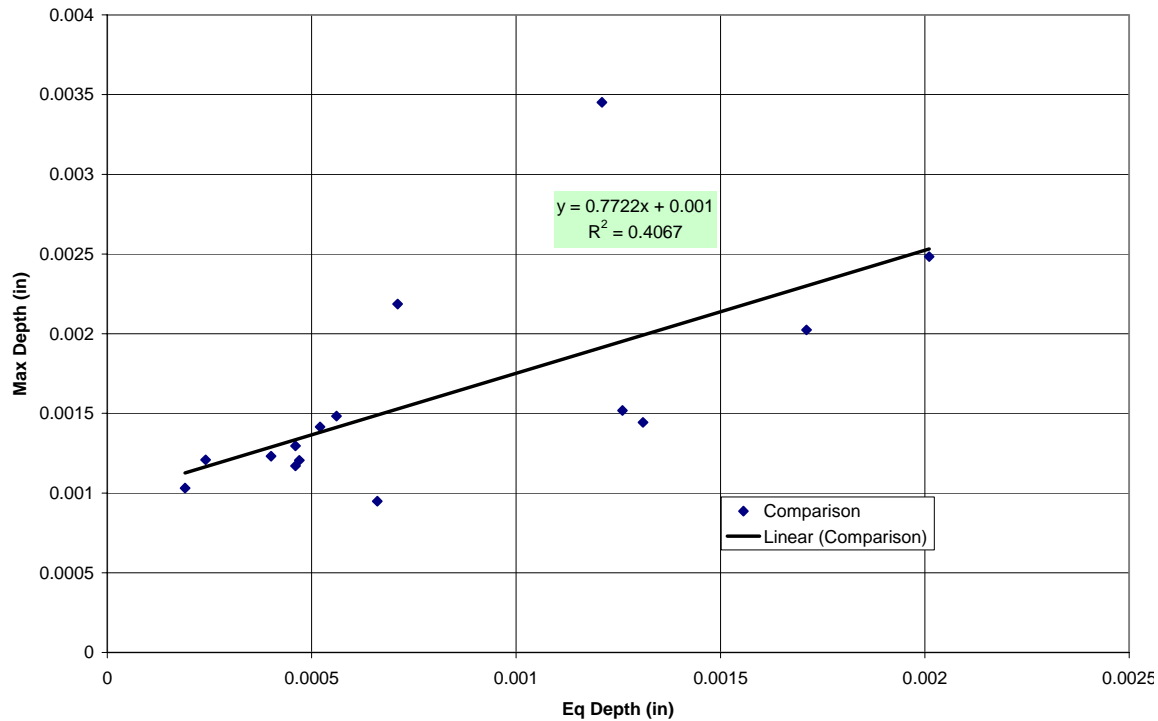


Figure 30. Maximum Extracted Depth vs. ECS (5000 points)

It was found that when a 5000 sample point extraction and a 16000 sample point extraction (from a field of ~16 million points, on average, per corroded region) were compared side by side, the correlation weakened (see Figures 31 and 32) as the number of sample points increased. This sensitivity is of great concern, as it appears that a “fit” or correlation of data sets can be forced, which is not the intention of this study. It is noted that the significance of using sixteen thousand (16000) points as opposed to an arbitrary number of points is due to the fact that the current sampling capability of ultrasound NDI sampling is roughly 16000 points per square inch. The average size of the corroded area is roughly one square inch, thus justifying the sampling population size.

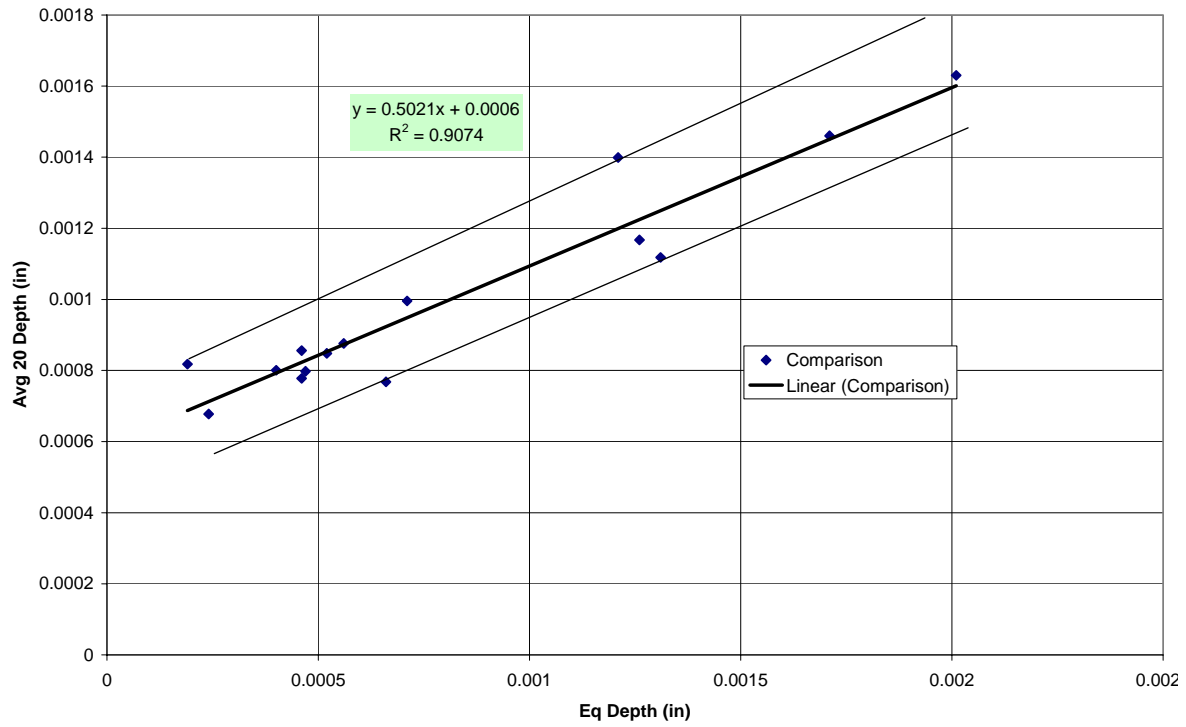


Figure 31. Mean of the Twenty (20) Maximum Extracted Depths vs. ECS (5000 points)

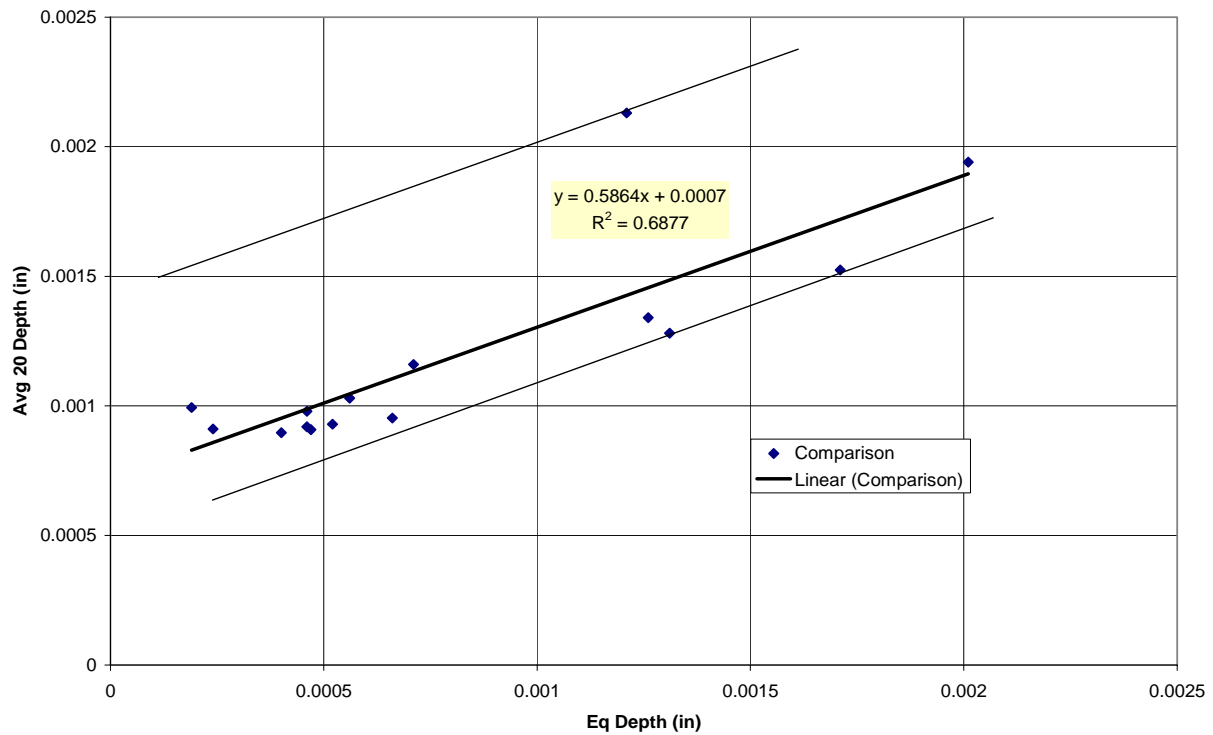


Figure 32. Mean of the Twenty (20) Maximum Extracted Depths vs. ECS (16000 points)

6.2.2d ECS vs. Crack Initiation Site Maximum Pit Depths for AF1410 Set A 6 Hour Corrosion

Also within the framework of this study was an effort to compare the actual pit depths (at the sites of crack initiation) with the predicted ECS for each specimen. These pit depths were reported by Dave Rusk of NAVAIR, and corresponded to specimens subjected to six (6) hours of corrosion. The number of pit depths reported as of 5/31/2006 was seven (7). As can be inferred from Figure 33, there is not yet a particularly strong correlation between the actual measured pit depths and the a posteriori computed ECS for the specimen set. As always, more pit depths are needed for generating a statistically significant population.

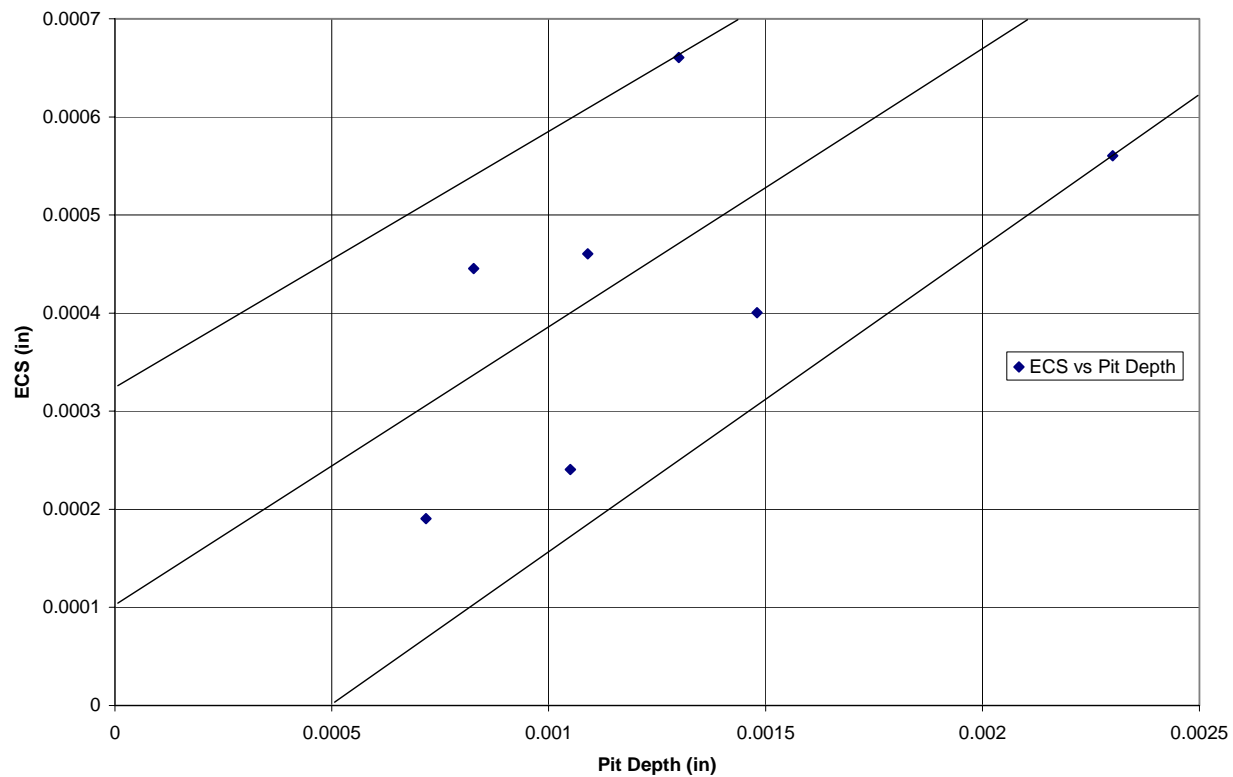


Figure 33. Comparison of ECS and Actual Measured Pit Depth

Although several independent variables have been restricted or removed now that the crack initiation location and corresponding feature dimensions are available, it is still extremely difficult to relate the physical pit feature to a metric defined a priori. More sample points are necessary to determine the distribution of the data, as this will determine the potential of the metric to relate measurable characteristics of corrosion to a life prediction.

6.2.2e StressCheck Analysis of the Effect of Pit Dimension on the Stress Intensity Factor

A simple sensitivity study was performed in which an equivalent initial flaw size, represented by a small crack, is added to the bottom of a pit-like feature, represented by a parametric ellipse. The computations were performed with StressCheck. The EIFS (crack) is then allowed to propagate (under tension loading) until a crack length of 1" is reached, after which the SIF (stress intensity factor) at each crack depth is reported. This process was performed for several different pit depths (see Figure 34). It is observed that the effect of the feature size on the SIF is quite significant, even though the dimensional aspect is constant. This behavior is essentially driven by a notch effect.

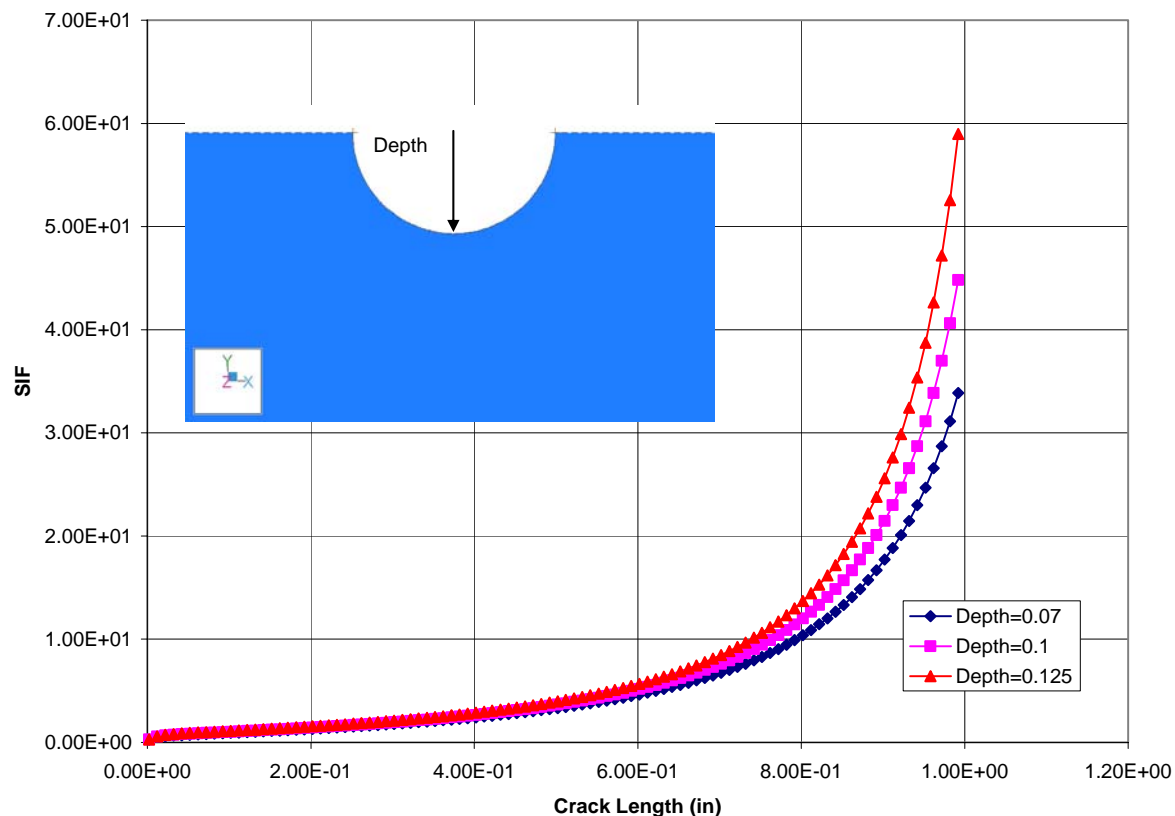


Figure 34. Sensitivity Study of the Effect of Pit Size on the SIF

6.2.3 Summary

A very attractive feature of this approach is that it is free from the burden of having to estimate notch intensity factors for corroded surfaces. In order for it to be useful for the purpose of predicting the number of loading cycles that will cause the first occurrence of a 0.01 inch crack, additional calibration and validation experiments would be necessary.

6.3 Discovery Experiment: Micro-Machined Features of Similar Kt

6.3.1 Introduction

A set of experiments were designed for the purpose of determining the statistical characteristics of crack initiation under very nearly ideal conditions. These experiments also serve the purpose of testing the predictive capabilities of the pit metric proposed by UDRI with respect to the first occurrence of a 0.01-inch crack under uniaxial conditions. ESRD's task was to propose surface features that could be produced by micro-machining techniques. The surface features were to be of simple geometric shape and each should have approximately the same geometric stress concentration (Kt) and therefore roughly the same probability of failure. The dimensions of these features, due to current limitations in machining and tooling technology, are to be an order of magnitude larger than typical corroded features encountered in testing.

6.3.2 Study Approach and Results

6.3.2a Proposed Features for Micro-machined Geometry

It was proposed that the micro-machined geometric features include a conical feature with a rounded tip (bucket-shape), a trough-like feature comprised of a cylinder with spherical ends (pill-shape), and an ellipsoid feature with a depth corresponding to the minor ellipse radius. These three geometric features were controlled such that they have approximately the same maximum geometric stress concentration ($K_{t_{max}} \approx 2.5$, which is almost twice the magnitude observed in corroded specimens); in this sense, they all have an equal likelihood of failure if the theory used to predict crack initiation is based on the location of maximum Kt. The proposed features and loading situation are given in Figure 35.

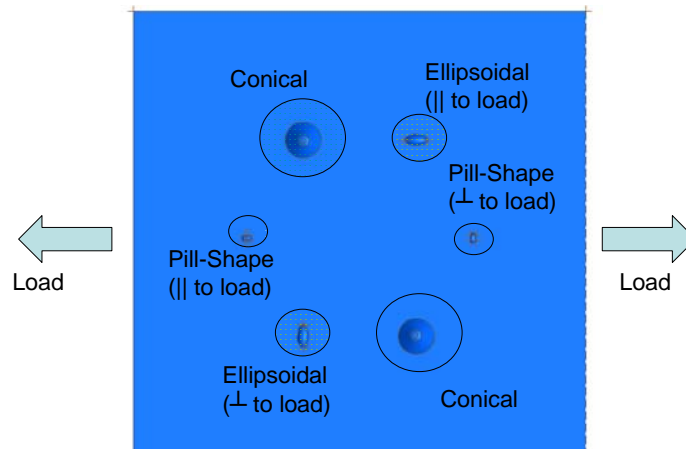


Figure 35. Proposed Arrangement of Features for Micro-machining Experiment

6.3.2b Conical Feature Dimensions

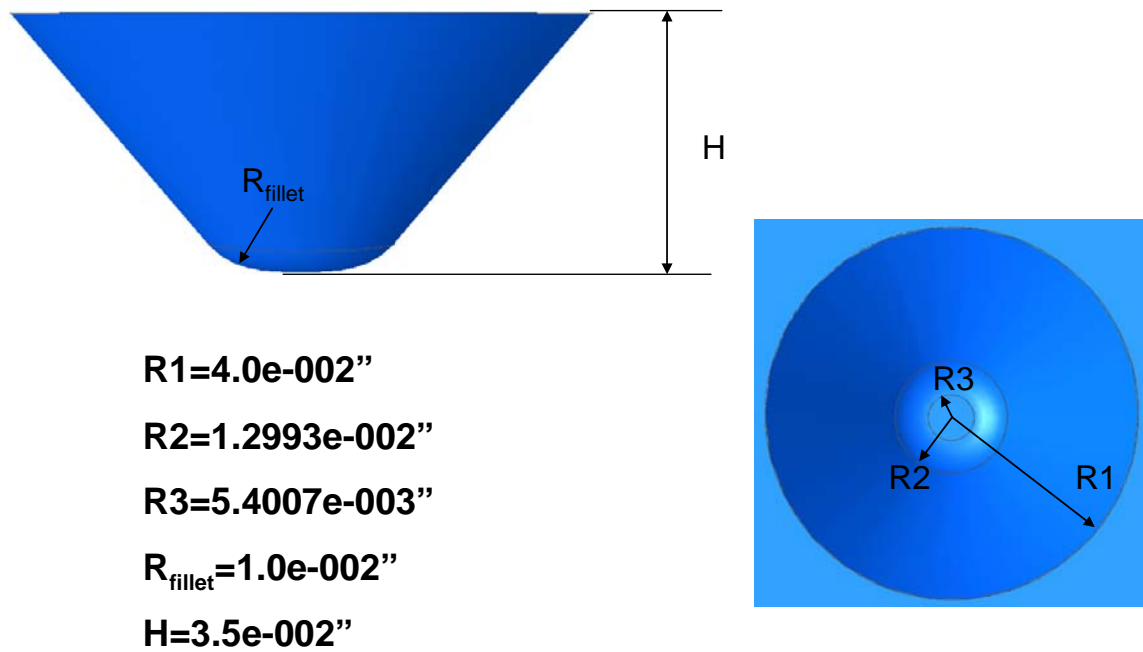


Figure 36. Conical Feature Dimensions

6.3.2c Ellipsoidal Feature Dimensions

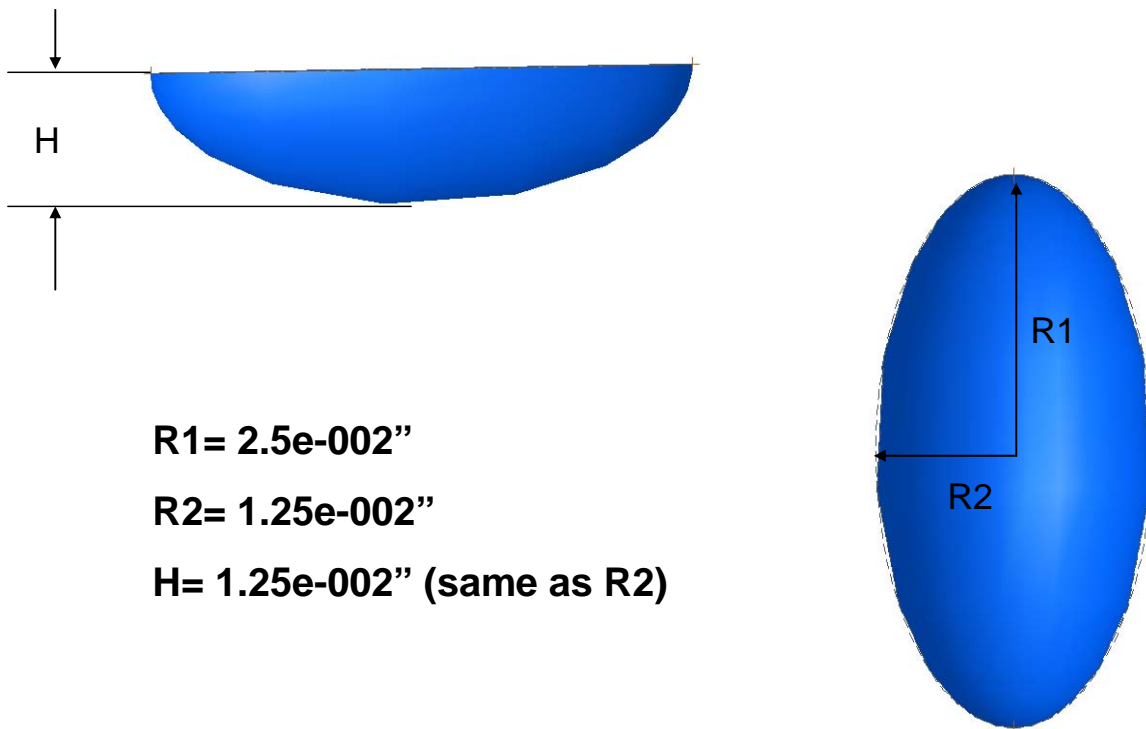


Figure 37. Ellipsoidal Feature Dimensions

6.3.2d Pill-Shape Feature Dimensions

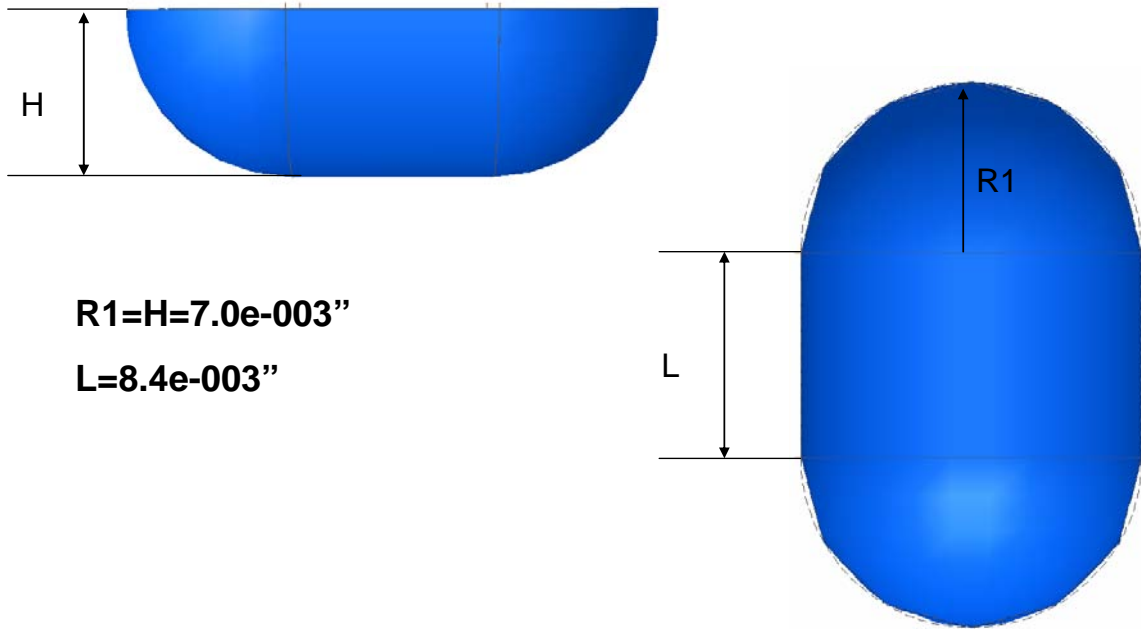


Figure 38. Pill-Shape Feature Dimensions

6.3.2d StressCheck Kt Verification for Micro-machined Geometry

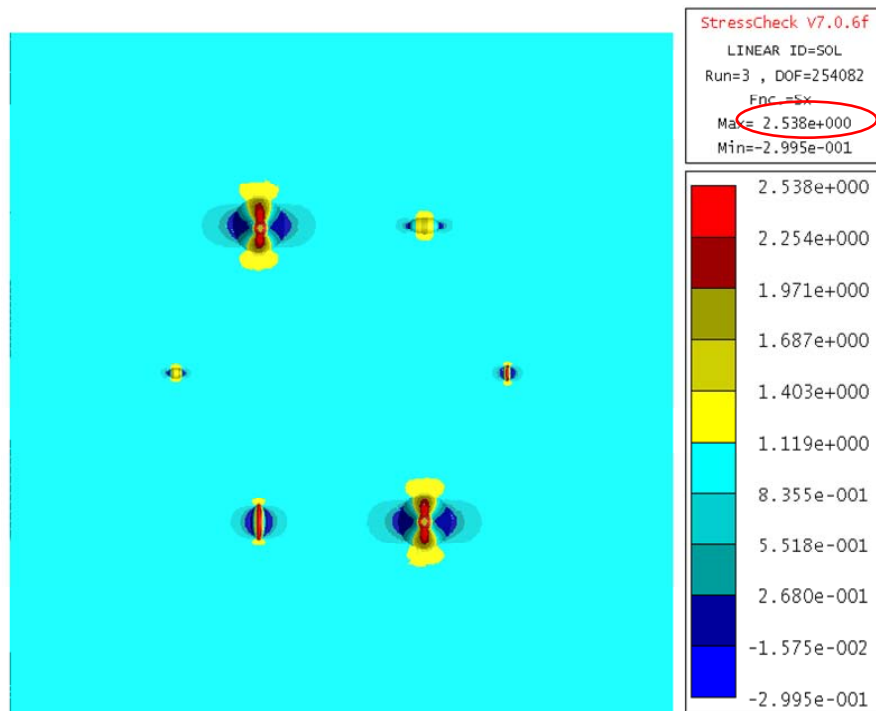


Figure 39. Kt Verification for Micro-machined Geometry

6.3.3 Summary

At the time of writing 10 specimens have been manufactured, delivered to UDRI and WLI measurements have been taken. Fatigue experiments, fractographic investigation and evaluation are yet to be completed.

6.4 Parametric Pit Studies Based on Idealized Corroded Surface Topologies

6.4.1 Introduction

A parametric study of corrosion assisted pitting was performed within the StressCheck environment for several different pitting configurations, with the purpose of determining the maximum K_t for each configuration. Four (4) AF1410 Set A corroded specimen pit configurations, each believed to be in the vicinity of crack initiation, were fit to ellipsoidal profiles by Dave Rusk of NAVAIR. These idealized ellipsoidal shapes were then modeled by StressCheck via formulas and Boolean operations.

All features were then incorporated into the center of a $1 \times 1 \times 1/8^{\text{th}}$ inch plate, representative of the specimen gage section. Unit tractions were then applied to the plate, and rigid body constraints were imposed. The general purpose of this study was to understand the behavior of the stress fields in the vicinity of these features, with particular focus on the maximum geometric K_t .

6.4.2 Study Approach and Results

6.4.2a Case 1: Single Pit Configuration (Specimen #20)

Case 1 is a single ellipsoidal pit of width 0.074 mm, height of 0.074 mm in the loading direction, and depth of 0.041 mm. The representation is given in Figure 40. The result for the maximum K_t is given in Figure 41.

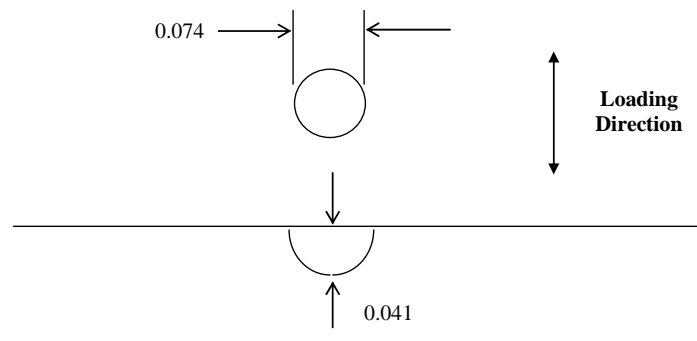


Figure 40. Case 1 Pit Configuration

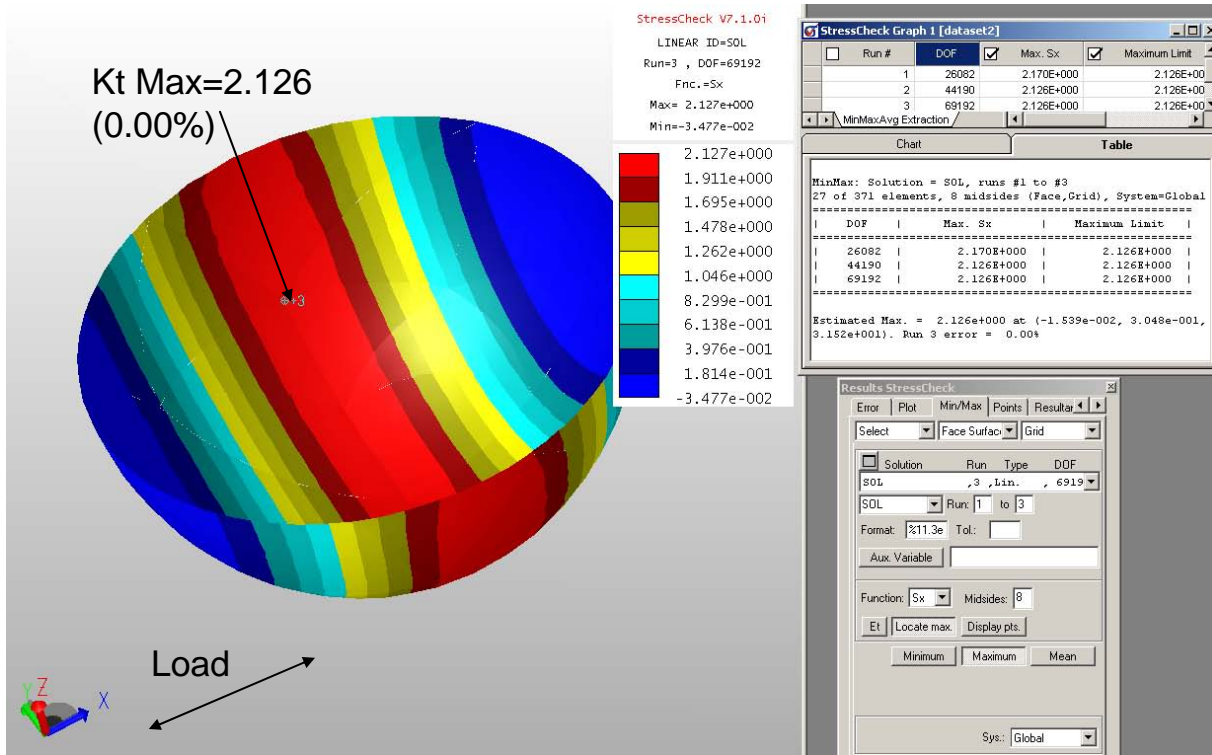


Figure 41. Case 1: Maximum Kt is 2.126 (0.00% Error)

An additional study was performed, using the idealized pit geometry for Specimen 20, in which the applied load (S) versus maximum first principal strain for the pit (ϵ_1) was extracted. The goal was to use these extractions as inputs for comparison of an elastic-plastic FEA based strain-life prediction with a Neuber's rule based strain-life prediction. In order to predict life for notched specimens using the strain-life methodology, the notch strains as a function of the applied load must be known (ϵ , S). An outline of the strain-life methodology, as well as Neuber's rule, is given in Figure 42. The AF1410 cyclic and monotonic material laws are given in Figure 43.

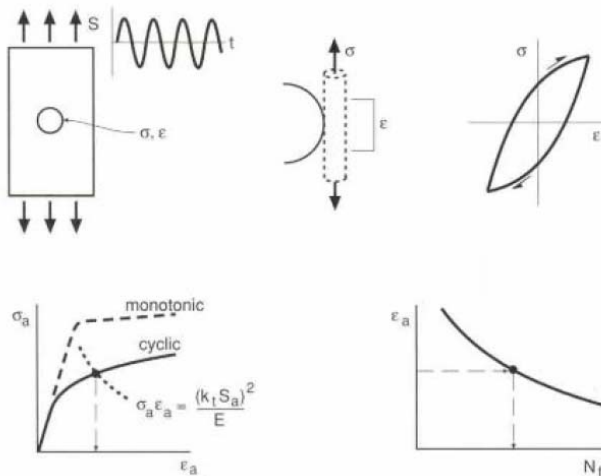
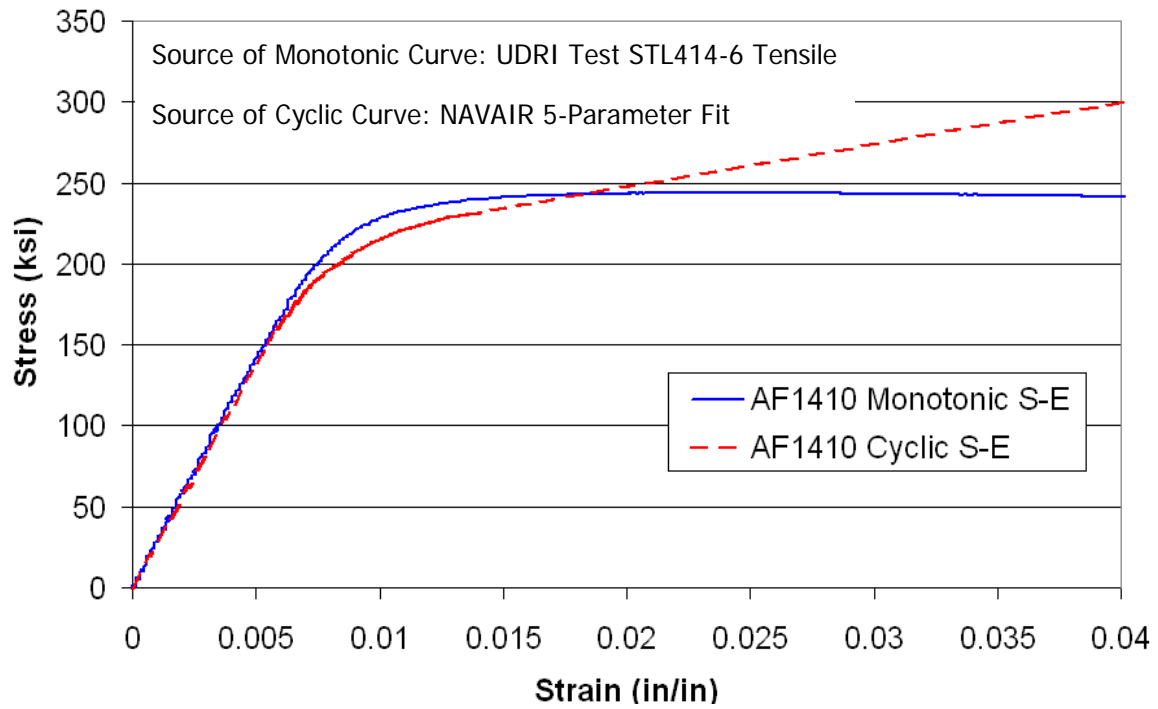
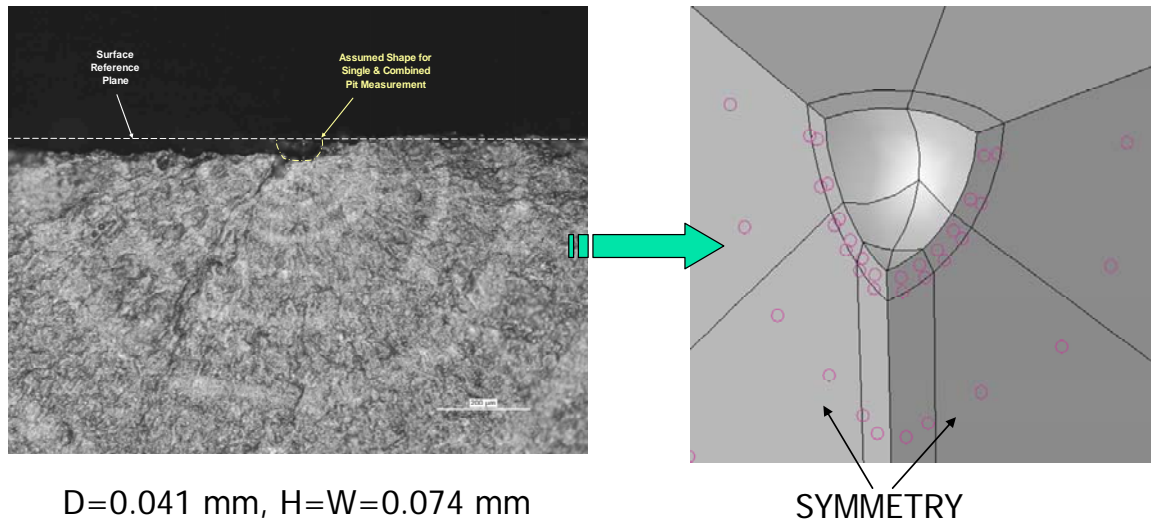


Figure 42. Strain-Life Methodology (Shown with the Neuber's Rule Equation)**Figure 43. Cyclic and Monotonic Stress-Strain Curves for AF1410**

The actual fractographic profile of Specimen #20, with the identified crack initiation pit location in yellow, and the finite element mesh used in the computation is given in Figure 44.

**Figure 44. Specimen 20 Crack Initiation Pit and Finite Element Mesh Idealization**

The load was applied to the finite element model through imposed displacements, and was incremented during a material nonlinear analysis until net section yielding was approached. After each load step was performed, and the solution obtained, an extraction of the maximum “notch” strain (ϵ_1) at the pit was made and stored with the resultant traction (S) for that load step. The results for the load step analysis are given in Figure 45. The comparison with the Neuber results is pending.

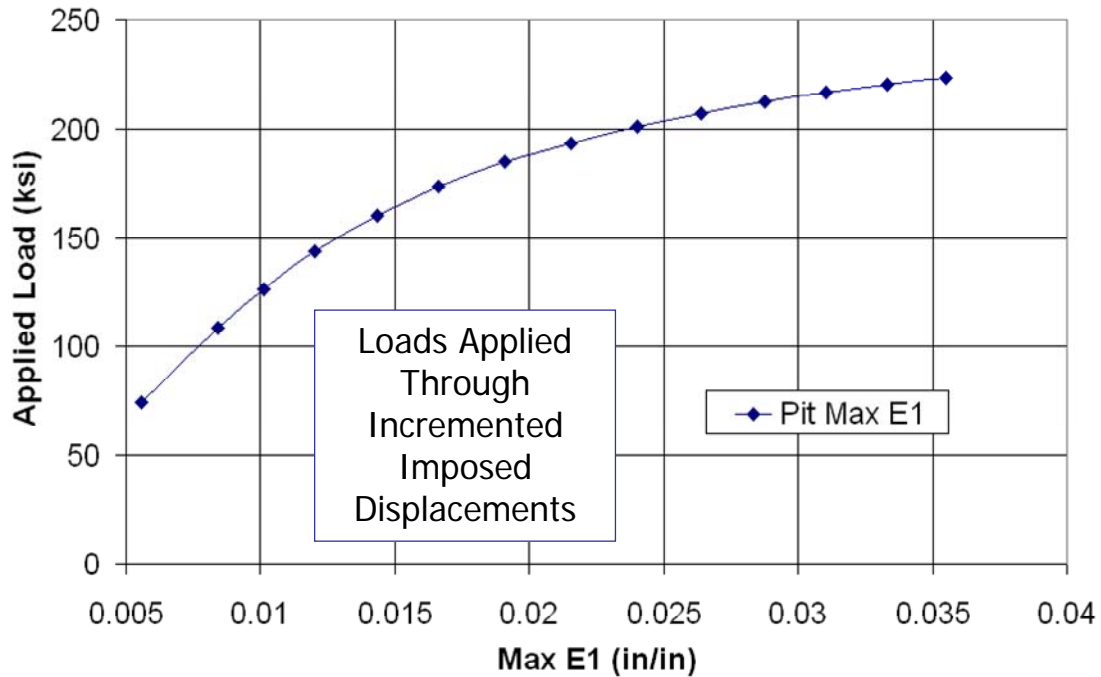


Figure 45. Specimen 16 Load Step Analysis: ϵ_1 -S Profile

6.4.2b Case 2: Elongated Pit (Specimen #15)

Case 2 is a single pit elongated in the width direction. The top of the feature is racetrack in shape (a special case of a rounded rectangle), while the thickness variation of the feature is ellipsoidal. Subcase 1 of this configuration (Figure 46) is under the constraint that the deepest point in the feature is offset from the centroid of the plane view. Subcase 2 of this configuration allows for the deepest point in the feature to be at the centroid. The results for the maximum Kt of each subcase are given in Figures 47 and 48.

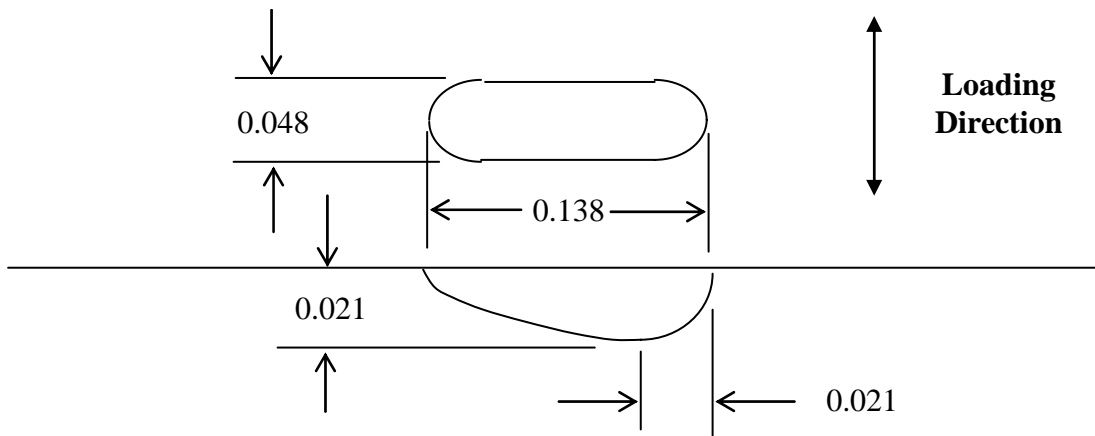


Figure 46. Case 2 Pit Configuration (Subcase 1 is shown)

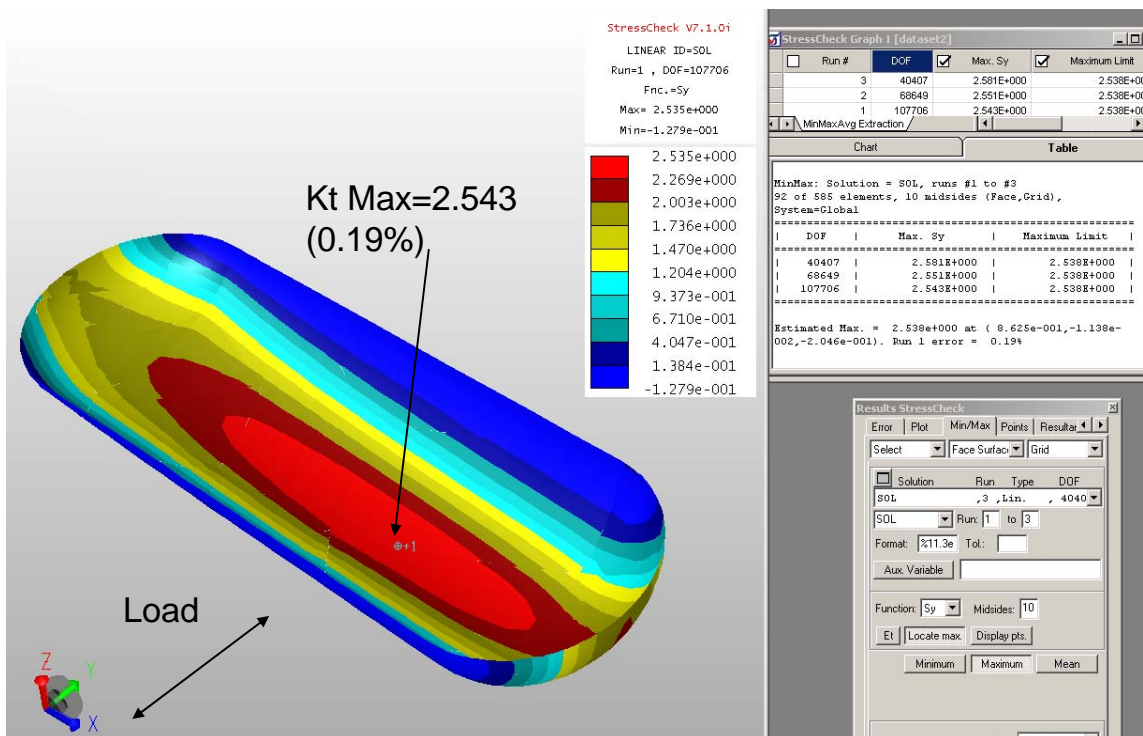


Figure 47. Case 2, Subcase 1: Maximum Kt is 2.543 (0.19% Error)

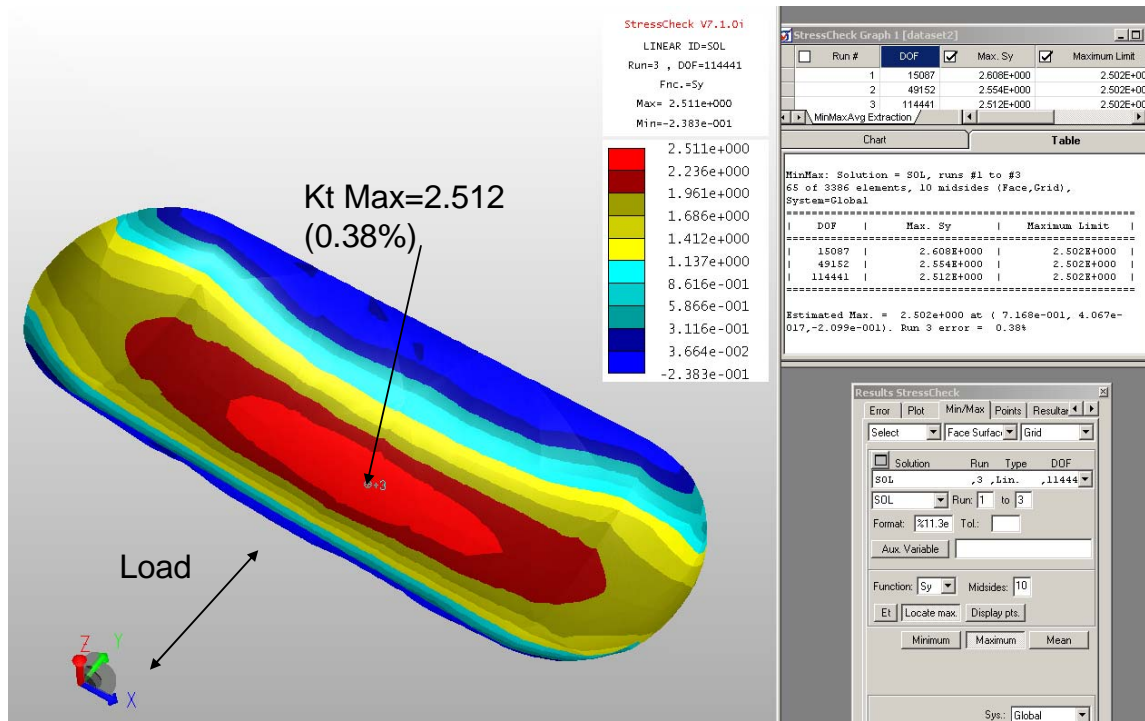


Figure 48. Case 2, Subcase 2: Maximum Kt is 2.512 (0.38% Error)

6.4.2c Case 3: Two Interfering Pits (Specimen #36)

Case 3 is modeled as two interfering pits. Subcase 1 is as shown in Figure 49, while Subcase 2 is a single elongated pit of width 0.069 mm, height 0.050 mm, and depth 0.023 mm. For Subcase 1 two sets of results were obtained: one set corresponds to no edge blending performed on the resulting intersection of pits, while the other set has slight blending incorporated. The results for the maximum Kt of each subcase are given in Figures 50a, 50b and 51.

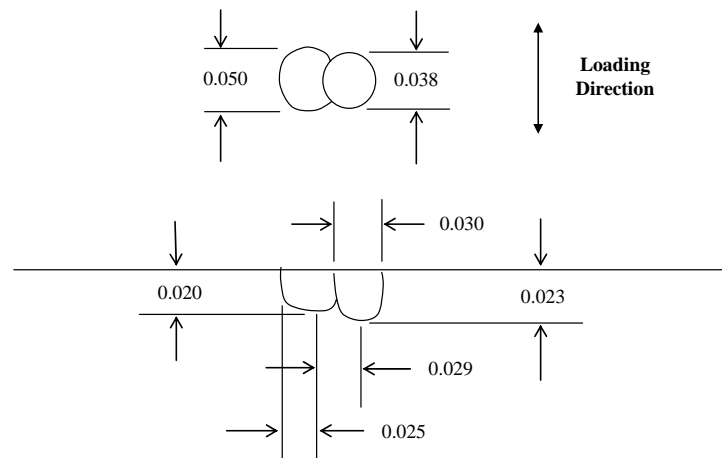


Figure 49. Case 3 Pit Configuration (Subcase 1 is shown)

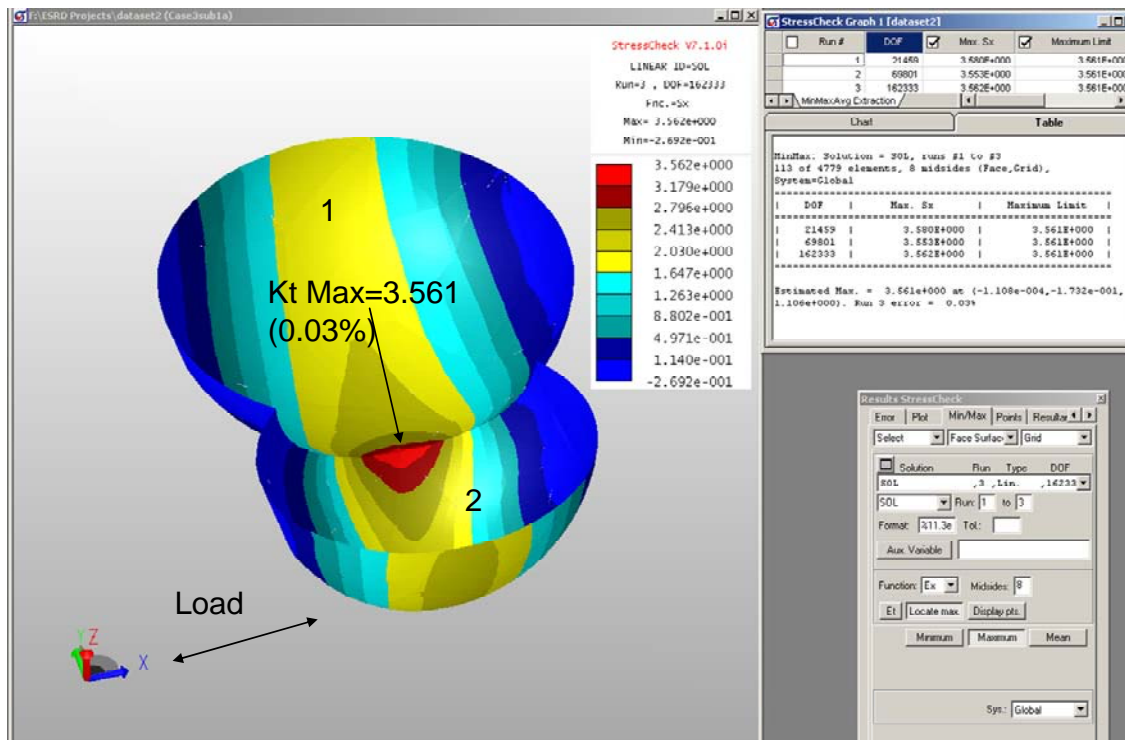


Figure 50a. Case 3, Subcase 1 (No Blending): Maximum Kt is 3.561 (0.03% Error)

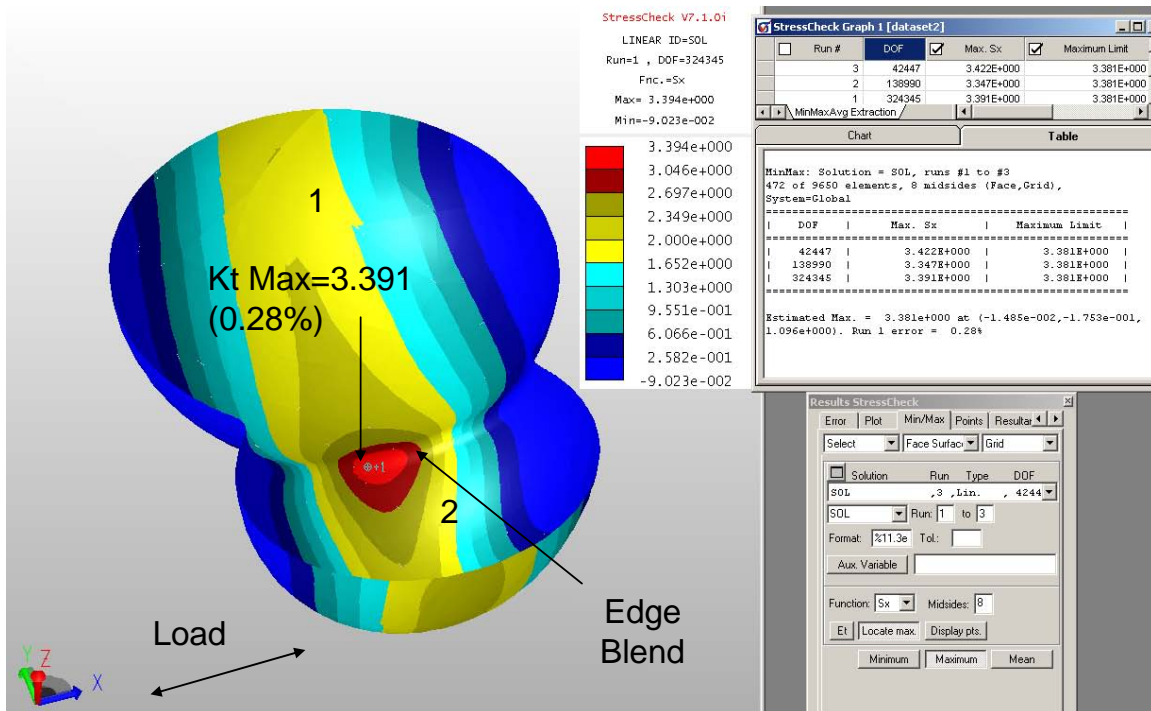


Figure 50b. Case 3, Subcase 1 (With Blending): Maximum Kt is 3.391 (0.28% Error)

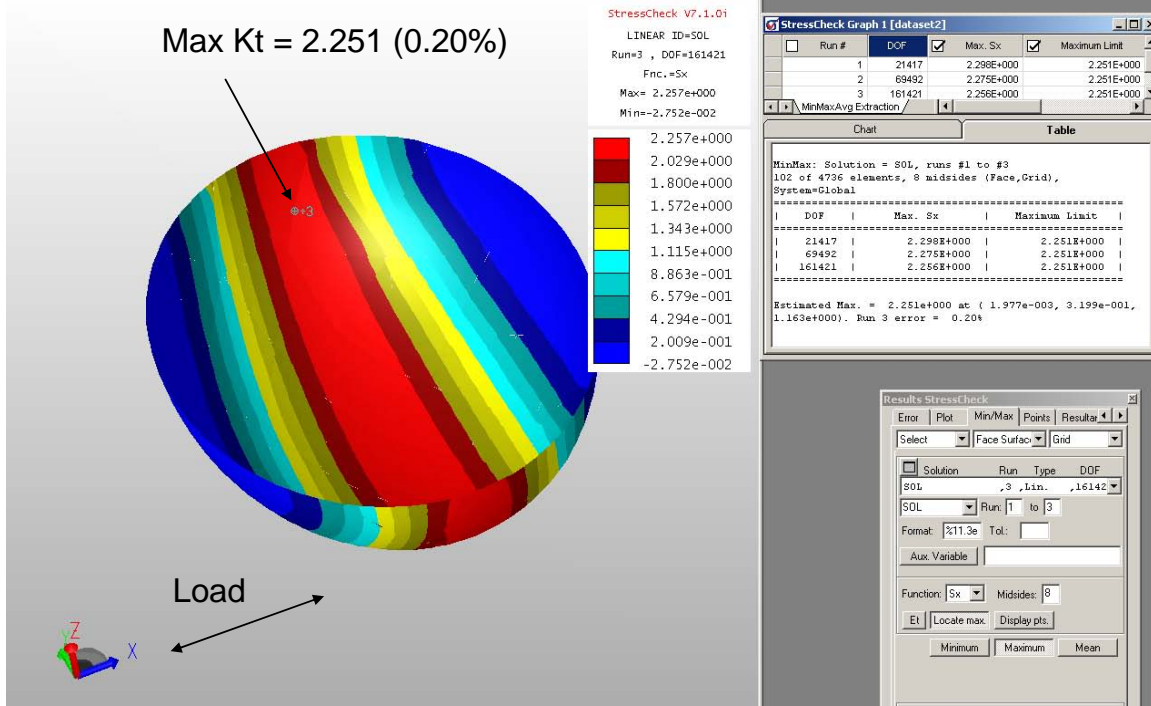


Figure 51. Case 3, Subcase 2: Maximum Kt is 2.251 (0.20% Error)

6.4.2d Case 4: Four Interfering Pits (Specimen #46)

Case 4 is modeled as four interfering pits. Subcase 1 is as shown in Figure 52, while Subcase 2 is a singled elongated pit of width 0.342 mm, height 0.146 mm, and depth 0.090 mm. Subcase 1 two sets of results were obtained: one set corresponds to no edge blending performed on the resulting intersection of pits, while the other set of results has slight blending (of the order of 10% of the largest curve formed by the intersection of the pits) incorporated. The results for the maximum Kt of each subcase are given in Figures 53a, 53b and 54.

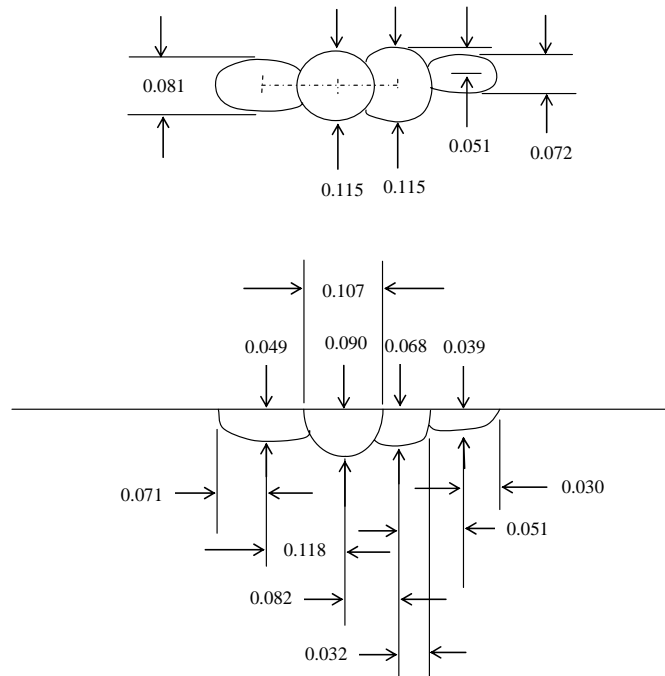


Figure 52. Case 4 Pit Configuration (Subcase 1 Shown)

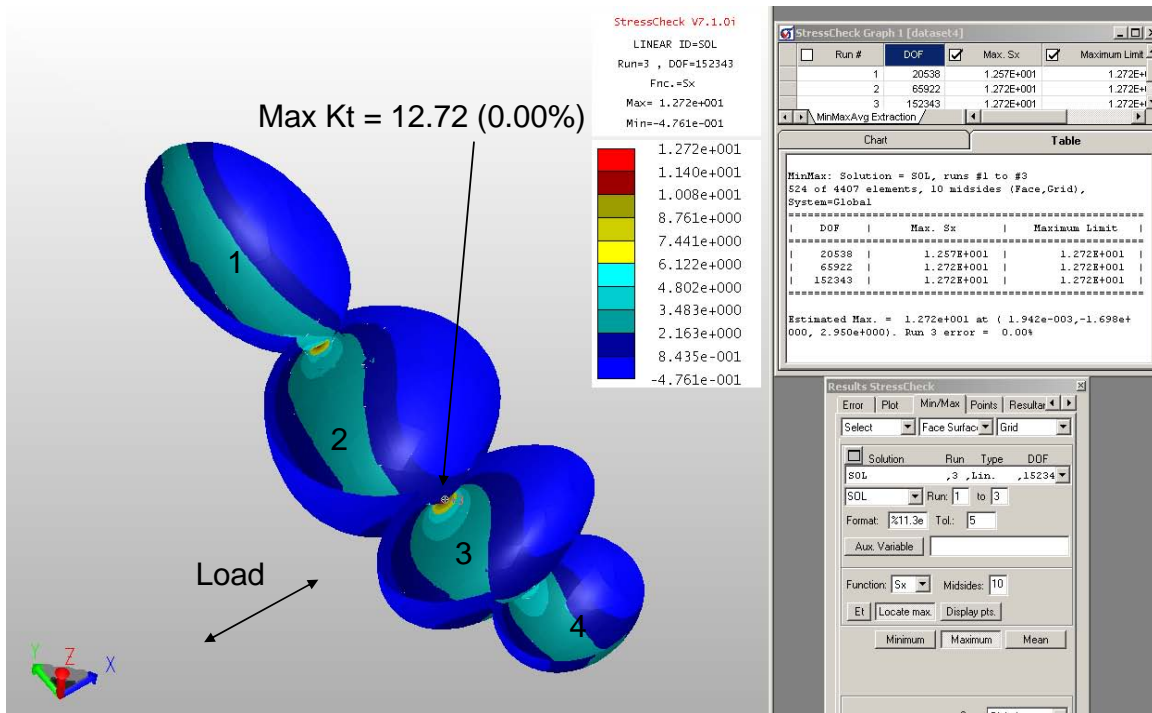


Figure 53a. Case 4, Subcase 1 (No Blending): Maximum Kt is 12.72 (0.00% Error)

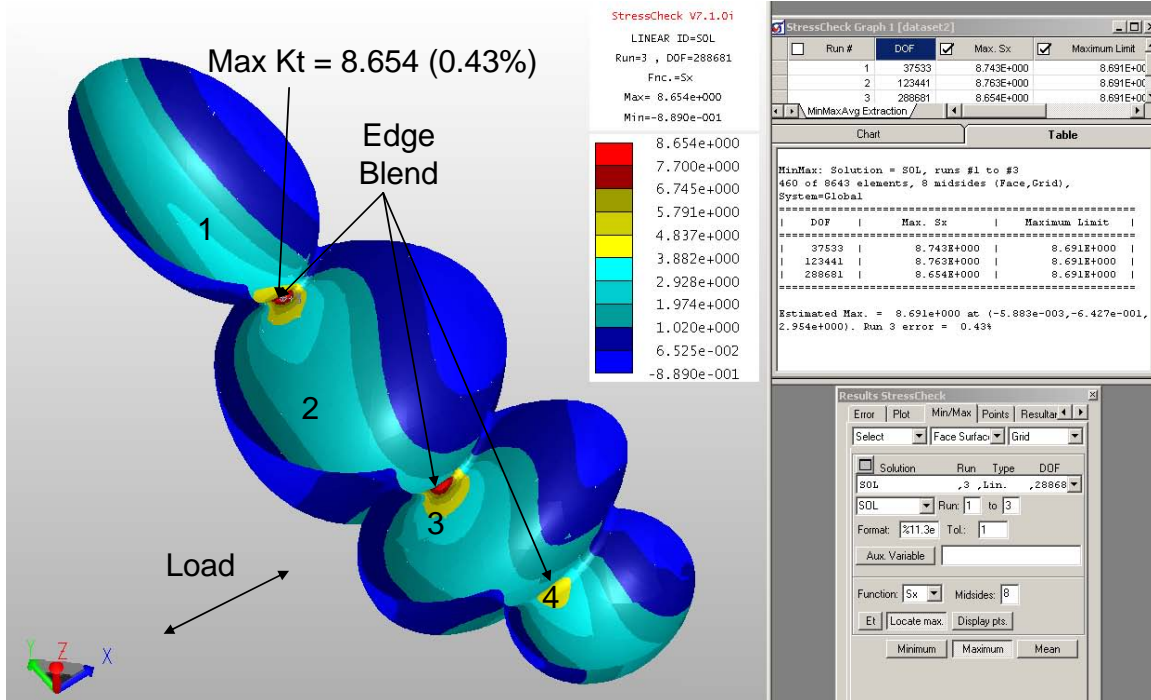


Figure 53b. Case 4, Subcase 1 (With Blending): Maximum Kt is 8.654 (0.43% Error)

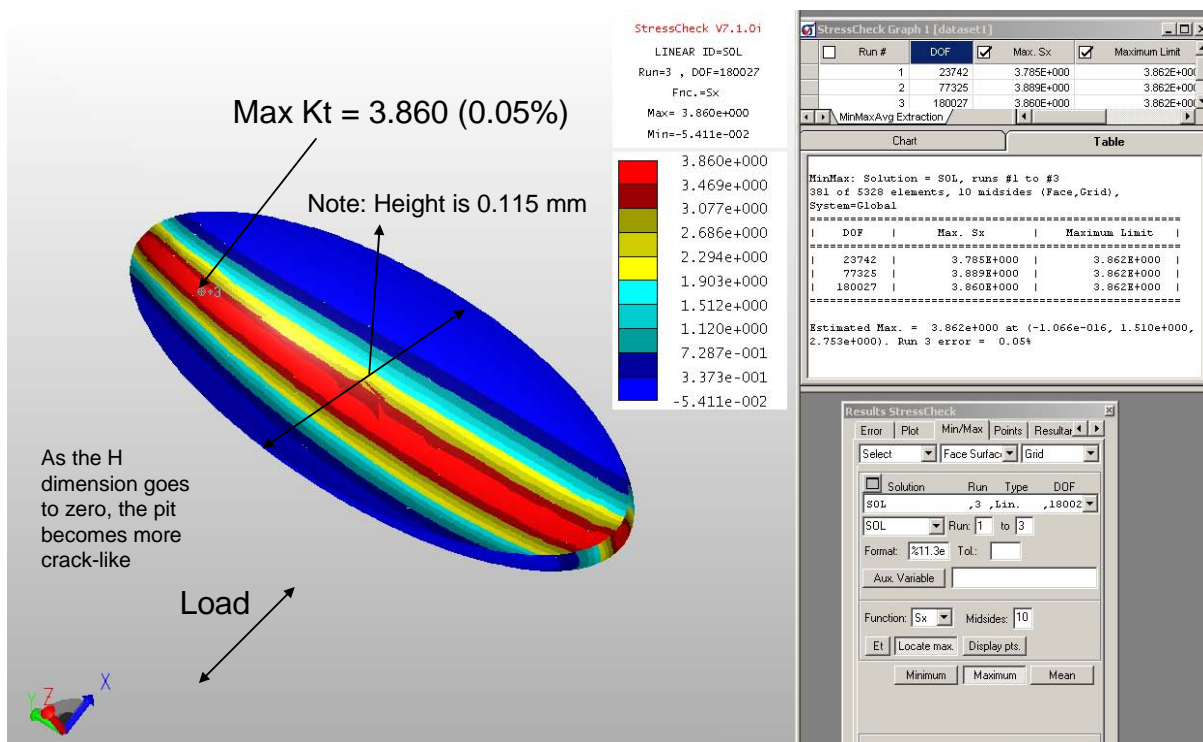


Figure 54. Case 4, Subcase 2: Maximum Kt is 3.860 (0.05% Error)

An additional numerical experiment was performed with the idealized geometry from Specimen 46. This involved an investigation into the sensitivity of the maximum K_t when the overlap (interference) of the interfering pits is increased or decreased. A schematic of the interference level is given in Figure 55.

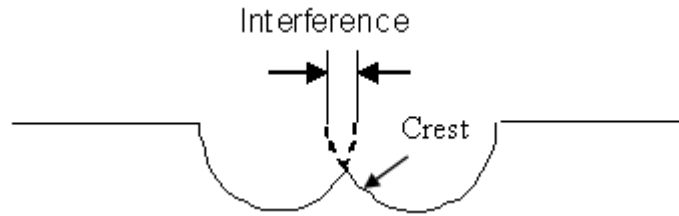
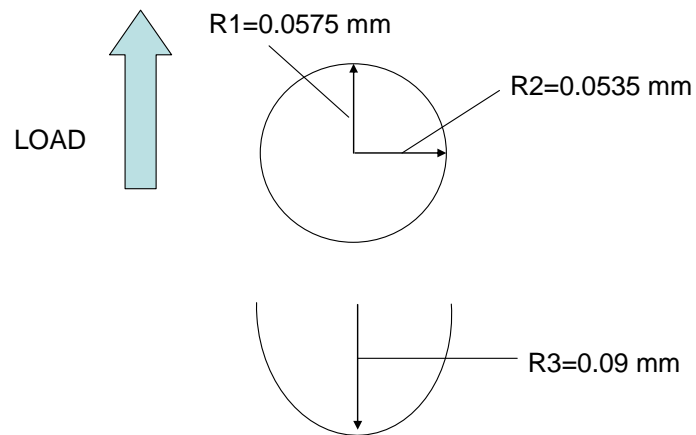


Figure 55. Schematic of Pit Interference Level

A pit from Case 4 of the previous study was extracted for use in this analysis. The pit will be mirrored such that the interaction of two identical pits can be examined. The dimensions are given in Figure 56.



*-Pit Dimensions are taken from Case 4, Pit #2.
Plate dimensions are 25X25X3.175 mm

Figure 56. Interfering Pit Geometry

As indicated, two identical ellipsoidal pits were modeled and subjected to symmetric boundary conditions as well as unit tractions. The level of interference between the pits is controlled by a parameter, “interference”. Four (4) levels of interference were studied for this analysis, with the level of interference gradually increasing from 0.001 mm to 0.025 mm. The results from the study can be seen in Figures 57-60, and summarized in Figure 61.

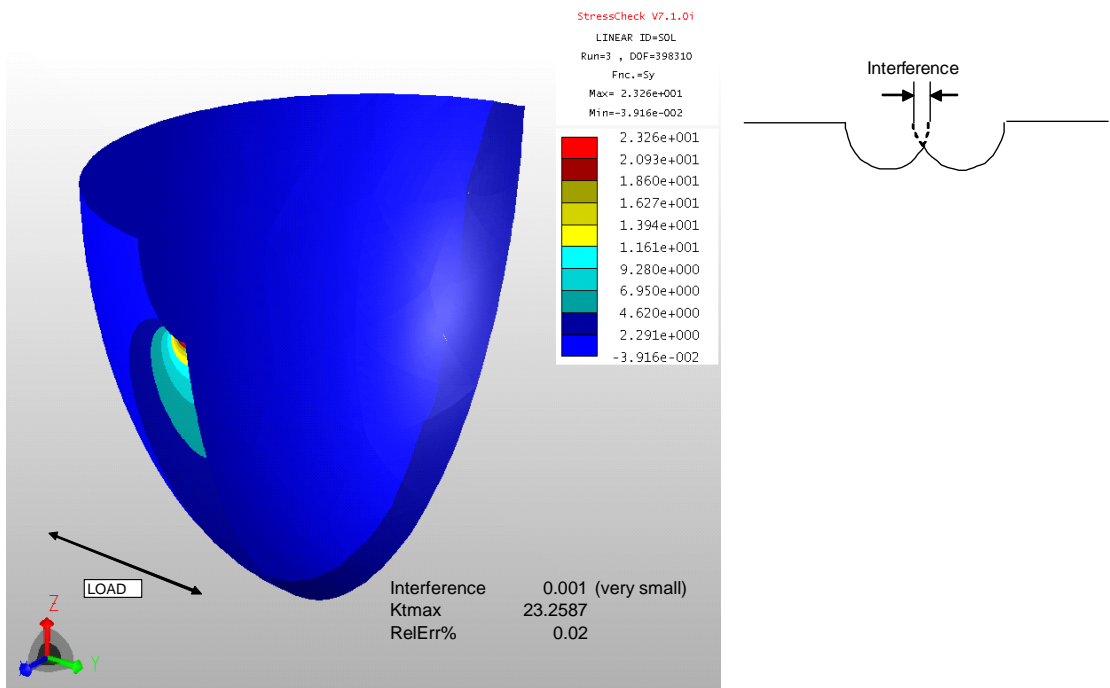


Figure 57. Interference Level of 0.001 mm (Kt=23.26)

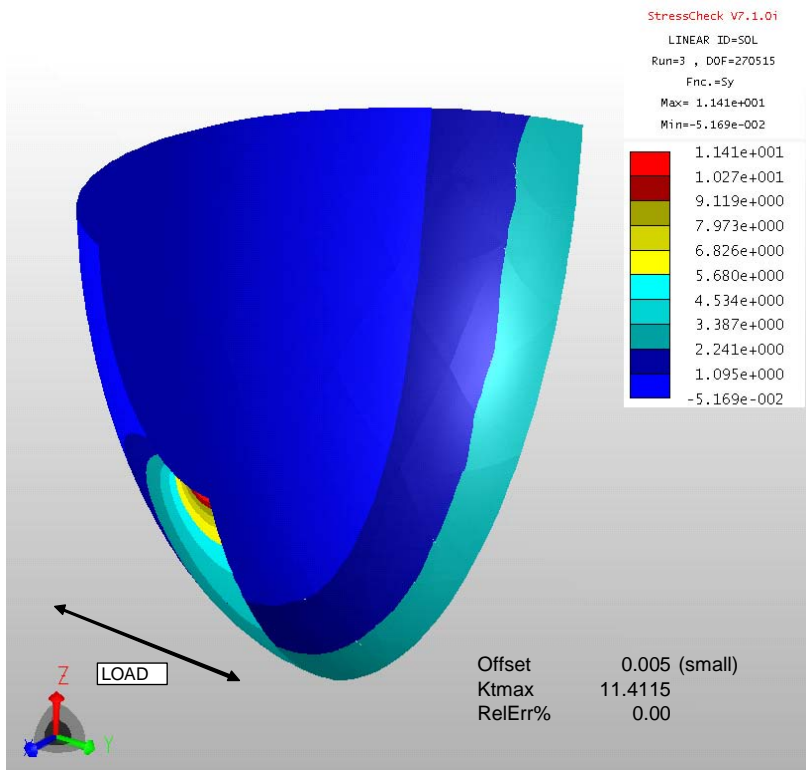


Figure 58. Interference Level of 0.005 mm (Kt=11.41)

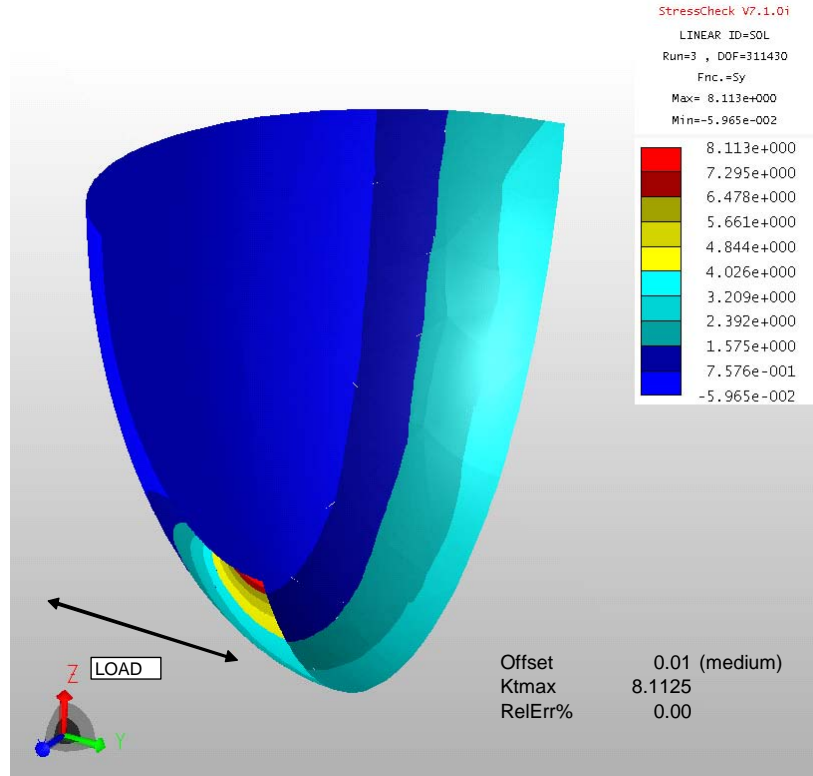


Figure 59. Interference Level of 0.01 mm ($K_t=8.11$)

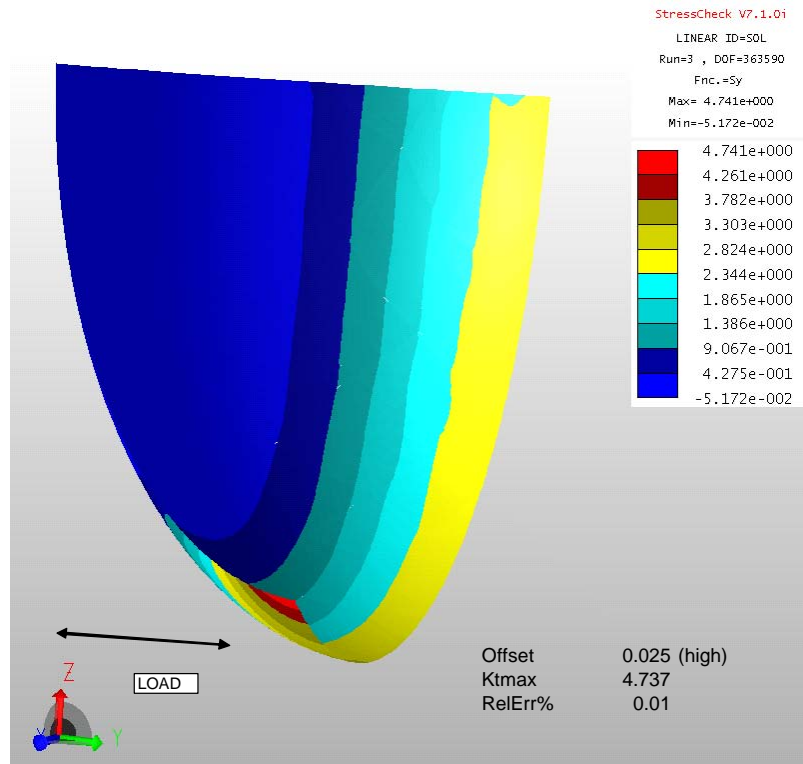


Figure 60. Interference Level of 0.025 mm ($K_t=4.74$)

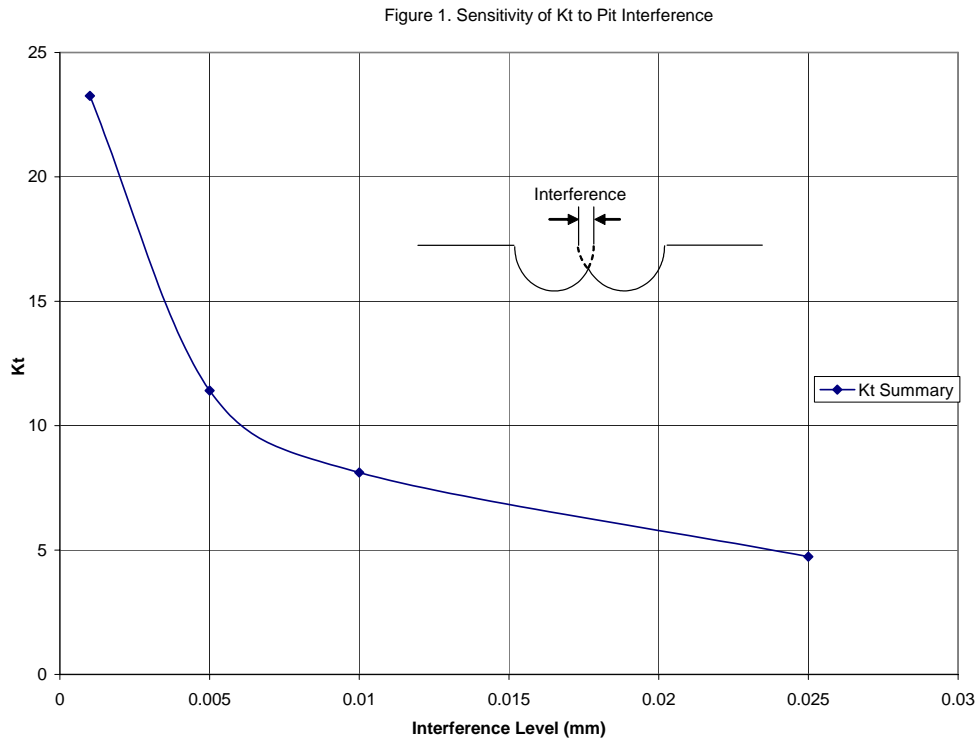


Figure 61. Comparison of Interference Level with Kt

6.4.2e Parametric Studies of Pit Metric Kt vs. StressCheck Kt for Ellipsoidal Features

A parametric study was performed to compare the behavior of $K_{t_{max}}$ for a single ellipsoidal pit defect centered in a uniaxially loaded plate. Three models were used for the comparison, and they are as follows: original pit metric Kt, StressCheck FEA Kt, and a modified Kt which is defined in this section. The original pit metric Kt is defined as follows in Figure 62:

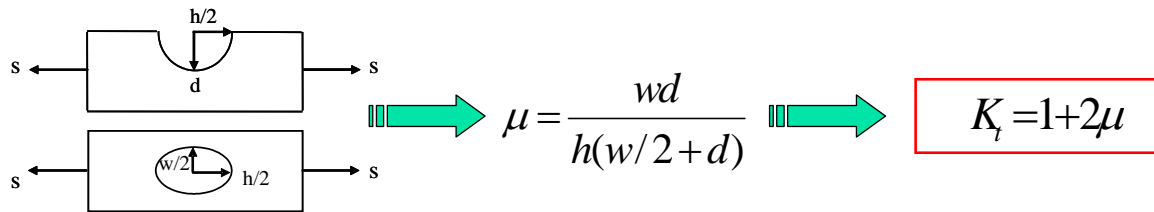


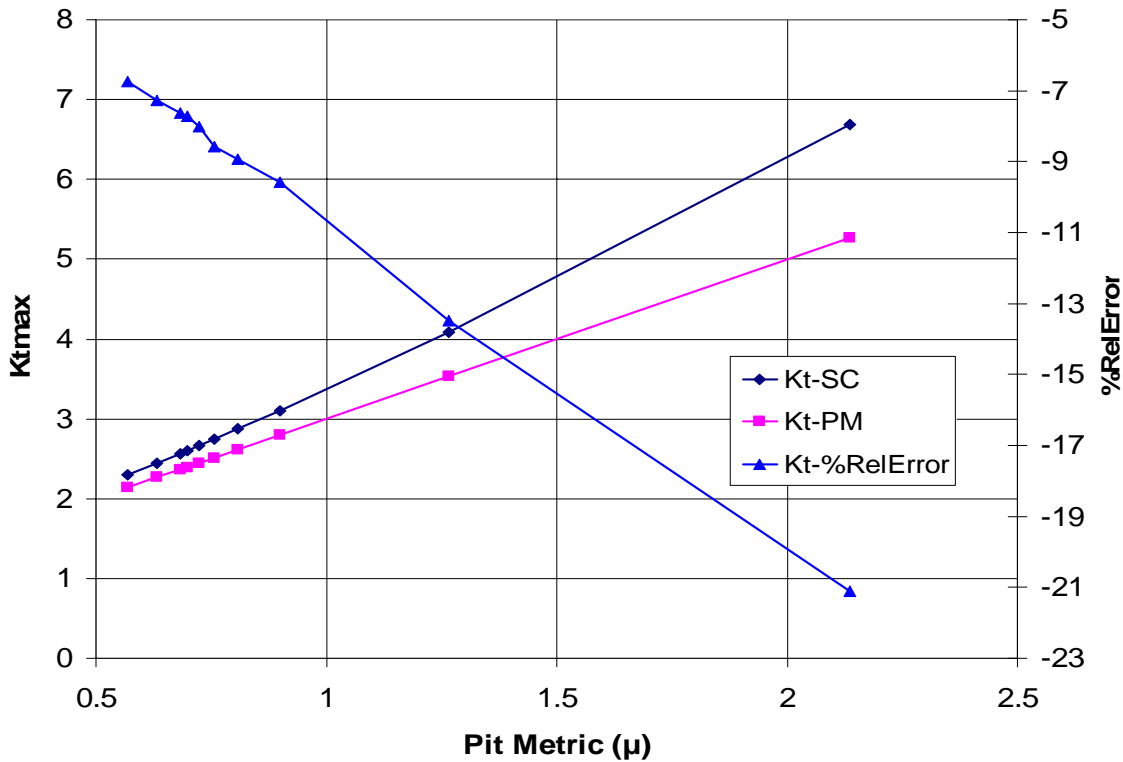
Figure 62. Original Pit Metric Kt

Representative pit dimensions were used in this investigation. These dimensions were defined by averaging the H, W, and D observed in fractographic analysis of corrosion-fatigue AF1410 specimens. See Table 3 for the representative pit dimensions used.

Single Pit Loaded in the "H" direction			
W/2	0.0415	mm	
H/2	0.0375	mm	
D	0.044	mm	

Table 3. Representative Pit Dimensions

In order to assess the behavior of K_t for variable μ , the pit metric, the dimensions H and D in Table 1 were varied parametrically such that μ varied between approximately 0.5 and 2.0. The results of the original pit metric K_t versus the StressCheck FEA K_t are given in Figure 63.

**Figure 63. Pit Metric K_t (Pink) versus StressCheck FEA K_t (Navy)**

As can be observed from the figure, the relative error is between 7 and 10 percent for the pit metric range of interest, which is $0.5 < \mu < 1.0$, and the FEA K_t is considerably underestimated by the pit metric K_t . There is also a one-to-one correspondence between K_t and μ . The range of interest is defined through observation of corrosion pits at the crack initiation region for each specimen. It is noted that the error continues to increase monotonically as the pit metric is increased. It was proposed, then, to modify the original pit metric K_t such that it more closely approximates the FEA results. Based on simple fitting techniques, the following modification is proposed and given in Figure 64:

$$K_t = 1 + 2\mu \quad \Rightarrow \quad K_t^* = 1 + \alpha\mu + \beta\mu^2$$

$$\left. \begin{array}{l} \text{Proposed} \\ \text{Fitting} \\ \text{Parameters} \end{array} \right\} \begin{array}{l} \alpha = 2.1 \\ \beta = 0.27 \end{array}$$

Figure 64. Proposed Modification to Pit Metric Kt

The modification to the original pit metric Kt, or Kt*, uses the alpha parameter to linearly scale the pit metric Kt by an additional 10%, then uses the beta parameter to slightly modify the pit metric Kt for a small nonlinearity in the FEA results. This beta parameter may not be necessary as it has a noticeable effect outside of the range of interest for the pit metric only. The modified pit metric Kt* versus the StressCheck FEA Kt is shown in Figure 65.

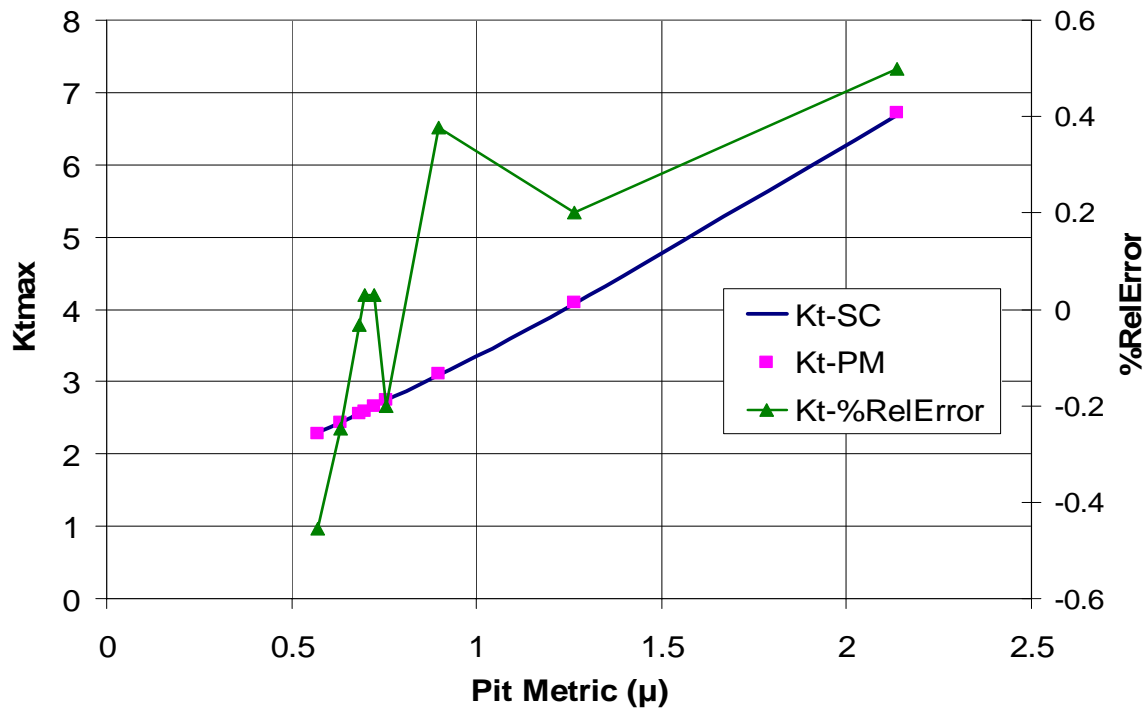


Figure 65. Modified pit metric Kt* (Pink) versus StressCheck FEA Kt (Navy)

As can be observed in Figure 65, a much better correlation between the two techniques exists.

An investigation was performed to determine how well the modified pit metric Kt* approximated the StressCheck FEA Kt for a sample pit case. Using measurements from a CI (crack initiation) pit in specimen 15 as the case study, the following indicates a good result: the StressCheck Kt and the modified

pit metric K_t^* differ by less than 1%, while the original pit metric K_t differs by ~10% (see Figure 66 for comparison).

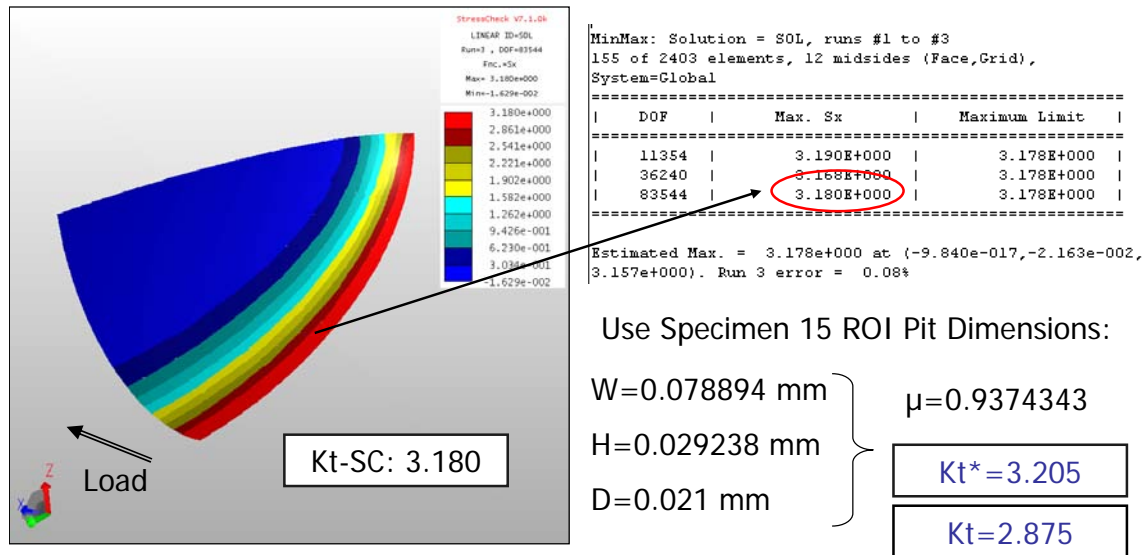


Figure 66. Results from Modified Pit K_t^* Validation Study

6.4.2f Effect of Orientation on Ellipsoidal Feature K_t

In July 2006, NAVAIR proposed a modified formula for the pit metric K_t in which the orientation of the pit relative to the load is taken into account. The formula accounting for this effect is given below in Figure 67:

$$K_t(\theta) = K_{t-90^\circ} + (K_{t-0^\circ} - K_{t-90^\circ}) |\cos \theta|$$

Figure 67. Pit Metric $K_t(\theta)$

An arbitrary ellipsoidal pit was selected and modeled in StressCheck. Then, the orientation of the pit relative to the load was varied such that the angle was between 0 and 90 degrees. The results of the orientation affected pit metric $K_t(\theta)$ versus the StressCheck FEA $K_t(\theta)$ are given in Figure 68.

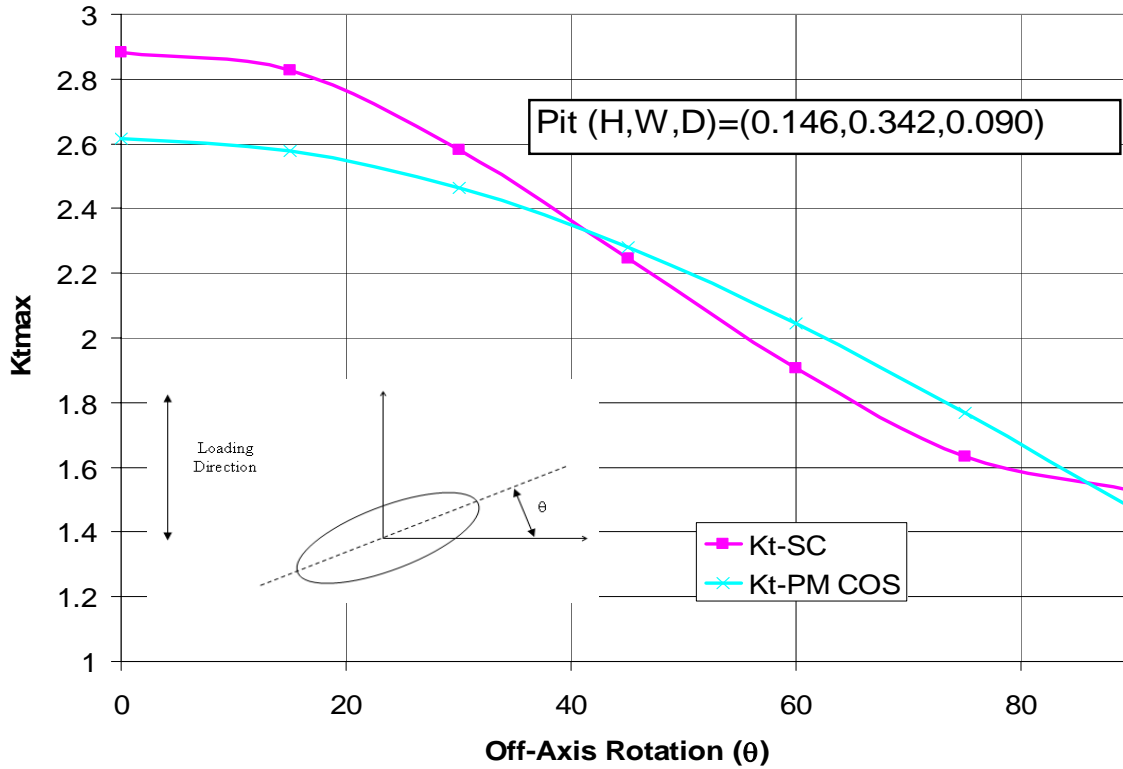


Figure 68. Pit Metric $K_t(\theta)$ (blue) versus StressCheck $K_t(\theta)$ (pink)

As can be observed, the proposed formula does not adequately represent the function $K_{tmax}(\theta)$ computed with StressCheck.

In order to capture the behavior of the K_t for an elliptical feature subjected to orientations relative to the load, an elliptical term ($\cos^2(\theta)$) was proposed instead of the original orientation term ($\cos(\theta)$). The revised formula is given in Figure 69 as:

$$K_t^{revised}(\theta) = K_{t,90} + (K_{t,0} - K_{t,90}) \cos^2 \theta$$

Figure 69. Revised Pit Metric $K_t(\theta)$

For the same StressCheck FEA $K_t(\theta)$ results shown in Figure 68, plotting the revised orientation affected pit metric $K_t(\theta)$ yields the following (Figure 70):

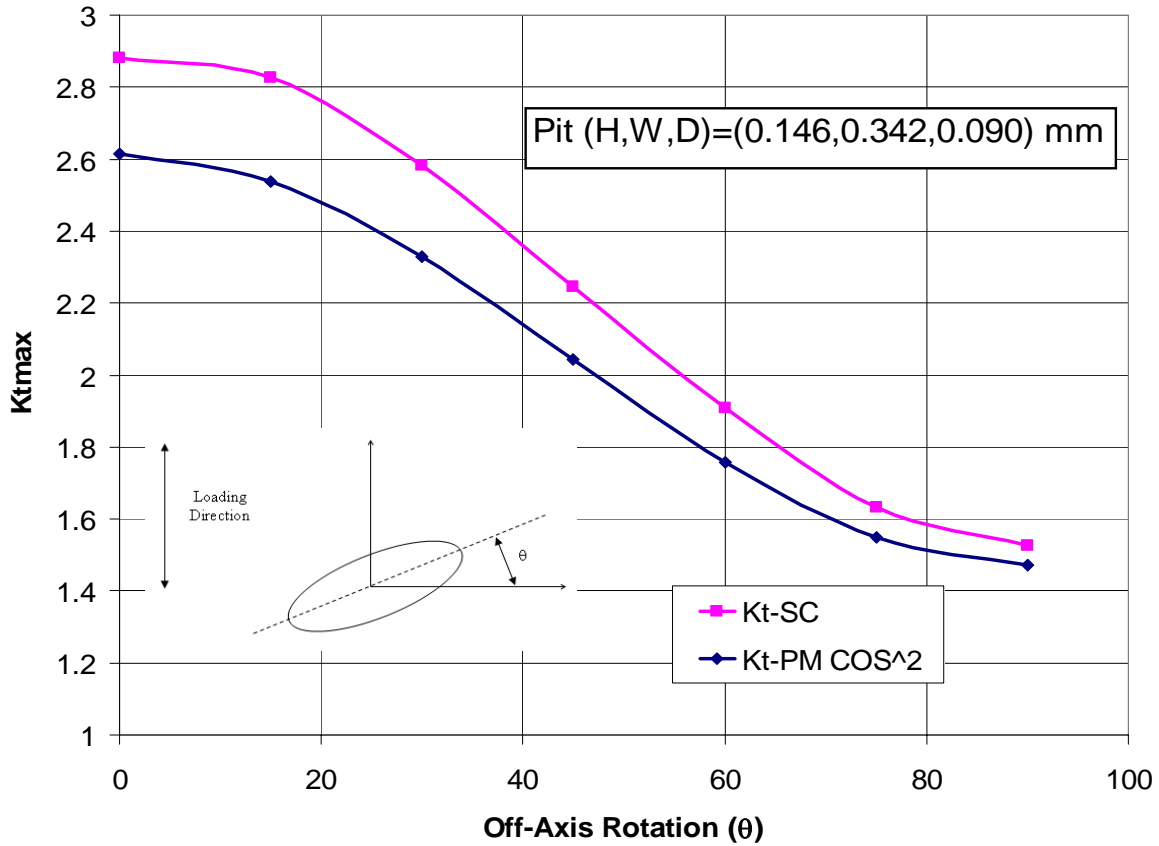


Figure 70. Revised Pit Metric $K_t(\theta)$ (blue) versus StressCheck $K_t(\theta)$ (pink)

It is apparent that the revised formula describes the general shape of the StressCheck FEA $K_t(\theta)$. However there still exists a considerable error between the two results for each off-axis rotation value. It will be shown that by incorporating the modified pit metric K_t^* into the expression given in Figure 69, a much better correlation can be observed. Figure 71 shows the appropriate modifications to the revised pit metric $K_t(\theta)$, and Figure 72 shows the resulting behavior.

$$K_t^{revised*}(\theta) = K_{t,90}^* + (K_{t,0}^* - K_{t,90}^*) \cos^2 \theta$$

Figure 71. Revised Pit Metric $K_t^*(\theta)$

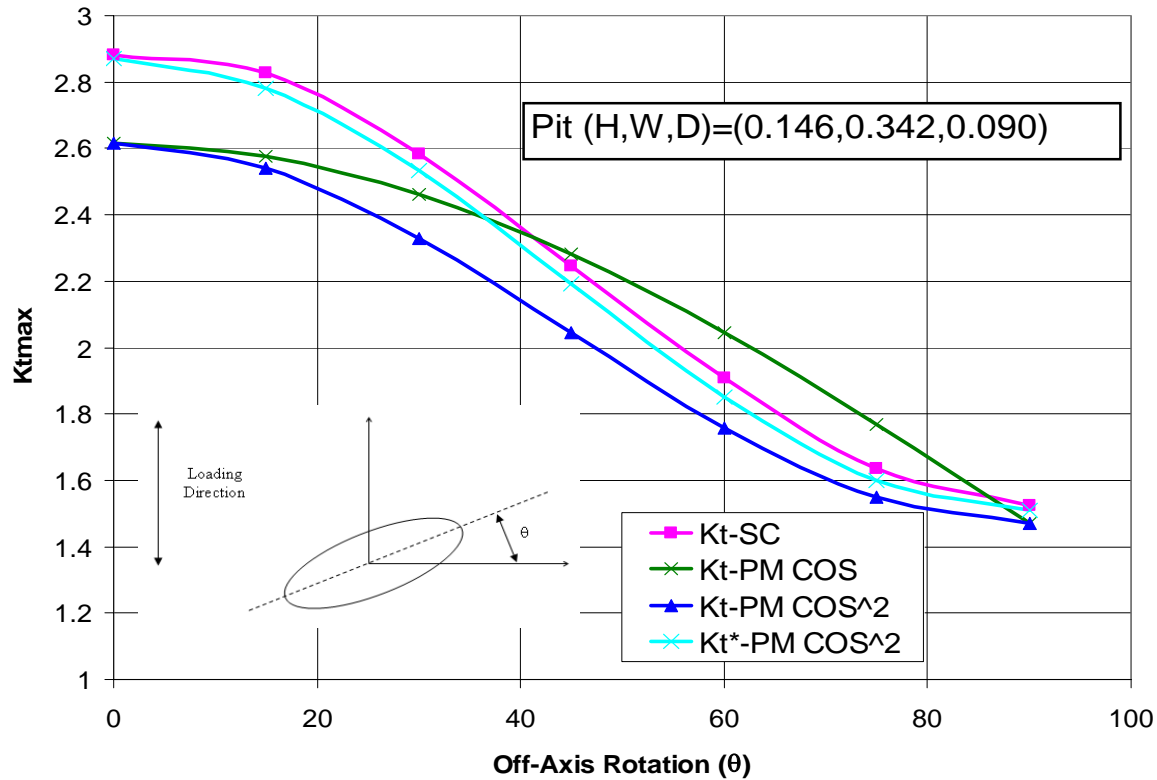


Figure 72. Final Summary of StressCheck FEA $K_t(\theta)$ and Proposed Pit Metric $K_t(\theta)$'s

The revised formula, using $K_t^*(\theta)$, is shown in Figure 72 (light blue). As can be observed, the behavior most closely approximates the StressCheck FEA $K_t(\theta)$.

6.4.2g Effect of Biaxial States of Stress on K_t for Single Pit Configurations

A study was performed for several pit cases, each with a different pit metric μ , to determine the influence of biaxial stress states (σ_1, σ_2) on the maximum K_t . The range of pit metric values was $0.54 < \mu < 1.0$, which appears to be a practical range based on known information regarding pit dimensions identified through fractographic examinations. Two loading types were incorporated in order to determine the boundary condition effects on the K_t :

- 1) Applied tractions: $-1.0 < \sigma_2 / \sigma_1 < 1.0$
- 2) Imposed displacements for the $\mu=1.0$ case: $-1.0 < S_{2avg} / S_{1avg} < 1.0$, where S_{2avg} and S_{1avg} are the average tractions on the element faces receiving the u_2 and u_1 imposed displacements.

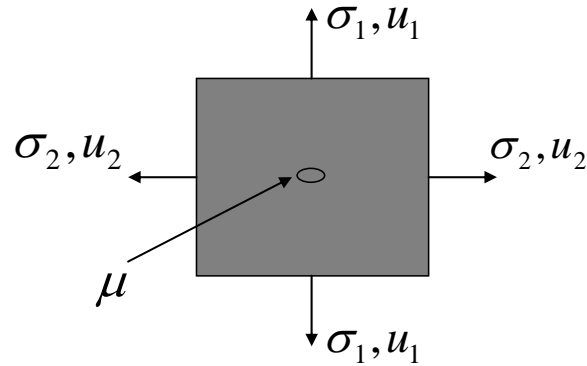


Figure 73. Biaxial Stress/Displacement for Pit Configuration

The load case in which biaxial applied tractions were used to supply loading information to the model incorporated four (4) different configurations of pits to generate four (4) different μ values. The results for the applied traction cases are shown in Figure 74. The load case in which imposed displacements were used to supply equivalent loading information to the model incorporated the pit configuration such that $\mu=1.0$. The results for the imposed displacement case are shown in Figure 75. The influence of biaxial states of stress is significant when the ratio σ_2/σ_1 is negative but small when the ratio is positive.

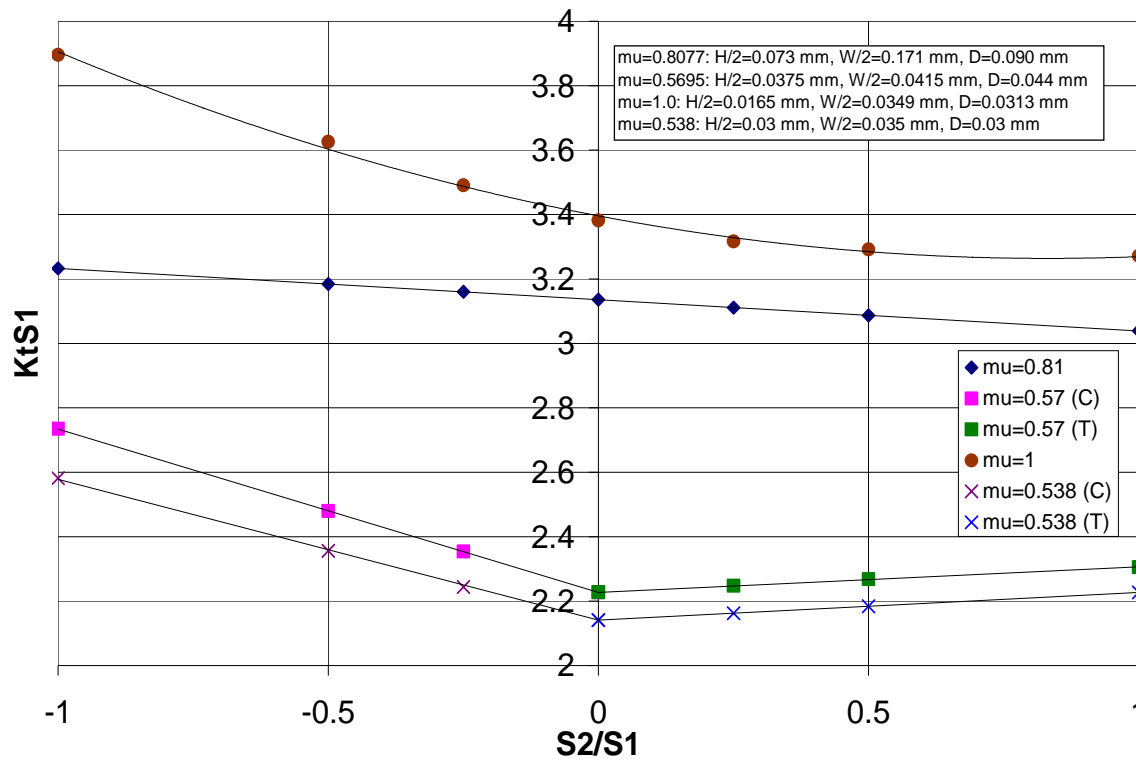


Figure 74. Kt Results Summary of Biaxial Applied Traction Load Case

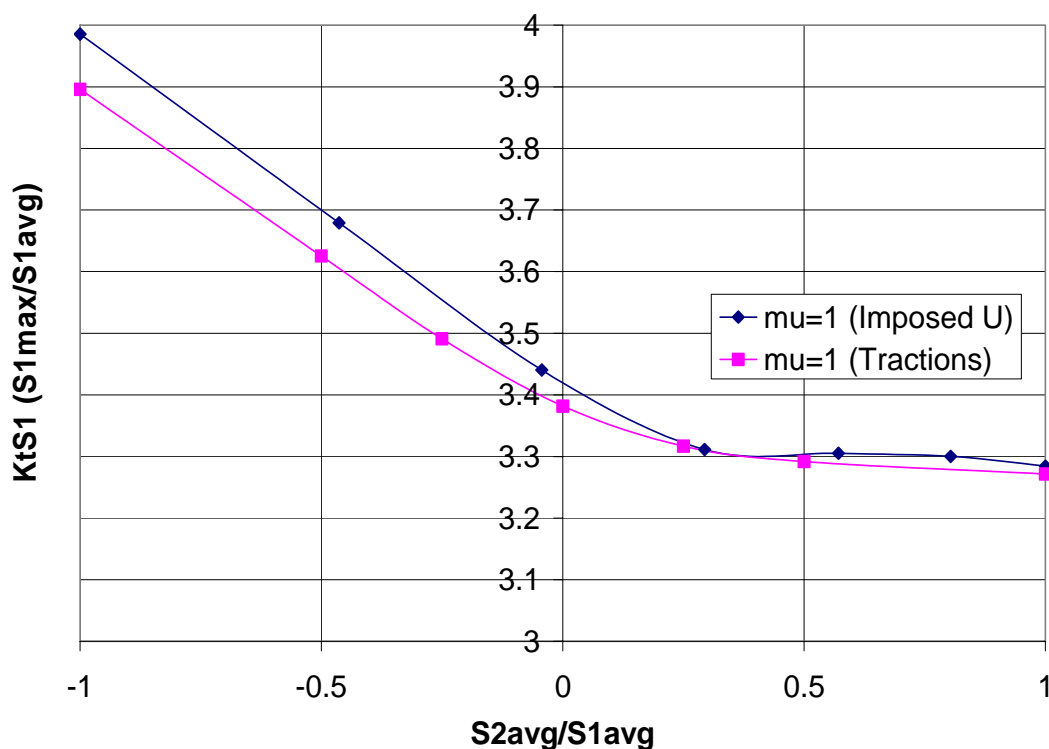


Figure 75. Kt Results Summary for Biaxial Imposed Displacement Load Case for $\mu=1.0$

6.4.3 Summary

ESRD proposed a modification to the current UDRI pit metric, which helped to calibrate the metric so as to account for orientation effects. This updated UDRI pit metric was then applied to a model problem with ellipsoidal geometry. Additionally, the effects of biaxial stress states were studied and it was seen that when both of the applied stresses are tensile then the effects are insignificant. This is expected to be the case for most applications of AF1410 parts.

7. Plan for Deployment

ESRD is engaged in the development of a framework for the distribution the corrosion assessment technology developed under this project to the USN and its subcontractors, utilizing the COM and Java interfaces of StressCheck[®]. The COM and Java interfaces are to provide a convenient communication protocol that integrates the necessary functions of other applications (e.g. MATLAB probability and statistical functions). The development of simple-to-use Windows desktop and web-based (or cross-platform) applications is envisioned. Web-based deployment of StressCheck capabilities is employed in [Web Book](#), which has been updated to use StressCheck 7.1 technology. These desktop and web-based (or cross-platform) applications comprise the StressCheck FEA Toolkit. A description of the StressCheck FEA Toolkit was given in the final technical report submitted in 2005⁷.

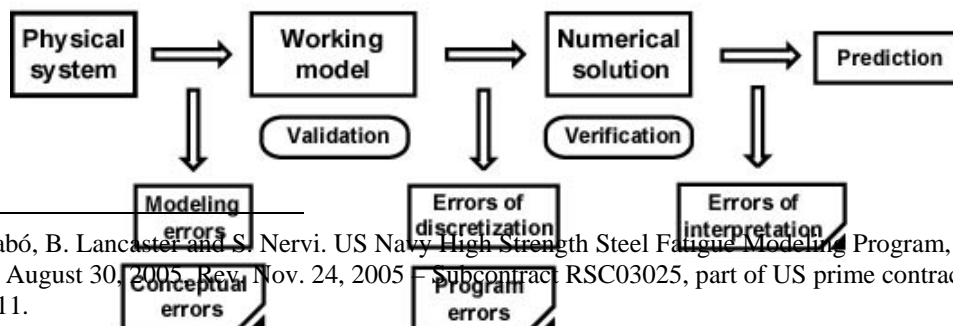
8. Summary

At the close of the third year of the USN High-Strength Corrosion Fatigue Modeling Program progress can be reported in the following areas: (a) Performed surface metric analyses for available WLI representations of corroded AF1410 Set A specimens, (b) performed preliminary investigations for an alternative life prediction method based on linear elastic fracture mechanics, (c) developed an experiment with the primary objective aimed at controlling errors in K_{teff} resulting from non-traceable surface approximation errors, (d) calibrated and validated the UDRI pit metric to verified StressCheck results for a range of pit metric values, e) incorporated appropriate orientation effects into the calibrated UDRI pit metric, and f) developed a working prototype for the implementation of Statistically Variable Non-Linear Material Properties into StressCheck.

9. Recommendations for Future Work

It was pointed out in the final technical report submitted in 2005⁷ that estimation of fatigue life expended (FLE) for high strength steel (HSS) structural components based on the pit metric-based model required validation. A general outline of the process of validation was presented by the PI to the project group at the meeting held at NAVAIR (Patuxent River) on October 28, 2005. The flowchart showing the main elements of predictions based on computed information is reproduced in Figure 76. The purpose of validation is to test the predictive capabilities of a mathematical model. There is an extensive literature on validation and verification. A selected list of references can be found in the Appendix (Section 10.3).

The main point is that the proposed model, called working model, is based on the assumptions that the effective stress concentration factor (K_{teff}) is a predictor of the number of loading cycles that will cause the first appearance of a 0.01-inch crack. As noted in Section 5, this implies the assumptions that (a) heterogeneities occurring in the material do not contribute to crack initiation, only the averaged properties of the heterogeneities are important; (b) corrosion progresses along a sharp front and (c) the essential features of corroded surfaces that determine the critical value of K_{teff} can be identified with sufficient accuracy for the purposes of life estimation and with a high probability of success.



⁷ B. Szabó, B. Lancaster and S. Nervi. US Navy High Strength Steel Fatigue Modeling Program, Final Technical Report, August 30, 2005. Rev. Nov. 24, 2005. Subcontract RSC03025, part of US prime contract No. F42620-00-039-0011.

Figure 76. The main elements of numerical simulation and the associated errors.

It is useful to view mathematical models as operators that transform one set of data (the input) into another set (the output). In the present case the input set consists of topological data, material properties and a load spectrum, the output is the predicted number of load cycles that cause a 0.01 inch crack to appear. Validation experiments are designed to test the predictive capabilities of a mathematical model. Validation involves a metric and a criterion. In our case the metric is the number of load cycles preceding the first occurrence of a 0.01 inch crack. The criterion is a range of cycles within which the prediction must lie if the model is to meet necessary conditions for acceptance. The criterion depends on the intended use of the model and therefore it must be set by NAVAIR on the basis of operational considerations. If the predictions are within an acceptable range then the model passes the validation test, i.e., it meets certain necessary conditions for acceptance, if not, then the model must be rejected.

The fatigue testing of the micro-machined specimens can be viewed as validation experiments in the following sense: The micro-machined specimens satisfy assumptions (a) to (c) enumerated above. It is not known whether the corroded specimens do. Therefore tests of the micro-machined specimens will in fact indicate whether the assumptions incorporated into the model based on the UDRI pit metric hold or not. Since calibration is based on corroded specimens, substantial differences between predicted and observed cycles in the micro-machined specimens would mean that one or more of the assumptions (a) to (c) do not hold and therefore the model would have to be rejected.

We note that there are substantial differences in size between the features of the micro-machined specimens and corroded specimens: The typical depth of the features in the micro-machined specimens is 0.035 inches (889 μm) whereas the typical depth of the corrosion features is $\sim 2.76\text{e-}3$ inches (70 μm), an order of magnitude difference. Since the K_t -based prediction was established for specimens with much larger notch radii, the prediction would not be outside of the scope of the model.

10. Appendix

The following appendix contains extended content relevant to Study 6.2.2b (ECS method) and Study 6.1.2e (Local RMS). Additionally, files and documents relevant to the Probabilistic Material Properties Implementation and Micro-machining geometry as well as an example StressCheck 7.1 input file of a characteristic pit case will be made available on a CD enclosed with this report.

10.1 Additional ECS Post-Diction Results for AF1410 Set A Specimens

Some additional ECS post-dictions (“predictions” made after a known experimental outcome) for AF1410 Set A corroded specimens are presented in the following tables (Table 4 and 5) and figures (Figures 77-80). The post-dictions were made for Specimens 16, 59, 22, and 56. The term “nuke” implies the cycles to crack nucleation/initiation (non-differentiable in this case).

Specimen	Stress (ksi)	Exposure hrs	Measured Crack Nucleation (cycles)	Measured Total Life (cycles)	WLIM Measured ECS mm	WLIM Measured ECS in.
16	200	6	17580	27896	0.037	0.0014567
59	180	6	41029	57766	0.017	0.0006693
22	180	12	28271	39651	0.035	0.0013780
56	165	12	31979	45140	0.0227	0.0008937

Table 4. Equivalent Crack Size (ECS) Computed from # of Cycles to Crack Nucleation

Specimen	Stress (ksi)	Exposure hrs	Measured Crack Nucleation (cycles)	Measured Total Life (cycles)	Predicted Crack Init. (cycles)	Predicted Total Life (cycles)
16	200	6	17580	27896	14185	26292
59	180	6	41029	57766	34526	49517
22	180	12	28271	39651	20471	37178
56	165	12	31979	45140	37809	58459

Table 5. Crack Initiation and Total Life Cycles, Measured and Predicted

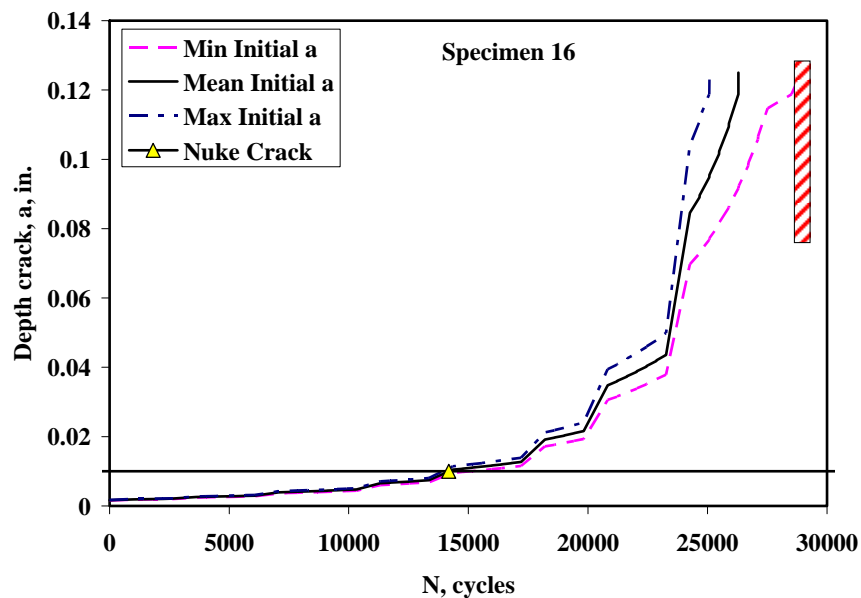


Figure 77. ECS Method Post-Diction for Specimen 16

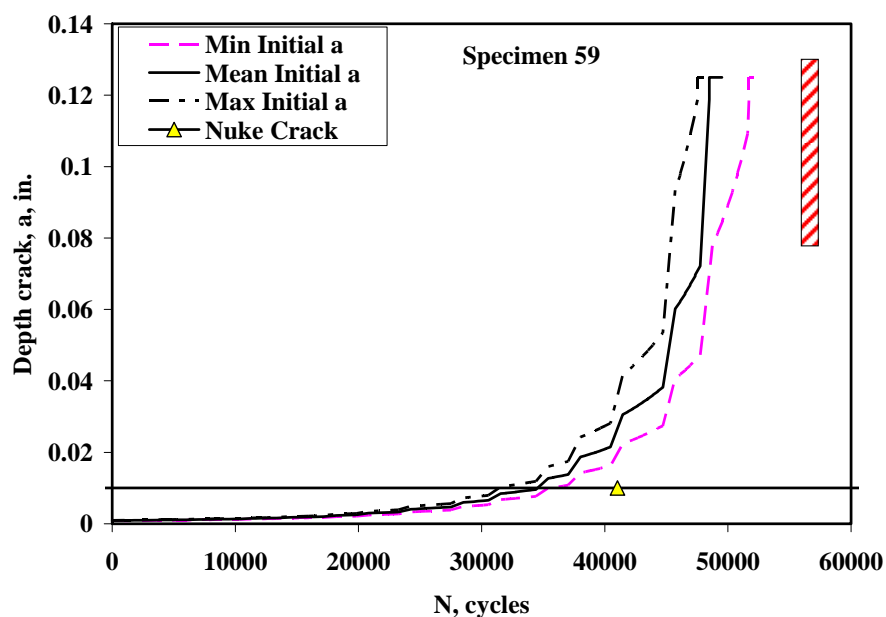


Figure 78. ECS Method Post-Diction for Specimen 59

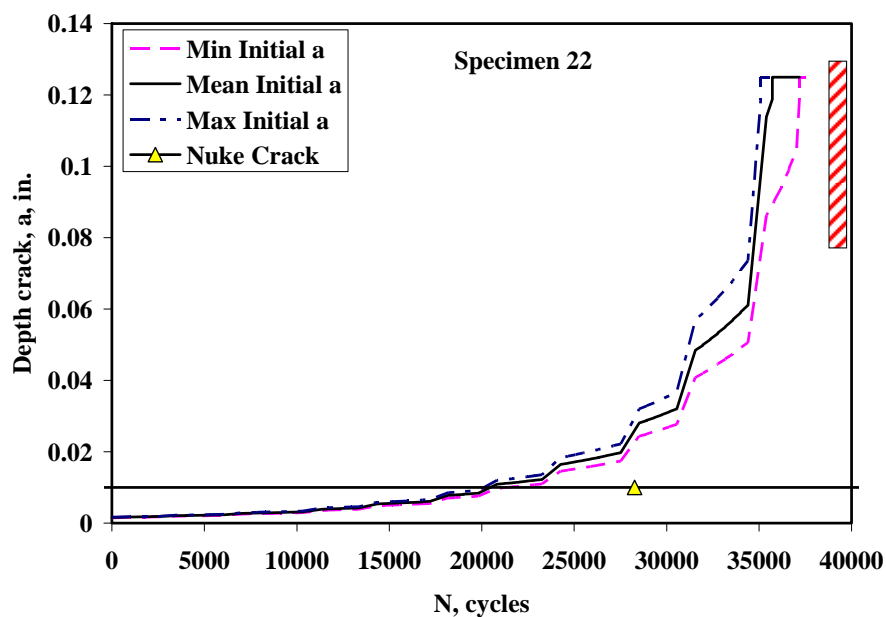


Figure 79. ECS Method Post-Diction for Specimen 22

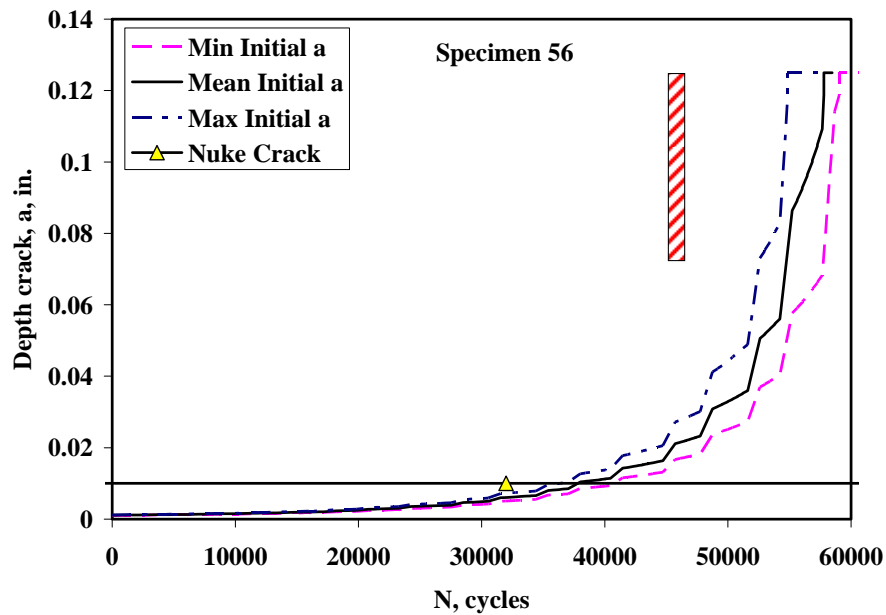


Figure 80. ECS Method Post-Diction for Specimen 56

The four available ECS post-dictions corresponding to the four corroded specimens (16, 59, 22, and 56) were normalized with respect to their actual experimental lives. This normalization is shown in Figure 81. C/E refers post-diction life divided by experimental life.

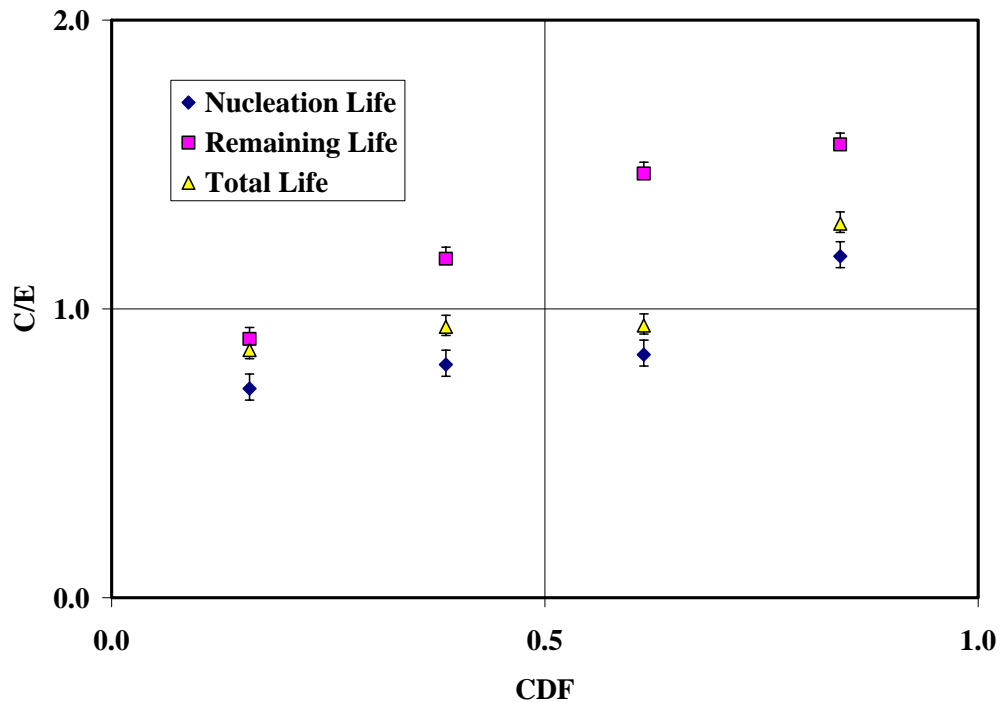


Figure 81. Normalization of Computed (Post-Diction) Lives with Experimental Lives

10.2 Case of Misleading Local RMS Prediction for Crack Initiation Location

For AF1410 Set A Specimen #5, which was corroded for six (6) hours, the location of crack initiation could not be determined with confidence from the Local RMS mapping of the surface. Figure 82 below shows the crack initiation location for this specimen.

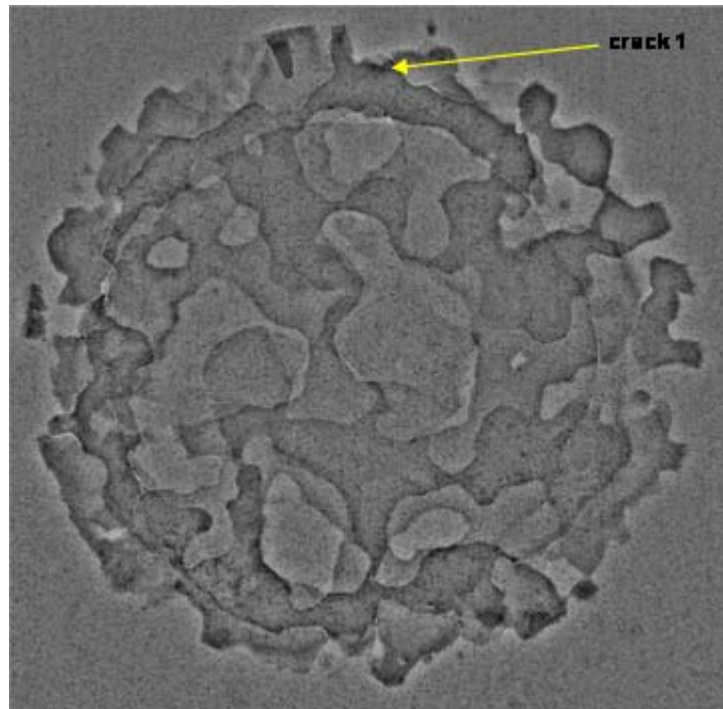


Figure 82. AF1410 Set A Specimen #5 Crack Initiation Location

A Local RMS extraction was performed for the Specimen #5 WLI data, using 50000 sample locations with an RMS window size of 30 by 30 pixels, and it was found that the crack initiation location was not visibly apparent. There are quite a few candidates for crack initiation in this case, none of which appear to be strongly favoring the crack initiation site. In this case, perhaps the orientation of the feature was highly influential to crack initiation. The results for the Local RMS extraction are shown in Figure 83.

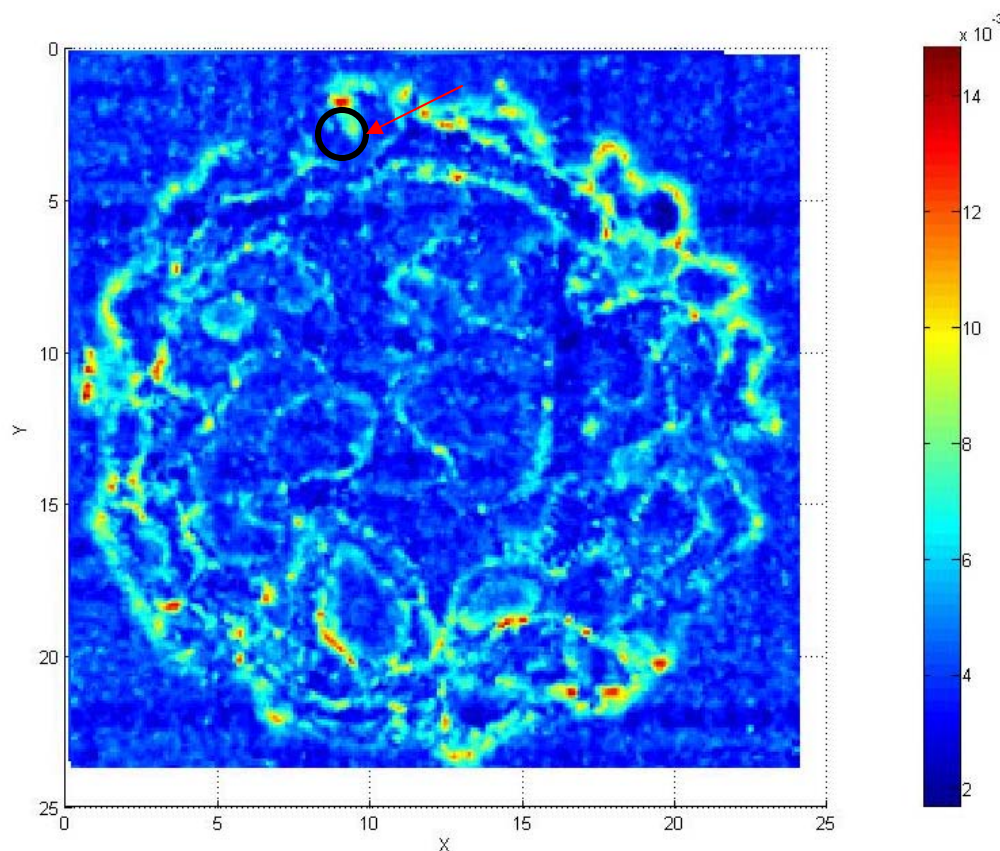


Figure 83. AF1410 Set A Specimen #5 Local RMS Extraction

10.3 Selected References on Verification and Validation

Roach, P. J. *Verification and Validation in Computational Science and Engineering*, Hermosa Publishing, Albuquerque, 1998.

Trucano, T. G., Swiler, L.P., Igusa, T., Oberkampf, W. L. and Pilch, M. Calibration, validation and sensitivity analysis: What is what. *Reliability Engineering and System Safety* **91** (2006) 1331-1357.

Oberkampf, W. L. and Barone, M. F. Measure of agreement between computation and experiment: Validation Metric. *Journal of Computational Physics* **217** (2006) 5-36.

Post, D. E. The coming crisis in computational science. Los Alamos National Laboratory Report LA-UR-04-0388, 2004.

Babuška, I. and Oden, J. T. The reliability of computer predictions: Can they be trusted? *International Journal for Numerical Analysis and Modeling*. **1** (2005) 1-18.

Szabó, B. Validation of working models with StressCheck®. ESRD Technical Brief 01/02/07, St. Louis, 2007.

Appendix B

ESRD StressCheck® Implementation Report

ESRD Final Technical Report FY2006
Deliverable Item #3
StressCheck Implementation for Statistically Variable Material Properties
June 28, 2007
Document Prepared By: Brent Lancaster

1. Introduction

ESRD implemented variable coefficients for material properties for linear and nonlinear isotropic materials into StressCheck. For linearly elastic materials the modulus of elasticity and Poisson's ratio can be defined by functions of the spatial variables specified either in the local or global coordinate systems. For elastic-plastic materials additional coefficients can be formula-based: the yield strength, the Ramberg-Osgood parameters, etc. The formulae can be defined internally in StressCheck, or can be provided through external function calls. In the latter case StressCheck will pass the formula name and the global coordinates to the external function and receive the corresponding values of the coefficients. The external function call is implemented in Windows OCX so that the user may write a subroutine in Visual Basic and communicate with StressCheck without having to re-compile or re-link. This required modification of the element stiffness matrices, load vectors and extraction (i.e., post-processing) procedures. The Windows OCX functionality is ready for testing, and ESRD is waiting for NAVAIR to provide a set of test cases that demonstrate these enhanced capabilities of StressCheck.

In the past year, however, NAVAIR requested ESRD to provide a means to use COM enabled functionality to communicate formulae from Matlab to StressCheck instead of using the existing Windows OCX approach. These formulae may be in any form, but in this case polynomial expressions based on least square (L2) fitting of pseudo-random distributions were used. The goal was to demonstrate the capability to interpret these formulae as StressCheck material properties, assign these properties to elements, and solve for a set of boundary conditions. A process map of the desired goal of generating and interpreting probabilistic material properties is shown in Figure 1. A basic guide for using the functionality is included in this document.

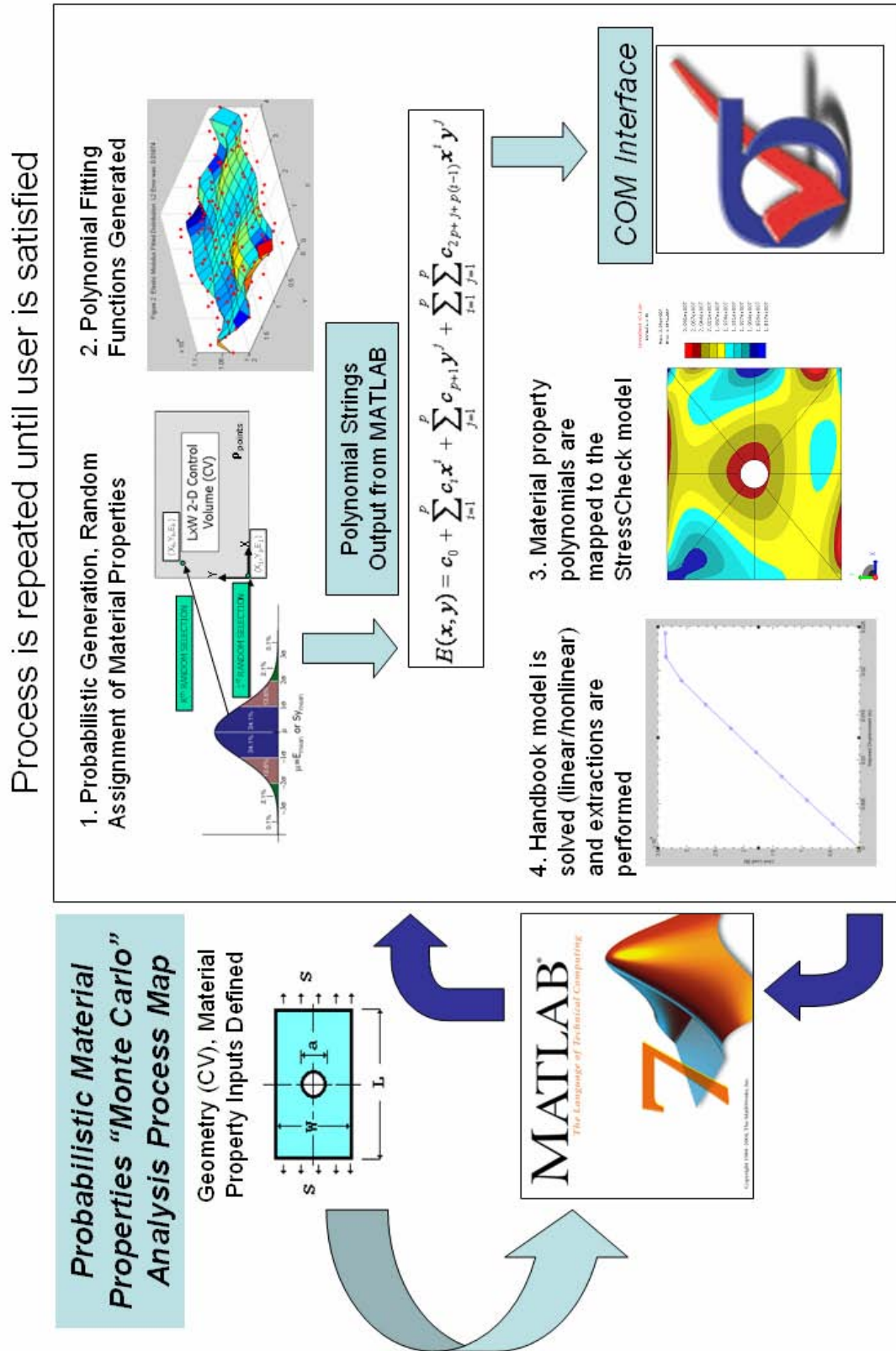


Figure 1. Process Map for the Probabilistic Material Properties Prototype

2. Instructions for the Usage of the Probabilistic Material Properties Prototype

The functionality has been tested for the StressCheck model: “Rectangular Plate with a Central Hole in Tension”. The instructions for using the functionality are given below.

I. Limit Load Analysis of a Rectangular Plate with Central Hole

The purpose of this study is to determine the effect of probabilistically generated material property distributions on the ultimate strength of the part. An imposed displacement is applied to the quarter-symmetric StressCheck model and the magnitude of the imposed displacement is incremented during the nonlinear analysis until the limit load is reached. The rules and guidelines implied by the current implementation of the process are given by the following:

Guidelines/Rules

1) Input Files/Scripts

- a. MATLAB M-files
 - i. Control Script (matlabcontroller.m)
 - ii. Probabilistic Material Property Generation Script (genmatlfunc.m)
 - iii. Probabilistic Distribution Script (randraw.m). This M-file must be located in the MATLAB Toolbox directory, and the Toolbox should be updated
- b. StressCheck 7.0.6c Input File
 - i. This is the StressCheck input file corresponding to the MATLAB control script parameter values (i.e. Plate Width, Height, Mean Elastic Modulus, Yield Stress, etc.)

2) Compatibility Considerations

- a. The MATLAB geometric dimensions (control volume) must encompass the StressCheck model geometry. The MATLAB script was written for problems in planar elasticity only.
- b. While the location of the StressCheck database may be arbitrarily defined in the MATLAB control script, the location of the StressCheck input file must be specifically defined.
- c. The extractions performed using the MATLAB control script must be pre-defined in the corresponding StressCheck input file. The StressCheck input file has several post processing and solution settings saved.

3) Before Running the Control Script...

- a. Skim over the comments to ensure that the process will perform as desired
 - i. Geometric inputs are consistent with StressCheck model?
 - ii. Material properties are defined as desired?
 - iii. Solutions/Extractions are consistent with Handbook settings?

Appendix B: ESRD StressCheck Implementation Report

- b. Modify the database and input file locations to meet local system requirements
- c. Make sure all active StressCheck sessions have been terminated

The appropriate MATLAB files and StressCheck input files will be made available on a CD to be enclosed with this document.

3. Summary

The requirements of this deliverable have been adequately fulfilled according to NAVAIR. However, additional guidance is expected for future work in this area.

Appendix C

Boeing Final Report

HIGH STRENGTH STEEL CORROSION - FATIGUE MODELING

Final Report ***Subcontract RSC06014***

S. J. Easley, A. L. Neal, K. K. Sankaran and H. G. Smith, Jr.

The Boeing Company
St. Louis, Missouri

August 2007

Final Report for the Period August 2006 – August 2007

Table of Contents

	Page
Table of Contents	C-2
Acknowledgments	C-3
1. Introduction	C-4
2. Micro-machining of AF 1410 Steel Specimens	C-7
3. Fractography of Fatigue Specimens with Micro-machined Features	C-9
4. Corrosion Metric Development	C-12
5. Software Verification	C-19
References	C-22

Acknowledgments

The effort described in this report was sponsored by the University of Dayton Research Institute (UDRI) under subcontract no. RSC06014 (August 2006 – August 2007). Mr. Wally Hoppe was the Technical Monitor at UDRI. The following Boeing personnel worked on this project: Mr. Albert Neal (Program Manager), Dr. K.K. Sankaran, Dr. Herb Smith, Jr and Mr. Sam Easley. Other Boeing participants included Mr. Gary Weaver, who performed the scanning electron microscopy. The other team members mentioned in this report are the Naval Air Systems Command (NAVAIR) and Engineering Software Research and Development Inc (ESRD).

1. Introduction

1.1 Overall Program Background

Corrosion increases the stress in an airframe part by reducing the effective cross sectional area of the structure carrying the load. Corrosion also causes stress concentrations, which can result in premature fatigue crack initiation. Therefore, the presence of corrosion reduces fatigue life and can result in greater risk of component failure. The prevention and repair of corrosion is a major maintenance cost for the U.S. Armed Services.

Corrosion-fatigue modeling and analysis are essential to determining the impact of corrosion on structural integrity. Efforts have focused principally on aluminum alloy applications and more recently on steel alloys (Reference 1). This report documents the results of the Boeing effort between August 2006 and August 2007 under Subcontract RSC06014, which is part of a high strength steels corrosion-fatigue modeling program conducted by UDRI. Boeing's efforts under the earlier subcontracts covered the following tasks and have been described in References 2 and 3.

1. Assisting UDRI in corrosion simulation, exposure and characterization procedures including specimen preparation and masking to avoid crevice corrosion.
2. Characterizing the magnitude of corrosion on specimens provided by UDRI by laser profilometry and spot check measurements using microscopy.
3. Determining the adequacy of laser profilometry to obtain valid corrosion metrics for use in life prediction models and developing software tool to provide these metrics.
4. Examining the laser profilometry data obtained previously and performing a comparative statistical and probabilistic fatigue life prediction analysis to determine the efficacy and adequacy of using this technique.
5. Defining the requirements for finite element analysis methods, which use the metrics to calculate stress concentrations caused by corrosion. These stress concentrations shall be applicable in fatigue life analysis procedures.
6. Identifying aircraft parts that have corroded in service, defining issues involved in correlating various corroded parts removed from in-service aircraft and selecting an in-service part for component testing with UDRI/USN concurrence.
7. Developing plans for testing the in-service parts and gathering of corroded and non-corroded parts for use in simulation tests.

These activities supported the overall program goal to quantify corrosion and conduct sufficient tests to obtain lives from specimens with various levels of corrosion. Presently different and inconsistent definitions of corrosion exist. The approach is to determine K_t 's and distributions/grouping of K_t 's and to analytically accomplish the following:

- Define corrosion categories with respect to Kt grouping
- Define characteristics for each corrosion category
- Correlate NDI signals to corrosion metrics, and
- Develop maintenance plans/practices/processes based on categories

1.2 Subcontract RSC06014 (August 2006 – August 2007)

The Boeing's company's SOW under subcontract RSC06014 (August 2006 – August 2007) included

1. Perform fracture analysis on corroded and failed corrosion-fatigue specimens to determine number of cycles to crack initiation (0.010 inch crack). No more than 20 specimens to be provided by NAVAIR or UDRI.
2. Identify crack initiation sites on corrosion-fatigue specimens. No more than 20 specimens will be provided by NAVAIR or UDRI.
3. Provide engineering support to NAVAIR, UDRI and ESRD to develop and evaluate corrosion metrics.
4. Characterize corrosion on Aeromet 100 components to compare to corrosion characteristics of AF1410 components. Boeing is to acquire the Aermet 100 components if sufficient funds and task priorities allow.
5. Provide information on 300M component corrosion history. Boeing to acquire 300M components for white light interference microscopy measurements if sufficient funds and task priorities allow.
7. Support AF1410 fatigue tests of micro-machined specimens including the micro-machining of selected micro-features in a number of specimens (not more than 30 specimens) and including preparation of the surfaces prior to micro-machining.

As a result of customer driven priorities, the statement of work for this contract changed in February 2007 to the following.

1. Perform fracture analysis on corroded and failed corrosion-fatigue specimens to determine number of cycles to crack initiation (0.010 inch crack). No more than 10 specimens to be provided by NAVAIR or UDRI. Specimens are expected to be provided to Boeing no later than 15 April 2007.
2. Identify crack initiation sites on corrosion-fatigue specimens. No more than 10 specimens will be provided by NAVAIR or UDRI. Specimens are expected to be provided to Boeing no later than 15 April 2007.
3. Provide engineering support to NAVAIR, UDRI and ESRD to develop and evaluate corrosion-fatigue models including a sensitivity study, model verification and life prediction from corrosion metrics.

5. Support AF1410 fatigue tests of micro-machined specimens including the micro-machining of selected micro-features in a number of specimens (not more than 10 specimens) and including preparation of the surfaces prior to micro-machining.

2. Micromachining of AF1410 Steel Specimens

The Mini mill used for micromachining was tuned for the small steel parts. The fixture to hold the part during the milling process was designed and fabricated. The micromachining tool is shown in Figure 2-1. The steel dog bone specimen is held in place by a triangular shaped magnetic fixture.



Figure 2-1 Micromachining Tool

The NC program was written to include part setup, machine work envelope settings, cutting tool parameters and the use of a 0.030 inch diameter ball nose roughing tool and a 0.010 inch diameter ball nose finishing tool. The larger tool is used to perform the roughing and the smaller tool is used to finish the larger surface features and to create and finish the smaller features. The .030 inch diameter tool runs for about 10 minutes and the 0.010 inch diameter tool runs for about 40 minutes. Each part takes about 1 hour to setup and mill.

Figures 2-2 shows the AF 1410 steel specimen in the fixture after the machining is completed and Figure 2-3 shows the set up to monitor the progress of machining.

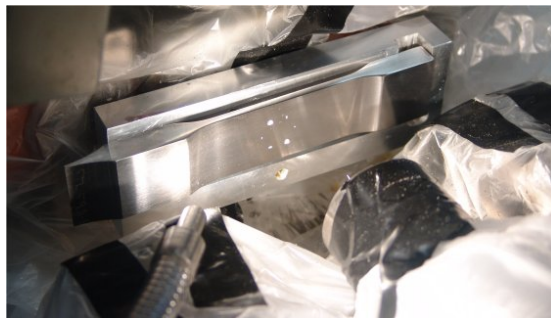


Figure 2-2 Micromachined AF 1410 Steel Specimen



Figure 2-3 Monitoring of Micromachining

Ten AF 1410 steel specimens were micro-machined with the features schematically shown in Figure 2-4, and provided to UDRI for profilometry and fatigue testing.

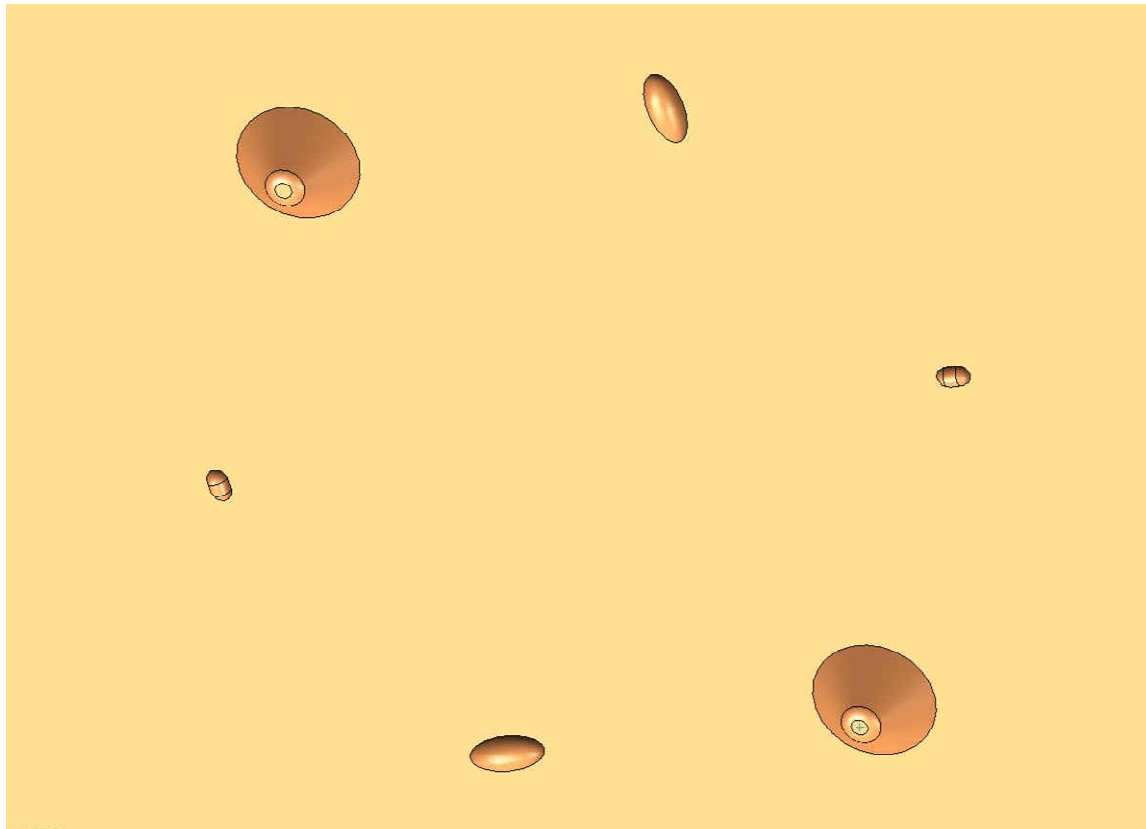


Figure 2-4 Micro-machined Features on AF 1410 Steel

3. Fractography of Fatigue Specimens with Micro-machined Features

Twelve AF 1410 fatigue specimens tested at 200 ksi maximum stress were provided by UDRI. Three of the specimens (baseline) had no micro-machined features and nine had such features. Quantitative fractography using scanning electron microscopy was performed on these specimens with the objective to determine the number of cycles to initiate a 0.01” size flaw.

The data from the fractography of one of the specimens (designated 598-3) is shown in Figures 3-1 and 3-2. Fracture in all of the nine micro-machined specimens resulted from a crack that originated in one of the two conical features as shown in Figure 3-1. In all of the micro-machined specimens, significant growth also occurred in the crack that initiated from the other conical feature. It is expected that the four other micro-machined features also would have initiated cracks, but these are not in the fracture plane and therefore not visible.

The complete set of fractographs for all the twelve specimens from which cycles for initiating a 0.01 in. (254 μ m) were estimated are provided in a CD form along with this report. The crack initiation life data for these specimens is shown in Table 1. Introduction of the micromachined feature reduces the lives by an order of magnitude, suggesting that such features could be useful in assessing the effects of corrosion on fatigue lives.

(Specimens 598-4, 598-11 and 598-14 are the baseline specimens with out micro-machined features)

Specimen Number	Crack Initiation at 254 microns (Cycles)
598-1	6,567
598-2	3,300
598-3	4,371
598-4	83,467
598-5	5,760
598-8	4,660
598-9	5,700
598-10	3,100
598-11	80,212
598-12	4,700
598-13	6,502
598-14	49,374

Table 1 – Initiation lives for 0.01 in. crack

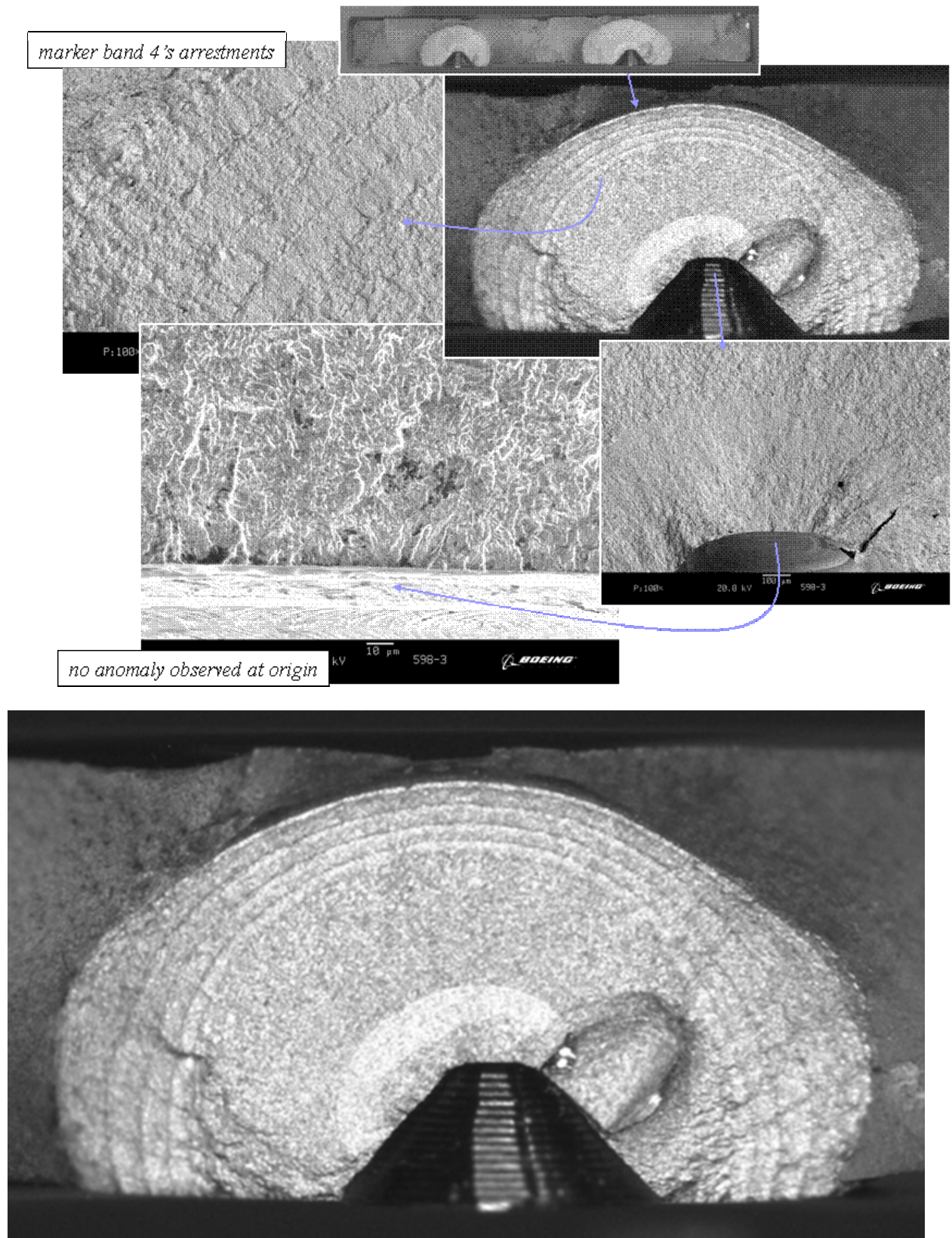


Figure 3-1 Fracture Surface of Specimen 598-3

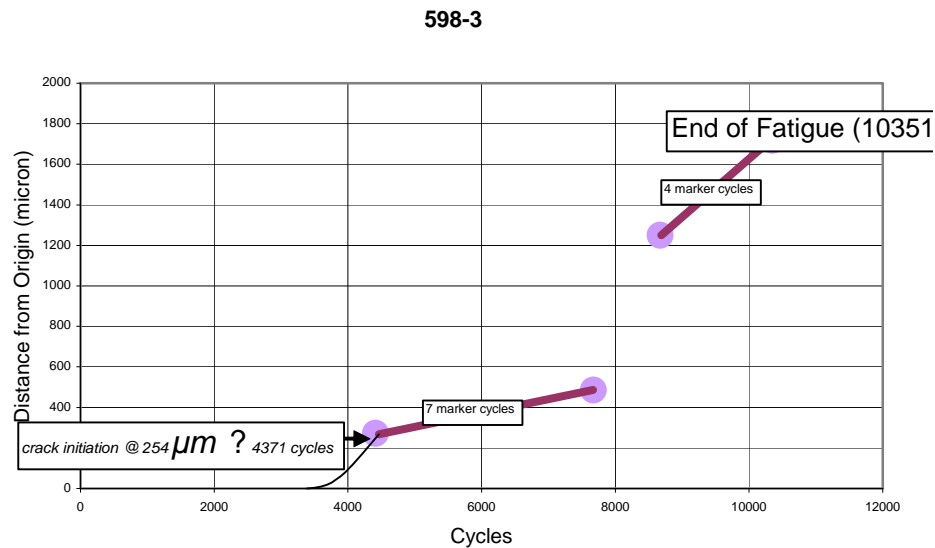


Figure 3-2 Crack Advance Determined from Fractography for Specimen 598-3

4. Corrosion Metric Development

4.1 Initial Metric Development

In light of the potential that the roughness measurements seem to hold and on our previous work with pitting in aluminum, we have been evaluating the corrosion profilometry data to determine the possibility of developing a metric based loosely on the previous technique and using the roughness measures. The primary focus of this initial investigation has been the average roughness, Ra.

Roughness data for each of the scanned images, concentrating on the interior of the corrosion area was used in this effort. This prevents the roughness from being biased either by the smoother, uncorroded area outside the circular corrosion, or the edge of the circle which seems to have a slightly more aggressive pattern perhaps due to the proximity of the atmosphere.

In addition, the data was plotted and analyzed for individual stress levels, as the life will depend on the stress level and the initial goal was to determine a metric based purely on the geometry of the corrosion irrespective of the stress level. Plots of the Life versus Ra for each stress level are shown in Figures 4-1 through 4-4. The figures are for stress levels of 160 ksi, 165 ksi, 180 ksi, and 200 ksi respectively. In constructing these plots, any specimen that failed from an initiation site other than in the corroded area or that broke at the grips were not included.

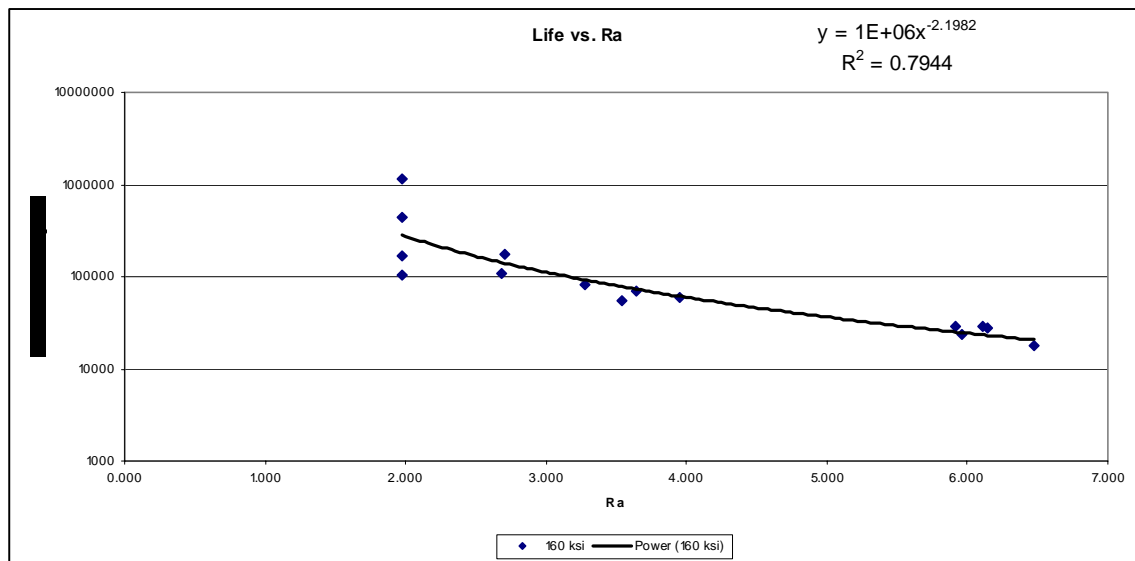


Figure 4-1. Life versus Ra for 160 ksi.

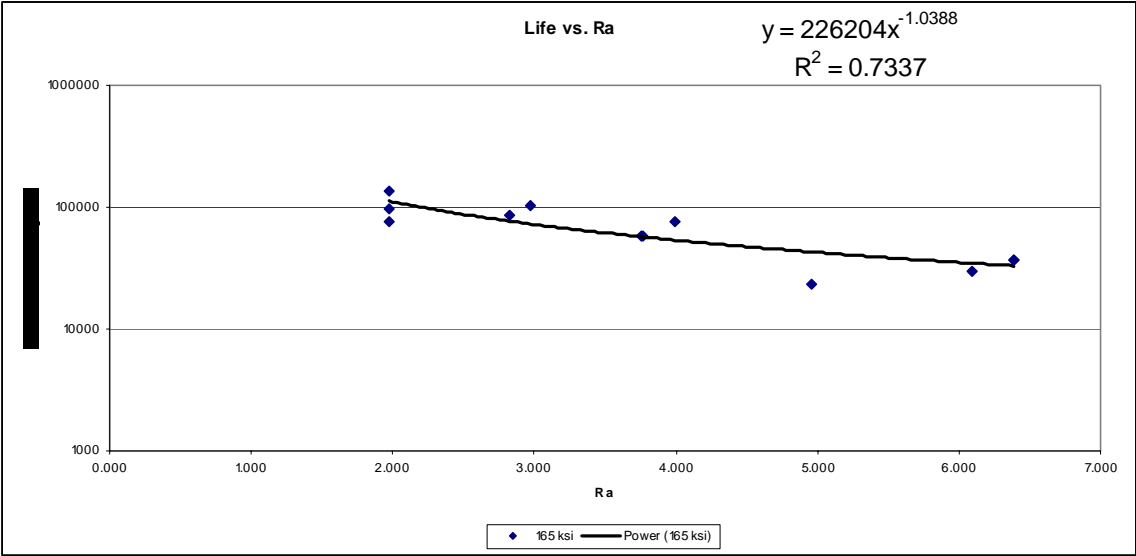


Figure 4-2. Life versus Ra for 165 ksi.

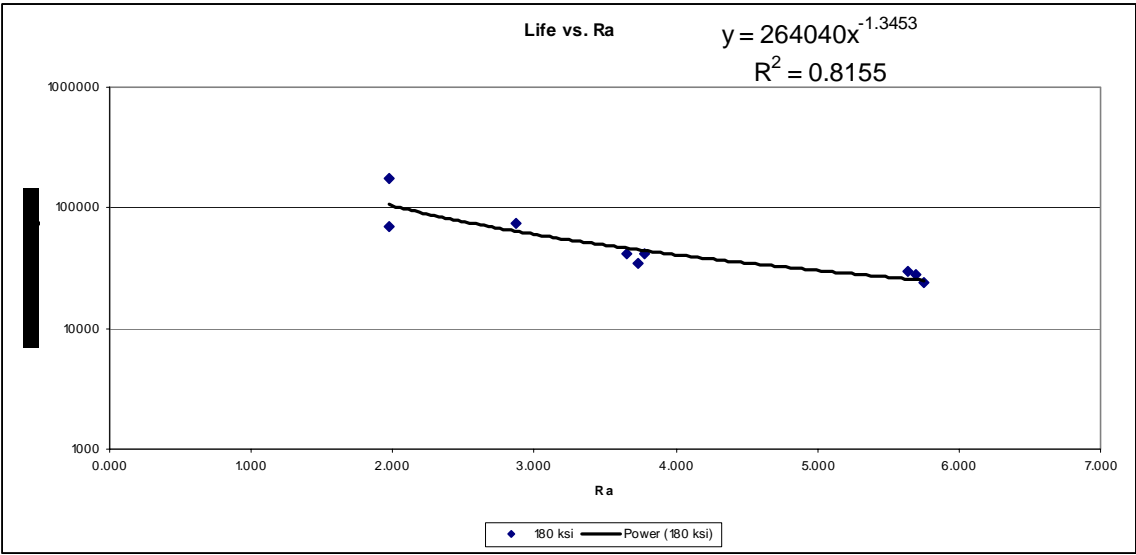


Figure 4-3. Life versus Ra for 180 ksi.

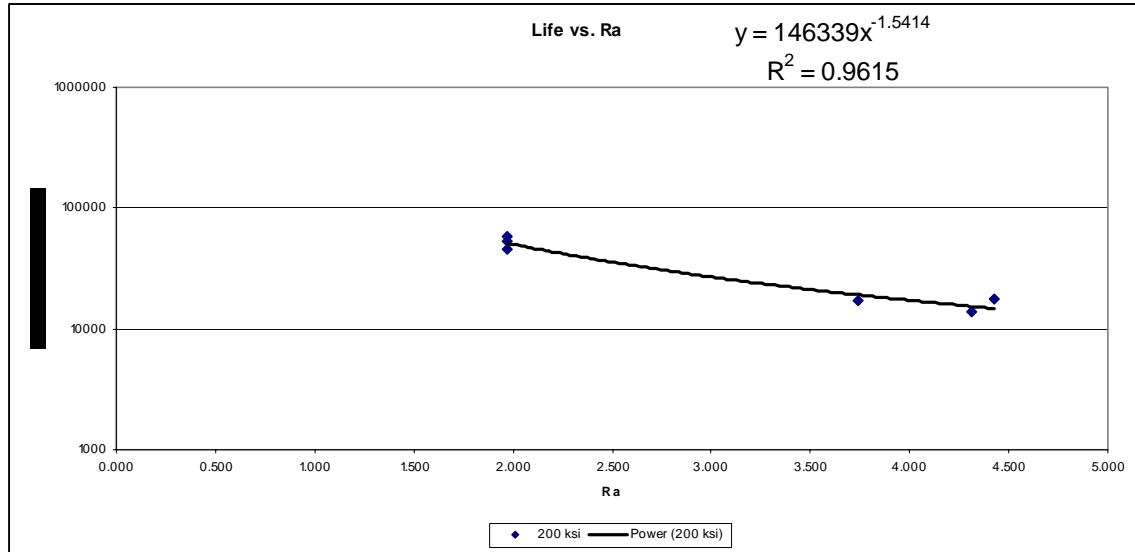


Figure 4-4. Life vs. Ra for 200 ksi.

Before proceeding further with the analysis of the data, several comments are worth noting. First, the baseline specimens (no corrosion) did not have profilometry scans made of their surface. In light of that, we made roughness measurements of the uncorroded portions of all the other coupons and computed an average uncorroded roughness. This value was 1.97. All baseline lives were plotted at that number, which is clearly an issue on the plots. The distribution of baseline roughness measurements varies from 1.41 to 2.42, so clearly some error is introduced as a result of this assumption. Profilometry scans have been made of all the AF1410B baseline specimens and the baseline specimens for AF1410A material have been sent to UDRI and will have scans done very soon. It is worth noting that there is very little difference in the roughness values from the baseline specimens and the 3 hour specimens.

Second, there is very little data in the 200 ksi group thus the behavior is less well defined than the other stress levels. Third, there are very few repetitions at the various roughness levels for each stress value, thus there is no ability to define the statistical scatter in the lives to any meaningful level of significance at this point.

Given these limitations, it can be seen that the overall behavior is very similar and a summary of the power curve coefficients to the trend line fits is shown below, where

$$y = A x^B$$

Stress	A	B
160	1.00E+06	-2.12
165	226204	-1.04
180	264040	-1.35
200	146339	-1.54

The values show some inconsistency, particularly with the data for the 165 ksi specimens, which is believed to be due to having a small data set and the fact that we do not currently have the correct values for the baseline coupons. We will be working to enhance the data set and use these curves to develop a notch factor that can be applied to a baseline curve giving the knockdown effects of the corrosion.

We will need to get laser profilometry scans of the baseline specimens to provide better definition of the baseline behavior and we also need to complete the roughness analysis for specimens 30 and 65 which will help fill in the 200 ksi data set.

4.2 AF1410B Specimen Roughness Analysis

Roughness measures for the first part of the AF1410B specimens have been obtained and evaluation has begun. We are waiting for the crack initiation lives for these specimens. We have received the profilometry scans of six of the AF1410B baseline coupons. The results of the roughness analysis of those specimens are shown in Figure 4-5.

Specimen	file	Rq	Ra	Rsk	Rku	Rv	Rp	Rt
544-6C	Center Section filtered.tif	0.76	0.61	-0.5	0.21	-4.03	2.16	6.19
545-4B	Center Section.tif	0.67	0.52	-0.86	0.84	-3.09	1.67	4.76
545-5C	Center Section.tif	0.69	0.54	-0.89	1.4	-3.18	1.86	5.04
545-7B	Center Section filtered.tif	0.23	0.19	-0.14	0.06	-3.31	0.96	4.26
545-8D	545-8D - Center Section.tif	0.25	0.18	-0.92	9.02	-4.05	5.48	9.53
547-15D	center stitch - filtering.tif	0.2	0.15	-0.46	2.16	-1.56	1	2.56

Figure 4-5 Roughness of AF1410B Baseline Specimens

It can be clearly noted that the average roughness (Ra) for these coupons is significantly smaller than for the AF1410A specimens where the uncorroded average roughness ranges from about 1.4 to 2.4. This was to be expected due to the polishing of the specimens.

The longest initiation life from the AF1410A baseline coupons was 1.14×10^6 cycles with a total life of 1.15×10^6 cycles. One of the AF1410B specimens tested at 160ksi was cycled for 2.07×10^6 cycles with no failure. This significantly longer life would make sense in light of the significantly smaller roughness measurement.

In an effort to get a more direct comparison of the corrosion-induced roughness on the life of the specimens, the average baseline roughness value of 1.97 was subtracted from all the A specimen roughness values and they were plotted with the B specimen data. The results are shown in Figures 4-6 through 4-9. Note that in one case the A-specimen 165 ksi data is plotted with the B-specimen 170 ksi data. Some errors are introduced due to this, although they were felt to be small for the illustration purposes here.

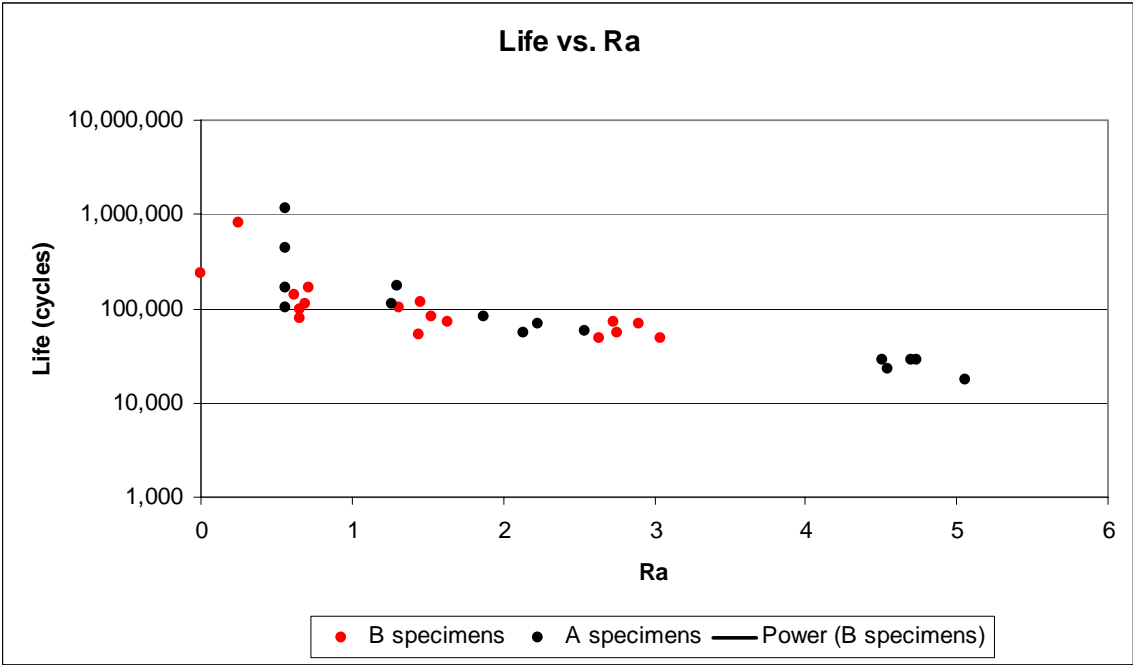


Figure 4-6. Life versus Ra for 160 ksi.

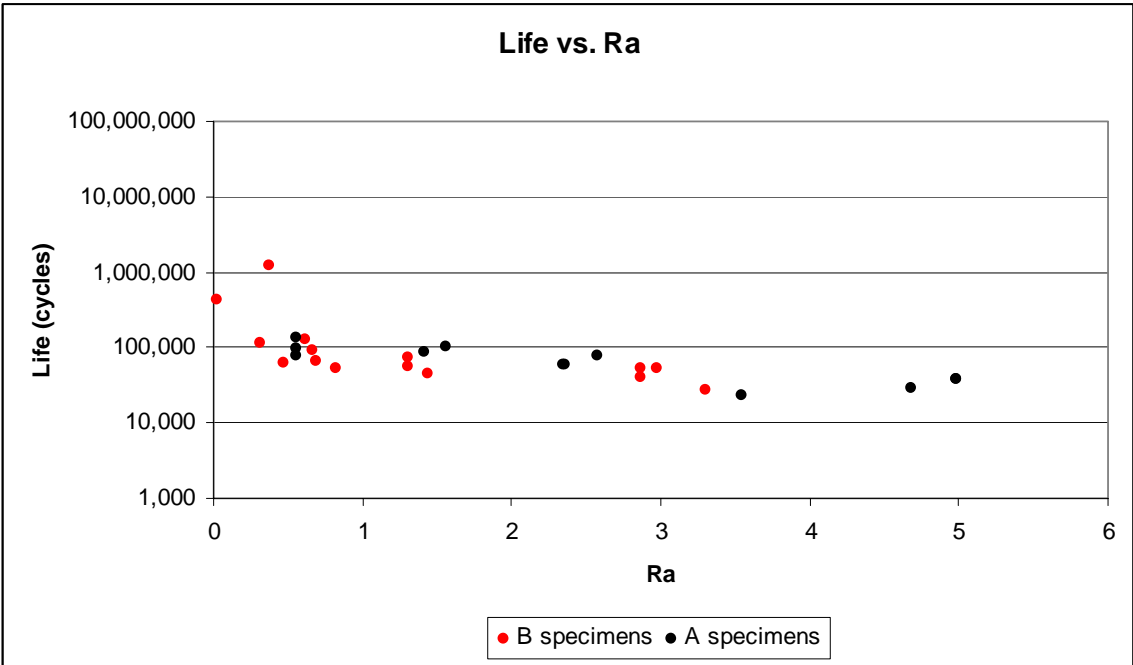


Figure 4-7. Life versus Ra for 170 (165 A specimens) ksi.

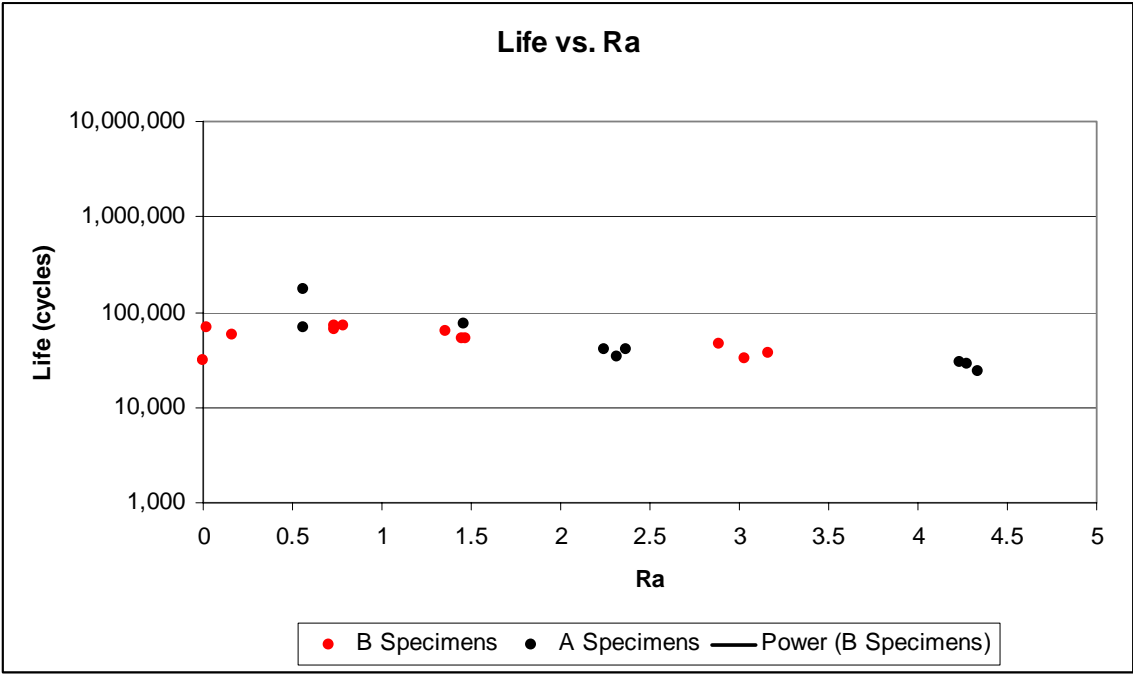


Figure 4-8. Life versus Ra for 180 ksi.

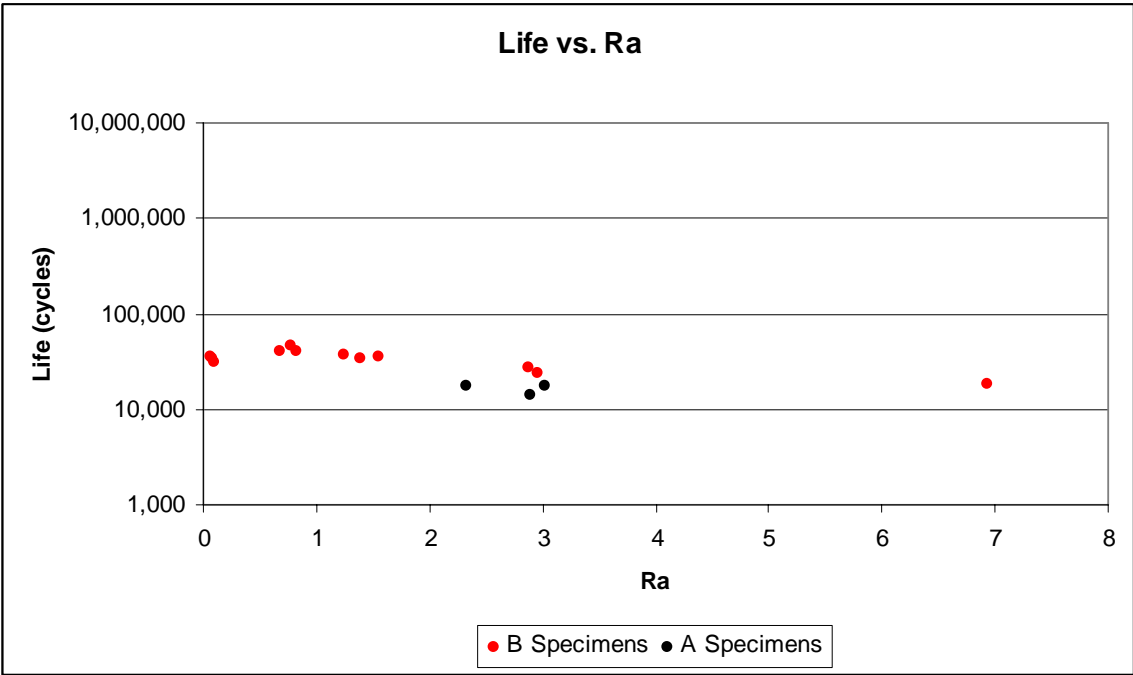


Figure 4-9. Life versus Ra for 200 ksi.

It is clear that the net effect of the corrosion on the life is the same for each stress level regardless of the underlying roughness of the specimen and that at the higher stress levels the effect tends to be neutralized, as would be expected.

Plotting the stress vs. life curves and grouping the data by ranges of roughness gives the following result shown in Figure 4-10. This shows the same pattern that was used to generate a notch factor from the aluminum pitting data. More data is required to define the endurance limit for the corroded specimens as only the baseline coupons show some significant runouts and longer lived examples. The power curve fit for each data set shows a similar behavior. Additional data would allow refinement of these fits which could then be used to establish a roughness-based notch factor.

The effects of the roughness at the lower exposure levels seems to have minimal impact on the life values for the higher stress levels. Due to customer driven priorities, this effort was terminated.

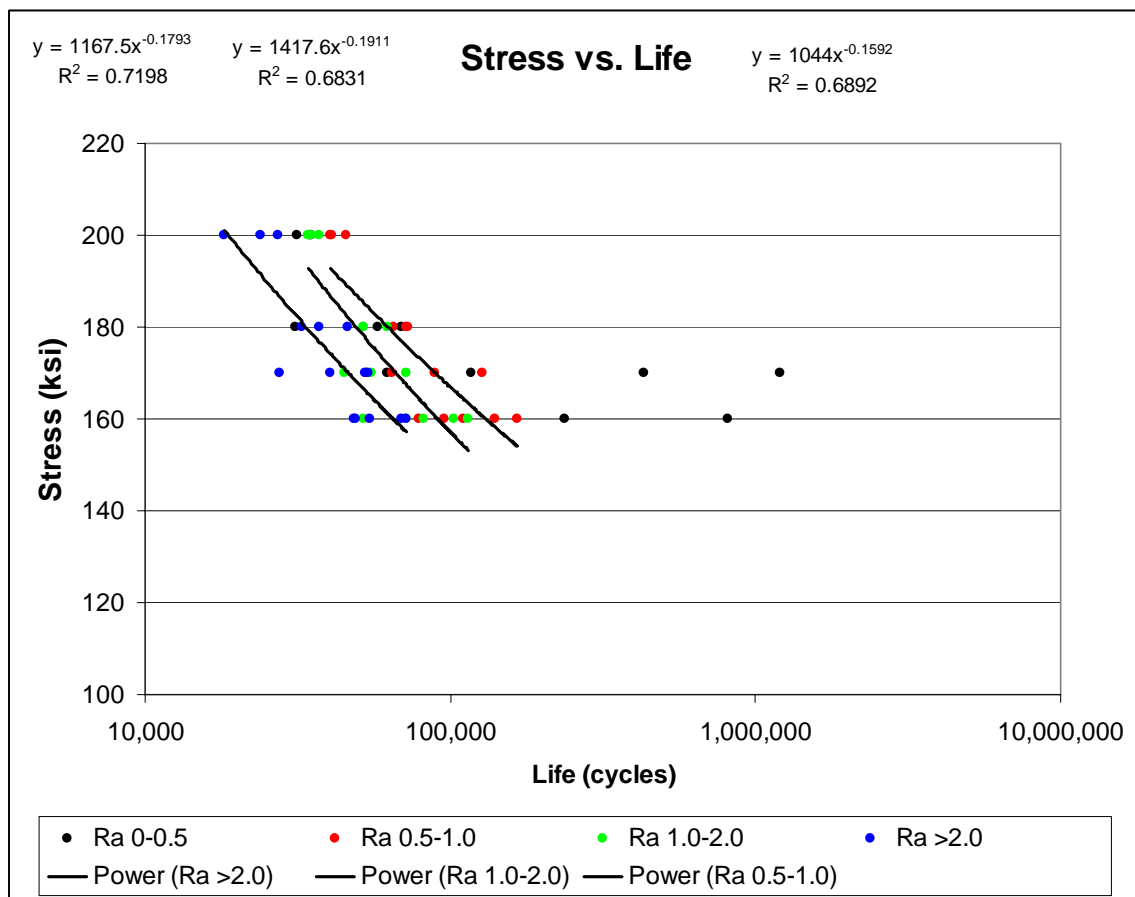


Figure 4-10. Stress vs. Life for all B Specimen Data

5. Software Verification

The list of verification tasks shown below is spread between this contract as well as RSC06048.

Code Verification: <ol style="list-style-type: none"> 1. PSL Curve to PSL Code 4. Notch Metric to ESR Life Prediction Algorithm 5. Notch Sensitivity Curve to ESR Life prediction 6. ESR Life Prediction Logic to ESR Life Prediction Algorithm 7. Roughness Metric Formulas to Roughness Metric Algorithm 8. Roughness Metric Correlation to Roughness Metric Algorithm 9. Equivalent Geometric Stress Concentration Logic to ESR Shank Life Predication Algorithm 10. Equivalent Geometric Stress Concentration Logic to Metric Shank Life Prediction Algorithm
Calculation Verification: <ol style="list-style-type: none"> 1. PSL Code to ESR Probabilistic Life Predictions 4. ESR Life Prediction Algorithm to ESR Probabilistic Life Predictions 5. Roughness Metric Algorithm to Metric-Based Probabilistic Life Predications 6. Metric Life Predication Algorithm to Metric-Based Probabilistic Life Predictions 7. ESR Shank Life Prediction Algorithm to ESR Probabilistic Life Predications 8. Metric Shank Life Predication Algorithm to Metric-based probabilistic Life Predictions 9. Shank FE model to ESR and Metric-Based Probabilistic Life Predications
Validation: <ol style="list-style-type: none"> 1. Confidence bounds on ESR Probabilistic Life Predictions <ol style="list-style-type: none"> a. Identification of sources of uncertainty b. Input uncertainty distributions c. Sensitivity analysis 3. Confidence bounds on Metric-Based Probabilistic Life Predictions <ol style="list-style-type: none"> a. Identification of sources of uncertainty b. Input uncertainty disruptions c. Sensitivity analysis 7. Confidence bounds on ESR Probabilistic Life predictions of Large Notch plate test (micromachine specimens) <ol style="list-style-type: none"> a. Identification of sources of uncertainty b. Input uncertainty disruptions c. Sensitivity analysis 10. Confidence bounds on ESR and Metric-based Probabilistic Shank Life predictions <ol style="list-style-type: none"> a. Identification of sources of uncertainty b. Input uncertainty disruptions c. Sensitivity analysis

We have been investigating the Matlab codes sent by Dave Rusk from NAVAIR. Task 1 was to compare the PSL curves generated by the code. These include the main program PSLcurveAF1410_UG02, which is a function to calculate prediction bounds for the fully reversed, AF1410 Strain-Life curve spline smoothing of inflection points UG coupons, at a 2.0% load drop, and the follow on program of Kfc_fitNeu1. The later is a function to fit Neuber

fatigue notch factor to a corrosion-fatigue marker block spectrum fatigue failure where the spectrum must have an elastic constant peak load and only two different stress-strain loops.

Strain-life data was collected for AF1410 from internal Boeing sources. This mostly consisted of stress versus cycle plots from the Aerospace Structural Metals Handbook and some random data. Data was also taken from the Lifeworks Database for AF1410.

Using the PSLcurveAF1410_UG02 code, plots have been created to address the influence of the standard normal pdf value of prediction bounds probability (k) on the strain to life curve using a elastic modulus of 27.5 Msi. This is shown in the Figure 5-1 below. The same data is plotted on a log-log scale in Figure 5-2.

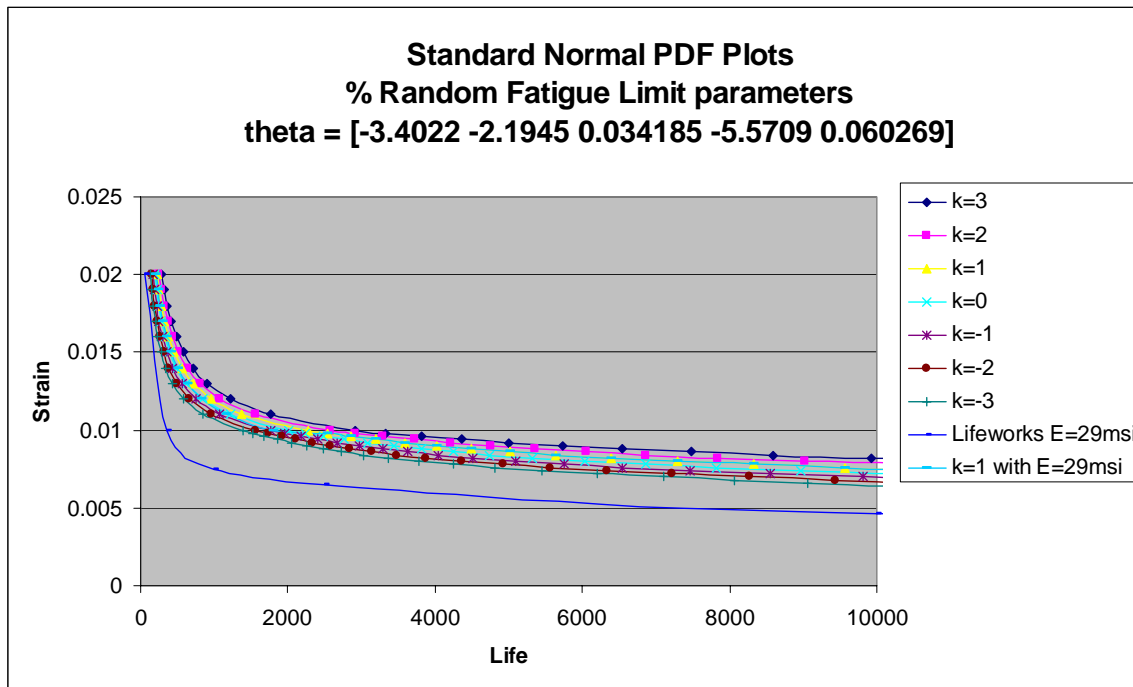


Figure 5-1. Plots of the PSLcurveAF1410_UG02 code compared to Lifeworks prediction

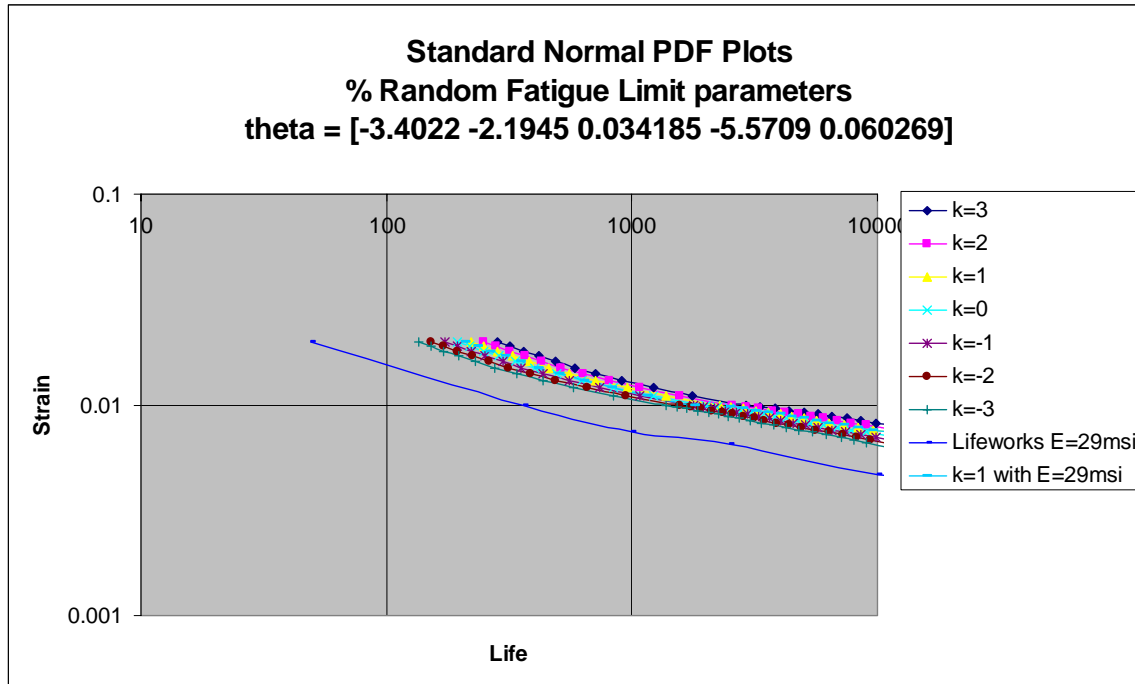


Figure 5-2. Plots of the PSLcurveAF1410_UG02 code compared to Lifeworks prediction

Whereas the code seems to produce the curves for various standard deviation values, there is a marked difference between what we would consider the nominal curve and the nominal value that is fitted to the test data. The curve predicted for the 29 Msi modulus is nearly the same as the original K=1 27.5 Msi curve, so no significant change as a result of the modulus results. The Lifeworks data is also plotted on this chart to show that the Lifeworks results do not match well with a k=1 modulus of 29 Msi curve. The Lifeworks curve is representative of the data in the Aerospace Materials Handbook and as such may represent a different product form. It is recommended that the curves generated to match the test data be used as correctly representing the coupon material behavior.

Verification of the remaining software modules that complete the ESR model will be conducted in another contract.

References

[1] Perez, R. Sankaran, K. K., and Smith, Jr., H. G. “Structural Life Enhancement -Corrosion Impact on Airframe Total Life Analysis”, The Boeing Company, Final Report submitted to NAVAIR, October 2003.

[2] Perez, R. Rich, D. Sankaran, K. K., and Smith, Jr., H. G. “High Strength Steel Corrosion-Fatigue Modeling ”, The Boeing Company, Final Report (Period January 2004 – April 2006), Sub Contract RSC03024, submitted to UDRI, April 2006.

[3] Easley, S.J., Neal, A.L., Sankaran, K. K., and Smith, Jr., H. G. “High Strength Steel Corrosion-Fatigue Modeling ”, The Boeing Company, Final Report (Period January 2004 – February 2007), Sub Contracts RSC03024 (January 2004 – April 2006) and RSC06014 (August 2006 – January 2007), submitted to UDRI, February 2007.

Appendix D

Computational Mechanics Final Report



Final Report to
UDRI
For Services Related To The Pitting Modeling
Project Tasks 1-4
Subcontract No RSC05040

Dr A. Peratta, Dr J. Baynham, Dr R. Adey

March 23rd 2006

Summary

The present document summarizes the results and methodology for the calculation of Stress Concentration factors in samples exposed to pitting corrosion. The numerical approach is based on a sub-modeling technique with the Boundary Element Method. The approach employs geometrical defeaturing of the original sampling data. Accuracy, stability and consistency of the results are assessed and shown in this report. Finally, the results for SCF in a particular sample provided by UDRI are presented.

Table of Contents

1. Introduction.....	4
2. Methodology.....	4
2.1 Summary	4
2.2 Iterative Solving Scheme.....	4
2.3 Iterative Assembly	5
3. Defeaturing technique	5
3.1. Summary	5
3.2. First defeaturing stage.....	5
3.3 Second defeaturing stage.....	9
3.4 Geometrical error	11
3.4. Fourier analysis of the original sample data	13
4. Validation	15
4.1. Summary	15
4.2. Optimum height of the submodel.....	15
4.2.1 Methods.....	15
4.2.2 Results.....	16
4.2.3 Conclusions.....	19
4.3. Convergence of results with mesh refinement	20
4.3.1 Method and Results.....	20
4.3.2 Conclusion	27
5. Results.....	28
5.1. Summary	28
5.2. Preliminary study	28
5.3 The Dogbone sample	29
5.3.1. Results.....	29
5.3.2. Conclusions.....	44
6. Conclusions	44
6.1. Concluding remarks.....	44
6.2. Future tasks.....	45
6.2.1 Task 5.....	45
6.2.2 Correlation between SCF and local curvature of the sample	45
6.2.3 Further Tasks.....	47
7. Appendices.....	48
7.1. APPENDIX A: Computational implementation.....	48
7.2. APPENDIX B: User reference.....	48
7.3. APPENDIX C: Dogbone example	49
7.4. APPENDIX D: Enhanced images of Figure 30	51

1. Introduction

The objective of this work is to develop and validate a computational tool which predicts in an efficient way stress concentration of thick samples corroded by pitting. The approach proposed is to use a multi resolution strategy.

Based on St Venant's principle, an individual pit has limited field of influence over the stress in the surrounding area. This fact motivates a sub-modeling technique in which a large plate can be solved by interconnected sub-models with appropriate boundary conditions. Each sub-model of the sample is solved by mean of BEASY Mechanical Design tool, based on the Boundary Element Method. The major obstacles in this project are first to cope with a large number of degrees of freedom coming from the geometrical information of the corroded surface, and second to obtain stable and accurate results for the Stress Concentration Factor.

2. Methodology

2.1 Summary

The methodology developed for the stress analysis caused by corrosion pitting is summarized as follows. First, the original geometrical data representing the top surface of the sample is used for building a hierarchical sequence of defeatured levels by means of a moving average approach. Details of this approach are given in section 3.

Then, an iterative solving scheme is launched in order to explore and solve the sample data at a defeatured level (calculation resolution level) selected by the user. When the iterative solving scheme ends, an iterative assembly scheme starts in which the results of stress concentration factor and the geometrical error of the model are collocated at sampling points corresponding to the resolution selected by the user (post processing resolution level).

Finally, and repeatedly if necessary, a new solving iteration sequence may be launched with increased resolution, in the regions of the sample data that require more accuracy, such as zones of high SCF, large geometrical error, or steep gradient of any of them.

The process continues until convergence of results is achieved.

2.2 Iterative Solving Scheme

The iterative solving scheme operates in the following way. An initial representation of the top surface, usually coarser than the original data, is used to automatically create a NurbsSurface by the geometry modeler BEASY_GiD. Then, a parametric wire frame structure is connected to the created Nurbsurface in order to build a 3D submodel of the corroded surface. The remaining wireframe is then filled with flat surfaces to define a closed six-faced volume. Next BEASY_GiD creates a computational grid of the 3D model with the resolution and quality chosen either by the user or automatically by the software in a configuration file. Since BEASY is based on the Boundary Element Method, the computational grid is created only for the surface of the submodel, thus avoiding meshing the volume. This represents an important advantage which helps to speed up model generation and further calculation time. Once the model is created by BEASY_GiD, the information is passed as input to the BEASY MECHANICAL DESIGN software which conducts the stress analysis. As output, BEASY provides the stress and strain tensors results in all points of the boundary mesh of the submodel.

BEASY results of each submodel are stored in a file for later assembly into the appropriate location of the overall result file.

The solving iterations stop once all the submodels are completed. The above mentioned tasks are automatically performed in non-interactive mode, so as to avoid time consuming graphical interactions during the iteration over a large number of submodels.

2.3 Iterative Assembly

Next the assembly iteration loop is launched as another stage independent from the previous calculation stage.

The assembly loop can be described in terms of the following pseudocode:

```
[1] For each submodel solved, do:
[2]   Read result file of each submodel
[3]   Select all points of the submodel that belong to the top surface.
[4]   Add selected point to set {a}.
[5]   Remove from {a} all points that fall within the overlapping area of the submodel.
[6]   For each point in {a}, do:
[7]     • Find closest sample point of the postprocessing resolution level
[8]     • Compute SCF = Syy / Syy0
[9]     • Transfer SCF results from the mesh to the corresponding sample points
[10]    • Compute geometrical error (d)
[11]    • Transfer d from the mesh to the corresponding sample points
[12]   End do
[13] End do
```

3. Defeaturing technique

3.1. Summary

This section describes the defeaturing technique adopted in order to represent the geometry with minimum amount of degrees of freedom. The sample data is defeated in two stages. The first stage is based on a moving average and operates on the original sample points. After the first stage, a reduced number of points extracted from the original data is used in order to build a parametric NurbsSurface. Then, the parametric Nurbs-Surface is meshed with bi-quadratic elements, giving rise to a second defeaturing stage. The next two subsections describe in more detail the defeaturing process.

3.2. First defeaturing stage

The original data consists of a matrix $Z_{ij} \in R^{(Nx \times Ny)}$ which contains the Z coordinate of the top surface of the sample. This work is based on Structured Uniform Quadrilateral Grids (SUQG) for the geometrical representation of the top surface. This assumption involves rectangular uniform grids with constant spacing in x and y directions. In this way, the coordinates of a given point can be expressed in terms of logical indices i, j according to:

$$\begin{aligned} x_i &= (i-1)\delta x \\ y_j &= (j-1)\delta y \end{aligned} \tag{1}$$

where $i = 1, \dots, Nx$ and $j = 1, \dots, Ny$; and Z matrix represents:

$$Z_{ij} = Z(x_i, y_j) \quad (2)$$

The main advantages of using SUQG are that: first, it minimizes the amount of geometrical information, thus reducing the storage requirements, and second SUQG simplifies the nodal connectivity structure of the data. On the other hand, the main disadvantages are that it is not very flexible for representing complex geometries (i.e. samples with holes, or non-rectangular samples), and that it does not allow adaptive-grid methods based on displacement of the original nodes.

The Z matrix of the original data is defeatured by mean of the following restriction operator:

$$R = \frac{1}{4} \begin{bmatrix} \frac{1}{4} & \frac{1}{2} & \frac{1}{4} \\ \frac{1}{2} & 1 & \frac{1}{2} \\ \frac{1}{4} & \frac{1}{2} & \frac{1}{4} \end{bmatrix} \quad (3)$$

In this way, the Z coordinate of the defeatured grid ($Z_{i,j}^1$) at the nodal position given by the logical indices $\{i,j\}$ is calculated according to:

$$Z_{i,j}^1 = \sum_{a,b=-1}^{+1} R_{a,b} Z_{i+a,j+b}^0 \quad (4)$$

Where R is the restriction operator, $a,b = -1,0,1$, are the corresponding logical indices, and $Z_{i,j}^0$ is the original finest grid (undefeatured). This approach can be applied recursively, up to the desired defeatured level. A highly defeatured geometry is very useful for solving the whole model in one step, and getting a quick overview of the features of larger scale.

Note that if the size of the original matrix is $Nx \times Ny$ then, the matrix of the first defeatured level will have a size given by: $\frac{Nx \times Ny}{4}$.

In general, the geometrical representation of the top surface at a defeatured level K is given by a matrix Z^K

$$Z_{i,j}^K = \sum_{a,b=-1}^{+1} R_{a,b} Z_{i+a,j+b}^{K-1} \quad (5)$$

of size:

$$size(Z^K) = floor \left[\frac{Nx \times Ny}{2^K} \right] \quad (6)$$

And the spacing between points is given by:

$$\Delta^K = 2^K \Delta^0 \quad (7)$$

where Δ represents either δx or δy and Δ^0 indicates the spacing of the original data.

A comparison of the different resolution levels, from $K = 0$ (original) to 6 is shown in Figure 1 to Figure 5. “Data1” in the legend of the figures corresponds to the original sampled data ($K=0$), i.e. undefeatured, “data2” to the first defeatured level ($K=1$), “data3” to the second level ($K=2$) and so on.

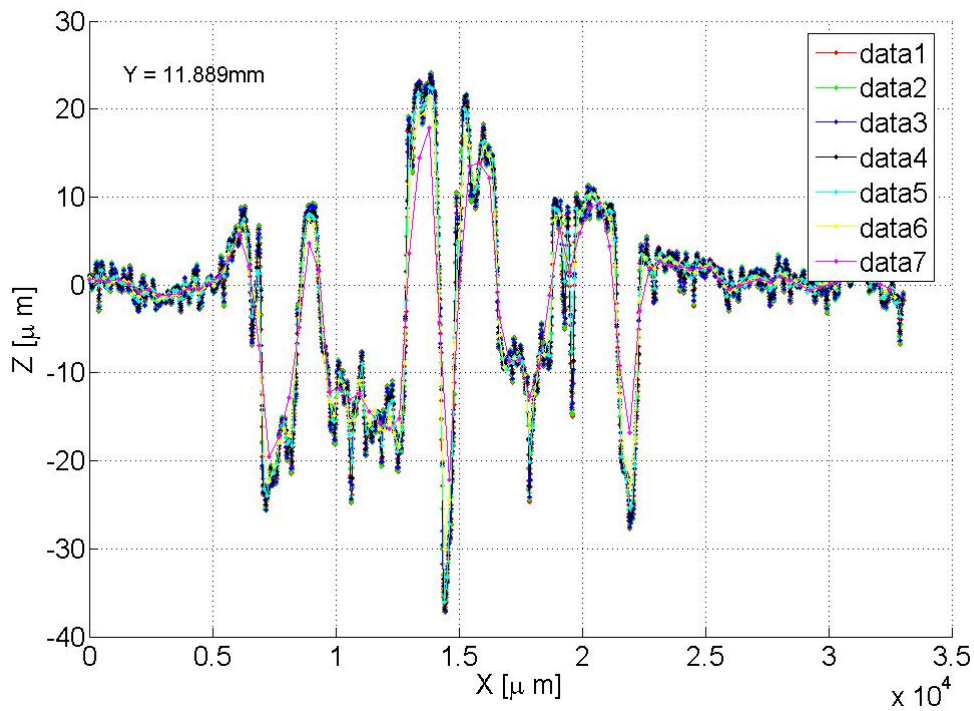


Figure 1. Z coordinate of sample data along $Y = 11.889\text{ mm}$, exploring the whole range of variation of the x coordinate in the Dogbone example.

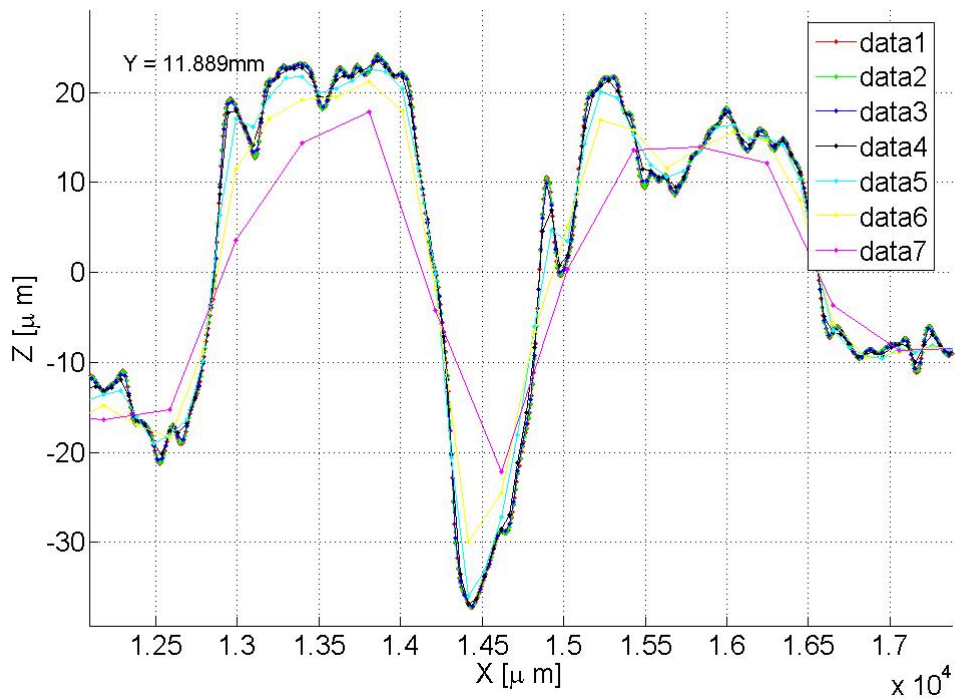


Figure 2. Close up view of the defeatured profiles shown in Figure 1

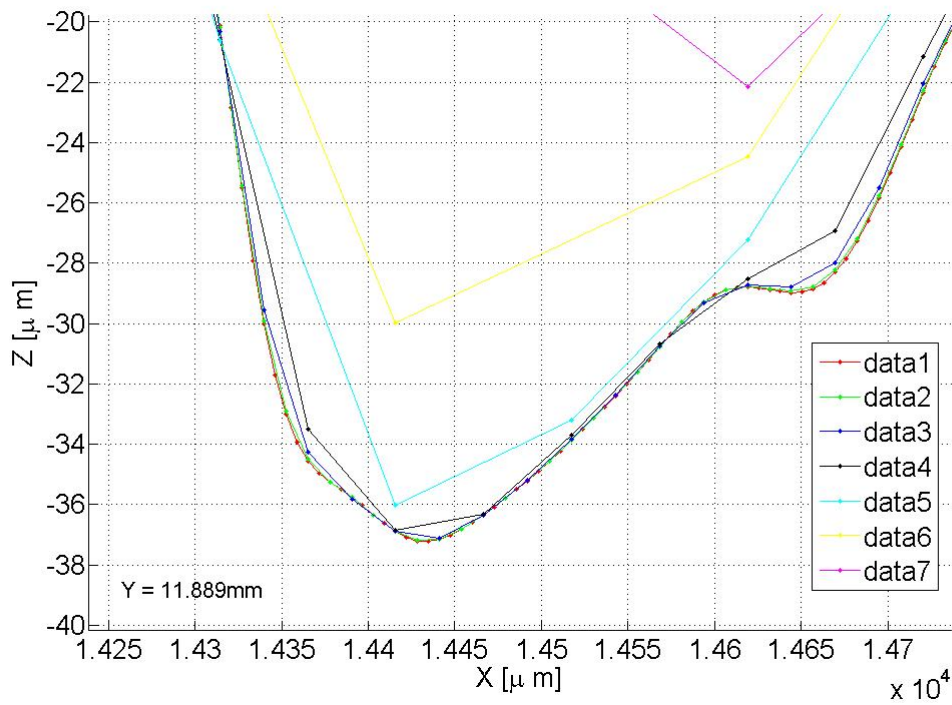


Figure 3. Close up view of the profiles shown in Figure 3, showing how the different defeaturing levels approximate the original sampled data in one of the deepest narrow pits of the sample.

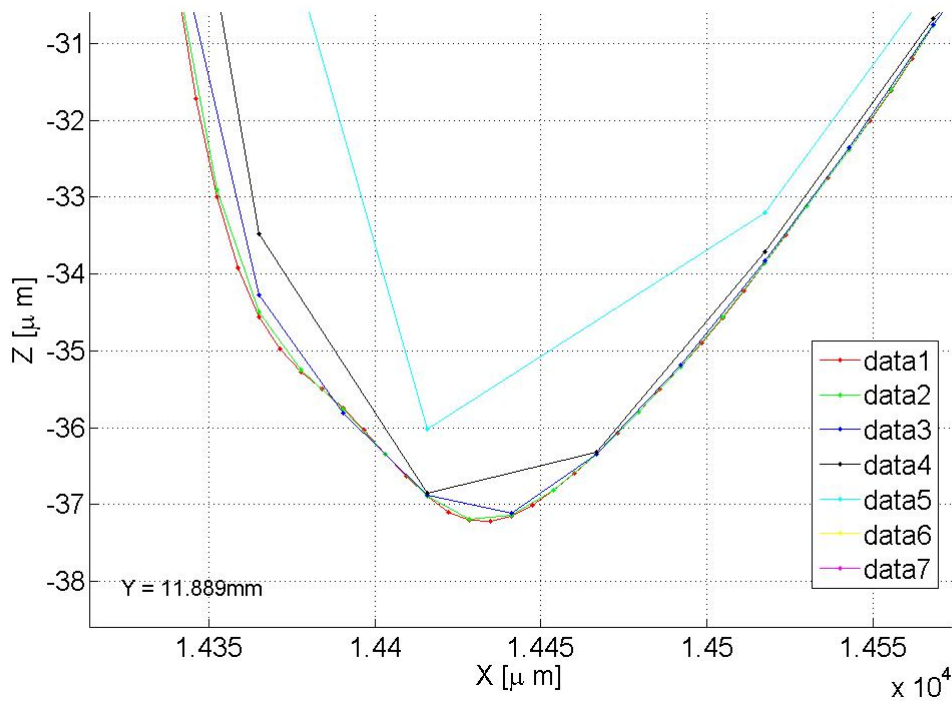


Figure 4. Close up view of the profiles shown in Figure 4.

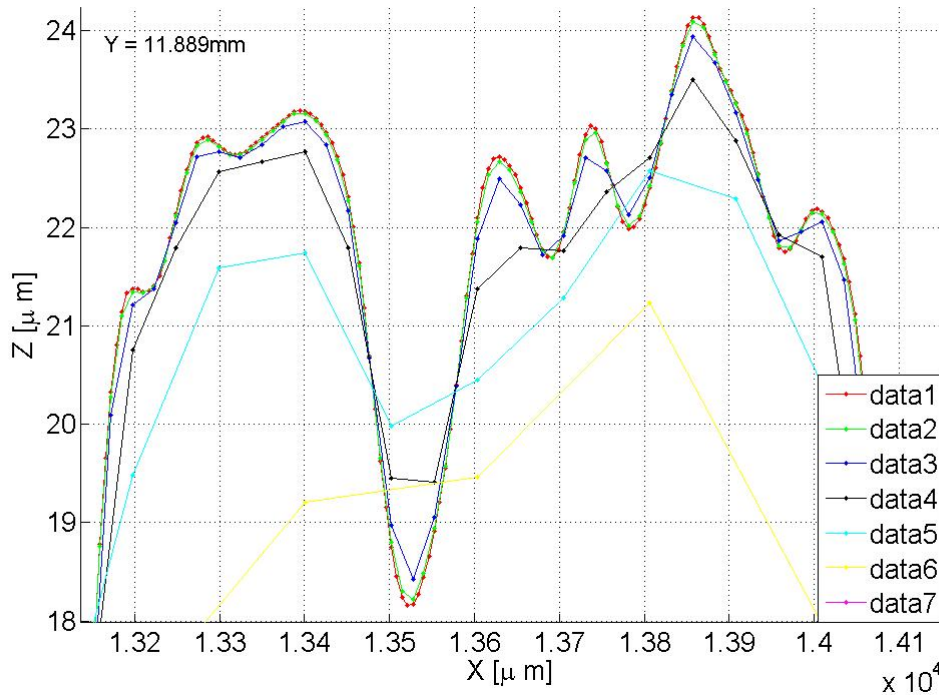


Figure 5. Detailed view of the different profiles approaching the original data in the positive peak found along $Y = 11.889$ mm

Each figure shows different views of the same profile which traverses the sample along $y = 11.889$ mm. The values of Z coordinate along this path represent a good example which illustrates the orders of magnitude of the different scales involved in the geometry.

3.3 Second defeaturing stage

Figure 6 illustrates the creation of the top surface of the submodel starting from the organized cloud of points contained in matrix Z^K . The heights stored in Z^K (Figure 6(1)) are used to build a sequence of pseudo-parallel poly-lines (Figure 6(2)) which generate an automatic Nurbs-Surface (Figure 6(3)), in the context of the GID geometry modeller. It is worth mentioning that a Nurbs-Surface created from a series of pseudo-parallel poly-lines is approximately ten times more accurate than a Nurbs-Surface created from a cloud of points. Then, the submodel creation continues by adding a wireframe of height h to the top surface and a volume. Finally, appropriate boundary conditions are established and a surface mesh created for the whole submodel. The mesh in the top surface can be meshed in many different ways, by mean of structured, unstructured or mixed meshes, with any number of triangular or quadrilateral elements.

The end-user can choose among any of these possibilities. However, it has been concluded from experience with the BEASY solver that the best option is to use uniform quadratic quadrilateral elements for the top surface, linear triangular elements for the laterals, and linear or even constant quadrilateral elements for the bottom surface, as seen in Figure 7.

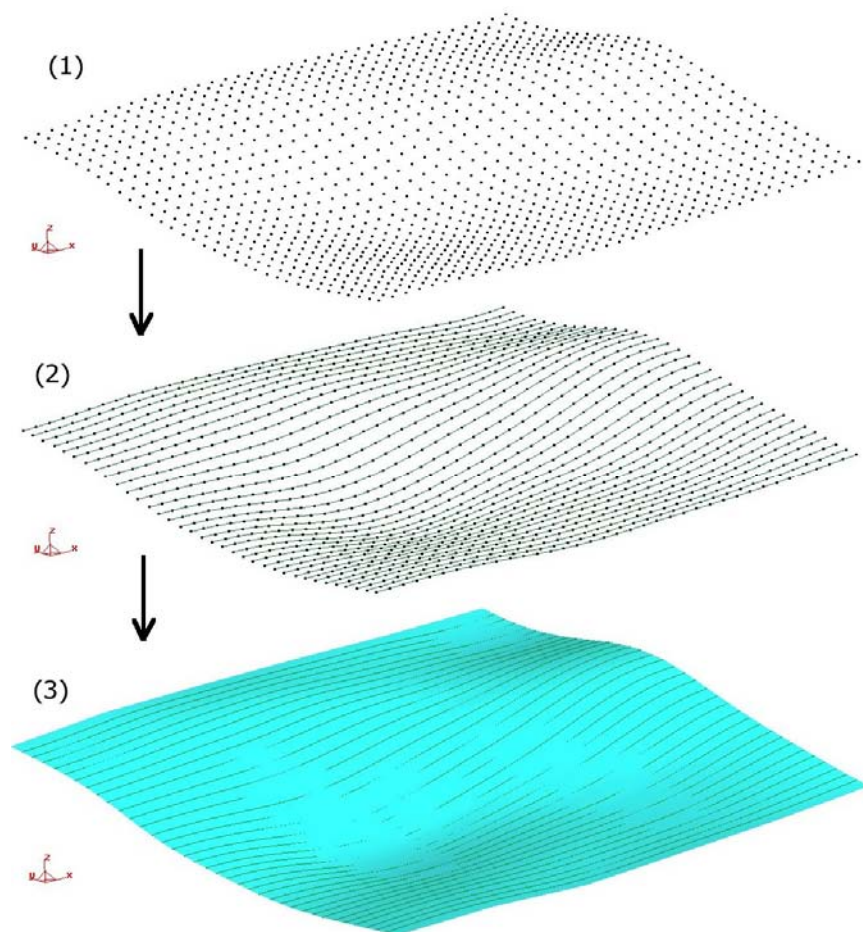


Figure 6. Creation of a GID Nurbs-Surface from a structured uniform quadrilateral grid

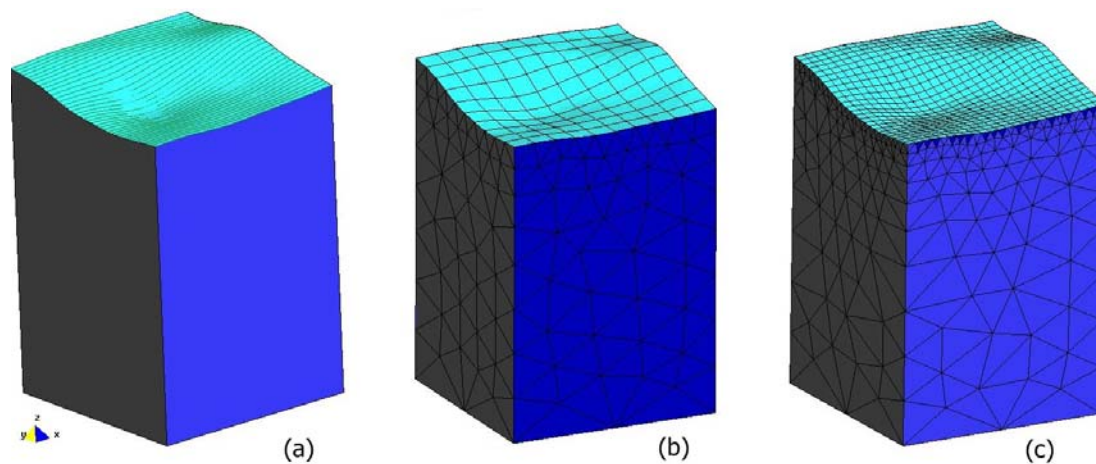


Figure 7. Submodel creation. (a) The wireframe submodel. (b) 10 x 10 grid associated to the top surface. (c) 24 x 24 grid associated to the top surface

3.4 Geometrical error

The geometrical error associated to each sampled point is evaluated as the distance between the point and its closest element of the mesh that discretizes the Nurbs-Surface. More specifically, the following parameters were adopted as indicators of geometrical errors:

$$\langle d \rangle = \frac{1}{N} \sum_{i=1}^{Ns} d_i \quad (8)$$

and

$$d_{\max} = \max[d_i]_{i=1, Ns} \quad (9)$$

where $d_i = \|\vec{x}_i - \vec{x}_{0,i}\|$ is the distance between a sampled point (\vec{x}_i) of the corroded surface (top surface of the sub-model) and the closest point in the mesh that approximates the mentioned surface ($\vec{x}_{0,i}$). Figure 8 shows the geometrical error associated to point x_i , close to a quadratic triangular element. The point $\vec{x}_{0,i}$ is found by an iterative algorithm, taking into account the shape function of the element.

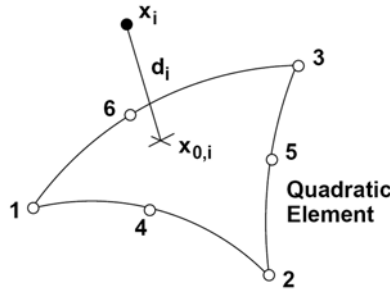


Figure 8. Distance between a sampled point x_i and a triangular curved element of the GID mesh whose surface is described by nodes 1 to 6, through standard shape functions.

Figure 9 shows the variation of the total error (maximum and average distance) for different meshes covering the same region of the sample data, a sub-model of 0.2 by 0.09 mm. In general, the geometrical error decreases with the mesh refinement. When the size of the element is close to the sampling spacing, the maximum distance between any sampled point and the mesh that approximates the surface stabilizes and becomes typically 3% of the grid spacing.

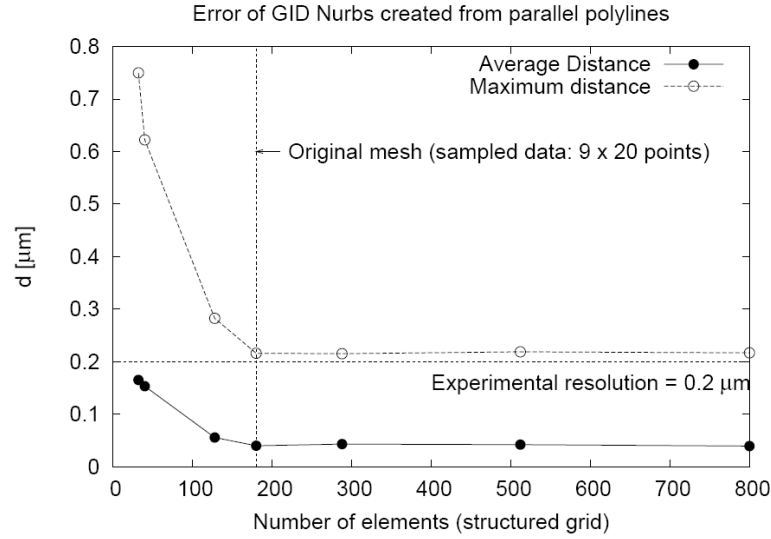


Figure 9. Error between mesh and sampled points, $\max(d)$ and $\text{mean}(d)$ for different meshes.

The data of Figure 9 is provided in **Table 1**.

$Nelem$	$N_x \times N_y$	$Nnod$	$\langle d \rangle [mm]$	$d_{max} [mm]$
32	8×4	121	1.6E-04	7.5E-04
40	10×5	149	1.5E-04	6.2E-04
128	16×8	433	5.6E-05	2.8E-04
180	20×9	599	4.0E-05	2.2E-04
288	24×12	937	4.3E-05	2.1E-04
512	32×16	1633	4.2E-05	2.2E-04
800	40×20	2521	3.9E-05	2.2E-04

Table 1. $Nelem$ = Number of elements. $Nnod$ = number of nodes. $\langle d \rangle$ mean distance between sampling points and mesh, d_{max} = distance between the most distant sample point and the mesh that approximates the surface.

As an illustrative example of this measurement, Figure 10 and Figure 11 show the geometrical error in a region of the Dogbone example (see appendix C). The mesh in this example consists of 20×20 9-noded quads covering the region $8521.3 \mu m < x < 8775.1 \mu m$, and $11719 \mu m < y < 11973 \mu m$ in the Dogbone⁸ example.

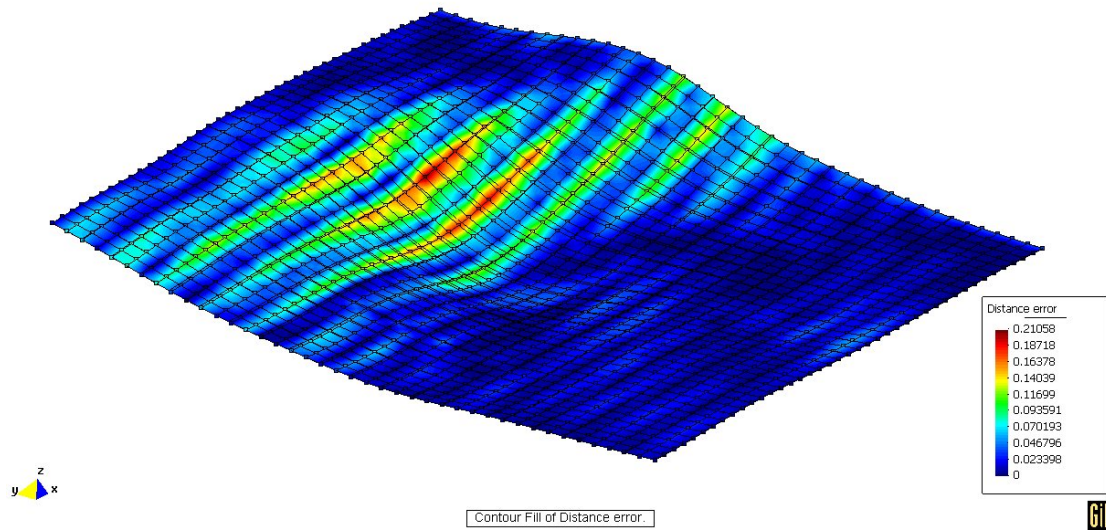


Figure 10. Geometrical error between a mesh of 20x20 quads covering the region $85213\mu\text{m} < x < 87751\mu\text{m}$, and $11719\mu\text{m} < y < 11973\mu\text{m}$ in the Dogbone⁸ example. The color indicates the minimum distance between an original point and the mesh in micrometers.

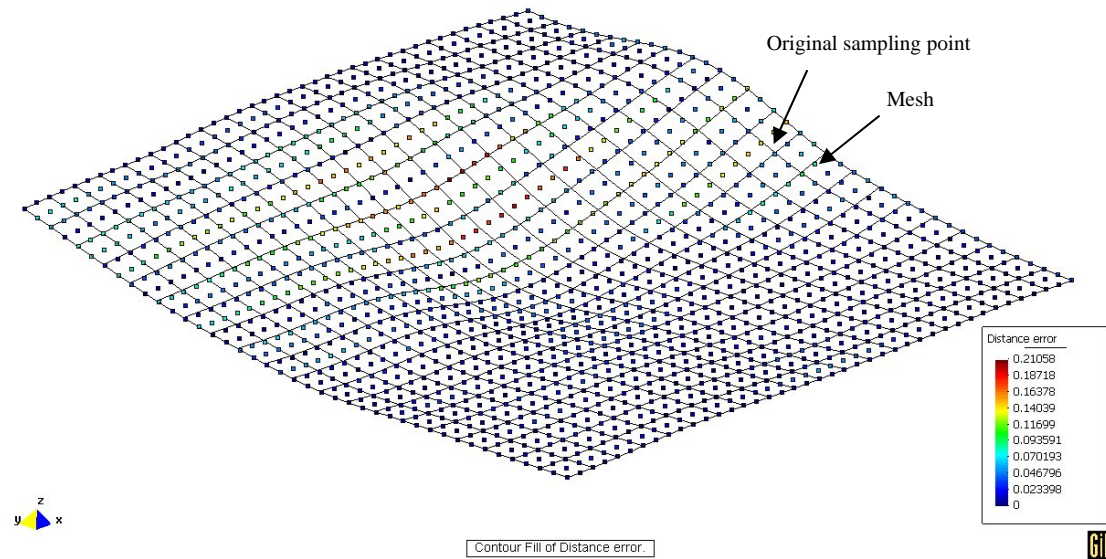


Figure 11. Mesh overlapped with original sample points. The legend indicates minimum distance between original point and mesh in micrometers.

3.4. Fourier analysis of the original sample data

Although eventually not used, a Two Dimensional Fourier Filter was initially considered as a way to remove possible spurious signals from the original data. A Discrete Fast Fourier Transformation of the Dogbone sample can be observed in Figure 12. A filtered image in the x direction can be observed in Figure 13. The results obtained show excessive error. Consequently, defeaturing methods based on FFT filters were disregarded during the development of the present work.

⁸ The Dogbone example is detailed in Appendix C

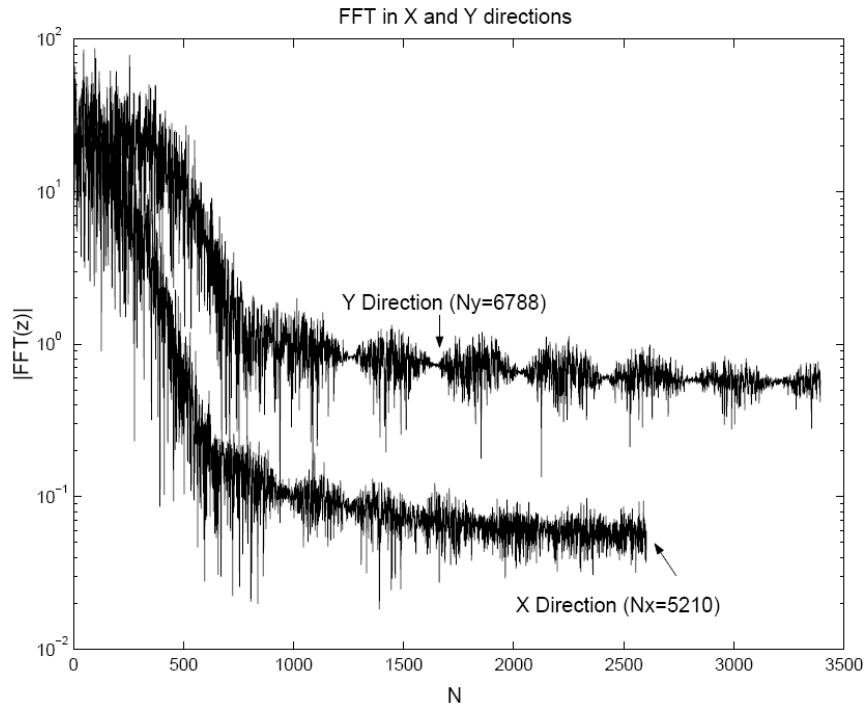


Figure 12. Two dimensional FFT transformation of the original sample data

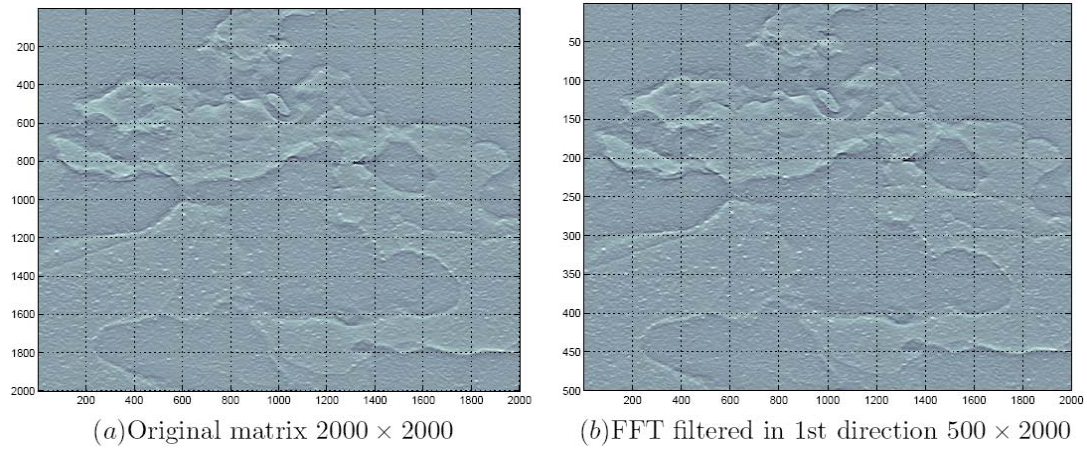


Figure 13. Subregion of the original matrix, and its corresponding FFT filtered image in X direction.

4. Validation

4.1. Summary

This section is concerned with the different aspects of validation of the sub-modeling approach.

4.2. Optimum height of the submodel

The depth (h) of the original sample is 3.125mm. Depending on the geometry, the submodeling approach might require submodels a few tens of micrometers wide. Thus, it is important to create submodels as “thin” as possible without losing accuracy in the results.

This subsection investigates the effect of variation of depth on stress concentration factor results on the surface.

4.2.1 Methods

The analysis shown in this subsection was conducted with 34 sub-models of different depths. The sequence of models was fully automated, controlled by a windows batch file which operates in the following way:

The sample data file (Dogbone.txt) is read by Submod_win.exe which yields a GID batch file (smod.bch) with instructions for GID to create a BEASY sub model. Then, GID is launched in non-interactive way with the batch file by mean of:

```
gid.exe -b smod1.bch -p pit.gid -n2
```

in order to create the corresponding BEASY model smod.dat. Then BEASY is launched in non-interactive way, reading the input data file and producing the results file for post-processed with GID (smod.post.res and smod.post.msh). The results are collected all together and summarized in the next section.

The following diagram illustrates the given explanation:

Sample data file	→ Submod_win.exe	→ BEASY_GID batch file
BEASY_GID batch file	→ BEASY_GID(non interactive)	→ BEASY_GID model BEASY .dat file
BEASY .dat file	→ BEASY SOFTWARE	→ projectname.post.res projectname.post.msh

The number of elements used for the top surface was constant equal to 20 x 20.

Lateral surfaces were meshed with triangular elements (BEASY T2 elements, triangular quadratic geometry). These results involve 2 different sampling resolutions, K=3, and K=0 (original data).

4.2.2 Results

Figure 14 shows the variation of the reduced SCF (defined below) with height of the submodel, for submodels with two different sizes. Figure 15 shows the reduced SCF as a function of the aspect ratio of the submodels. In all cases the maximum fluctuation of Z coordinate is below $20\text{ }\mu\text{m}$, therefore, the condition $\delta Z \ll h$ is always fulfilled.

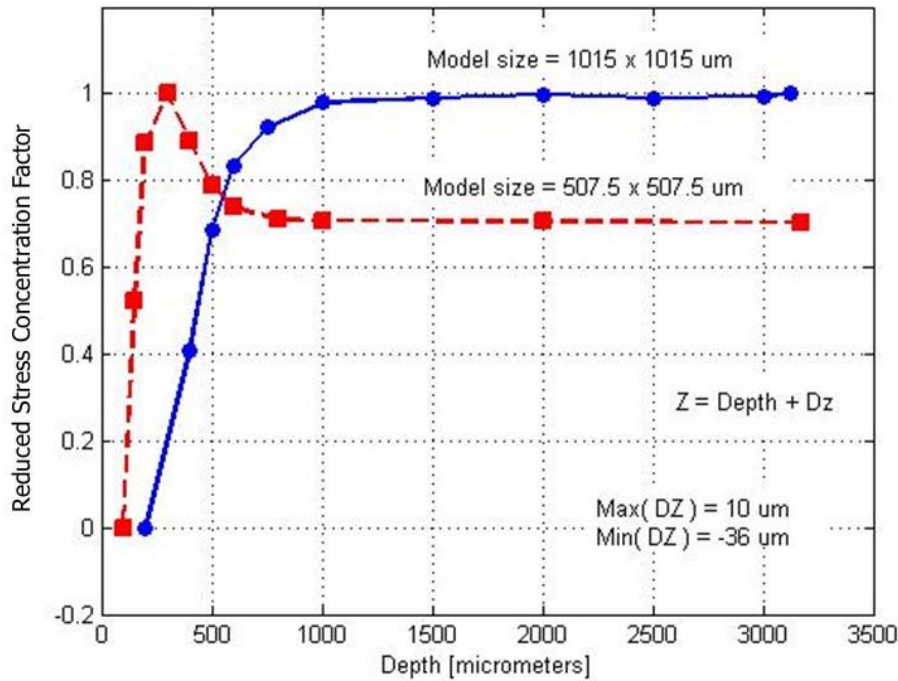


Figure 14: Reduced stress concentration factor as a function of depth for different submodel sizes

Table 2 to Table 4 present the results corresponding to Figure 14 and Figure 15, and Figure 16 shows some of the sub-models used for this test.

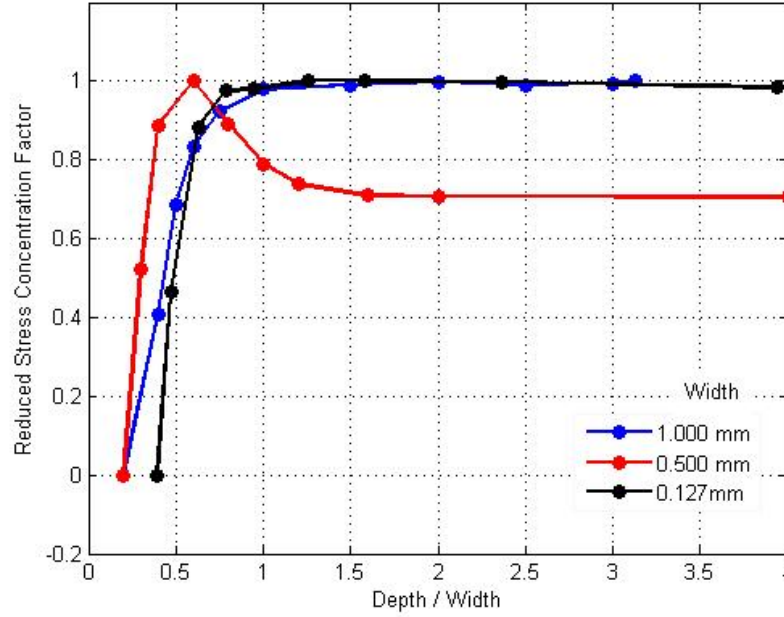


Figure 15: Reduced stress concentration factor as a function of the aspect ratio of the sub-model.

The Reduced stress concentration factor is computed as:

$$S' = \frac{S_{yy} - \min(S_{yy})}{\max(S_{yy}) - \min(S_{yy})}, \quad (10)$$

where S_{yy} is the yy component of the averaged stress tensor, and the corresponding minimum and maximum values, $\min(S_{yy})$ and $\max(S_{yy})$ respectively, are the local values of S_{yy} in the series of results.

Thus in Figures 14 and 15 the reduced SCF fits in the range 0 to 1 of the vertical axis.

Depth (um)	Syy_av_min	Syy_av_max
200	0.65277	1.7073
400	0.56522	1.7236
500	0.56903	1.7347
600	0.54366	1.7405
750	0.55141	1.7441
1000	0.57372	1.7464
1500	0.56840	1.7468
2000	0.58152	1.7471
2500	0.56825	1.7468
3000	0.55205	1.7470
3125	0.57022	1.7472
3175	0.57017	1.7473
3500	0.57378	1.7469
4000	0.57015	1.7472

Table 2: Results for Syy max as a function of depth. The size of the model is approx: 1000 um x 1000um. Depths are given in micrometers

depth	Syy_av_min	Syy_av_max
0100	0.51184	1.1317
0150	0.54516	1.1754
0200	0.55971	1.2058
0300	0.56487	1.2152
0400	0.55616	1.2061
0500	0.54712	1.1977
0600	0.54165	1.1934
0800	0.53840	1.1909
1000	0.53814	1.1908
2000	0.53831	1.1907
3175	0.53858	1.1905

Table 3. Results for Syy max as a function of depth for smod2 model. The size of the model is approx: 500 um x 500um. Depths are given in micrometers

depth	Syy_av_min	Syy_av_max
050	0.74715	1.3387
060	0.73282	1.3645
080	0.70701	1.3878
100	0.69741	1.3929
120	0.69746	1.3931
160	0.70244	1.3942
200	0.70429	1.3942
300	0.70791	1.3941
500	0.75671	1.3933

Table 4. Results for Syy max as a function of depth, from Dogbone16.txt. The size of the model is approx: 126.9 um x 126.9um. Depths are given in micrometers.

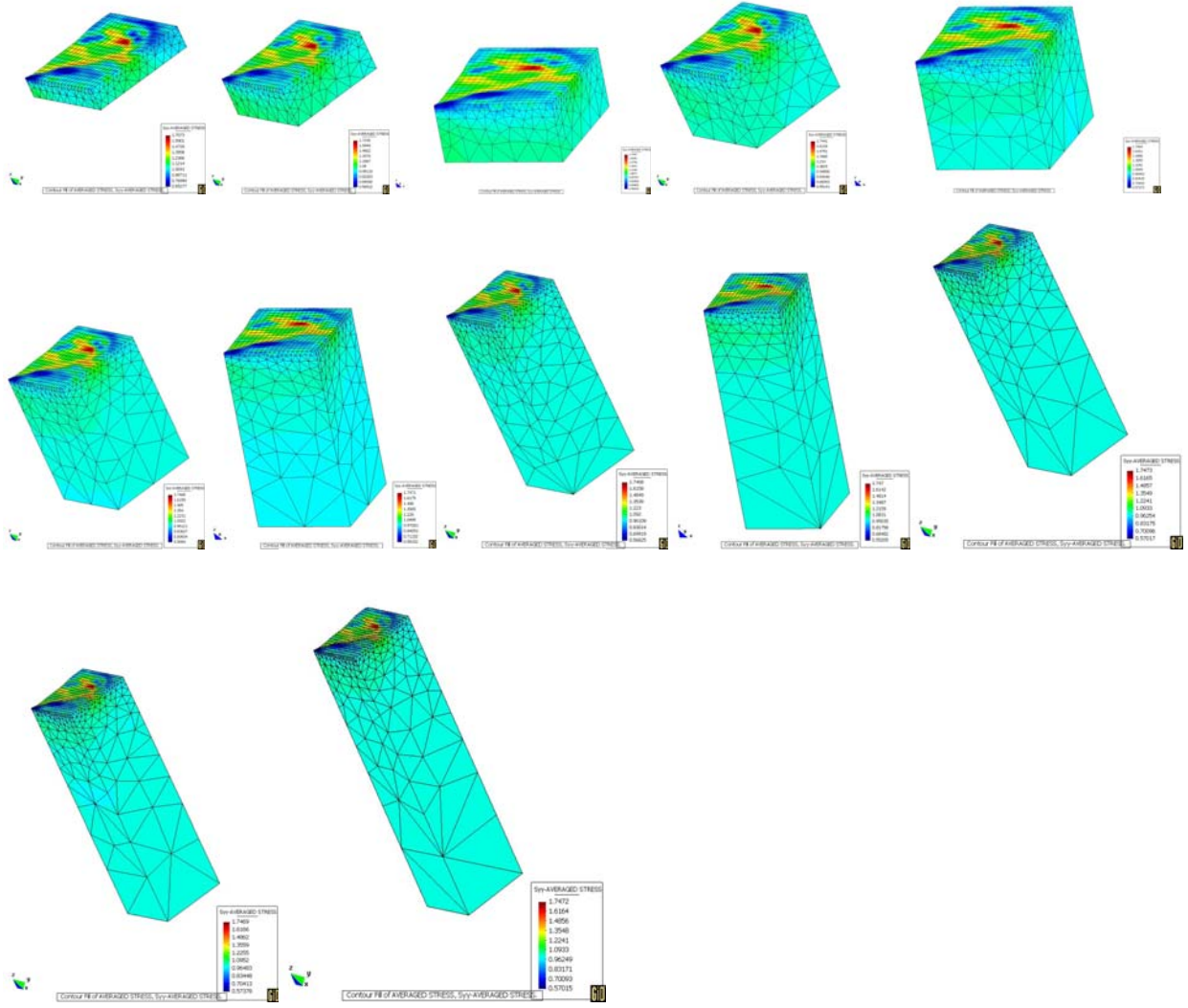


Figure 16: Sequence of test models with different aspect ratios, used to evaluate the influence of the total depth of the sample on the results at the top surface.

4.2.3 Conclusions

All conducted tests indicate that the depth of the submodel can be taken as:

$$h_s = \min(h, 1.5W) \quad (11)$$

where

h_s is the depth of the submodel, W is the width of the submodel, and $h = 3.175\text{mm}$ depth of the whole sample.

It is interesting to note from figures Figure 14 and Figure 15 that the stress concentration factor computed for $h < h_s$ (i.e. before convergence) is not necessarily either bigger or smaller than the stress concentration factor after convergence.

4.3. Convergence of results with mesh refinement

This section investigates the stability of the solution as a function of mesh refinement. The region selected for this study is shown in Figure 17. Figure 18 shows the geometry of the surface and the sub-model in real aspect ratio.

4.3.1 Method and Results

A sequence of refined representations of the top surface was employed in order to assess the stability of the maximum SCF. The methodology employed is similar to the one used for iterations with varying height, but in this case, the mesh refinement is continually increased up to the maximum resolution available, at which the element size is about the same as the distance between the sample points.

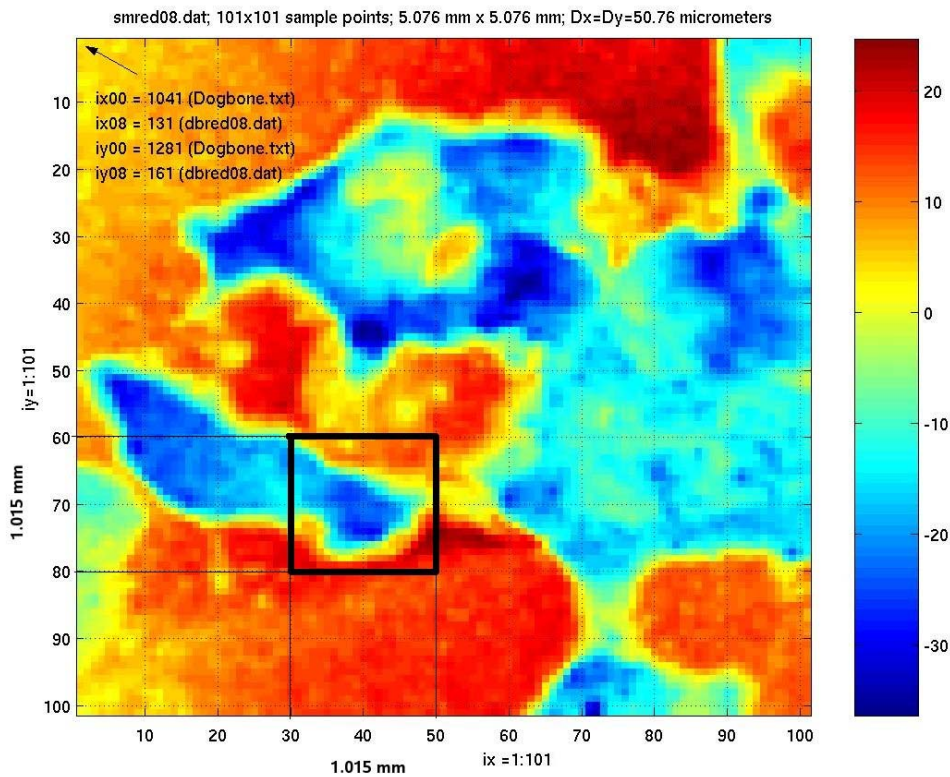


Figure 17: Submodel adopted for testing the stability of the solution, indicated with a square. Color represents height of the sample (Z coordinate in micrometers)

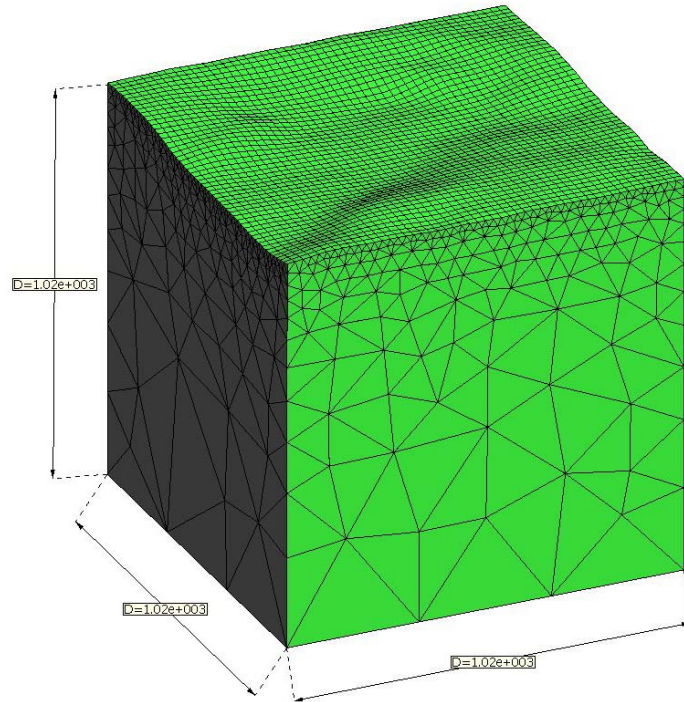


Figure 18: Meshed submodel with 50x50 elements in the top surface

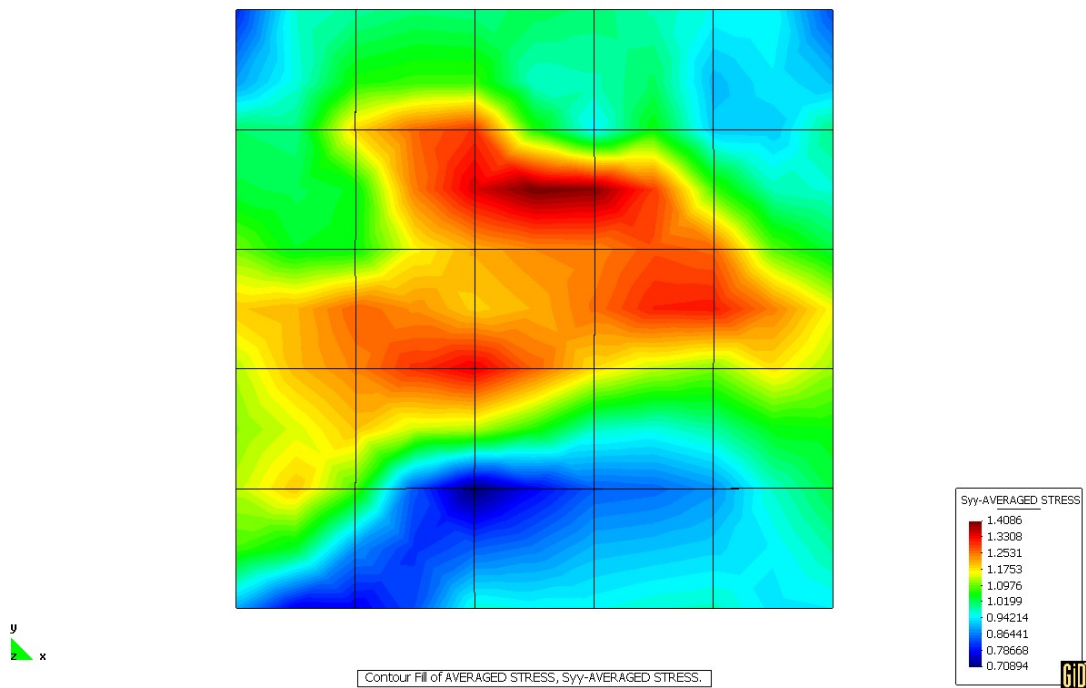


Figure 19: 5x5 SCF in a coarse mesh

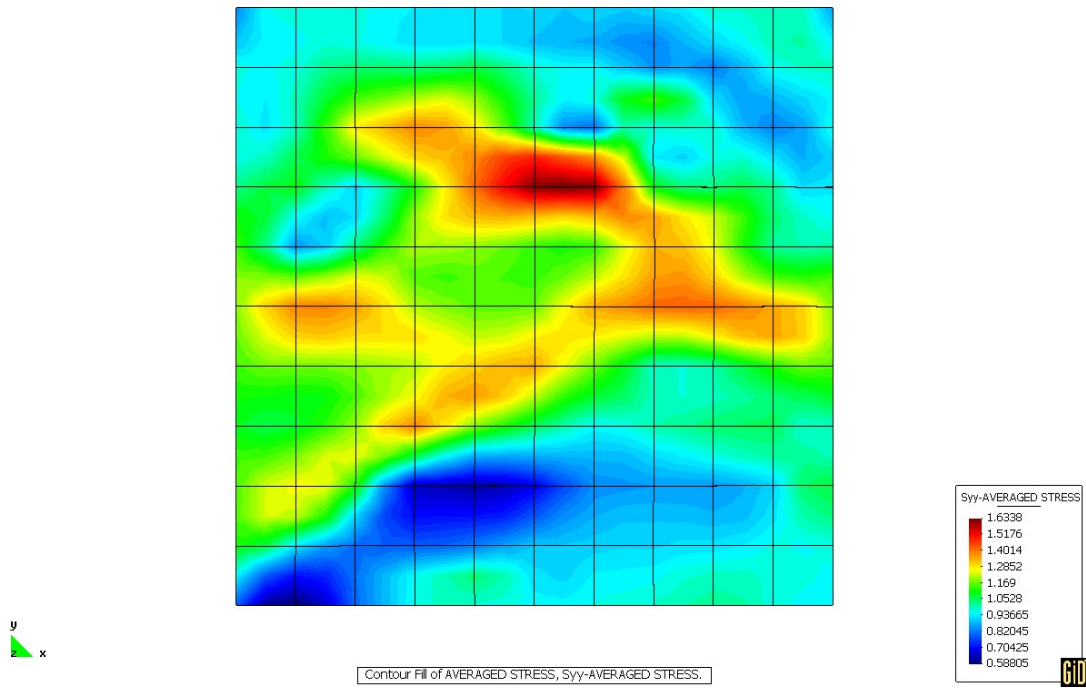


Figure 20: 10 x 10 Mesh for the top surface

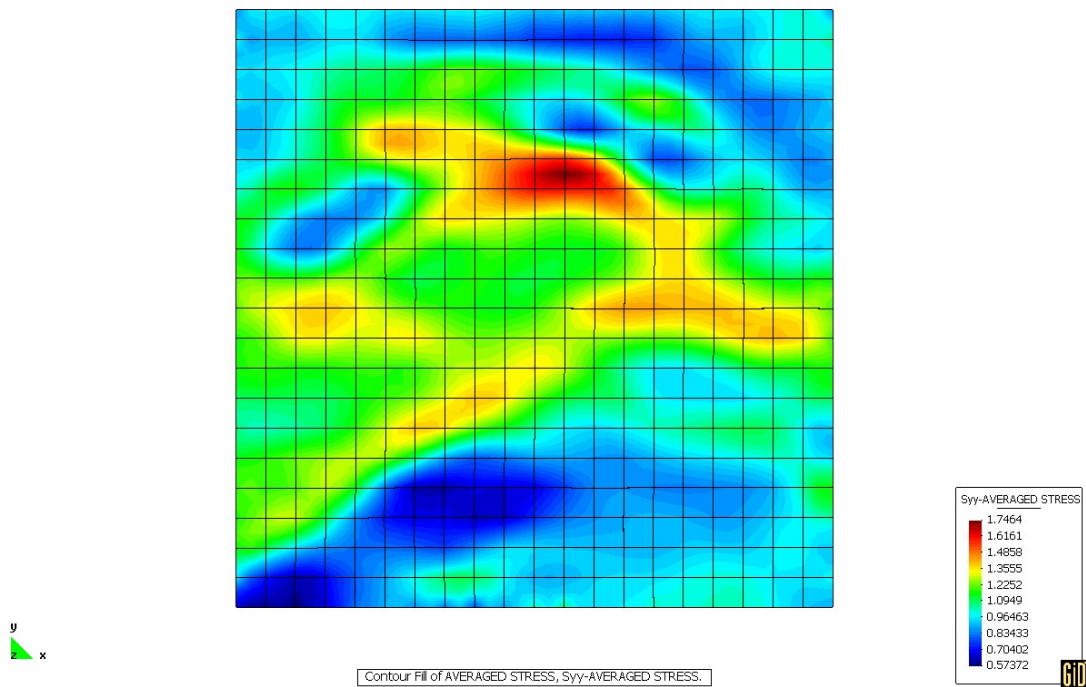


Figure 21: 20x20 mesh for the top surface

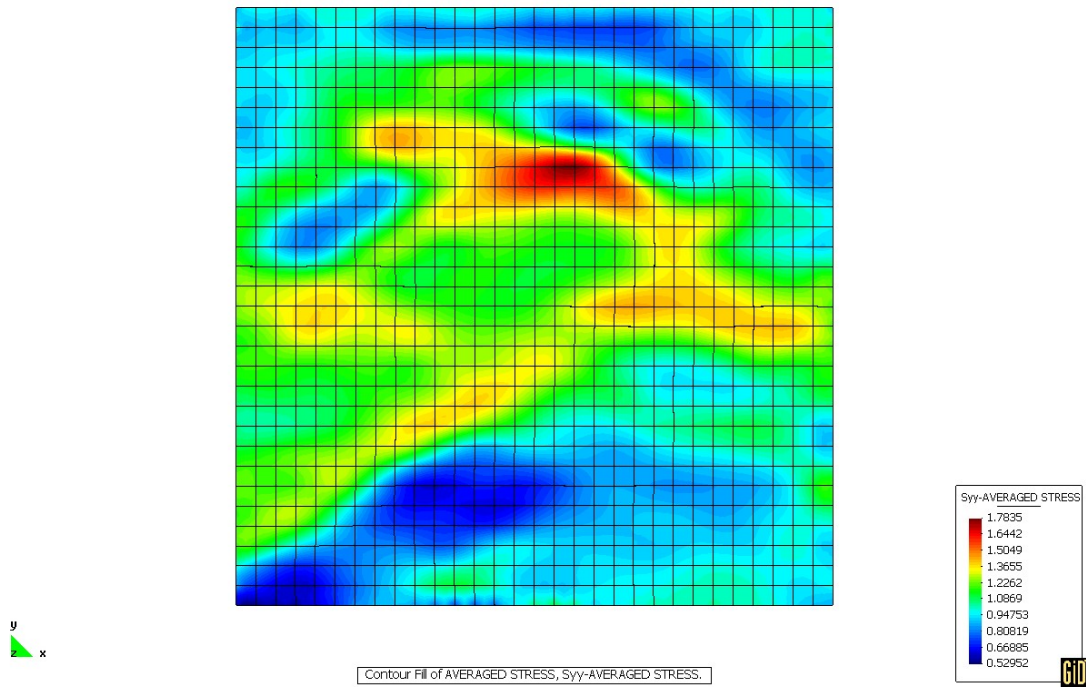


Figure 22: 15x15 mesh for the top surface

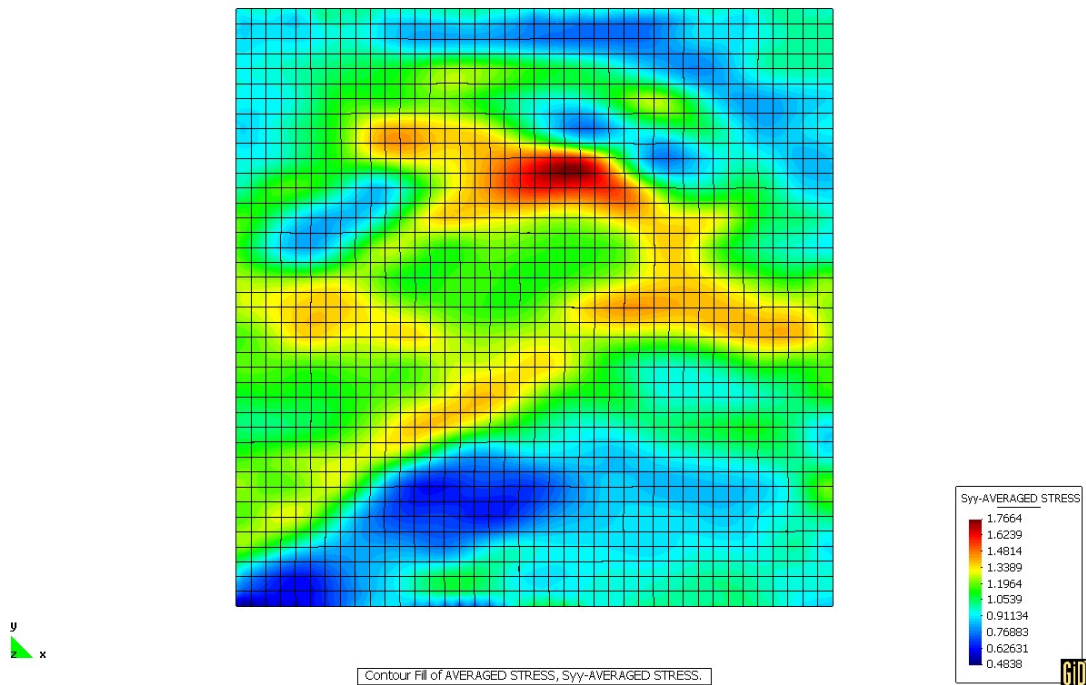


Figure 23: 40x40 mesh for the top surface

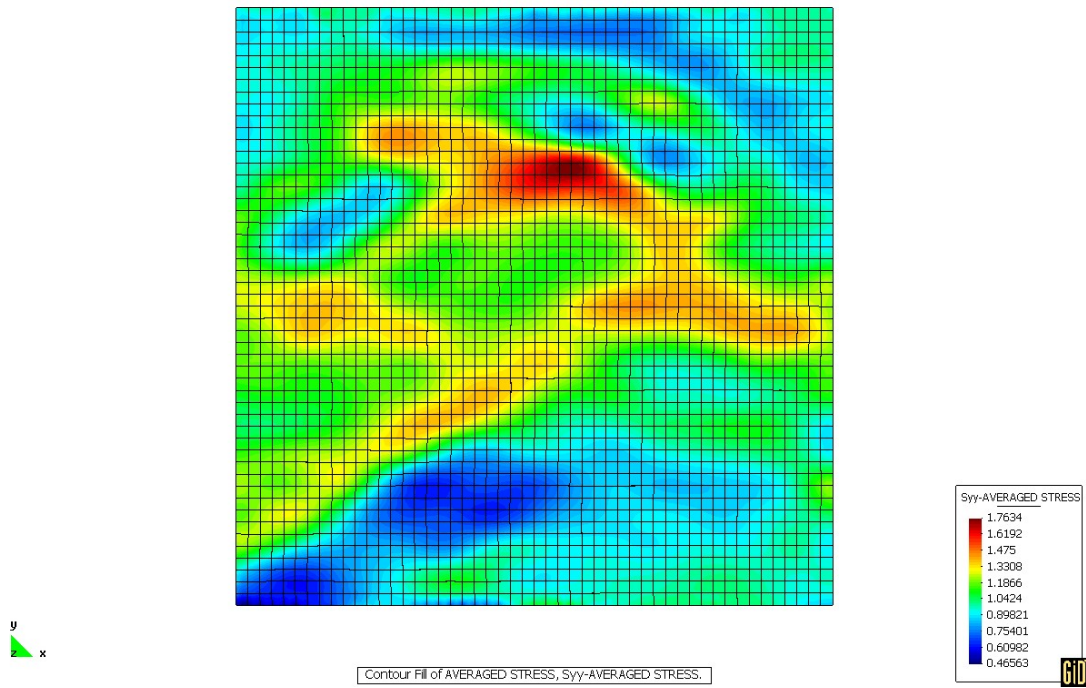


Figure 24: 50 x 50 mesh, for the top surface

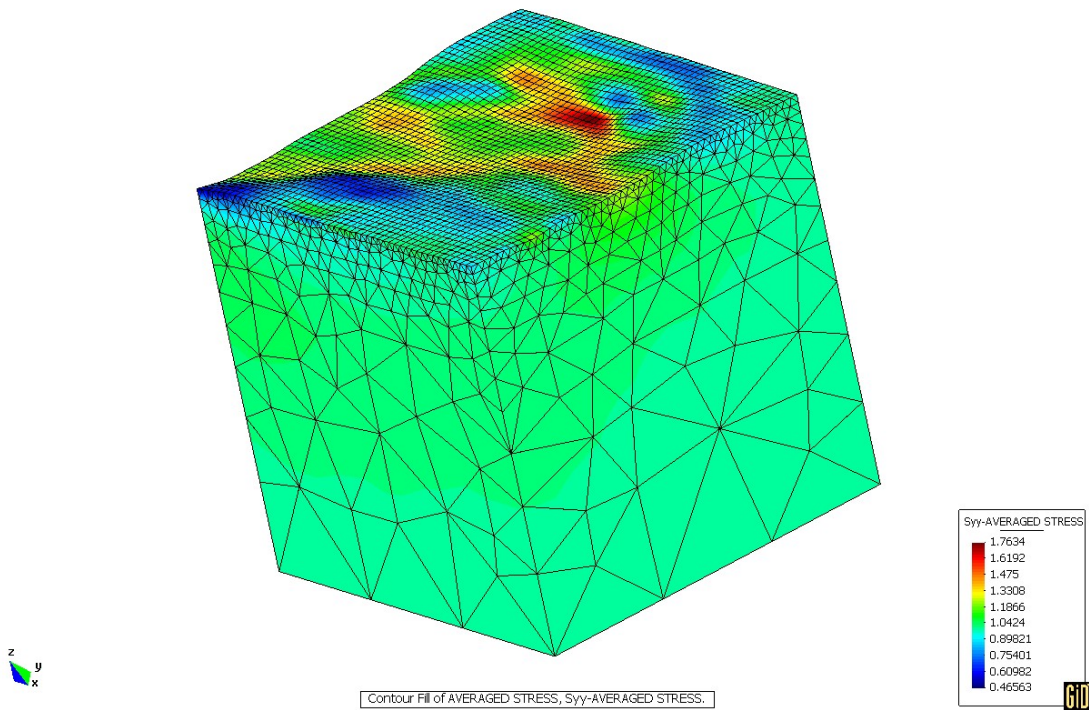


Figure 25: 3D view of the submodel meshed with 50x50 elements on the top surface

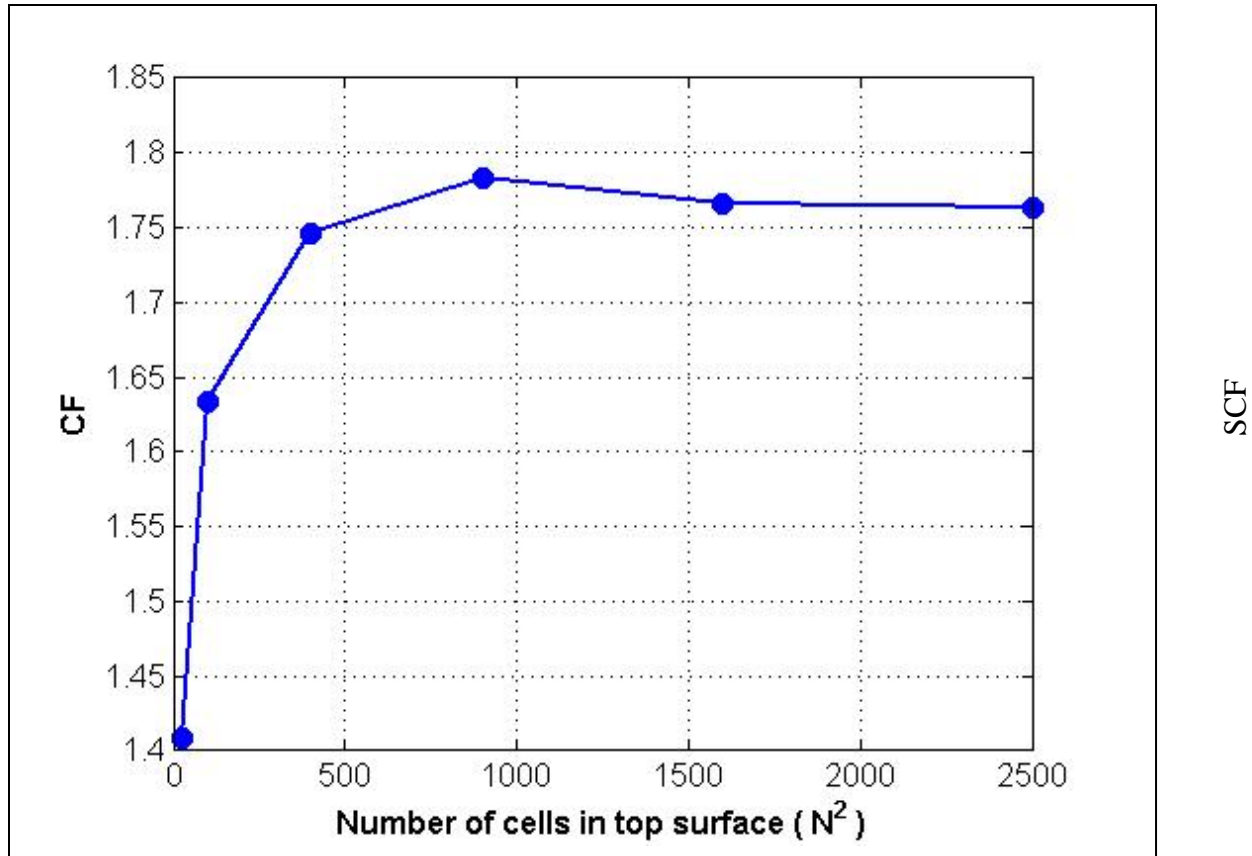


Figure 26: Maximum SCF computed for the different meshes shown in this section as a function of the number of elements on the top surface of the mesh

The SCF for sub-models of different sizes with slightly varying resolution has been evaluated along a path in the top surface from point P1 = (8648.39, 11617.5 -24.5915) to P2 = (8648.2 12084.5 -761.4)⁹. The results can be observed in Figure 27.

The definition of each sub-model is shown in Table .

Id	Ix0	Ix1	Iy0	Iy1	Nx	Ny	Ry [μm]
A	1334	1394	1838	1898	20	20	19.0
B	1344	1384	1848	1888	20	20	12.7
C	1354	1374	1858	1878	20	20	6.34
D	1362	1378	1864	1880	20	20	5.08
E	1362	1378	1864	1880	24	24	4.23
F	1324	1404	1828	1908	20	20	25.4
G	1281	1441	1761	1921	70	70	14.5

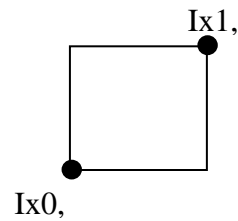


Table 5: Dimensions and location of the sub-models used for the mesh refinement analysis.

⁹ The coordinates of the points are (x,y,z) given in micrometers.

The first column indicates the sub-model Id. Columns 2 to 5 (IX0 IX1 Iy0, Iy1) indicate the coordinates of the corners of the region covered by the sub-model in logical indices corresponding to the resolution level K=0 (SUQG format). For example Ix0 and Ix1 ranges from 1 to 5210, and Iy ranges from 1 to 6788 in the Dogbone example, in which the total number of sampling points in x and y directions are 5210 and 6788 respectively. Nx and Ny indicate the number of elements of the mesh for the top surface in x and y directions, respectively. Ry expressed in microns represents the resolution of the mesh along y direction, given as

$$R = \left(\frac{Iy1 - Iy0}{Ny} \right) \delta y$$

Note that all of them are centered approximately in the same point which is the maximum SCF found in sub-model “A”.

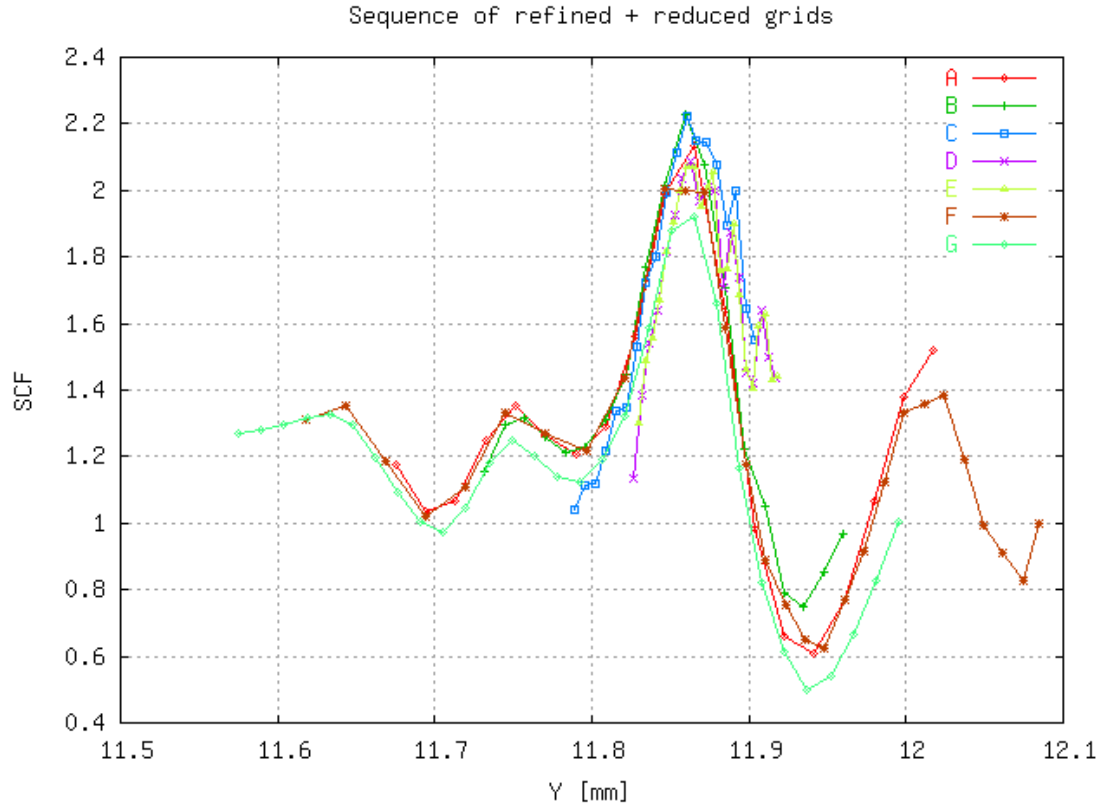


Figure 27. Stress concentration factor in the top surface along Y coordinate evaluated with different levels of geometrical resolution.

Figure 28 shows the location of the cut-wire in the sub-model “C” considered for this analysis.

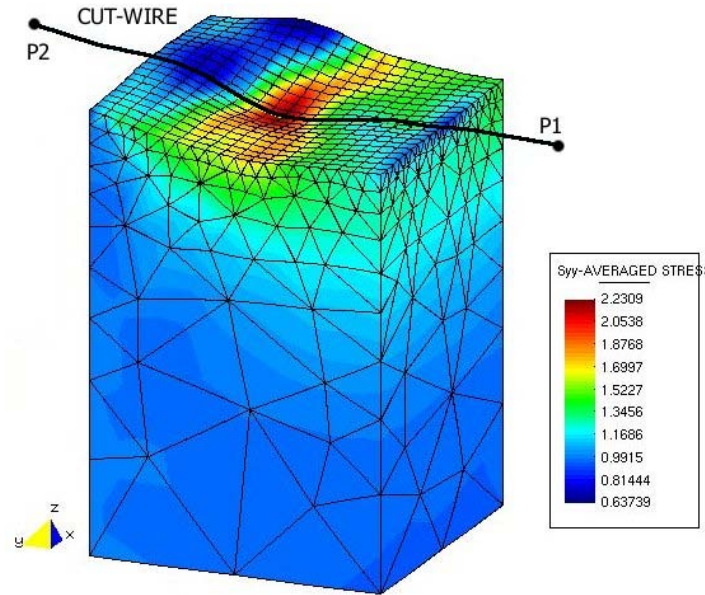


Figure 28: Location of the cut plane in the submodel C. The color indicates SCF according to the scale on the right.

4.3.2 Conclusion

The sequence of sub-models F, A, G, B, C, D, E represents gradually decreasing element size, and simultaneously decreasing sub-model size.

Although this sequence of models does not conform to the normal rules of a classical convergence study as for example the nodes are not in the same position in each of the models, it does however provide indication of the effects of mesh refinement, changing sub-model size, and gradually better conformance to the geometry represented by the sample points.

For the sub-models where element size is much bigger than the sample point spacing (i.e. F, A and G) it is clear from figure 27 that the precise position of the elements relative to the geometry of the surface has an influence on the peak SCF observed at $y \sim 11.87$ mm. This explains why the peak for sub-model G is lower than that for sub-model A. (As an aside, it is clear from curve G that simply “joining the dots” is not the best way to interpolate the SCF, since doing so has in this case apparently cut-off the peak at $y \sim 11.87$ mm.)

For the sub-models B and finally C (where the element size is the same as the sample point spacing) the observed peak is virtually identical, and has a value only slightly increased above that for sub-model A.

Noting that sub-model C is only about 20% the size of the largest sub-model, it is clear that the sub-model approach is able to capture the peak stresses whilst substantially restricting the model size.

Sub-models D and E (which have element sizes which are smaller than the sample point spacing) show slightly lower peak SCF (about 5% lower than for sub-model C).

It can generally be concluded that the sub-modeling method converges as both element size and sub-model size are reduced.

It is possible that a limit on the “smallness” of the sub-model may exist, below which the SCF may gradually decrease as the sub model would become smaller than the feature it is trying to model.

5. Results

5.1. Summary

This section presents the results obtained for the Dogbone example provided by UDRI. The first section illustrates the scanning method in a subregion of the sample and shows the local behavior of the SCF in a qualitative way. The second subsection presents the values of SCF for the whole sample, together with the geometrical error and a description of the calculation stages employed to find the solution.

5.2. Preliminary study

The purpose of this section is to show the local behavior of the SCF, and to illustrate the numerical scanning of a region of the top surface by mean of a fixed sub-model.

The results corresponding to this analysis are observed in Figure 29.

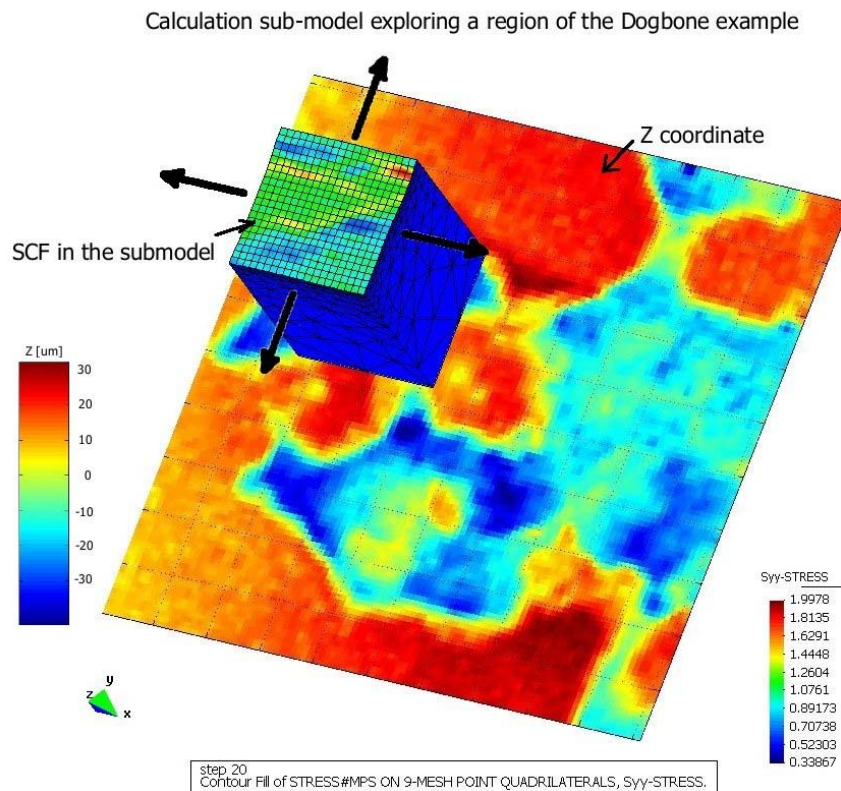


Figure 29: A 3D sub-model exploring a region of the original sample. The sub-model moves in any of the four directions indicated in black arrows. The color in the background image indicates height of the sample corresponding to the color scale on the left, the color in the top surface of the sub-model indicate local SCF, according to the scale at the bottom right.

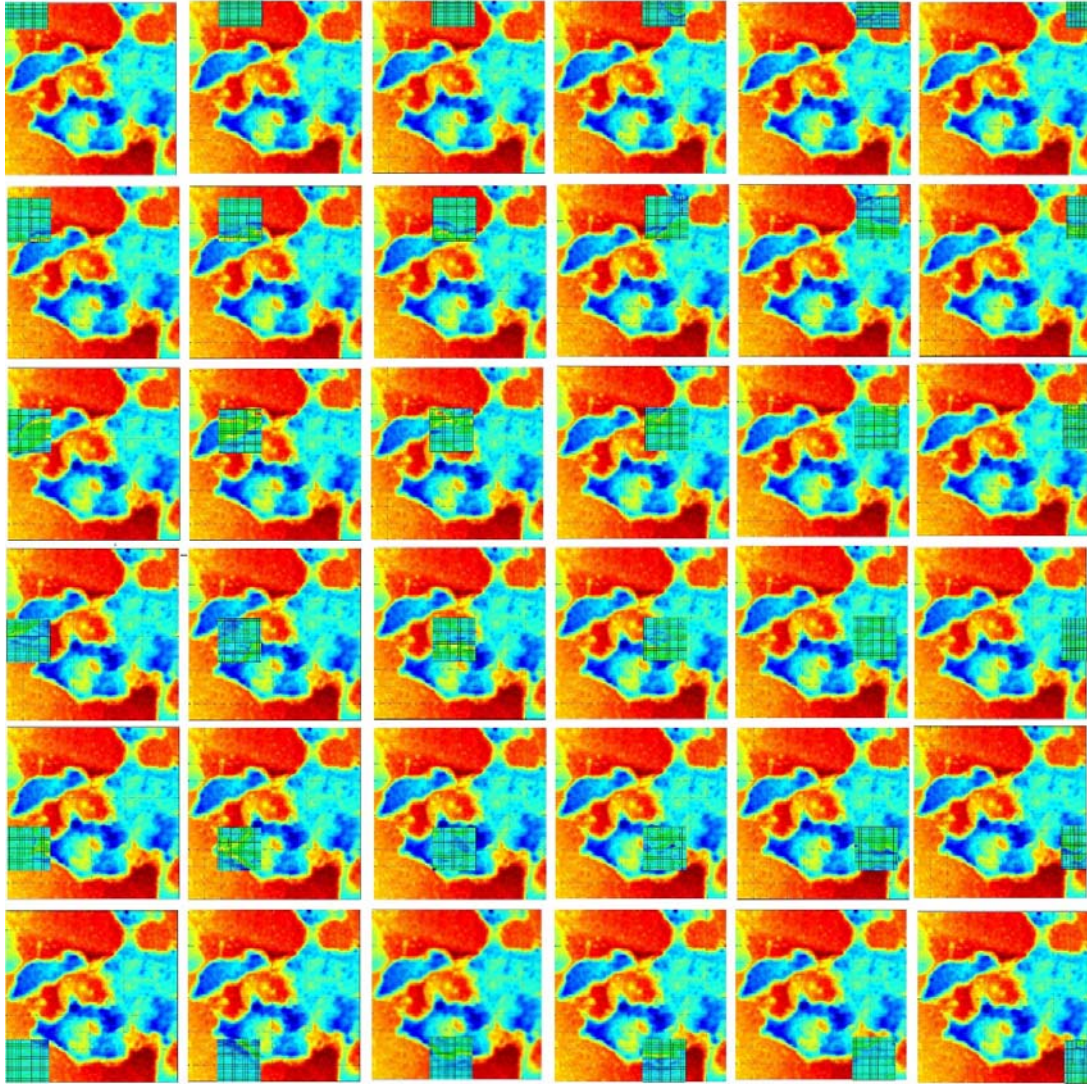


Figure 30: Parallel scanning of this surface enabled the localization of the maximum SCF values.

This sequence of images leads to the conclusion that the overlapping between sub-models can be reduced to one or two elements of the mesh. It can be observed that the SCF is a local effect. Appendix D shows an enlarged view of each sub picture in Figure 30.

5.3 The Dogbone sample

5.3.1. Results

This section presents the numerical results of stress concentration factor corresponding to the sample file 'Dogbone.txt' provided by UDRI. The experimental data consists of a structured array of 6788 by 5210 points describing the geometry. The spacing between points is $\delta x = \delta y = 6.345$ microns. The moving average technique applied to the original data yields the defeatured grids summarized in Table . K_f indicates the defeature factor, N_{px} , N_{py} , δx , and δy are the number of points and the corresponding spacing in x and y directions, respectively.

Kf	Npx	Npy	δx	δy
0	5210	6788	6.345	6.345
1	2605	3394	12.690	12.690
2	1302	1697	25.380	25.380
3	651	848	50.760	50.760
4	325	424	101.520	101.520
5	162	212	203.040	203.040
6	81	106	406.080	406.080

Table 6: Defeatured grids obtained by moving average applied to the original sample. db00 represents the original sample (without defeaturing)

The defeature level given by $K_f = 1$ is the highest resolution level adopted in this case study, since it is enough to provide the required geometrical accuracy. In general the maximum resolution level can be adjusted to any value, including $K_f = 0$ which represents the full resolution coming from the geometrical measurements.

The numerical approach used for this case included the following steps:

STAGE 0

The first stage involved solving the 5th degree defeatured level in order to obtain global (approximated) results for the whole sample without sub-modeling. This initial step provides a very rough estimate of SCF for the whole sample taking into account only large scale features whose characteristic length is close to the original size of the sample. This stage is unable to resolve small deep features and therefore it is not expected to provide reliable results of maximum values of SCF, which is due to local effects.

However large scale features are properly represented, thus the solution at this stage serves as good reference for the far field solution of small features solved further with more refined grids and sub-modeling. The results obtained at this stage can be observed in Figure 31.

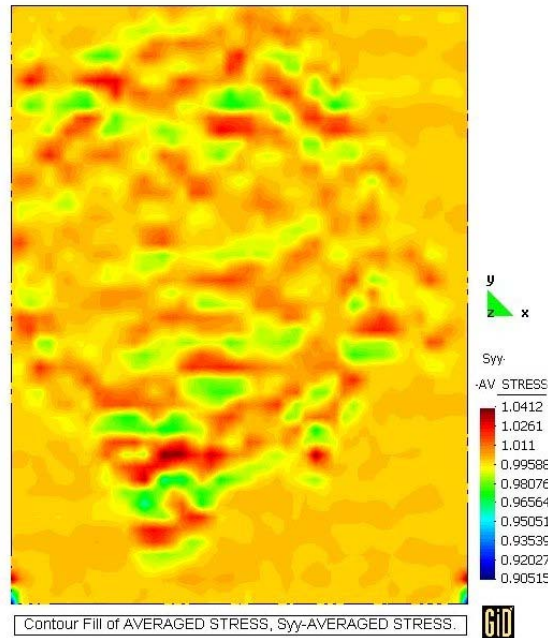


Figure 31: SCF obtained at calculation Stage 0.

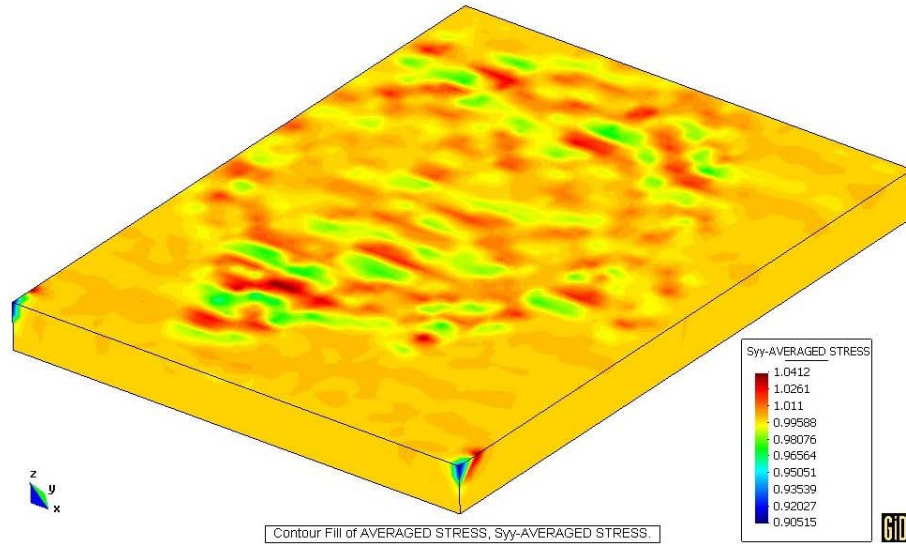


Figure 32: 3D view of the whole sample, and surface distribution of SCF. The model was solved at 5th resolution level without sub-modeling. The top surface was discretized with a mesh of 24x24 9-noded quadrilaterals.

STAGE 1

The second stage involves solving the 3rd degree defeatured geometry with 36 sub-models arranged in a 6 by 6 array. An overlapping of 20 sample points between sub-models was chosen in order to eliminate undesired border effects, introduced by boundary conditions. The top surface of each sub-model was represented by Nurbs-surfaces, computed from 151 by 151 sample points of the 3rd resolution level. Then, a computational grid of 20 by 20 quadrilateral curvilinear 9-noded elements was used in order to represent the nurbs-surface. The quads used for the top surface use quadratic interpolating functions (Q3_8 BEASY elements). Having created the mesh for the top surface, a proper 3D sub-model is created with its height specified according to eq $h_s = \min(h, 1.5W)$ (11). The lateral surfaces of the sub-model were meshed with triangular curvilinear elements with linear interpolating functions (T2 BEASY elements). The bottom surface of the submodel was meshed with Q3_8 BEASY elements. The boundary conditions applied to this submodel are shown in Figure 33. After solving each submodel the results for the SCF were assembled into a single array of results of 2605 by 3394 entries, corresponding to the first defeatured resolution level. The results obtained at this stage can be observed in Figure 34.

The dimensions and location of each submodel in this stage, as well as the CPU computation time in a PC Pentium IV 3GHZ 2GB RAM running under Windows XP, are summarized in Table 7.

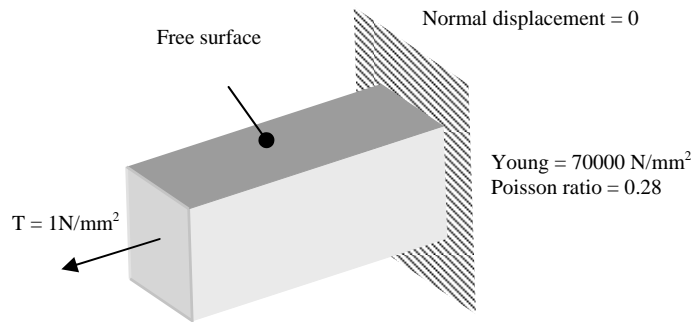


Figure 33: Boundary conditions applied for the sub-model. The front face is subjected to unitary traction, the top surface (with roughness) is considered as free, and the remaining four surfaces have zero normal displacement.

#	lx0	lx1	ly0	ly1	Time
1	1	151	1	151	20:27:36
2	131	281	1	151	20:39:57
3	261	411	1	151	20:52:08
4	391	541	1	151	21:04:15
5	521	650	1	151	21:16:30
6	1	151	131	281	21:28:56
7	131	281	131	281	21:41:14
8	261	411	131	281	21:53:42
9	391	541	131	281	22:05:39
10	521	650	131	281	22:17:24
11	1	151	261	411	22:29:48
12	131	281	261	411	22:41:53
13	261	411	261	411	22:54:09
14	391	541	261	411	23:06:21
15	521	650	261	411	23:18:43
16	1	151	391	541	23:31:33
17	131	281	391	541	23:43:47
18	261	411	391	541	23:55:57
19	391	541	391	541	00:07:54
20	521	650	391	541	00:20:22
21	1	151	521	671	00:33:00
22	131	281	521	671	00:44:51
23	261	411	521	671	00:56:49
24	391	541	521	671	01:09:07
25	521	650	521	671	01:21:02
26	1	151	651	801	01:33:33
27	131	281	651	801	01:45:38
28	261	411	651	801	01:57:42
29	391	541	651	801	02:10:03
30	521	650	651	801	02:21:55
31	1	151	781	847	02:34:34
32	131	281	781	847	02:52:14
33	261	411	781	847	03:09:34
34	391	541	781	847	03:26:46
35	521	650	781	847	03:43:51

Table 7: Table summarizing location, and size of each submodel based on a third resolution level ($K_f = 3$). The first column is the Id of the submodel, I_{x0} , I_{x1} , I_{y0} , I_{y1} are the coordinates of the corners of the sub-model, in SUQG indices corresponding to $K_f=3$, the last column indicates the time when the calculation of the sub-model started.

The relevant properties common to all sub-models in this stage are the following:

Resolution level: $K_f = 3$

$N_{px} = 651$, Number of points in x direction (fields)

$N_{py} = 848$, Number of points in y direction (records)

$\Delta x = 50.76$, ! x spacing of original data [microns]

$\Delta y = 50.76$, ! y spacing of original data [microns]

depth = 3175., ! Depth of the sample [microns]

Sequential submodelling

overlap = 20, ! Number of sample points to be ignored from edge of submodel

size_x = 151, ! Size of submodel in size_x = x (ixb - ixa)+1

size_y = 151, ! Size of submodel in size_y = y (iyb - iya)+1

Ncell_x = 20, ! Number of structured cells in x direction for top surface

Ncell_y = 20, ! Number of structured cells in y direction for top surface

The results for SCF obtained in this stage are shown in Figure 34, the circles indicate critical spots surrounding regions of SCF greater than 1.15. The corresponding geometrical error is shown in Figure 37.

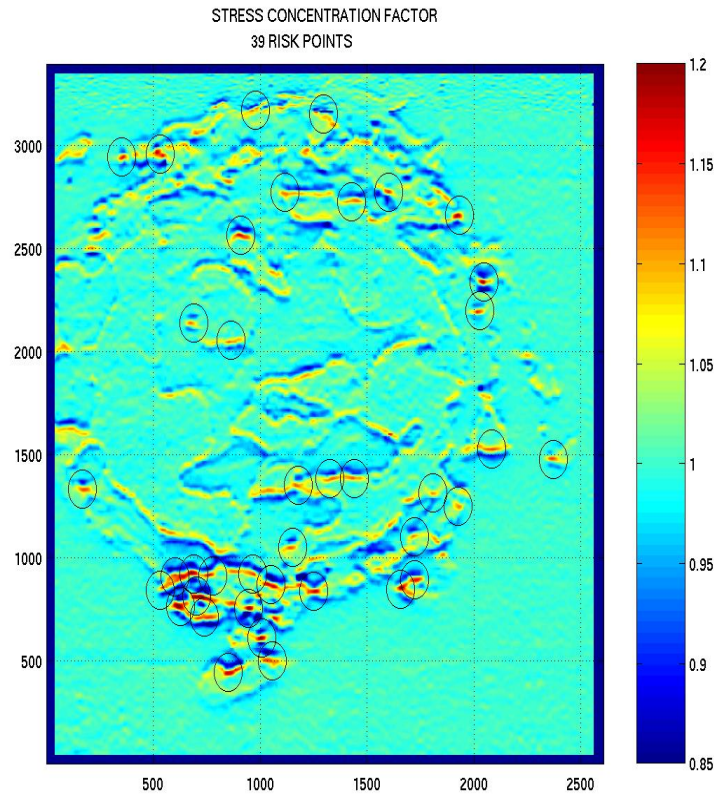


Figure 34: SCF obtained after stage 2. Panning of the whole sample data with 36 sub-models, specified in Table 7. The calculation is based on the Dogbone sample with a 3rd resolution level. The results were assembled into a matrix of, corresponding to the resolution level $K_f=1$ of the original sample data.

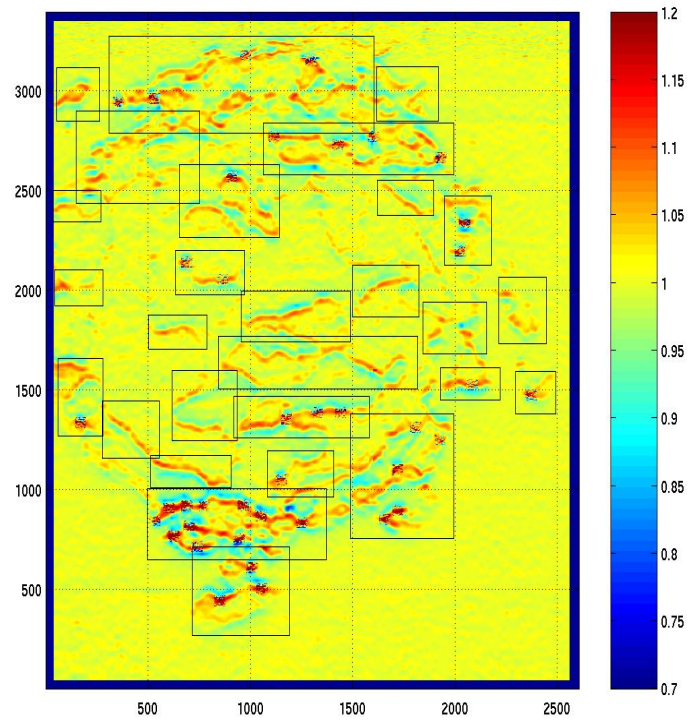


Figure 35: Definition of sub-regions for stage 2 from the results obtained in stage 1 for the SCF.

STAGE 2

This calculation stage involved 74 iterations of sub-models based on a resolution level $K_f=2$. The results of SCF obtained in the previous stage are used in order to detect the regions of the sample with SCF higher than 1.05, as shown in Figure 35. The regions identified are then solved with more refined sub-models, i.e. with increased geometrical resolution. All regions having less than $SCF=1.05$ are excluded from further calculation in order to reduce as much as possible redundant computing time.

It should be noted that threshold values and resolution levels can be set to any level depending on the particular sample being solved.

The results obtained at this stage can be observed in Figure 36.

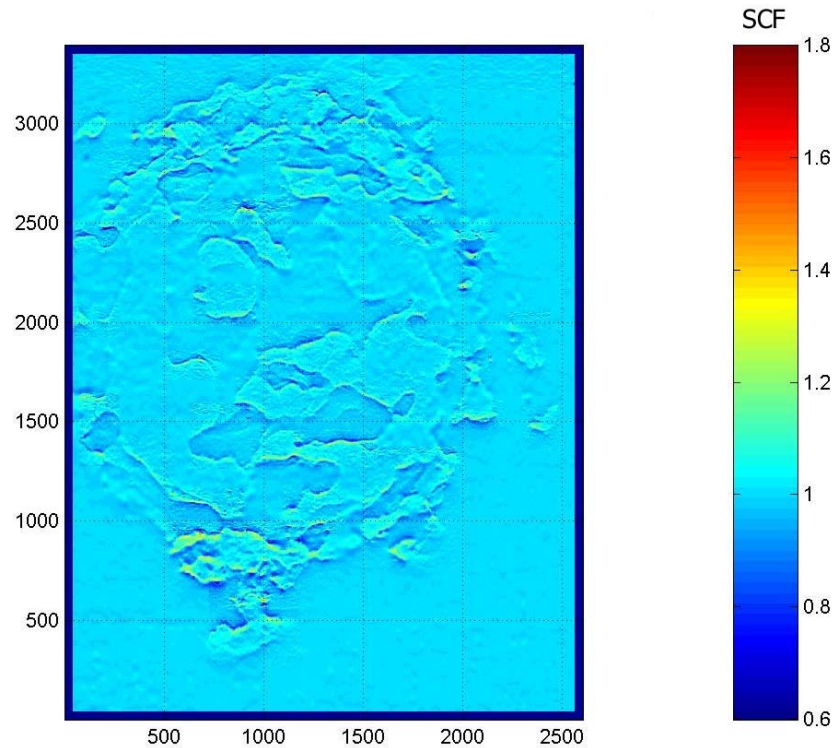


Figure 36: SCF obtained in Stage 2

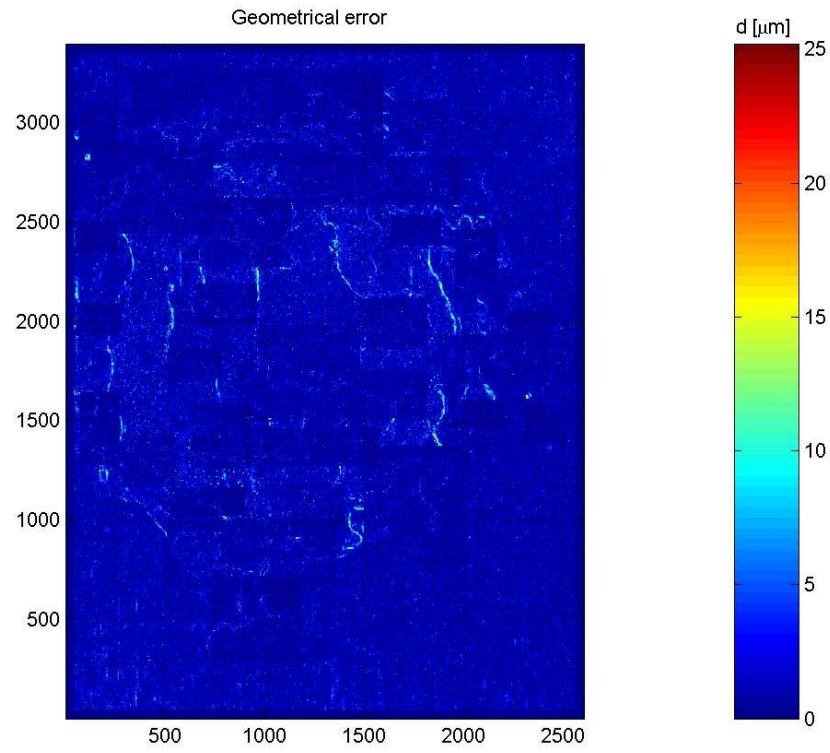


Figure 37: Geometrical error in stage 2.

STAGE 3

Results obtained in stage 2 were used in order to define the location of the sub-models in stage 3, which consisted in 223 sub-models distributed as indicate in Figure 38. The threshold SCF for this stage is 1.2, i.e. each sub-model considered at this stage presented a SCF higher or equal than 1.2 from the previous stage.

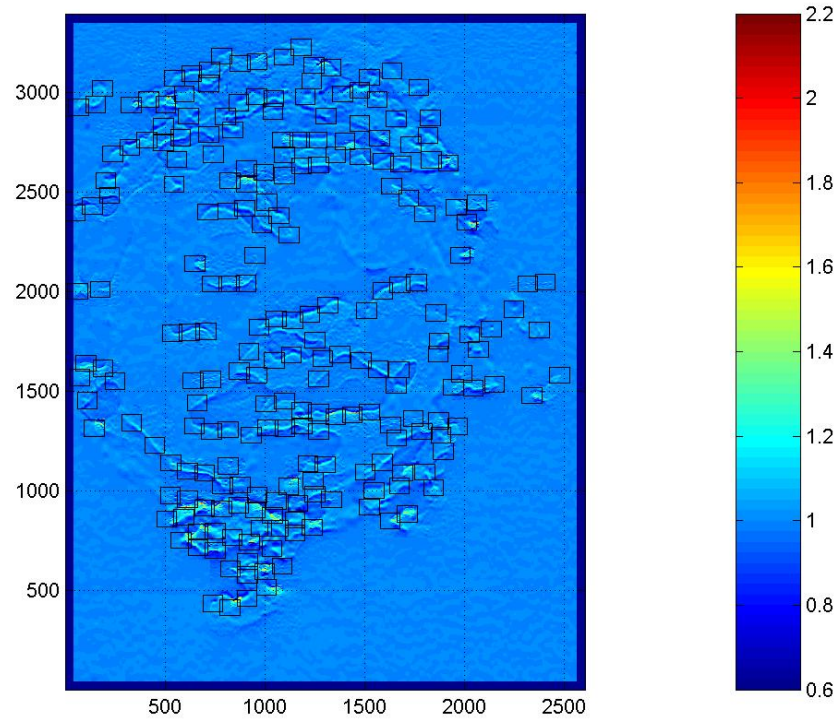


Figure 38: Definition of sub-models for stage 3 from the SCF computed in stage 2.

The results obtained in stage 3 can be observed in Figure 39, together with the regions.

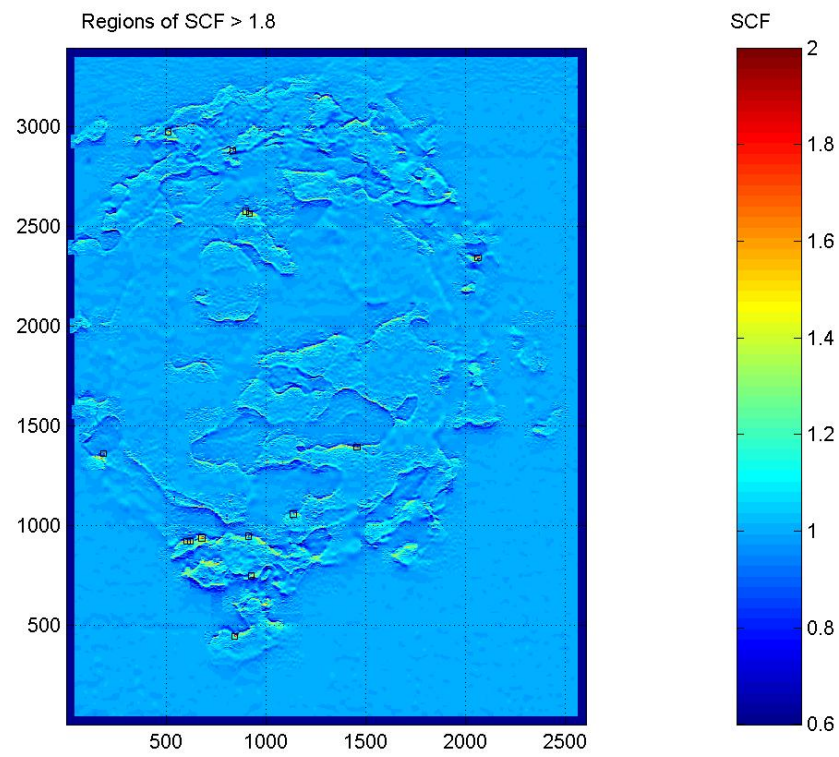


Figure 39: SCF obtained in Stage 3.

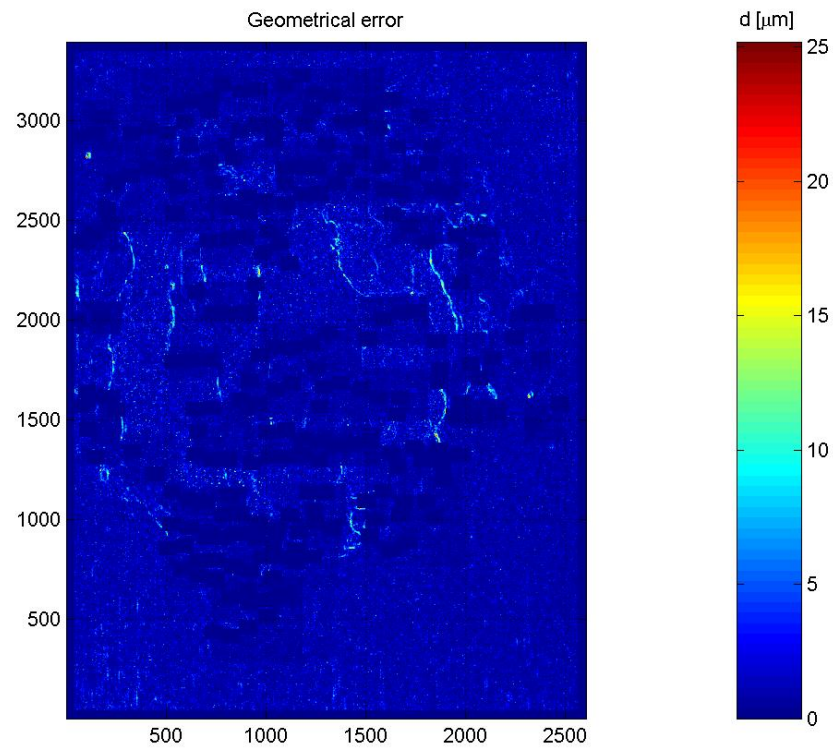


Figure 40: Geometrical error at Stage 3.

STAGES 4-7.

Each subregion spotted in the previous stage is solved with an assembly of sub-models located at points where SCF is greater than a certain threshold (manually defined). Calculation stages 4 to 7 are based on the same procedure, but the threshold in each one of them increases gradually, the size of the sub-models reduces, and the grid resolution increases. The geometrical error at each stage has been measured and assembled into a matrix in the same way as the SCF.

In this way, the accuracy is measured by the degree to which each sub-model represents the geometry given by the original sample data. The convergency of the results is then ensured by refining the mesh and reproducing the same results obtained in a coarser mesh.

The final results for the Dogbone example are shown in Figure 41, a close up view of the results in the lower region which presents more risky zones is shown in Figure 42 and Figure 43. Finally, the assembled picture of geometrical error corresponding to the final results is presented in Figure 44. The geometrical error in the submodels of the last iterations is lower than 0.5 micrometers.

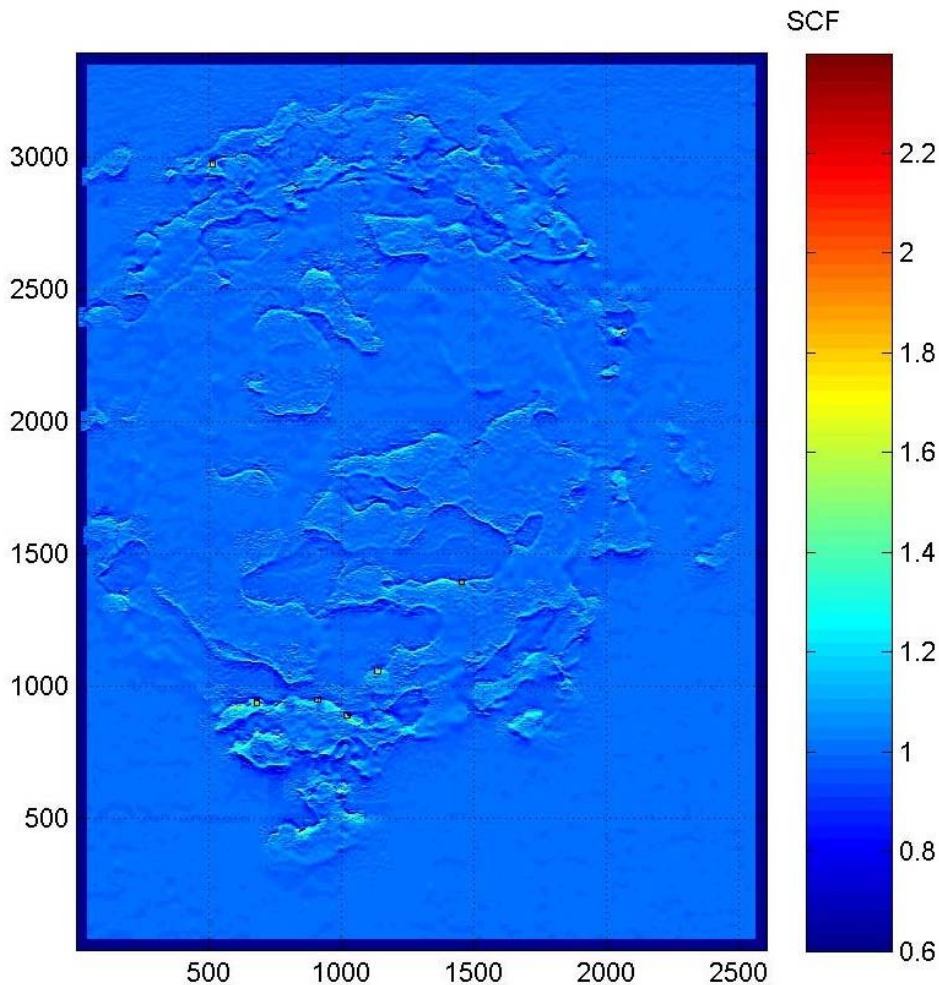


Figure 41: Final result for SCF obtained at the end of stage 7. The square symbols indicate the points of maximum SCF. (SCF > 2.2). The colorbar on the right indicates the scale of SCF.

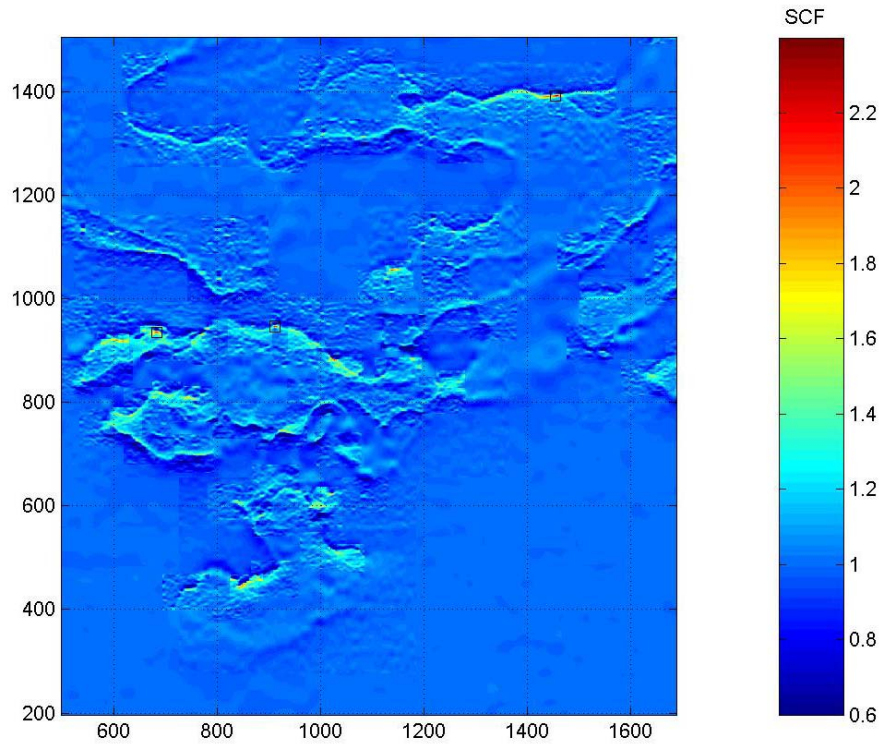


Figure 42: Close up view of the SCF in the lower region of the sample

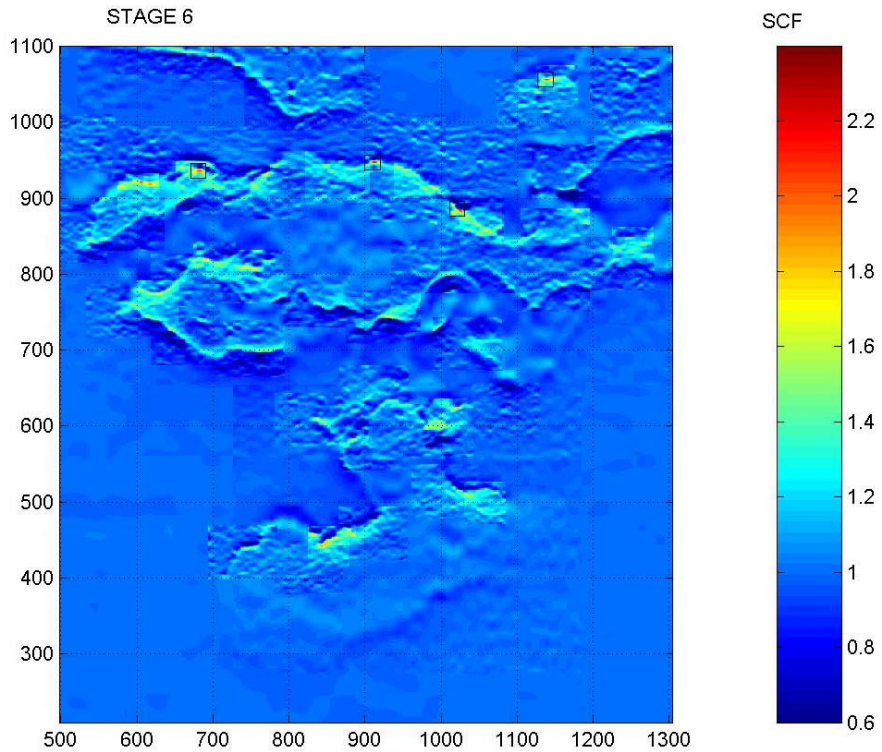


Figure 43: Close up view in the lower region of the sample.

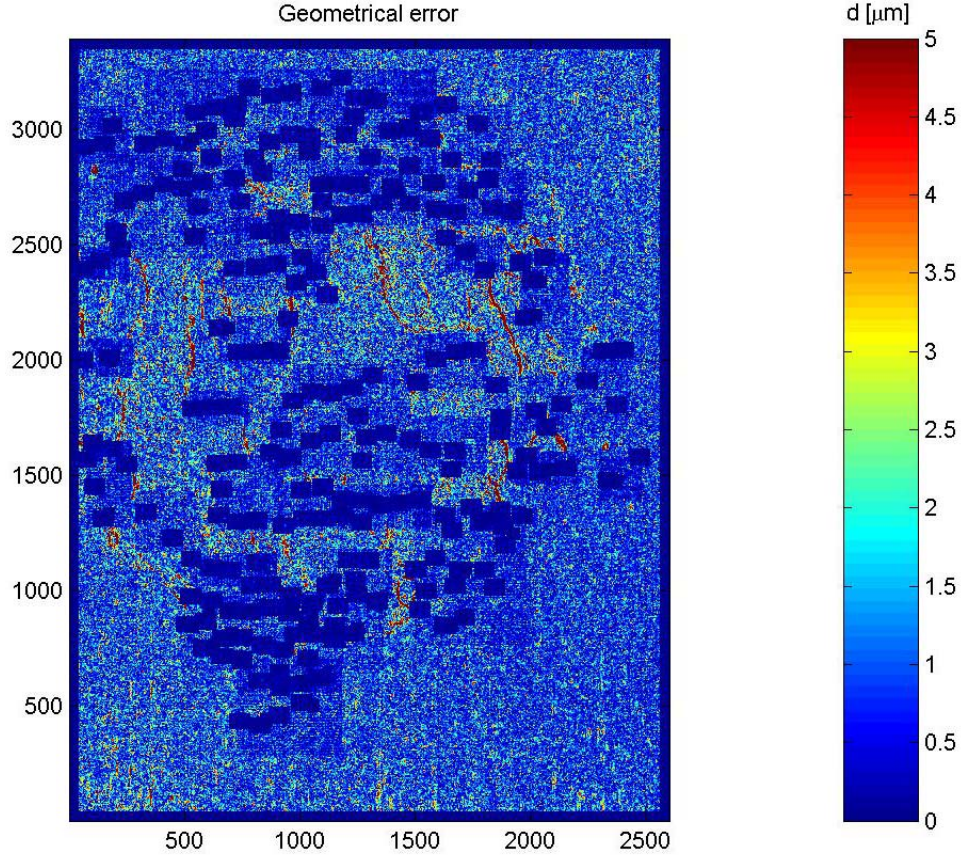


Figure 44: Geometrical error of the final result, measured in micrometers. For the sub-models of the last iterations, the error is less than 0.5 microns, and these regions show up as dark rectangles.

The evolution of maximum SCF computed for the whole sample at the different calculation stages can be observed in Figure 45. The relative error between a given calculation stage and the converged maximum value of SCF is defined according to:

$$\eta := \frac{\max(SCF)_S - \max(SCF)_F}{\max(SCF)_F} \quad (12)$$

where $\max(SCF)$ is the maximum SCF computed at a given stage, the subindex S indicates a calculation stage from 0 to 7, and the subindex F indicates the final calculation stage, for which a converged solution is accepted.

The quantity η , as a measure of the relative error of SCF, as a function of the accumulated number of iterations can be observed in Figure 46.

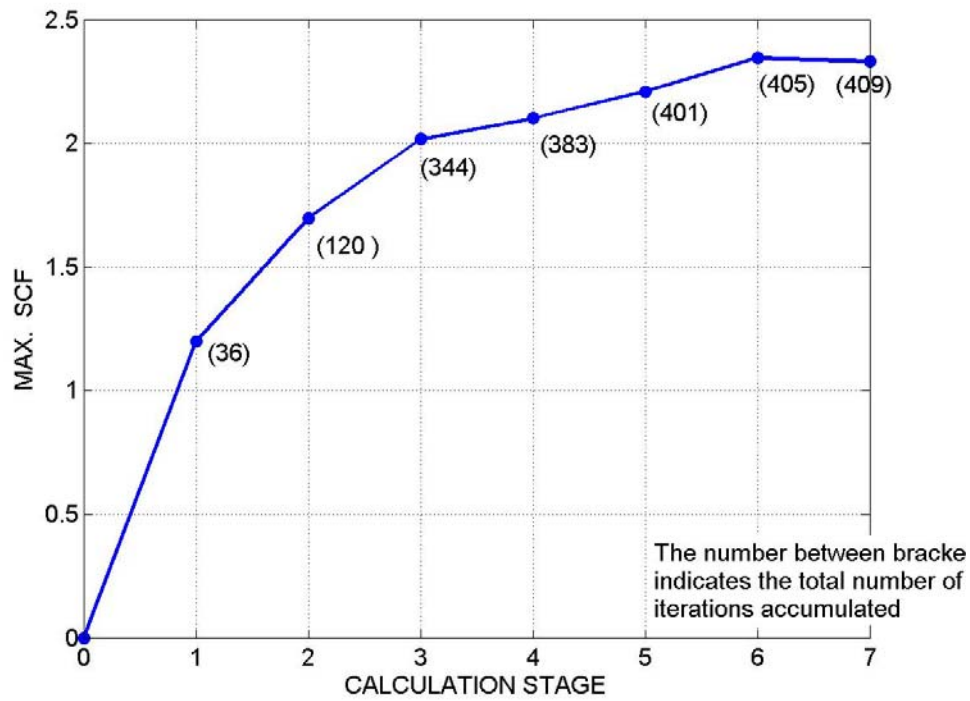


Figure 45: Evolution of the maximum SCF found after each calculation stage. This shows the convergency property of the method.

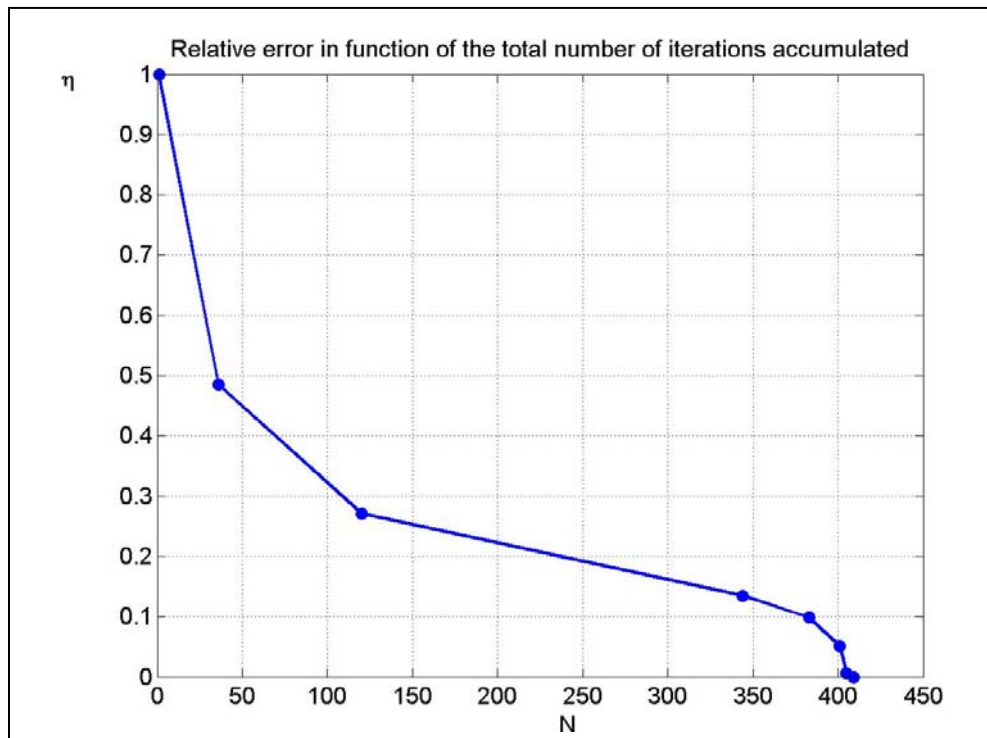


Figure 46: Relative error of Maximum SCF as a function of the accumulated number of iterations.

5.3.2. Conclusions

The results obtained in this case study allow us to validate the proposed numerical approach, and at the same time to conclude that the maximum value of stress concentration factor is $SCF = 2.38$. The local geometrical error in each sub-model has been reduced to approximately $0.5 \mu m$. The total number of iterations employed for this example was 408, although less than 100 iterations would have been enough to find the total maximum ignoring the regions of the sample with SCF lower than 1.5. Each iteration requires the solution of a small BEASY model consisting of less than 1000 elements, with quadratic elements on the corroded surface and linear elements on the other faces. This calculation takes between 8 and 15 minutes in a Pentium IV 3GHz processor 516MB RAM PC with a relatively slow disc. The technique developed has many aspects that provide opportunities for optimization. Thus, a more efficient implementation, based on the approach proposed in this work would reduce dramatically the total number of iterations.

6. Conclusions

6.1. Concluding remarks

The computational tool developed allows the user to:

- 1- Defeature the original geometrical data to any resolution degree,
- 2- Create automatic 3D sub-models (models) out the surface data, suitable for conducting stress analysis with the BEASY software.
- 3- Utilize an automatic sub-modeling technique, including: panning, zooming, change of geometrical resolution, and size of sub-model.
- 4- Assemble results coming from different sub-models into a unique data set.

The validation tests conducted so far indicate that the sub modeling approach offers stable and consistent numerical results of SCF. The SCF converges with grid refinement factor.

The maximum SCF found for the Dogbone sample is: $SCF = 2.38$. The total number of iterations required to obtain the field of SCF in the potentially most dangerous edges of the sample was 408. This figure may be reduced to around 100 iterations by disregarding SCF results near but not at the local maximum. Thus, the 223 iterations required in the third calculation stage may all be skipped in this case, as well as some other intermediate results.

The procedure provides the full stress and strain tensor on the surface not just the SCF. Therefore data is available for fatigue life simulations.

The sub-modeling strategy presented in this work can be adopted as long as the thickness of the sample is large in comparison to its characteristic fluctuation (i.e. the depth of the pitting damage). Hence, the local behavior of the solution allows simulation of independent sub-models and eliminates the need of a more expensive multigrid scheme. A multigrid approach would be useful in cases of thin samples, having a thickness of approximately 100 microns or less.

The defeaturing tool is able to remove pit-like features below a specific size and to generate new models suitable for stress analysis. In addition, the defeatured data is used to create a nurbs-surface which can then meshed with any number of elements, thus adding more flexibility to the overall defeaturing process.

The suite of tools developed has been successfully applied to the sample data contained in Dogbone.txt yielding stable results for the stress concentration factor.

6.2. Future tasks

6.2.1 Task 5

Future tasks contemplated for Task 5 are summarized in the following itemized list:

- 1) To develop a user-friendly interface to control and automate the whole solution process. At the moment the set of tools is controlled by setup scripts, graphical output is done by mean of BEASY_GiD and Matlab.
- 2) To systematically run a series of test models with the automated process to fully validate and test the software.
- 3) If data is available, compare the predicted locations of the high stress areas with experimental test data.
- 4) The models solved provide the full stress tensor on the corroded surface. If strain life based fatigue models are to be used it would be of value to define an export format for this data in addition to the SCF.

6.2.2 Correlation between SCF and local curvature of the sample

It is recommended that an additional study be added to the proposed Task 5 based on the following.

- 5) Regions of high SCF are related to regions of high local curvature, as can be seen by comparing the results shown in Figure 47 and Figure 48, which represent a density plot of SCF and of the quantity $\|\nabla\|\nabla Z(x, y)\|$, respectively.

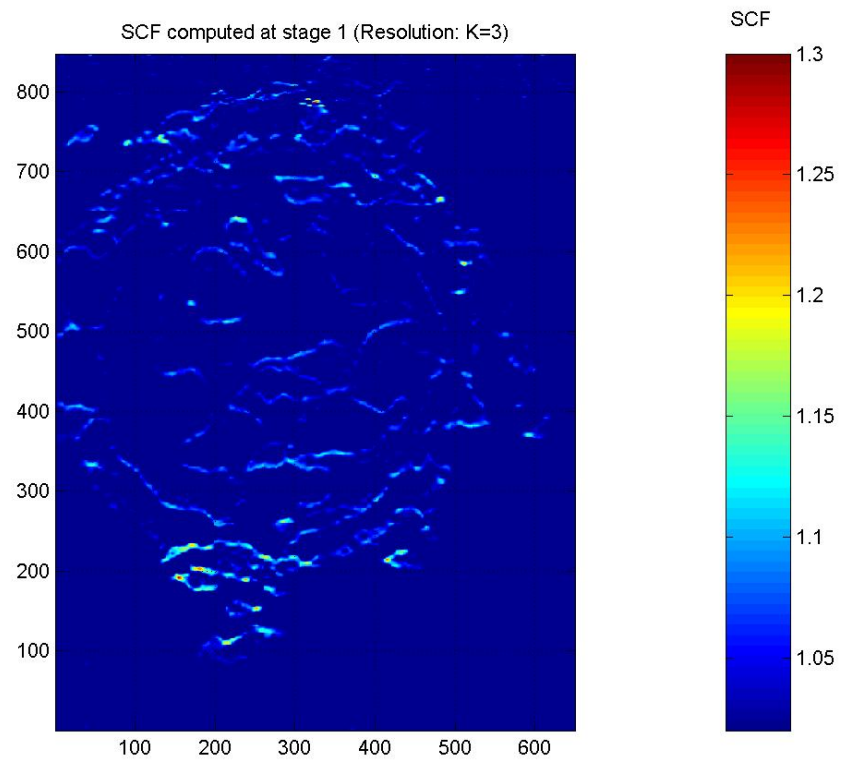


Figure 47: SCF results of the Dogbone example computed at resolution level $K = 3$.

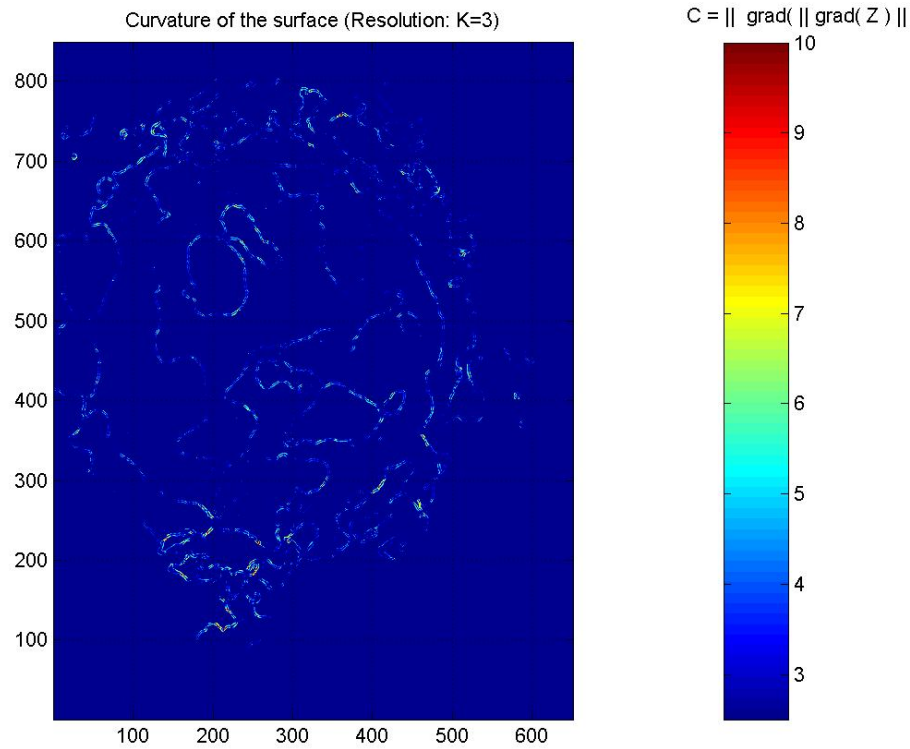


Figure 48: Local curvature of the top surface of the sample. This figure can be compared with the results for SCF in order to appreciate the correlation between SCF and curvature.

In order to reduce the total number of iterations for very large samples, intermediate submodels should be avoided as much as possible. In particular a low resolution scanning of the whole sample requires a significant number of iterations. But only few of them will lead to critical SCF's. This initial stage could be avoided by solving only those sub models whose local curvature exceeds certain threshold. Hence, in order to optimize the sub-modeling technique, it is important to investigate the correlation between the local curvature of the top surface and the SCF.

6.2.3 Further Tasks

If further optimization of the technique was deemed necessary the following tasks could be performed.

6) At the moment all geometrical information is based on structured grids, with constant spacing. A step forward in this approach would be to contemplate both structured grids with varying grid spacing and unstructured grids with triangular meshes for the top surface. The more organized the geometrical information, the higher computational efficiency; however in many cases structured grids are not suitable for irregular geometries. In addition, variable spacing between geometrical points will be more adequate for grid adaptive methods based on moving existing points towards regions of steep gradients of SCF.

7) To integrate an adaptive method that increases the grid resolution in regions of the top surface with both small local radius of curvature and steep gradient of SCF.

7. Appendices

7.1. APPENDIX A: Computational implementation

The set of tools developed are intended to be used in the following way:

Step 1) Create all the defeatured sample files that will be considered during the analysis

...> `defeature.exe`

This step will create all the required defeatured levels of the original sample data

Step 2) Propose an iteration scheme in order to start solving the problem

> `design_iterations.exe`

Step 3) Supervise the sequence of iterations to be performed by editing as much as you like the file `iterations.dat`

Step 4) Launch the sequence of calculations

> `iterate.exe`

Step 5) Once finished, a series of BEASY_GID and BEASY result files will be created. At this stage the user can examine them and conduct detailed analysis of stress concentrations.

Step 6) Merge the sequence of results selected by the user in `setup_merge.dat` in order to put them altogether in the same format as the input data file of the original sample. (same format as `dogbone.txt`) This step creates geometrical analysis files and SCF files at the defeatured level required by the user.

7.2. APPENDIX B: User reference

`create_gid_batch.exe`

Creates a BEASY_GID batch file in order to build a model in non-interactive way.

`setup_submodel.dat`

Is used to configure the submodel that `create_gid_batch.exe` will create. It is written automatically by `iterate.exe`, but also for a particular model, it can be adjusted automatically.

`iterate.exe`

Is the program that control the iterations. It takes as an input the files: `setup_iterations.dat` and `iterations.dat`

The iterations will be performed according to the contents of file `iterations.dat`.

On each loop of iteration, it executes the batch file prescribed in the `setup_iterations.dat` file.

The purpose of this batch file is to give full control to the user through a batch process after the iteration is processed.

In this case, the batch file used is called `runall.bat`

`runall.bat`

Batch file that launches BEASY_GID in non interactive way, launches BEASY and performs some file rearrangements. The commands used to launch beasy or BEASY_GiD can be changed in this file

`design_iterations.exe`

Its purpose is to aid the user with different iteration strategies:

- + Parallel scanning/ panning (Mode 2)
- + Zooming in/out (mode 3)
- + Sequential mesh refinement in a fixed size model (mode 4)
- + Sequential change of depth of the submodels
- + Defeaturing
- + Analysis of existing SCF files. The series of windows will be centered at point whose SCF exceed a threshold given by the user. (mode 5)

The input of this program is `setup_submodel.dat`, the output is the file `iterations.dat` which is required in order to control the iterations by `iterate.exe`. The outcome of this file may be inspected by the user in order to customize the windows.

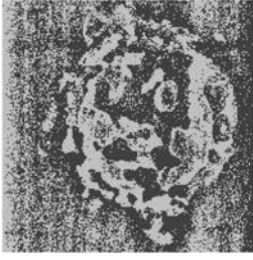
At the end of `iterate.exe`, a sequence of solution files (BEASY plus BEASY_GID files) will be created in the working directory. The files can be sequentially read by BEASY_GID, by using the command `load_multiple_files`. It is advisable to conduct a BEASY_GID analysis before continuing solving other submodels in the sample file. Once the results are produced, geometrical errors can be analyzed for each particular submodel, by using `geoerror.exe`

defeature.exe

This program creates a defeatured sample file out of the original one (Dogbone.txt, for example)
The output is another file of the same format as the original, but with simplified geometry. The setup file: "setup_defeature.dat" is self explanatory.
SAMPLE FILES.

7.3. APPENDIX C: Dogbone example

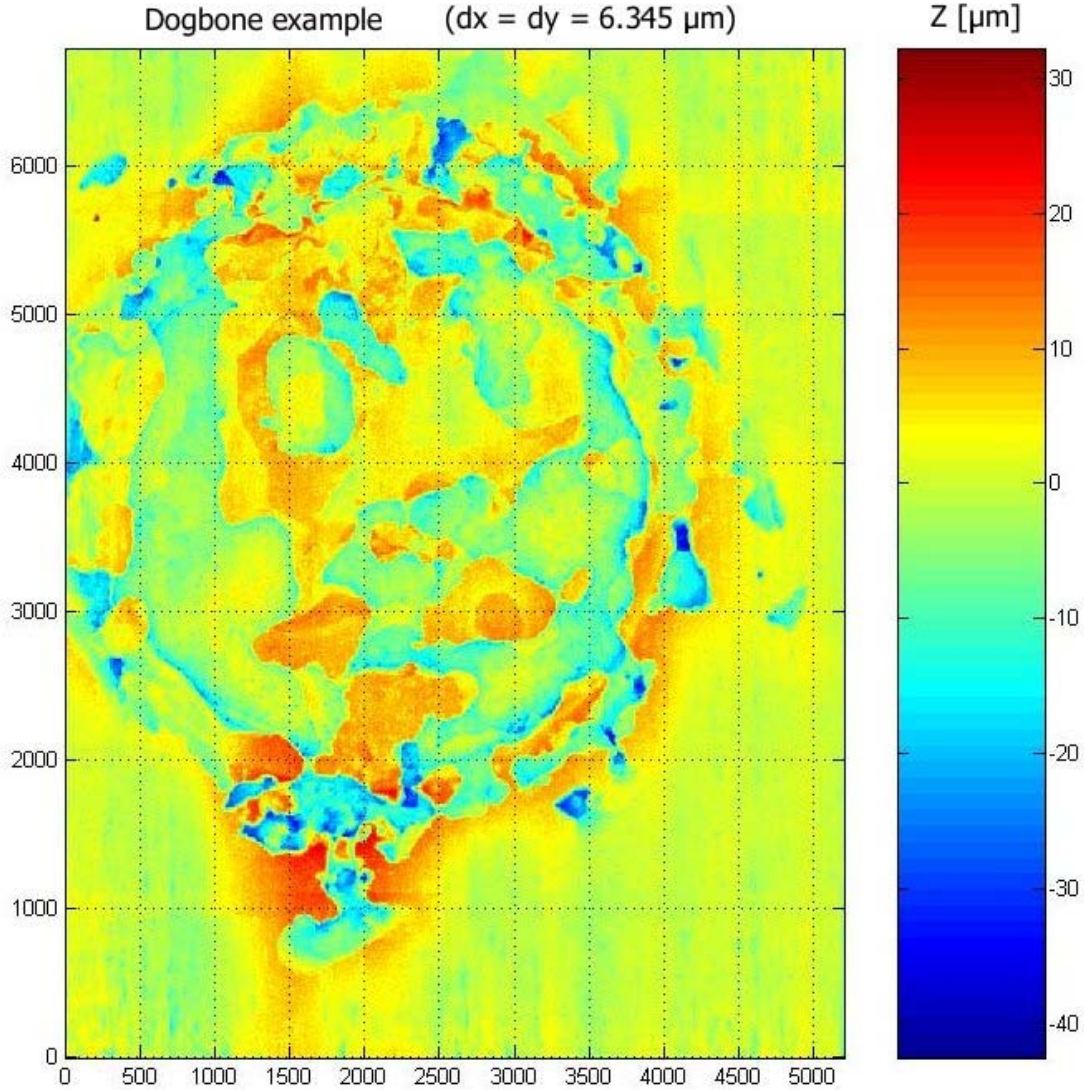
The Dogbone example is the name given to the original data provided by UDRI. Pattern and statistics of this sample are summarized below:



(a) Pattern

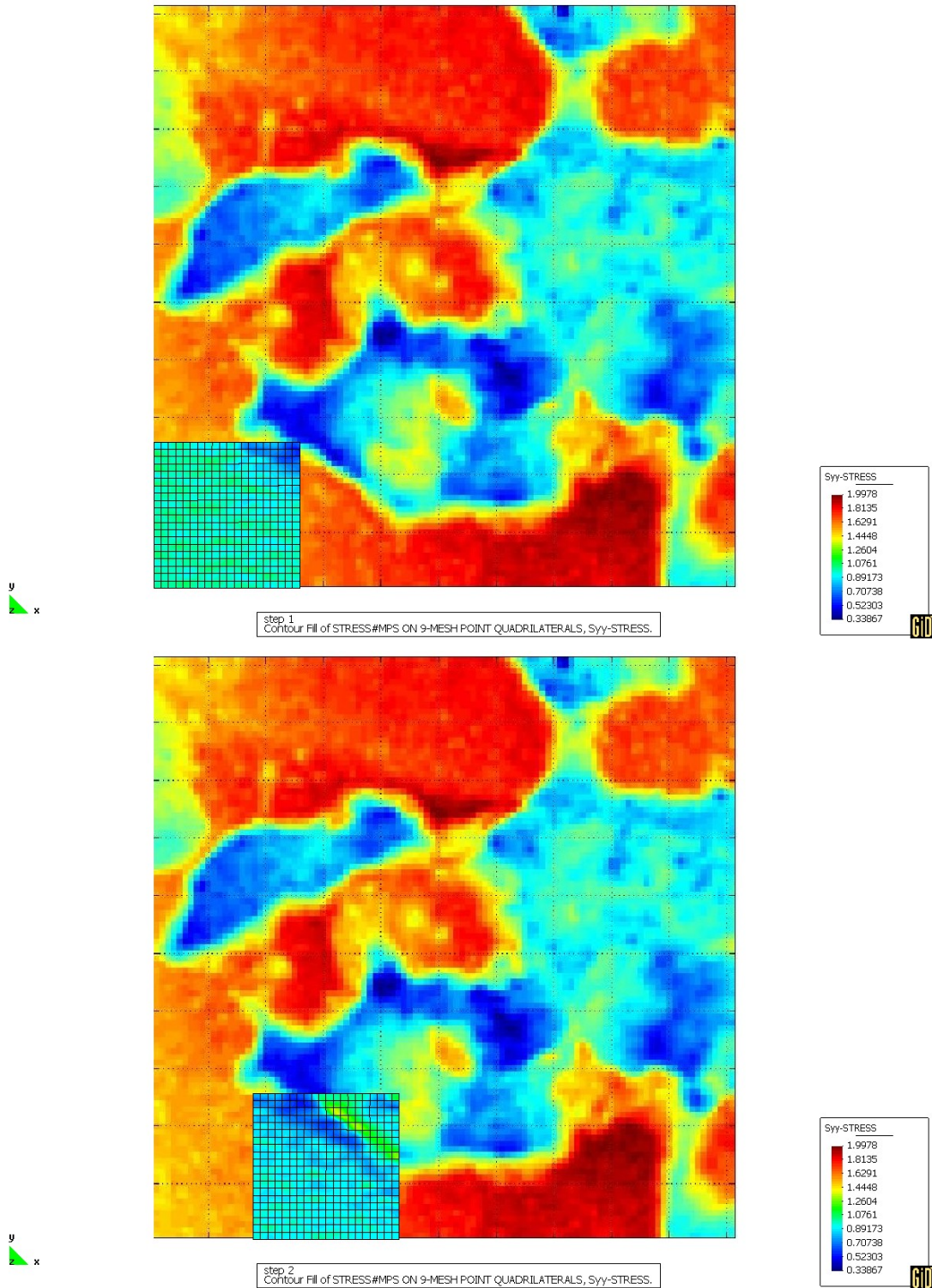
$N_x = 5210$
 $N_y = 6788$
 $N_{points} = 35365480$
 $\Delta x = 6.345 \mu\text{m}$
 $\Delta y = 6.345 \mu\text{m}$
 $Z_{max} = +35.9930 \mu\text{m}$
 $Z_{min} = -44.8560 \mu\text{m}$
 Size = $(33.051 \times 43.064) \text{ mm}$
 Thickness = $1/8 \text{ inch} = 3.125 \text{ mm}$

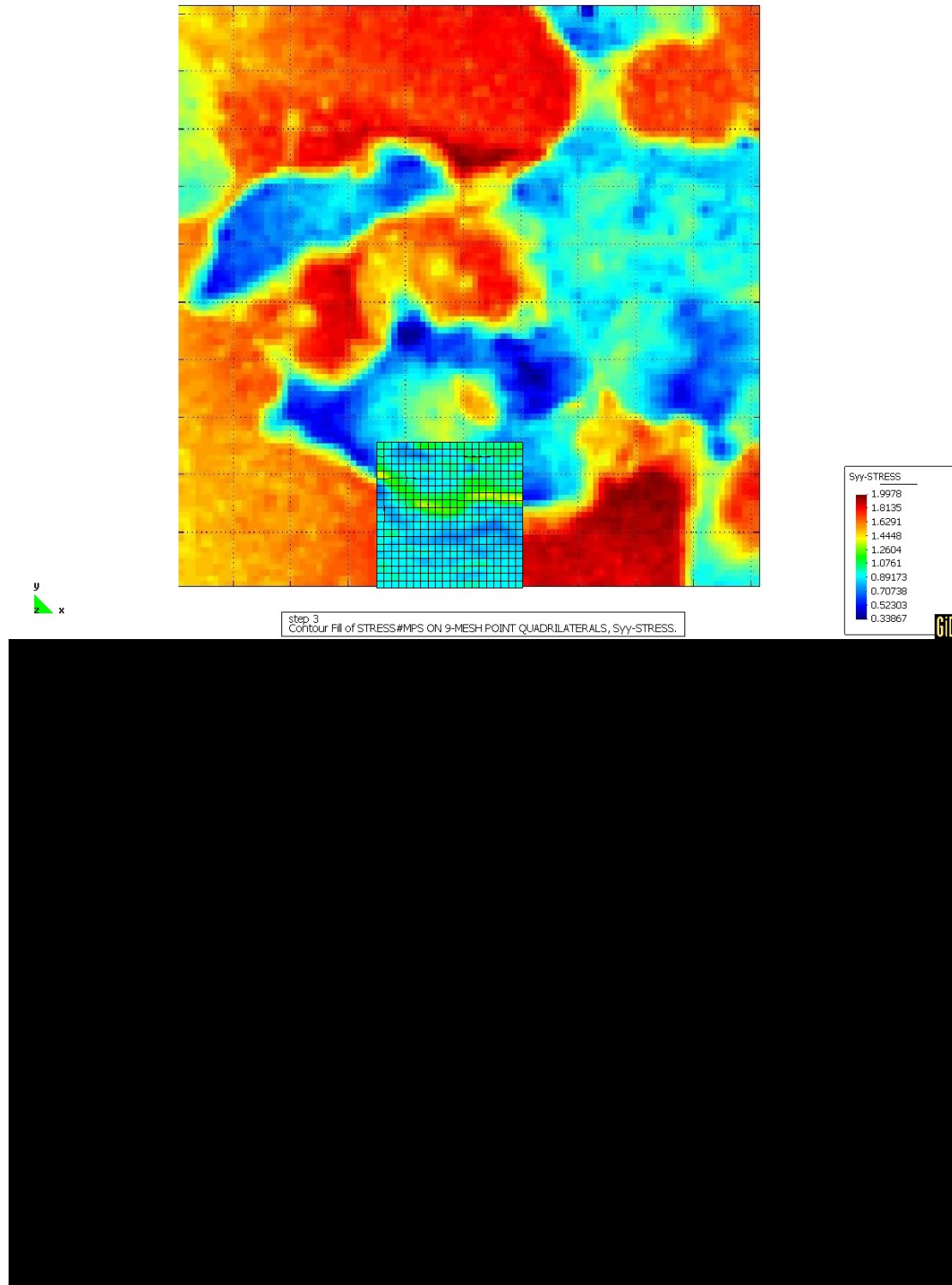
(b) Statistics

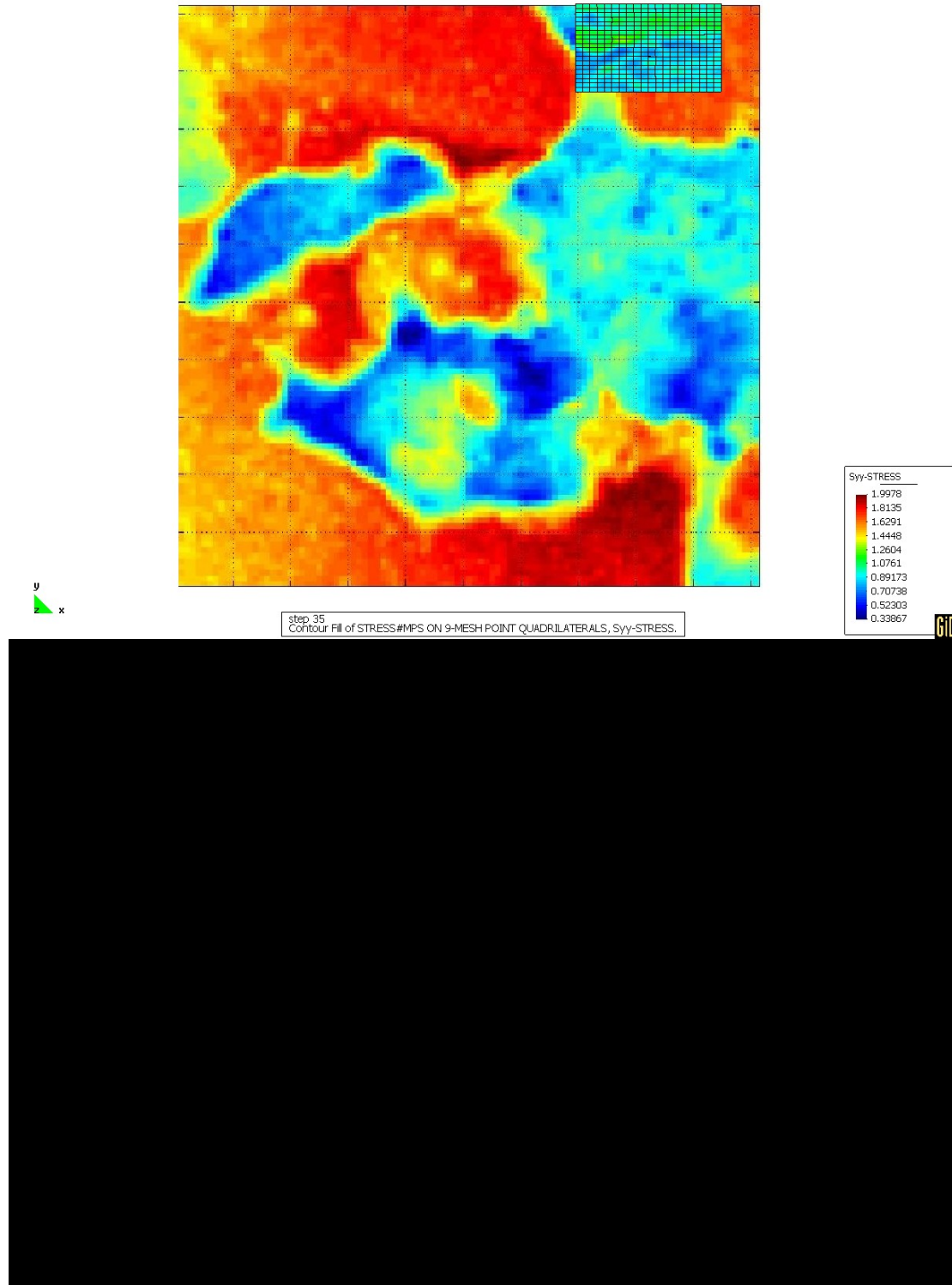


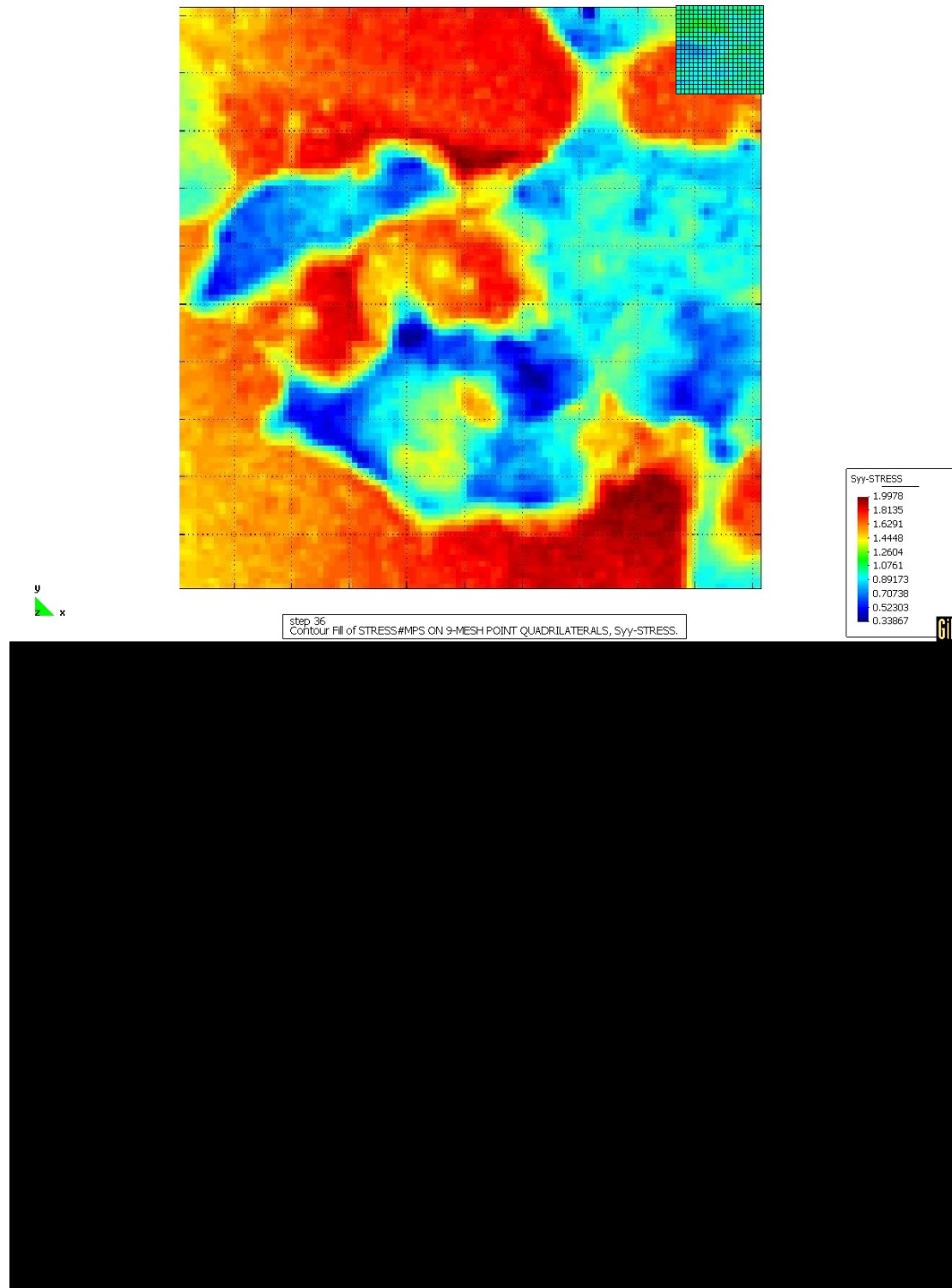
7.4. APPENDIX D: Enhanced images of Figure 30

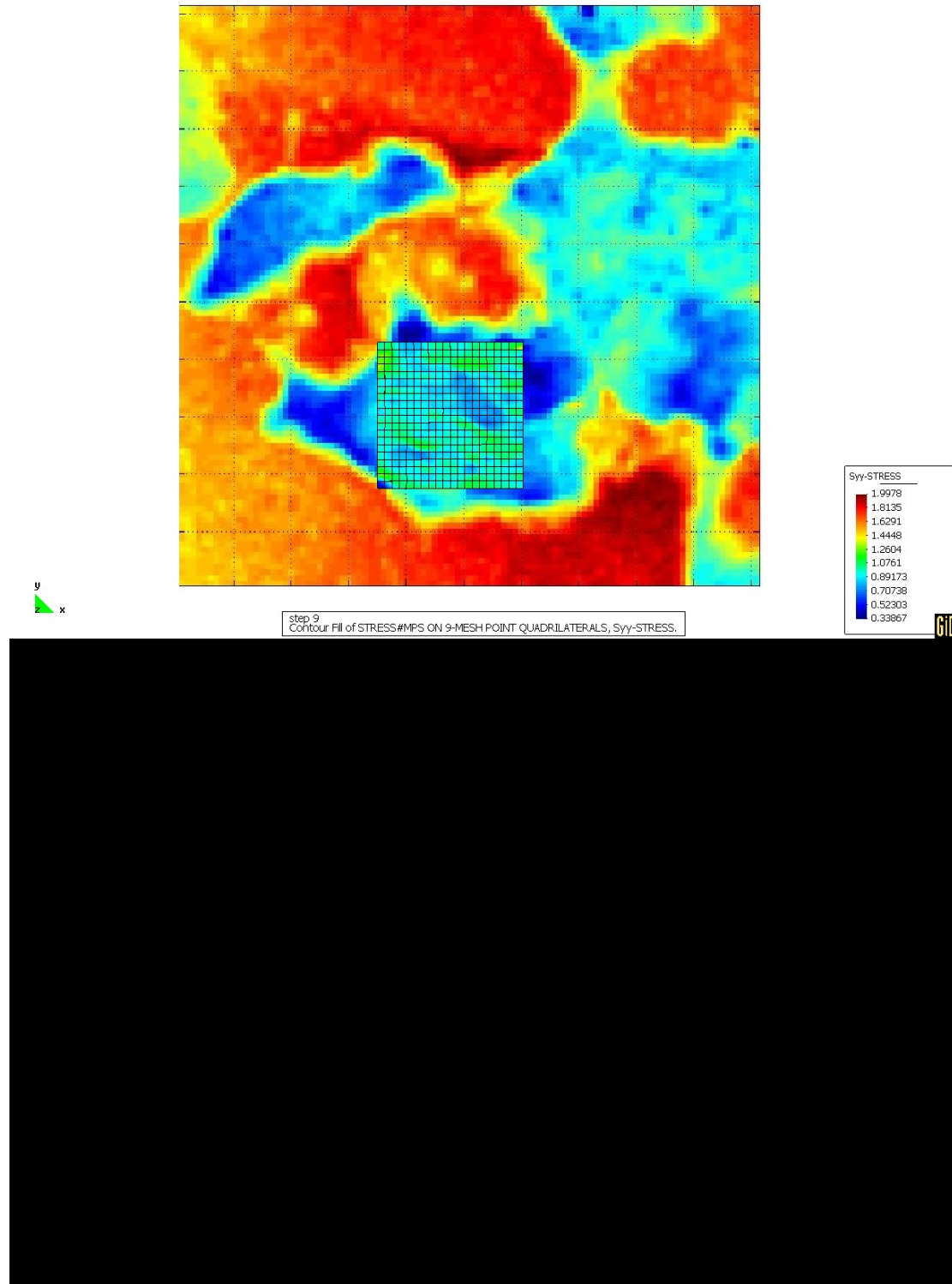
This appendix presents a sequence of images of a sub-model exploring the top surface, corresponding to Figure 30.

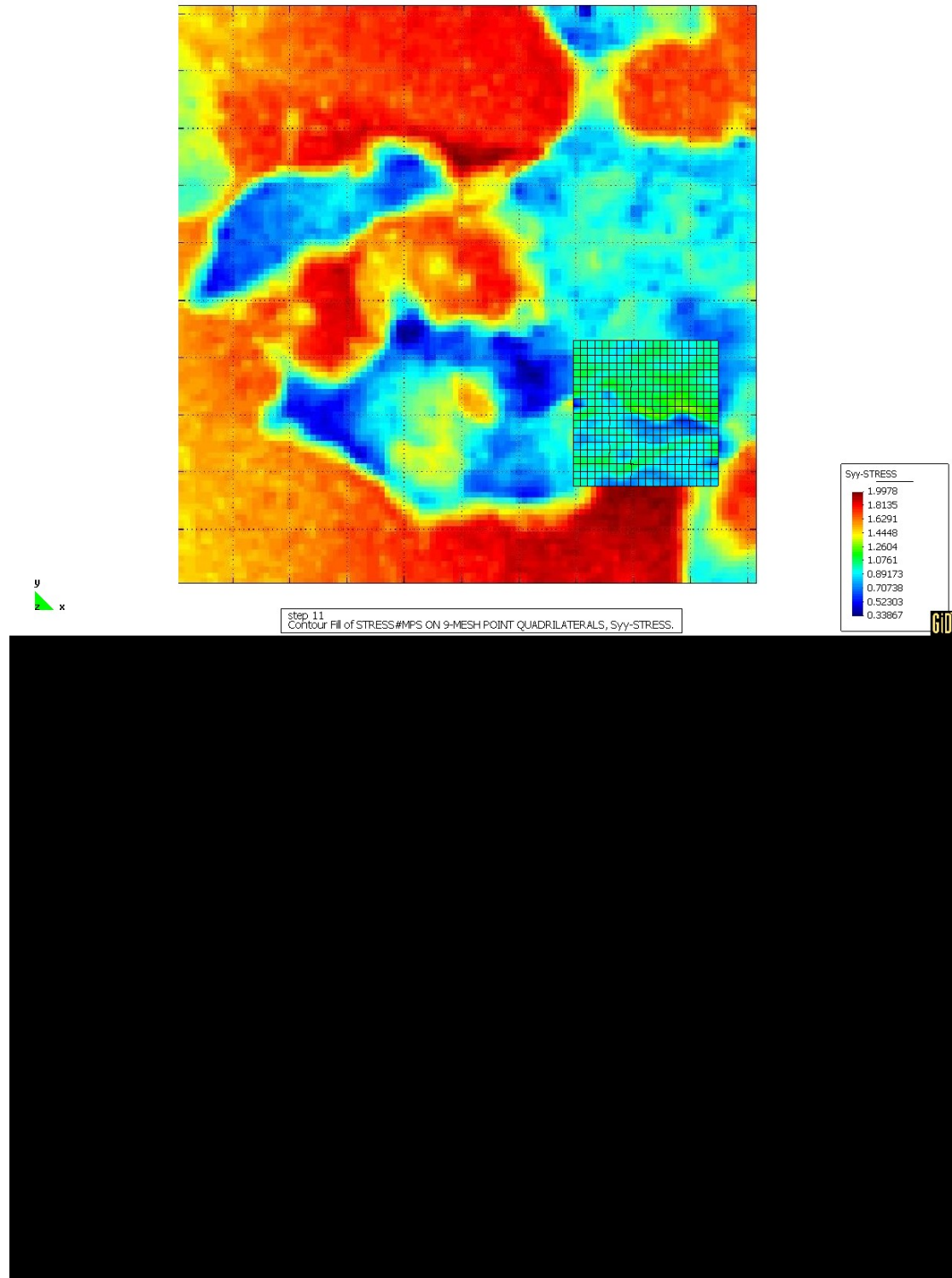


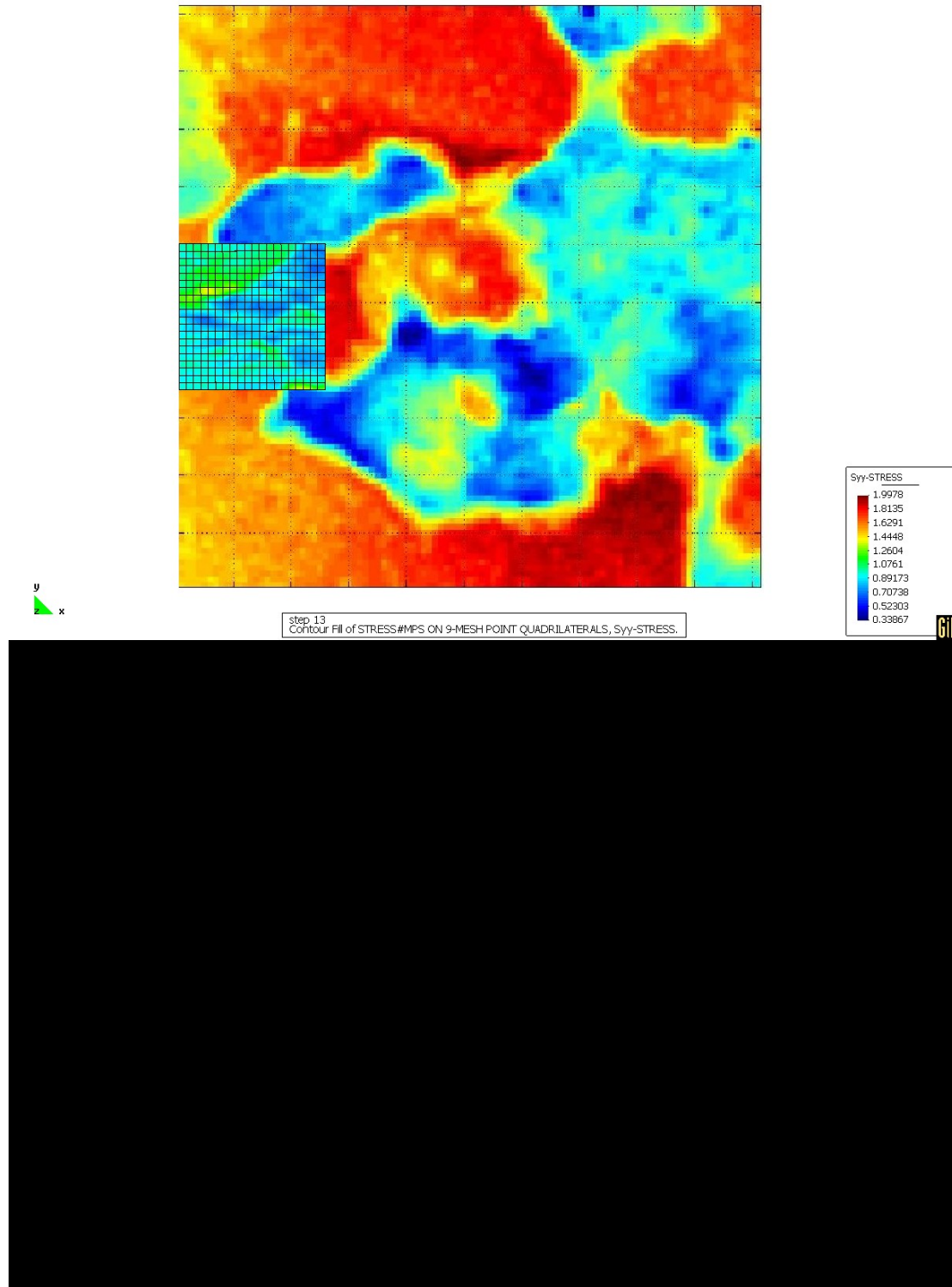


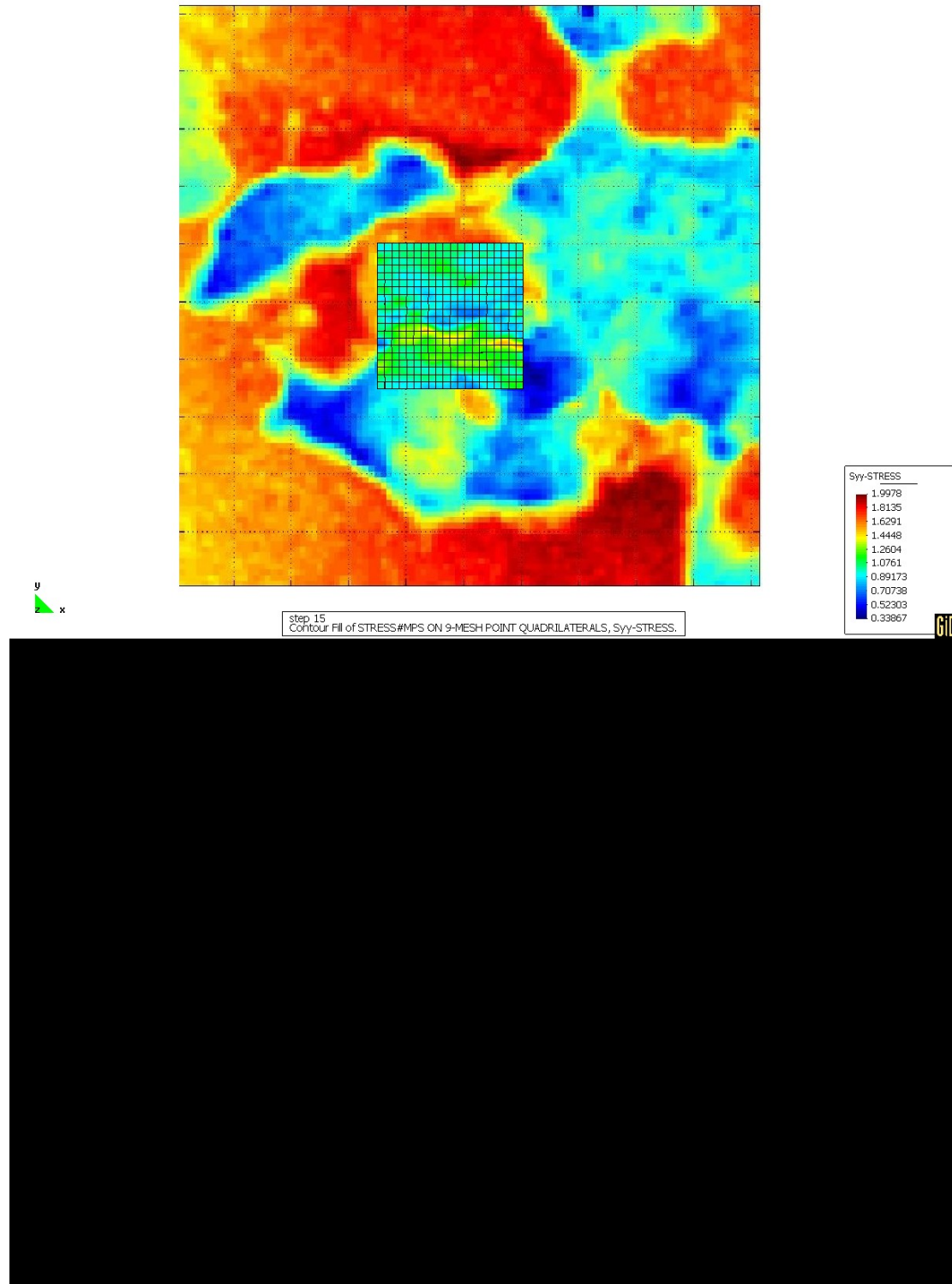


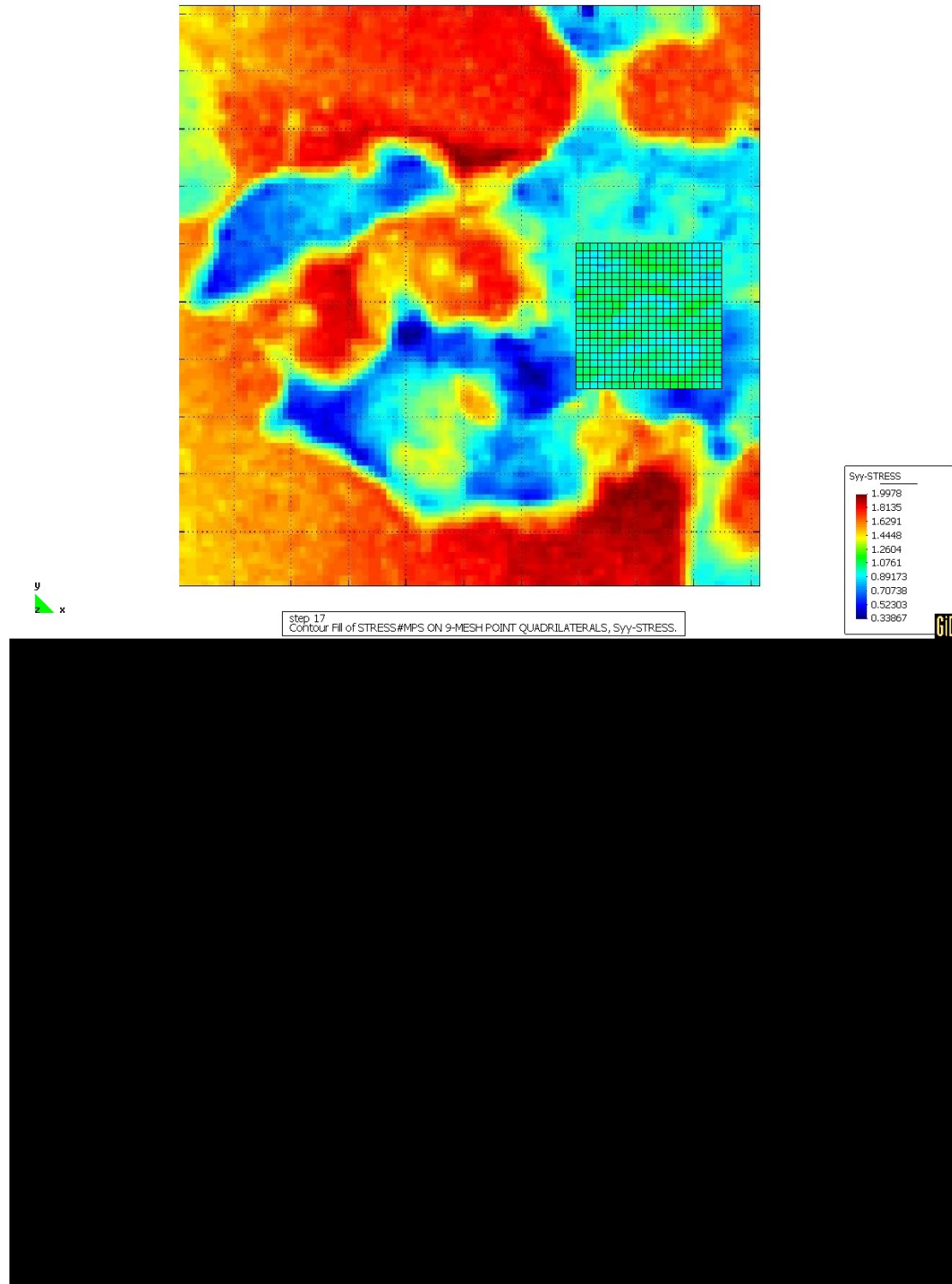


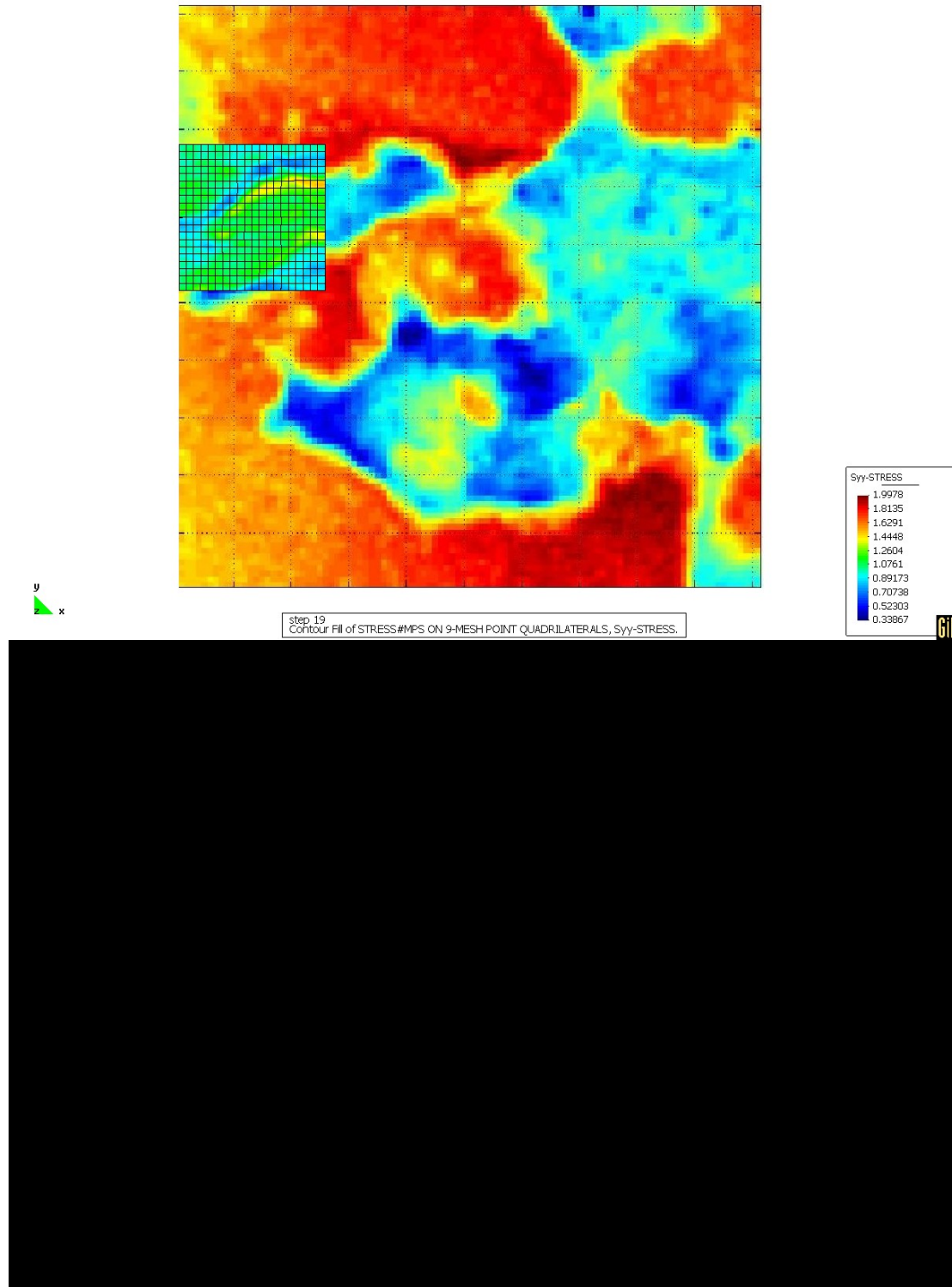


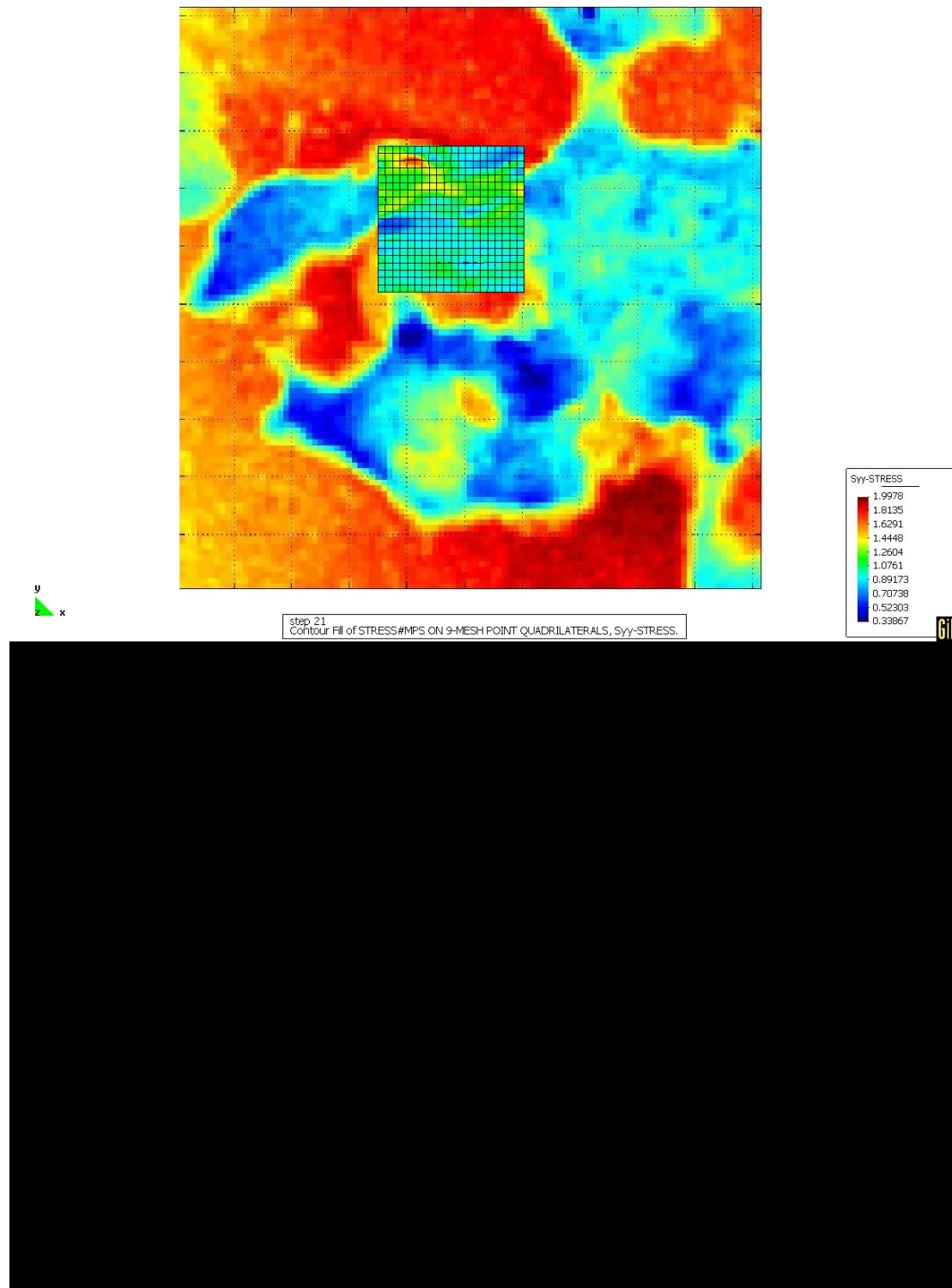


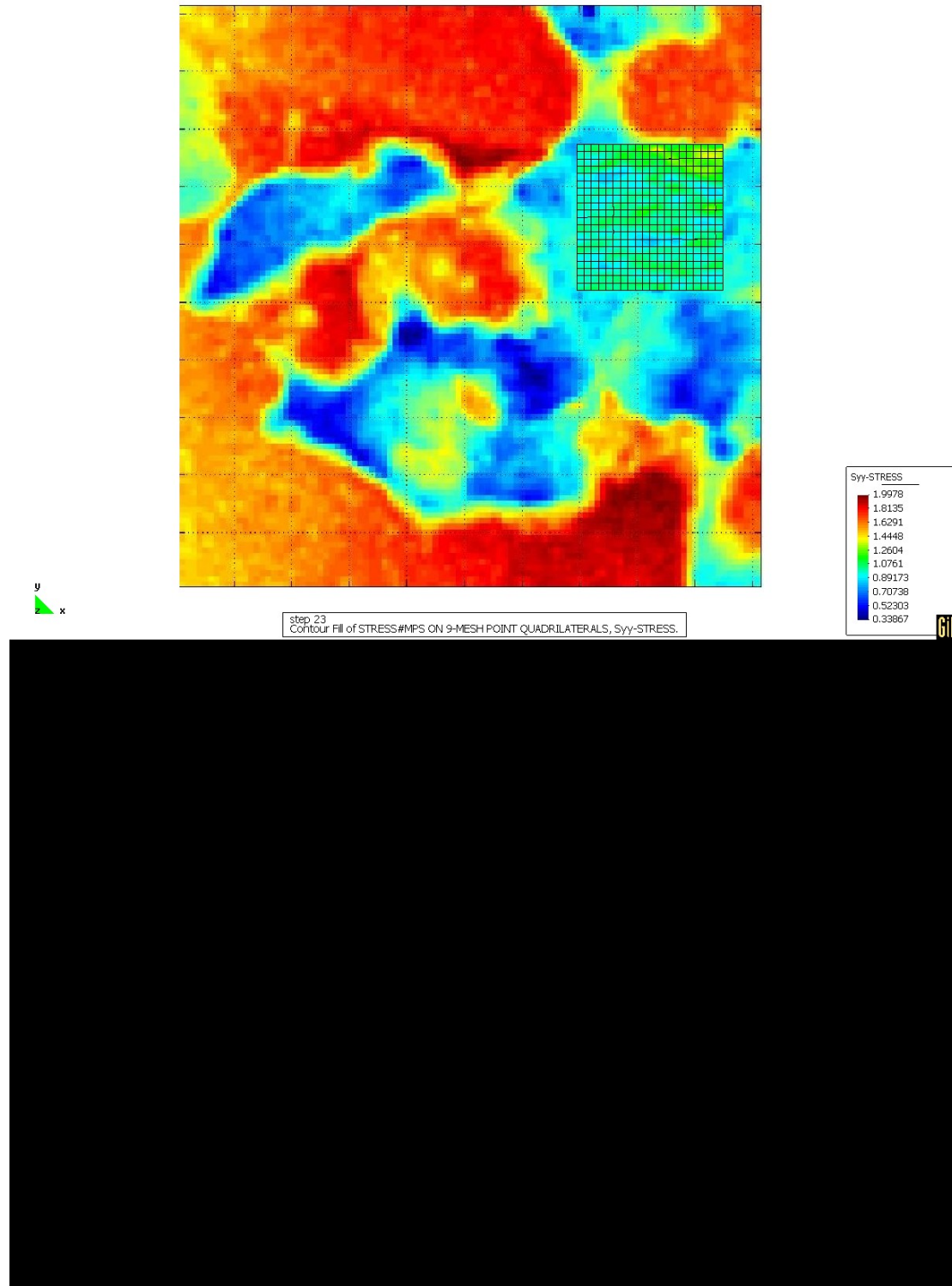


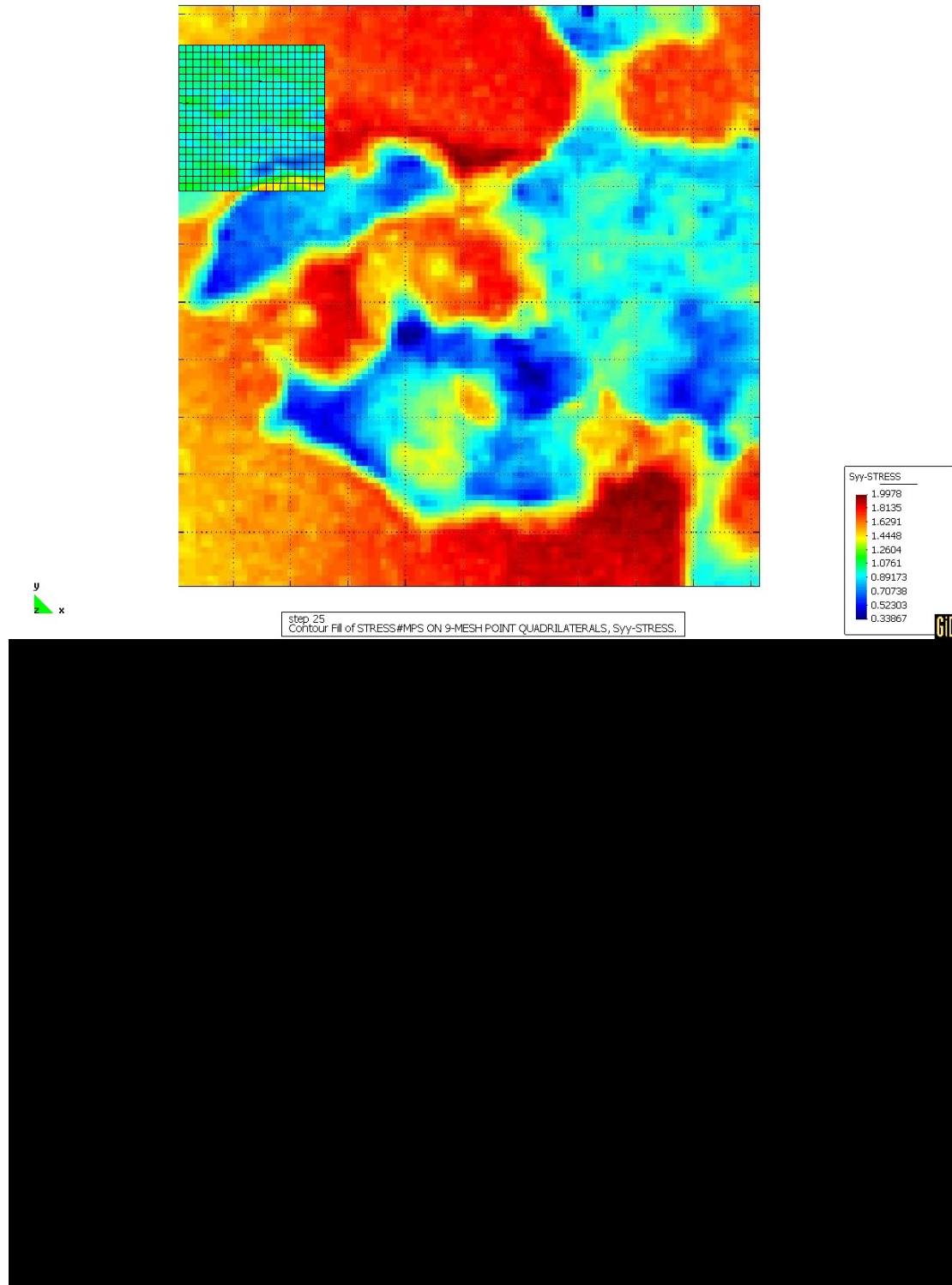


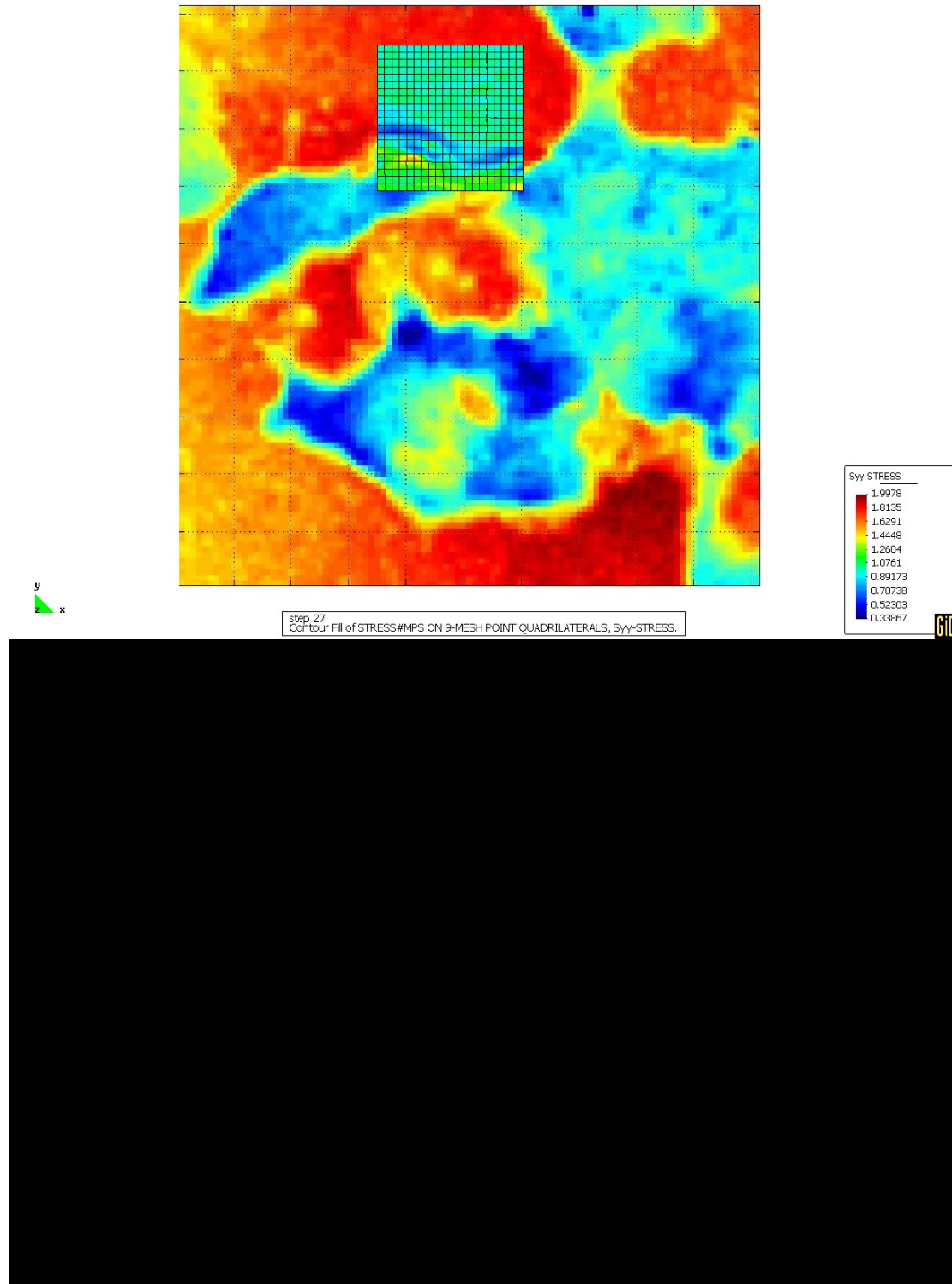


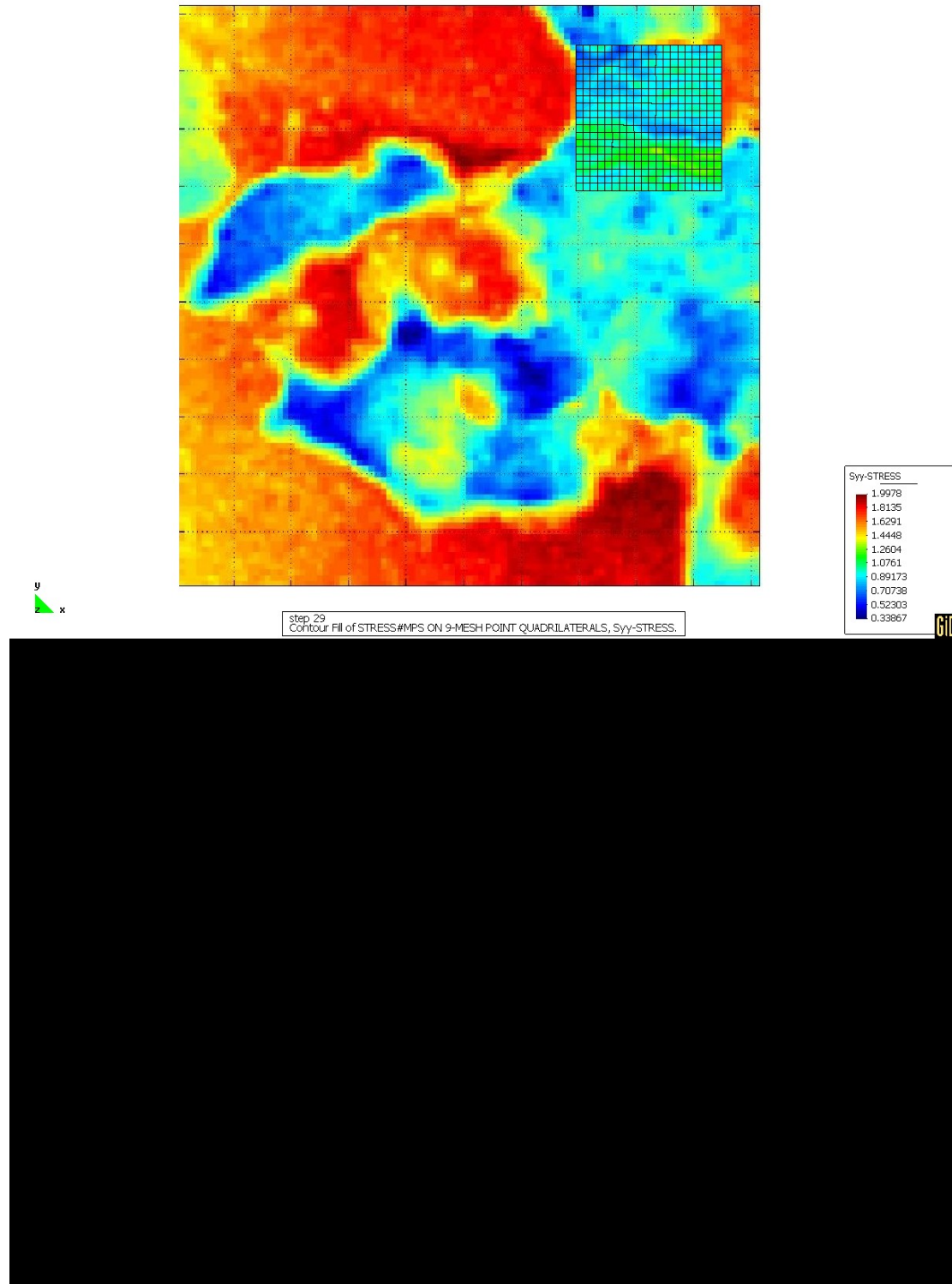


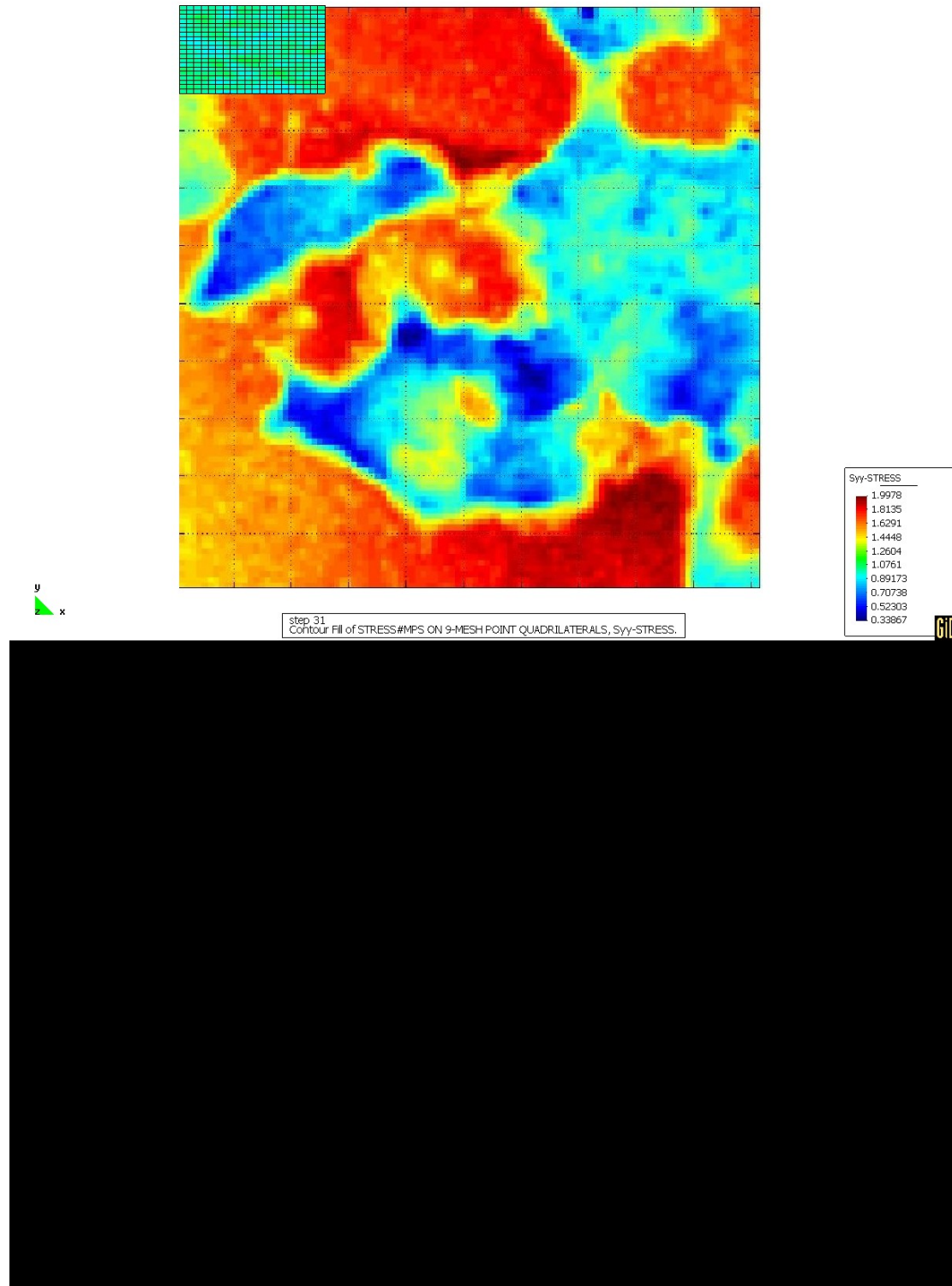


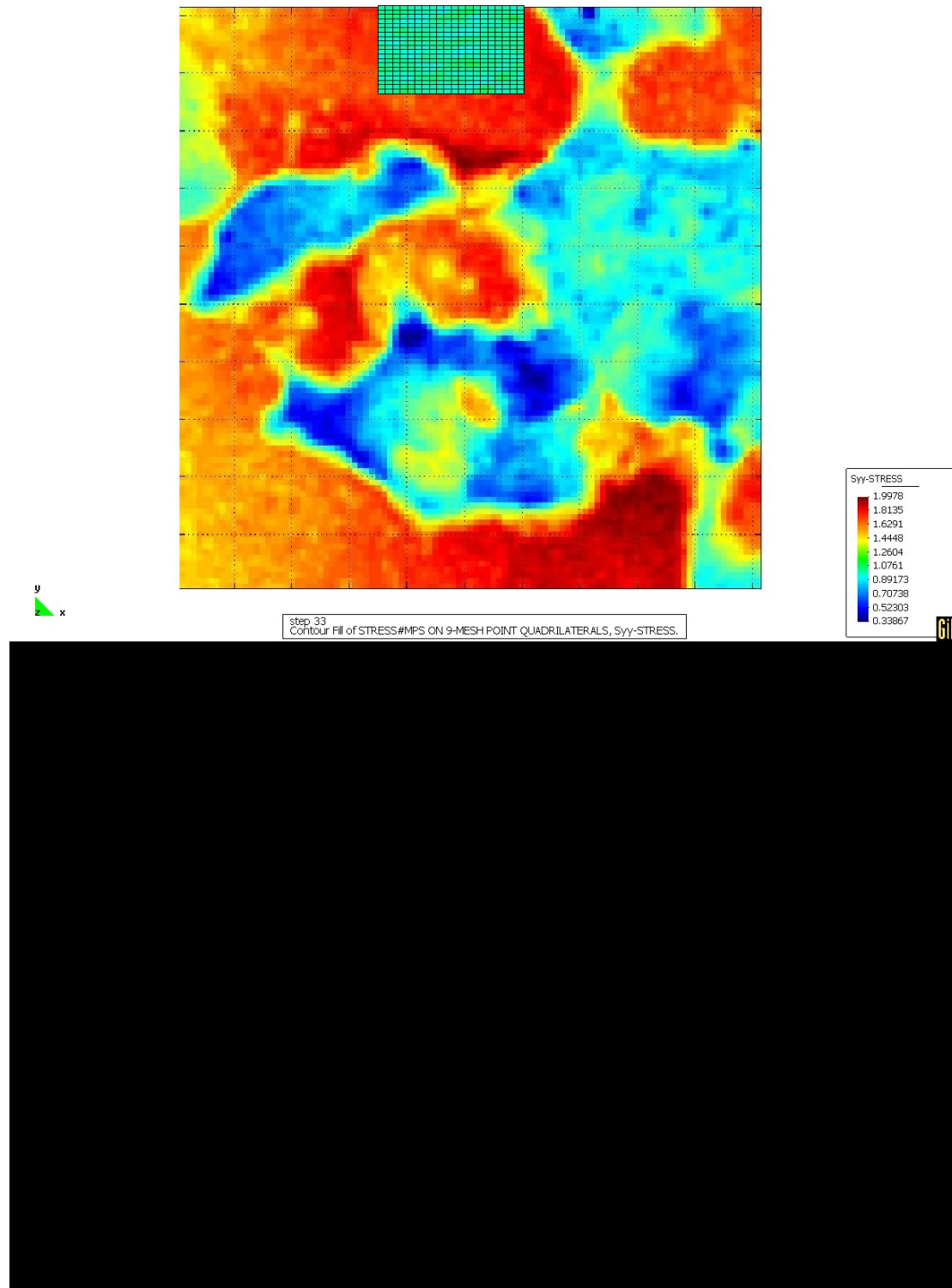


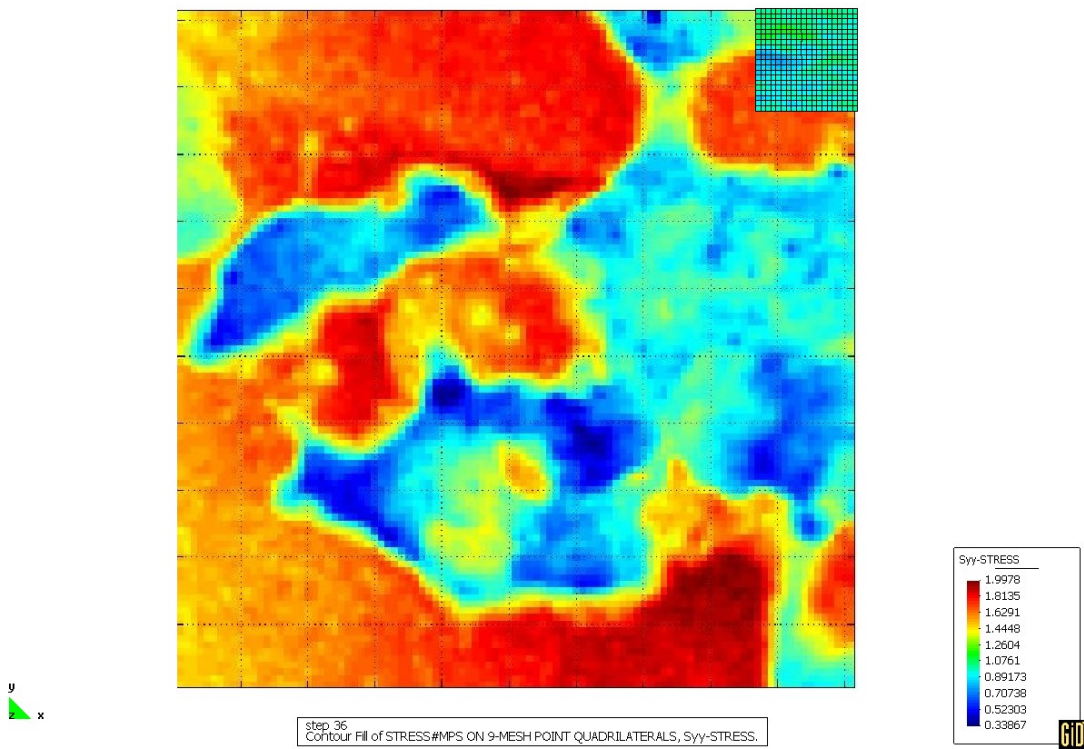
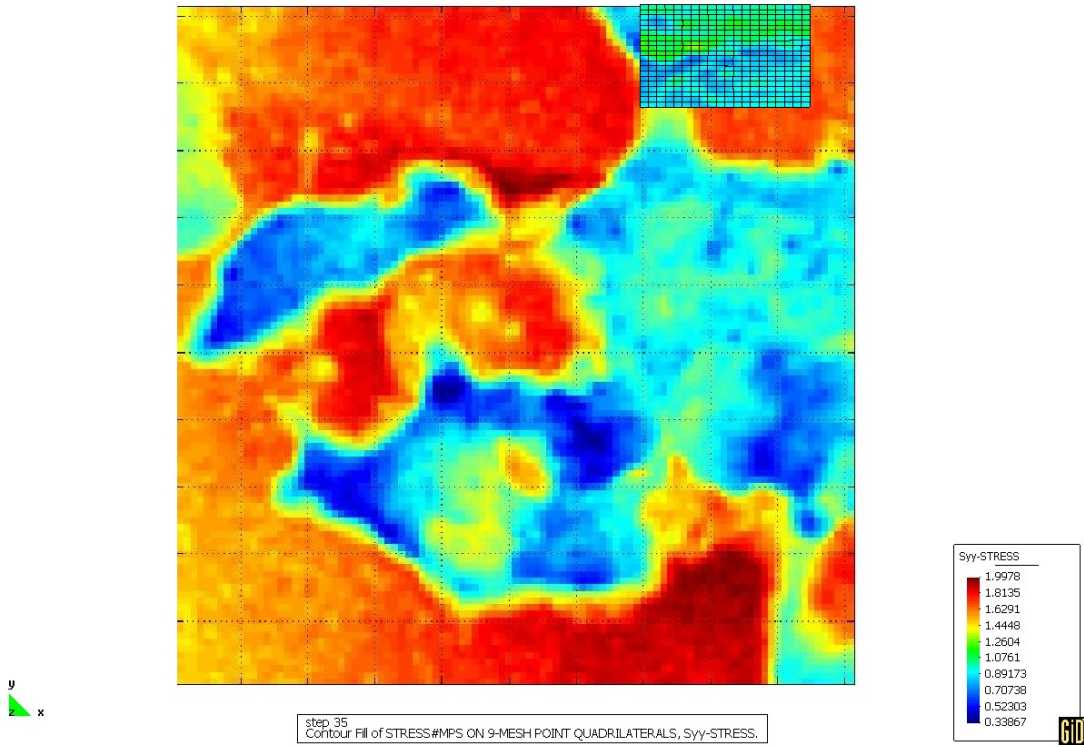












Appendix E

Computational Mechanics Software Instructions & Examples

SCF PITTING CORROSION CODE

1. QUICK REFERENCES

These are quick reference instructions in order to start using the code without a GUI interface

- 1) Copy the binary, setup, example and configuration files according to the file structure shown below
- 2) If necessary, edit **setup.dat**, **runall.bat** and **setup_sample.dat**, according to the particular need.
- 3) In order to launch a new calculation, issue: "**pit0.exe**" at the command prompt
- 4) The results for the stress concentration factor and geometrical error at the resolution level "**kout**" (chosen in **setup_sample.dat**) will be compiled into the following files, respectively: **scfKK.ascii.dat** and **geoKK.ascii.dat**

where **KK=kout** is the post-processing resolution level

The geometrical error is expressed as the minimum distance between the calculation mesh of the submodel and the exact original sample data. Intermediate files of geometrical error and SCF will also appear under the name convention: **geoKKNN.ascii.dat** and **scfKKNN.ascii.dat**, respectively, where NN is the iteration step.

- 5) The file "**user.log**" provides the x,y location of dangerous pits in logical (computational coordinates) at the resolution level kin. It then should be multiplied by Dx and Dy corresponding to kin in order to obtain physical (x,y) coordinates. In addition the maximum geom. error and SCF are given.

2. FILE STRUCTURE

The following directory structure is recommended:

Binaries

\$(PIT_PATH)\bin\pit0.exe	! binary file
\$(PIT_PATH)\bin\setup.dat	! configuration file
\$(PIT_PATH)\bin\runall.bat	! batch file
\$(PIT_PATH)\bin\out\	

Sample to solve

`$(PIT_PATH)\sample\out\` ! subdirectory for collecting intermediate sub-model results

`$(PIT_PATH)\sample\setup_sample.dat` ! input data file

`$(PIT_PATH)\sample\sp00.dat` ! geometrical information of the sample

where `$(PIT_PATH)` is the top level directory

3. CONFIGURATION FILES

"setup.dat"

This is a configuration file which specifies the path and file name of the sample to solve.

The file should be in the `$(PIT_PATH)\bin\` directory.

The entries of setup.dat are as follows:

&setup ! This keyword should be written as it is

path_dat = `'..\sample\'`, ! Either relative or absolute path to the working directory (i.e. the directory where the sample file is placed)

sample_file = `'sp00.dat'` , ! Name of the sample file

root_sample_file = `'sp'`, ! Root name of sample file. 'KK.dat' will be appended, where K = resolution factor

/

Note that any character on the right side of an exclamation sign is ignored and regarded as a comment by the code

"runall.bat"

DOS batch file launched by the code at each iteration step.

It normally instructs GID in order to prepare the submodel in a non-interactive way and then launches **BEASY MECHANICAL DESIGN** in order to solve the submodel

Note that runall.bat should contain the correct path to BEASY, and GID.

4. INPUT DATA FILES

"setup_sample.dat"

The input data file for a specific sample file is called, should be placed in the working directory (PATH_DATA) and named: setup_sample.dat

Any character on the right hand side of the exclamation symbol "!" are comments ignored by the code.

The file contains a series of namelists with parameters to be customised by the user.

```

&sample_info
  Npx = 700 ,      ! Number of points in x direction (fields) of the original sample file
  Npy = 840 ,      ! Number of points in y direction (records) of the original sample file
  delta_x0 = 25.38, ! Delta x of original sample file [microns]
  delta_y0 = 25.38, ! Delta y of original sample file [microns]
  sample_depth = 3175.0, ! Sample depth [microns]
/

&defeature_info !! This keyword should be written as it is
  max_red_factor = -1, ! Maximum Reduction factor R, overrides default only if .ge. 0
  default_window = .true. ! [1 , Npx] x [1,Npy]
  irx0 = 1041 ,! Use these values in order to define the corners of
  irx1 = 1849 ,! the region to defeature in case that default_window = .false.
  iry0 = 1281 ,!
  iry1 = 2089 ,!
/

&submodeling ! This keyword should be written as it is
  kout=1, ! Resolution level for postprocessing the results (original sample has resolution k=
0)
  max_iters=30, ! Max number of submodels to solve per cycle
  Ncellx=10, ! Number of cells in x direction for the submodel
  Ncelly=10, ! Number of cells in y direction for the submodel
  Npmaxx=200, ! Maximum number of points for defining the top surface of the submodel
along x direction
  Npmaxy=200, ! Maximum number of points for defining the top surface of the submodel along
x direction
  overlap=1, ! Overlapping factor between submodels
  batch0='runall.bat', ! Batch script to run at each iteration
  max_iterid = 60, ! Total Max. number of submodels to solve
/

&gidata ! This keyword should be written as it is
  Nnod_max = 3000, ! Maximum number of nodes in the mesh that defines each submodel
  Nelem_max=700 ! Maximum number of elements for the mesh defining each submodel
/

&postdata ! This keyword should be written as it is
  scf_threshold = 0.999 , ! Percentage of temporal maximum SCF
  geo_threshold = 20.0, ! Max geom. error allowed
  max_ncen = 10000, ! Maximum number of calc centres expected
/

```

5. RESULTS

The sample file shown in Figure 1 has been taken as a test example in order to illustrate the outcome of the PIT code. The data has been obtained from a small defeatured region of the Dogbone example provided by UDRI.

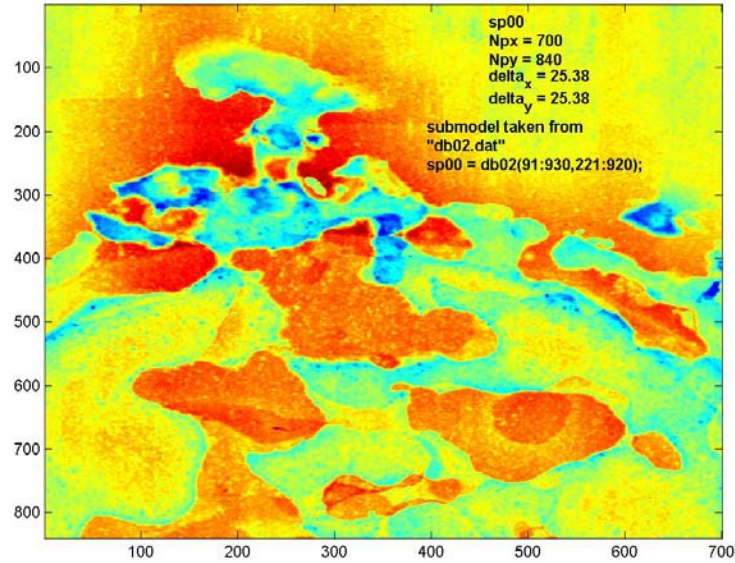


Figure 49. Density plot of Z coordinate. This data has been used as a test example. $D_x = 25.38 \text{ um}$ $D_y = 25.38 \text{ um}$

A density plot of the geometrical error in the 1st and 12th iterations steps are shown in Figure 2,

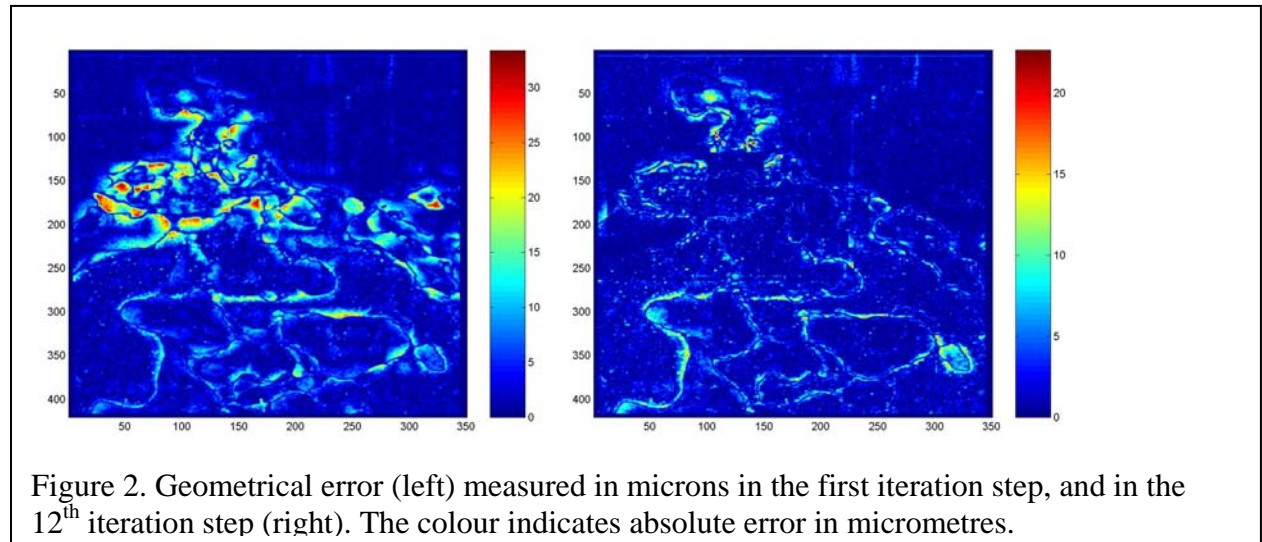
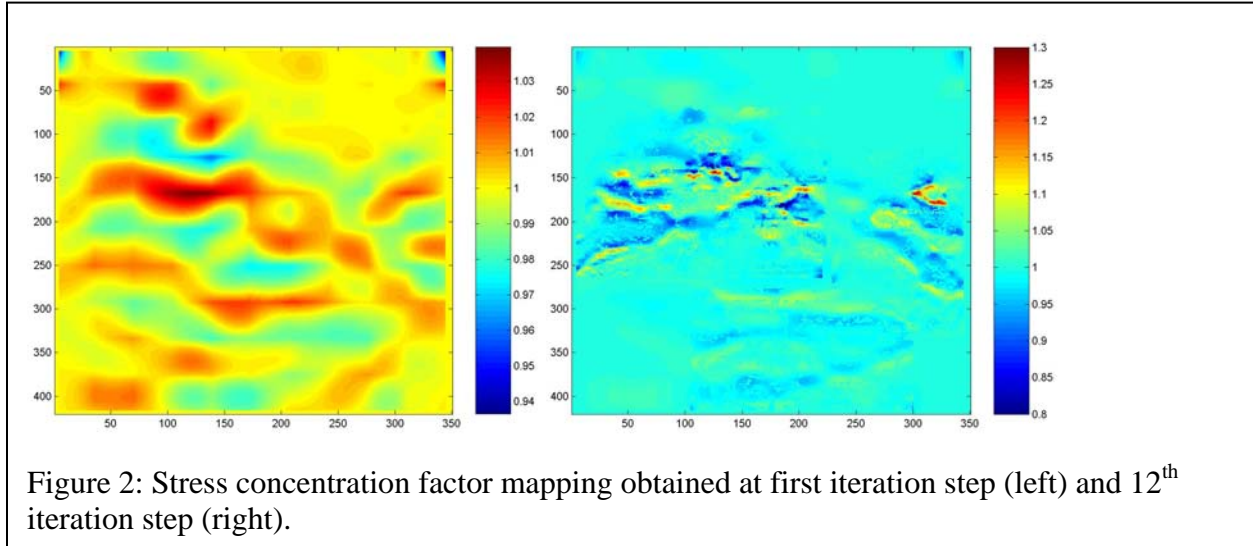


Figure 2. Geometrical error (left) measured in microns in the first iteration step, and in the 12th iteration step (right). The colour indicates absolute error in micrometres.

while Fig. 3 shows the corresponding stress concentration factors.



These results can be reproduced by launching the code with the setup options provided above.

Initial distribution of BEASY Pitting Software

=====

1. The contents of this initial distribution CD are as follows:

instructions.txt	this file
doc\readme.txt	text file with brief instructions
doc\QUICK_REFERENCES.doc	Word doc file with more detailed instructions
GiD\GiD7.5.6b-win.exe	GiD installation executable
GiD\problemtypes\pit.gid	Folder containing the various files required to make GiD export the BEASY data file
pitting_bin\	Folder containing various files as follows:
pitting_bin\setup.dat	Text file which is accessed by "pit0.exe".
pitting_bin\RUNALL.BAT	Batch file which is accessed by the executable "pit0.exe"
pitting_bin\pit0.exe	Executable which controls the simulations etc.
pitting_bin\OUT	Folder into which the data files and results files are transferred during the solution process.
sample\sp00.dat	Text file containing heights of the surface. This is a small defeatured region of the Dogbone example provided by UDRI.
sample\setup_sample.dat	Text file giving information about the sp00.dat file.

2. In order to test this preliminary software you must:

- A. Copy the software on this CD to some location on your machine.**
- B. Install BEASY V10R7 software (using the usual BEASY installation CD).**

Set up the BEASY licensing.

Note you MUST have a license for the BEASY feature "BEASY_GID", as well as for the feature "BEASY_STRESS".

- C. Install the version of GiD contained in this CD, by running the executable "GiD\GiD7.5.6b-win.exe".**

- D. Copy the folder "GiD\problemtypes\pit.gid" to the subfolder called "C:\Program Files\GiD\GiD7.5.6b\problemtypes" which was created during step 2.**

E. Edit file "RUNALL.BAT" as follows:

i. Change the line "set BEASYLMD_LICENSE_FILE=C:\apps\beasy" to point to your BEASY license file.

ii. Change the line which contains text "C:\apps\beasy\beasyand.exe" to make the path correctly point to the file "beasyand.exe" in your BEASY installation.

F. Create a command shell (eg using "Run cmd"), and cd to folder "pitting_bin".

G. In the command shell type "pit0.exe" followed by <RETURN> to start the simulation.

3. What "pit0.exe" does:

The "pit0.exe" executable performs actions as follows:

A. It reads the various setup files.

B. It creates a series of submodels, and solves them using BEASY

**C. It places the data file and various results files into folder:
pitting_bin\OUT**

**D. It collects results, and puts them in a file containing stress concentration factors. This file is in the same format as the original surface heights, so can be viewed using
any software which is able to view the surface heights.**

E. At the end of successful solution the "cmd" shell should show text similar to the following:

```
D:\pitting\pitting_bin\out\smo1_0032.gdf
D:\pitting\pitting_bin\out\smo1_0032.log
D:\pitting\pitting_bin\out\smo1_0032.post.msh
D:\pitting\pitting_bin\out\smo1_0032.post.res
Calculation concluded
scf_file = ..\sample\scf01.dat
```

F. The stress concentration factor file called "scf01.dat" is binary.

The file called "scf01.ascii.dat" is ASCII text, and contains the same data as file "scf01.dat".

Appendix F

Abbreviations and Symbols

Sa – Average Surface Roughness

Sq – Root Mean Square surface roughness.

Sp – Maximum Surface height Peak.

Sv – Maximum Surface height Valley

St – Maximum difference from the highest peak to the lowest valley.

Sz – Average maximum height of the profile.

S index (Surface Area Index) – The ratio of the surface area of the profile to the surface area of an ideal plane.

NVL (Normalized Volume Loss) – The ratio of the volume missing to the lateral area.

Skewness – A measure of the symmetry of the profile about the mean line.

Kurtosis – A measure of the sharpness of the profile about the mean line.

Rpk (Reduced Peak Height) – The top portion of the surface that will be worn away during the run-in period.

Rvk (Reduced Valley Depth) – The lowest portion of the surface that will retain lubricant.

Htp – Defined by setting the tp1 (peak threshold bearing ratio value) and tp2 (the valley threshold bearing ratio value) to be separated by 40%.